THE UNIVERSITY *of* EDINBURGH

On incorporating bone microstructure in macro-finite-element models

Finn Ewan Donaldson

Doctor of Philosophy

The University of Edinburgh

2011

Declaration

This thesis and the associated research has been completed by Finn Ewan Donaldson and has not been submitted for any other degree or professional qualification.

Finn Ewan Donaldson
March 2011

For Amanda

"*So convenient a thing it is to be a reasonable creature, since it enables one to find or make a reason for every thing one has a mind to do.*"

Benjamin Franklin

Abstract

Bone is porous and has a complex microstructure. This study considers the effect of microstructural morphology on the macrolevel mechanical properties of bone. Improved incorporation of such properties is required to advance current finite element approximations of bone behaviour.

A technique to computationally generate realistic trabecular bone microstructures is developed. This provides the possibility of examining the effect of different microstructures on the macrolevel mechanical behaviour of bone. They would also permit direct incorporation of bone microstructure in macroscale finite element analyses without the prohibitive computational and experimental costs of donor-image based mesh generation. Micro-finite-element analyses are used for the first time to evaluate the macrolevel orthotropic elastic constants of cortical bone resulting from variations of microstructural morphology. It is concluded that the ratio of canal volume to tissue volume is the most powerful predictor of cortical bone elastic constants and that considerable periosteal-endosteal variations in these constants can develop with bone loss. The role of microstructure in cortical bone toughness is investigated using nano-finite-element analyses of murine cortical bone samples to simulate the initiation and propagation of microcracks. Results confirm the experimentally observed ability of canal and lacuna pores to act as stress raisers, thereby guiding the growth of microcracks. A novel and numerically efficient strain-based plasticity algorithm is presented which permits easy incorporation of strength anisotropy in finite element analyses of bone. The previously evaluated elastic properties of cortical bone are combined with the developed plasticity algorithm to conduct a detailed macro-finite-element investigation of external fixation of tibial midshaft fractures. Old patients are found to be at considerably higher risk of implant loosening under both unilateral and Ilizarov fixation, compared to younger patients.

Acknowledgements

Many characters contributed to this work. Besides the key roles below, I thank the supporting cast of friends too numerous to name here individually.

First thanks go to my Supervisor Dr Pankaj for his guidance and essential skill of explaining even the most complicated of concepts in a couple of sketches and well chosen words. I can only hope future bosses become as good friends.

Also to my second supervisor Professor Hamish Simpson for his regular support and for sharing his great research and clinical experience with me over the past years.

The lead role was originally shared in Chapter 2 with Dr Angus Law. I thank him and Dr Ben Cowan for all their technical input, puns and banter.

Chapter 3 built on much work by Dr David Cooper, Dr David Thomas and Professor John Clement. I thank them also for their encouragement throughout my PhD.

I am grateful for the warm welcome provided to me by all at the ETH Institute for Biomechanics in Zurich. Alina Levchuck, Alexander Zwahlen, Dr Davide Ruffoni, Dr Philipp Schneider and Professor Ralph Müller provided critical input to the work presented in Chapter 4.

Several fellow PhD students directly aided me in developing this research. I would specifically like to thank Noel Conlisk, Dr Chong Zhou, Dr Jun Ai, Dr Craig Warren, Dr Vijay Narayanamurthy, Dr David Lange and Dr Cornelia Doerich for their help.

I extend special thanks to all at the Carnegie Trust for the Universities of Scotland who have repeatedly honoured me by investing in this research.

With their skill and enthusiasm Dr Waterstone, Mr Harkins and Mr Latona equipped me with the mathematics, physics and computing knowledge used so extensively in this PhD. I see now that grad school started in their high school classrooms.

My ability to even knock on this door is due in large part to my parent's efforts to ensure that so many preceding it lay open to me; I'm sure my siblings Lauren and Neil would agree that far more than two-fifths of the Donaldson doctorates can be attributed to their efforts.

Most of all I thank Amanda for her patience with this third member of our relationship, for her love and for the future.

Contents

List of Figures

List of Tables

Nomenclature

Throughout this work tensor quantities are indicated by a $\underset{\sim}{}$ symbol; accordingly, x is a scalar and $\underset{\sim}{x}$ is a tensor.

1D,2D,3D	One, two or three dimensional
a	Half of the length of a crack
c_{ij}	Entry i, j of the elasticity tensor in Voigt form
$d\lambda$	The plastic multiplier
$d\psi^{x,y,z}$	Infinitesimal rotation angle about the x, yor$z$ axis
eigval($\underset{\sim}{x}$)	Function which returns the eigenvalues of $\underset{\sim}{x}$
f	Yield surface defined in stress-space
$f\left(\frac{a}{w}\right)$	Geometrical scaling factor in toughness tests
g	Yield surface defined in strain-space
$g_{1,2,3c}$	Compressive yield surface in the max. mid. and min. principal strain directions
$g_{1,2,3t}$	Tensile yield surface in the max. mid. and min. principal strain directions
$k_1,\ k_2$	Stiffness of elastic springs 1 and 2
k_o	Stiffness of a reference elastic spring
l_i	Exposed length of an Ilizarov wire at site i
max_{del}	Maximum number of deleted voxels per cluster with the *CL* algorithm
min_{del}	Minimum number of deleted voxels per increment without increased applied displacements
p	Statistical significance
p_{ent}	Significance for addition to stepwise regression
p_{exit}	Significance for removal from stepwise regression
r^2	Coefficient of determination
r^2_{ave}	Average coefficient of determination
$\underset{\sim}{r}^l$	A vector parallel to the line defined at the intersection of two yield surfaces
t	A parameter to determine the elastic strain during a return to a line
vBMD	Volumetric bone mineral density
vox	The edge length of single, cube-shaped voxel
$x,\ y,\ z$	Orthogonal axes in a Cartesian coordinate system
$\hat{x},\ \hat{y},\ \hat{z}$	Cartesian coordinate system aligned with the principal elastic strain directions
$\left\|\underset{\sim}{x}\right\|$	Euclidean vector or matrix norm of $\underset{\sim}{x}$
$\underset{\sim}{A}$	A 6×6 transformation tensor to produce a coordinate system rotation
$A_{\text{Ca.Dm}}$	Coefficient of Ca.Dm in multiple linear regression
$A_{\text{Ca.S/TV}}$	Coefficient of Ca.S/TV in multiple linear regression
ACP	Axial connectivity probability
$A_{\text{Ca.V/TV}}$	Coefficient of Ca.V/TV in multiple linear regression
A_{DA}	Coefficient of DA in multiple linear regression
AFM	Atomic force microscopy
A_{ind}	Coefficient of index ind in multiple linear regression
A_n	Cross-sectional area of the notched region of murine femora in DIGFA experiments
A_u	Cross-sectional area of the unnotched regions of murine femora in DIGFA experiments

B6	Genetic strain of inbred mice C57BL/6J
BMC	Bone mineral content
BMD	Bone mineral density
BV/TV	Ratio of bone volume to tissue volume
C3H	Genetic strain of inbred mice C3H/HeJ
Ca.Dm	Mean canal diameter
Ca.Sp	Mean canal spacing
Ca.S/TV	Canal surface area to tissue volume ratio
Ca.V/TV	Canal volume to tissue volume ratio
$\text{Ca.V/TV}_{\text{ave}}$	Mean specimen Ca.V/TV
CCD	Charge-coupled device
$\underset{\sim}{C}^e$	Effective elastic compliance tensor
$\hat{\underset{\sim}{C}}^e$	$\underset{\sim}{C}^e$ referred to the principal elastic strain directions
$\hat{C}^e_{ij}$	Entry i, j of $\hat{\underset{\sim}{C}}^e$
$\underset{\sim}{C}_K$	Kelvin form of the elasticity tensor
CL	The component labelled microcracking algorithm
CP	Connection point
CRS	Edge length of a cubic region used to evaluate the finite element gradient
CT	Computed-tomography
Ct.BV/TV	Cortical BV/TV
Ct.Th	Mean cortical thickness
$\underset{\sim}{C}_V$	Voigt form of the elasticity tensor
D	Applied displacement in DIGFA experiments
DA	Degree of morphological anisotropy
$\underset{\sim}{D}^e$	Effective elastic stiffness tensor
$\hat{\underset{\sim}{D}}^e$	$\underset{\sim}{D}^e$ referred to the principal elastic strain directions
$\hat{D}^e_{ij}$	Entry i, j of $\hat{\underset{\sim}{D}}^e$
$\underset{\sim}{D}^{e,\text{ORT}}$	Orthotropic form of the effective elastic stiffness tensor
$\hat{\underset{\sim}{D}}^{ep}$	The tangent modulus matrix referred to the principal elastic strain directions
$\left\langle \hat{\underset{\sim}{D}} \right\rangle^{ep}$	A tensor containing only the terms of $\hat{\underset{\sim}{D}}^{ep}$ relating normal stresses and strains
$\underset{\sim}{D}^{epc}$	The consistent tangent modulus matrix
$\hat{\underset{\sim}{D}}^{epc}$	$\underset{\sim}{D}^{epc}$ referred to the principal elastic strain directions
$\underset{\sim}{D}^e_t$	Tissue-level elastic stiffness tensor
DDV	The deletion direction vector from a crack tip
DDV^i	The component of DDV contributed by voxel i
DIGFA	Dynamic image guided failure assessment
E	Young's modulus
EDT	Euclidean distance transform
$\text{EDT}^i_{p,e}$	EDT at point i relative to the periosteum (p) or endosteum (e)
$E^{(i)}$	Young's modulus at location i
E_i	Young's modulus in the i direction
F	Applied force
F_n	Force carried by a notched bone cross-section
FE	Finite element
F_u	Force carried by a unnotched bone cross-section
$\hat{\underset{\sim}{G}}$	A tensor containing only the shear stiffness terms of $\underset{\sim}{D}^e$, referred to the principal elastic strain directions
$G^{(E\nu\beta)}$	Shear modulus calculated using linearly interpolated E and ν at β
$G^{(i)}$	Shear modulus at location i
G_{ij}	Shear modulus in the ij plane
I	Cross-section second moment of area
$\underset{\sim}{I}$	The identity tensor

I_c	A temporary image containing clusters of elements for the CL algorithm
IM	Intramedullary (nail)
J	The J-integral
K	Stress intensity factor at a crack tip
K_C	The critical value of K at crack initiation in plane stress
K_{IC}	The critical value of K at crack initiation in plane strain
$\hat{K}_o$	Reference stiffness of a system of springs
$\hat{K}_{o\pm\alpha}$	Stiffness of a system of varied springs
K_R	Values of K at crack propagation with rising crack resistance behaviour
LEFM	Linear elastic fracture mechanics
L_n	Length of the notched region of murine femora in DIGFA experiments
L_p	Half-pin length
L_u	Total length of the unnotched regions of murine femora in DIGFA experiments
$\underset{\sim}{M}$	The local structure tensor
MFC	Melbourne Femur Collection
MRI	Magnetic resonance imaging
NLG	Non-linear geometry (large deformation)
NLM	Non-linear material
NLMG	Materially and geometrically non-linear
R,C,L	The radial, circumferential and longitudinal directions
ROI	Region of interest
SAXS	Small angle x-ray scanning
SCL	Stress concentration limiter
SLS	Swiss light source
SMI	Structure model index
S_{ob}	Object surface area
SRCT	Synchrotron radiation based computed tomography
PMMA	Poly-methyl-meth-acrylate
$\underset{\sim}{T}$	Consistent tangent operator
Tb.N	Trabecular number
Tb.Pf	Trabecular pattern factor
Tb.Sp	Trabecular spacing
Tb.Th	Trabecular thickness
Th^i	Cortical thickness at point i
T_o	Ilizarov wire pre-tension
Tol.1,2,3	Microcracking algorithm tolerances 1, 2 and 3
TOMCAT	Tomographic microscopy and coherent radiology experiments beamline at the SLS
V	Total sample volume
$V_i^{(1)}$	Eigenvector i of the material elasticity tensor at location 1
$V_i^{(avg)}$	The i^{th} eigen-averaged eigenvector of multiple $\underset{\sim}{C}_K$
$V_i^{(na)}$	The i^{th} nominally weighted average eigenvector of multiple $\underset{\sim}{C}_K$
V_{ob}	Object volume
X-FEM	The extended finite element method
Y_c	Compressive yield strain
Y_t	Tensile yield strain
α	Linear scale factor of spring stiffness
β	Linear position interpolation variable
γ^{app}	Applied shear strain
γ_{ij}	Shear strain in the ij plane
ΔS_{ob}	Change in object surface area from one-voxel dilation
$\underset{\sim}{\epsilon}$	Strain tensor
$\hat{\underset{\sim}{\epsilon}}$	Strain tensor referred to the principal elastic strain directions
$\epsilon_{1,2,3}$	Max. mid. and min. values of total strain
ϵ^{app}	Applied strain
$\underset{\sim}{\epsilon}^{\mathrm{app}}$	Applied state of strain
ϵCF	Strain concentration factor

$\underset{\sim}{\epsilon}^e$	Elastic strain tensor
$\hat{\underset{\sim}{\epsilon}}^e$	Elastic strain tensor referred to the principal elastic strain directions
$\epsilon^e_{1,2,3}$	Elastic max. (1), mid. (2) and min. (3) principal strain components
$\hat{\underset{\sim}{\epsilon}}^e_T$	Vector of trial principal strains
$\epsilon^e_{T1,2,3}$	Trial max. (1), mid. (2) and min. (3) principal strains
ϵ_{homo}	Homogenised strain
ϵ_{ij}	Component i, j of $\underset{\sim}{\epsilon}$
$\hat{\underset{\sim}{\epsilon}}^l$	A point on a line of intersection between two yield surfaces in principal strain space
$\underset{\sim}{\epsilon}^{loc}$	Local state of strain
ϵ_n	Longitudinal strain applied over the notched region of murine femoral samples
$\underset{\sim}{\epsilon}^{\mathrm{ORT}}$	State of strain calculated using $\underset{\sim}{D}^{e,\mathrm{ORT}}$
$\underset{\sim}{\epsilon}^p$	Plastic strain tensor
$\hat{\underset{\sim}{\epsilon}}^p$	Plastic strain tensor referred to the principal elastic strain directions
$\dot{\underset{\sim}{\epsilon}}^p$	Plastic strain rate
$\epsilon_{R,C,L}$	Strain in the radial, circumferential or longitudinal directions
ϵ^{ref}	Reference triaxial applied state of strain in microcracking FE analyses
ϵ_{solid}	Strain in the solid region of a sample (non-homogenised)
ϵ_T	Strain applied over the total embedded length of murine femoral samples
ϵ_u	Longitudinal strain applied over the unnotched region of murine femoral samples
ϵ_y	Yield strain
$\Lambda_i^{(1)}$	Eigenvalue i of the material elasticity tensor at location 1
$\Lambda_i^{(avg)}$	Average eigenvalue i referred to the average eigenbasis
μ_{cc}	Compression-compression singularity indicator
μ_{ccc}	Compression-compression-compression singularity indicator
μ_{cct}	Compression-compression-tension singularity indicator
μ_{ct}	Compression-tension singularity indicator
μCT	Micro CT
μFE	Micro finite element
μ_{tc}	Tension-compression singularity indicator
μ_{tcc}	Tension-compression-compression singularity indicator
μ_{tct}	Tension-compression-tension singularity indicator
μ_{tt}	Tension-tension singularity indicator
μ_{ttc}	Tension-tension-compression singularity indicator
μ_{ttt}	Tension-tension-tension singularity indicator
$\mu\epsilon$	Micro strain ($\epsilon \times 10^6$)
ν	Poisson's ratio
$\nu^{(i)}$	Poisson's ratio at location i
ν_{ij}	Poisson's ratio of strain in the j direction induced by strain in the i direction
$\underset{\sim}{\sigma}$	Stress tensor
$\hat{\underset{\sim}{\sigma}}$	Stress tensor referred to the principal elastic strain directions
σ_1	Maximum principal stress
σCF	Stress concentration factor
σ_d	The damage stress
σG	The stress gradient based microcracking algorithm
σ_{homo}	Homogenised stress
σ_1^i	Maximum principal stress in voxel i

σ_{ij}	Component i, j of $\underset{\sim}{\sigma}$
σ_{lim}	Microcracking algorithm based on a limiting value of max. principal stress
σ_{solid}	Stress in the solid region of a sample (non-homogenised)
$\hat{\underset{\sim}{\sigma}}_T$	Vector of trial principal stresses
σ_y	Yield stress
τ_{ij}	Shear stress in the i, j plane
$\psi^i_{\hat{j}}$	Angle from axis $\hat{j}$ to i
$\underset{\sim}{\Gamma}_i$	Constituents of $\hat{\underset{\sim}{D}}^{epc}$ for deformation in direction i
$\underset{\sim}{\Omega}^i$	A 3×3 transformation tensor to perform a rotation about axis i

Chapter 1

Introduction

Finite element (FE) analysis is a widely employed tool in the study of bone biomechanics. At the macro-level in particular it has found numerous applications relevant to the prediction of bone fracture (Lotz et al., 1991a; Keyak and Rossi, 2000; Schileo et al., 2008; Ural, 2009), hip arthroplasty (Phillips et al., 2006; Lennon et al., 2007), total knee replacement (Donahue et al., 2002; Au et al., 2005), limb fracture fixation (Huiskes et al., 1985; Stoffel et al., 2003; Watson et al., 2007), vertebral fixation (Zhang et al., 2004) and dentistry (Hart et al., 1992; Geng et al., 2001). The results of any FE analysis are dependent upon the modelling assumptions regarding geometry, material properties, boundary conditions and loading. In FE studies of bone biomechanics, many (if not all) of these features can be challenging to quantify and model.

Perhaps the most challenging features of bone to include in FE studies are its geometry and material properties. Bone outer profiles are characterised by sweeping curves and considerable variations in thickness; their inclusion in FE models therefore frequently requires three-dimensional scans and conversion to numerical meshes (Schileo et al., 2008). Internally, bone geometry becomes more complicated. A dense outer shell is formed by cortical bone, but on the microscale this material is riddled with pores and lamina which imbue it with a complex microstructure. Macrolevel mechanical properties of cortical bone are dependent upon its underlying microstructure such that it can exhibit a remarkable variation of stiffness (Cowin and Mehrabadi, 1989), strength (Reilly and Burstein, 1975) and toughness (Koester et al., 2008) with orientation and anatomical location. Trabecular (or cancellous) bone lies internal to the cortical shell at many anatomical sites. This low-density tissue grows in a combination of intricate rod-

and plate-like porous microstructures (Stauber et al., 2006). Trabecular bone is known to grow in a manner which targets optimum functioning as a load carrying system; this is achieved by alignment of trabecular struts with principal stress directions under routine loading at anatomical locations (Goldstein, 1987). Trabecular bone stiffness (van Rietbergen et al., 1996), strength (Niebur et al., 2000) and fracture resistance (Thurner et al., 2006) vary considerably with its microstructure. Direct modelling of the complex microstructures of cortical and trabecular bone in FE analyses requires high-resolution (e.g. μCT) scans and conversion to computationally expensive numerical meshes. The geometry and material properties of bone are further complicated by the continual action of remodelling. This biological process removes old, damaged bone and replaces it with fresh tissue in new configurations (Carter, 1984; Cowin, 1986). An additional source of heterogeneity is thus introduced between old and new tissue. Furthermore, the ability of bone to remodel reduces with ageing, resulting in lower bone density (solid volume fraction and mineralization). The considerable age-related variations of bone geometry at the macro- (Russo et al., 2006) and microlevels (Cooper et al., 2007; Silva, 1997) produce changes in its mechanical properties. These must therefore be accounted for to achieve accuracy in FE analyses.

To avoid the difficulty of directly including bone microstructure in FE models, many studies use the continuum assumption; complex bone microstructures are thereby simplified to solid regions with mechanical properties which are intended to mimic the macrolevel behaviour of the original microstructure. For simulations in which the global dimensions are large compared to the microstructural dimensions, direct modelling of the geometry becomes impractical and the use of continua is often essential. In most locations (away from material interfaces and high stress gradients) the continuum assumption can accurately represent the macrolevel behaviour of bone microstructures (Harrigan et al., 1988). However, many FE studies of bone employ the generally unrealistic assumptions of isotropy or homogeneity which have been found to introduce errors as large as 260 % and 200 % respectively (Au et al., 2005). These assumptions are often necessitated because in many anatomic sites there is insufficient data which quantifies the anisotropic properties of bone and their variation with location. Techniques which enable these key effects of bone microstructure to be included

in FE analyses are developed as part of this study.

Bone fails through the initiation and propagation of cracks. The microstructure of cortical bone imbues it with a variety of toughening mechanisms which act to resist the growth of cracks and inhibit fracture. Among these mechanisms, vascular canals and osteocyte lacuna pores have been found to influence the location of crack initiation and their propagation characteristics (Voide et al., 2009). Part of this study considers the use of high resolution FE analyses to investigate the role of these microstructural features in cortical bone microcracking.

The inelastic behaviour of bone is considerably influenced by its microstructure; it was noted previously that bone strength can vary considerably with orientation. However, the strength anisotropy of bone is often not modelled in FE studies and isotropic yield criteria are used instead (Lotz et al., 1991a;b; Ford et al., 1996; Voor et al., 1997; Keyak et al., 1998; 2001; Keyak, 2001). The assumption of strength isotropy has been associated with errors as high as 82.4 % (Fenech and Keaveny, 1999). Yield criteria that include the strength anisotropy of bone have been developed and can provide accurate failure predictions (Tsai and Wu, 1971; Fenech and Keaveny, 1999; Arramon et al., 2000; Gupta et al., 2007). However, wide usage of these criteria is hindered by the difficulty of determining the numerous required parameters, and their potentially high computational expense. Part of the present work details the development of a plasticity algorithm with strength anisotropy which can be readily defined and rapidly executed in continuum models of bone.

Bone microstructure plays an important role in determining the stability of orthopaedic implants. External fixation is a widely used orthopaedic technique (Bhandari et al., 2001) in which screws (half-pins) and wires are inserted through the skin and into the bone. The ends of these implants that are protruding from the skin are connected together using an external framework. The combined structure stabilises the bone fragments, resisting excessive displacements at the fracture site while enabling the patient to mobilise. Considerable localised stresses must be transferred at the implant-bone interfaces. Implant loosening can occur when these stresses exceed the strength of surrounding bone tissues (Behrens, 1989). As noted previously, bone strength can reduce considerably following the

microstructural changes which accompany ageing or diseases such as osteoporosis. Achieving stable implant fixation in elderly patients therefore represents a greater challenge than in younger patients. However, previous FE studies of external fixation have considered only the stiffness of fixation and have focused on the case of healthy, young patients. The effect of age-related microstructural changes on the stability of external fixation implants are considered as part of the present study.

1.1 Summary of Chapters

In Chapters 2–7 the topics indicated below are preceded by a discussion of the relevant literature.

Chapter 2 describes the development of a technique to generate virtual FE models of trabecular bone. Morphological properties of the generated samples and their ability to mimic the elastic and post-elastic properties of trabecular bone are examined.

Chapter 3 details the first use of micro-finite-element (μFE) analysis for the evaluation of cortical bone elastic properties. Orthotropic elastic constants of female, human bone from the femoral midshaft are measured. The age and microstructural dependency of elastic constants and their variation through the cortex are investigated.

Chapter 4 considers the role of vascular canals and osteocyte lacuna in microcrack initiation and propagation. Experimental testing of murine cortical bone samples are used to inform the development of FE algorithms to investigate the role of these pores in microcracking.

Chapter 5 presents a strain-based plasticity algorithm for including anisotropic bone failure properties in macro-FE analyses. The formulation of the algorithm is reported and its behaviour in critical states of strain is examined.

Chapter 6 describes the development of non-linear FE models of unilateral

fixation of tibial midshaft fractures. The influence of age-related bone loss on the risk of half-pin loosening is examined. In addition, the effect of pin number and material on bone failure at the implant-bone interface is studied.

Chapter 7 presents a FE study of Ilizarov fixation of tibial midshaft fractures. The study focuses on the potential for thin Ilizarov wires to induce bone failure at the wire-bone interface. The effect of ageing, the number of wires used and wire pre-tension are considered.

Chapter 8 highlights the conclusions which can be extracted from this work.

Chapter 2

Virtual modelling of trabecular bone

2.1 Introduction

μFE models of trabecular bone have found a variety of possible applications that include evaluation of its macrolevel mechanical behaviour (Simon et al., 2006; van Rietbergen et al., 1998a) and understanding microarchitectural changes with age and disease (Huiskes et al., 2000; Fagan et al., 2004). Generally these models are created by using CT attenuations or images (e.g. μCT, MRI) of real bone samples (van Rietbergen et al., 1998a; Ulrich et al., 1998). Considerable sample collection and processing is required to examine variations due to factors such as anatomical site, sex, age or degree of osteoporosis. Some investigators have used regular scaffold-type structures to represent trabecular bone (Gibson, 1985; Guo et al., 1995; Kowalczyk, 2006). While these regularised units help in understanding the anisotropic nature of representative cellular structures, they are unable to represent the highly variable microarchitecture of real bone samples. There have also been some good attempts to develop models using bone remodelling procedures (Huiskes et al., 2000; Fagan et al., 2004). In these, either regular lattice structures or scanned samples of bone undergo remodelling simulations (to mimic osteoblast and osteoclast activity) using either stochastic or deterministic rules that represent biological processes.

Previous studies have defined a variety of indices to quantify the microarchitecture of trabecular bone and identify correlations with its mechanical response. The apparent density, represented by the bone volume to total volume ratio

(BV/TV) is the most commonly employed variable in these correlations (Carter and Hayes, 1977; Rice et al., 1988; Wirtz et al., 2000). For a sample represented as a 3D binary image, this is simply defined as the ratio of solid phase to solid and void phase voxels. Mean trabecular thickness (Tb.Th) and spacing (Tb.Sp) can be evaluated in 2D for rod and plate-like models (Parfitt et al., 1987), or directly in 3D following Hildebrand and Rüegsegger (1997a) by fitting maximal spheres within solid or void phases. Trabecular number (Tb.N) is a measure of the number of traversals across a unit length within a sample. This can be calculated as the ratio of BV/TV to Tb.Th (Parfitt et al., 1987). Trabecular connectivity is another important index which has been defined in terms of mathematical topology as the number of 'handles' or loops present in a sample (Odgaard and Gunderson, 1993). A commonly employed measure of trabecular connectivity is trabecular pattern factor (Tb.Pf) (Hahn et al., 1992). This is defined as the ratio of surface area change to volume change following image dilation. Since dilation of an enclosed region will reduce the surface area, but dilation of a free end will increase it, lower Tb.Pf indicates a better connected structure. Structure model index (SMI) provides a measure of surface convexity and the relative prevalence of rods and plates within a structure (Hildebrand and Rüegsegger, 1997b). SMI is calculated as $6\Delta S_{ob} V_{ob} S_{ob}^{-2}$, where S_{ob} is the object surface area, V_{ob} is the object volume and ΔS_{ob} is the change in surface area from dilation by one voxel. Like Tb.Pf, SMI calculation involves the dilation of model images by one voxel, which explains why these parameters are often well correlated. The extent of preferential trabecular orientation is evaluated by assessment of the directional anisotropy (DA). DA has been assessed using either mean intercept length (Whitehouse, 1974) or volume orientation methods (Odgaard and Gunderson, 1993). DA is generally expressed as a fabric tensor (Cowin and Laborde, 1985) which represents the relative alignment of trabecular fabric in space. Recently, techniques have been developed which allow the separate analysis of trabecular rods and plates from the same samples (Saha and Chaudhuri, 1994; Stauber and Müller, 2006b). This has led to plate and rod specific versions of many of the older indices.

The ability to create models with specific microarchitectural indices would permit evaluation of their influence on the resulting changes in mechanical behaviour. It would be advantageous in FE simulations at higher scales to include the porous nature of bone microstructure rather than assigning solid elements

with homogenised mechanical properties. Indeed, Harrigan et al. (1988) concludes that 'within three to five trabeculae of an interface, a continuum model is suspect'. It can be inferred that the use of microstructural models to refine the regions of bone near implant interfaces could offer potential increases in simulation accuracy. μFE models are necessarily high resolution, and therefore computationally expensive relative to their physical size. In order to include the porous nature of bone in larger scale FE simulations it is necessary to develop models of a lower resolution. This Chapter considers the creation of virtual FE samples of trabecular bone, i.e. samples that look like and mechanically behave like real trabecular bone, but are generated computationally. A key requirement for these models was to be of low mesh resolution to be potentially incorporated into larger simulations. Considerable research shows that the key determinants of the apparent-level mechanical properties of trabecular bone are related to its microarchitecture (Ulrich et al., 1999; van Rietbergen, 2001). So, if the computationally created models satisfy microarchitectural characteristics of trabecular bone, the mechanical behaviour of these models is very likely to be realistic.

This study uses a novel approach, initiated by Pankaj et al. (2006), that employs some of the indices to generate virtual μFE models of trabecular bone (Donaldson et al., 2008). The approach permits generation of any number of models, with suitable porous structure, for the same or different levels of porosity. The generated models are examined computationally for their elastic and post-elastic mechanical behaviour.

2.2 Methods

The methods described in the following were implemented using programs written by the author in Matlab (The MathWorks, Inc., Natick, MA, U.S.A.).

2.2.1 Virtual generation of models

Typical virtual models created using the algorithms discussed in this Section are shown in Fig. 2-1. At this stage of development four key indices were directly employed in the generation of virtual models: BV/TV, Tb.Th, Tb.Sp and DA. A

simplified form of DA was used in an attempt to produce transversely isotropic models. The algorithm developed for the generation of virtual models can be described conceptually as follows.

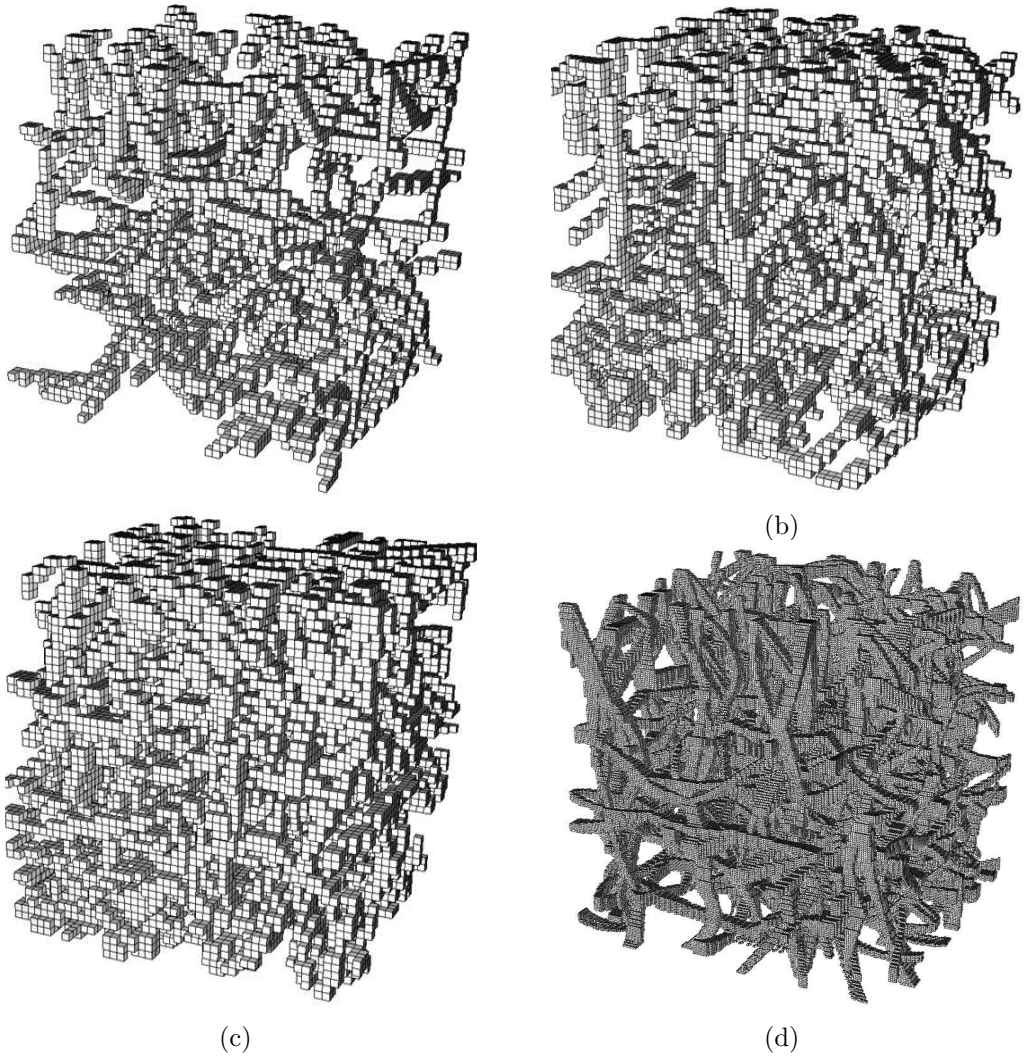

(b)

(c) (d)

Figure 2-1: Example models of virtual trabecular bone from this study - low resolution models (8 % BV/TV(a), 16 % BV/TV(b), 24 % BV/TV(c), and a high resolution model 12 % BV/TV(d).

A cubic domain of empty voxels was defined. Empty voxels correspond to the void phase and activated voxels to the solid bone phase. In the FE analyses of the models, activated voxels were directly converted into hexahedral finite elements. Trabeculae were created by activating voxels along paths through the domain. Trabecular paths were defined in sections, each passing through one local cubic re-

gion of the global domain. In Fig. 2-2, three local regions are highlighted and the corresponding propagation of several trabeculae is illustrated. In most examples considered in this study each local region comprised of 1728 ($12 \times 12 \times 12$) voxels. The choice of this sample size is discussed later.

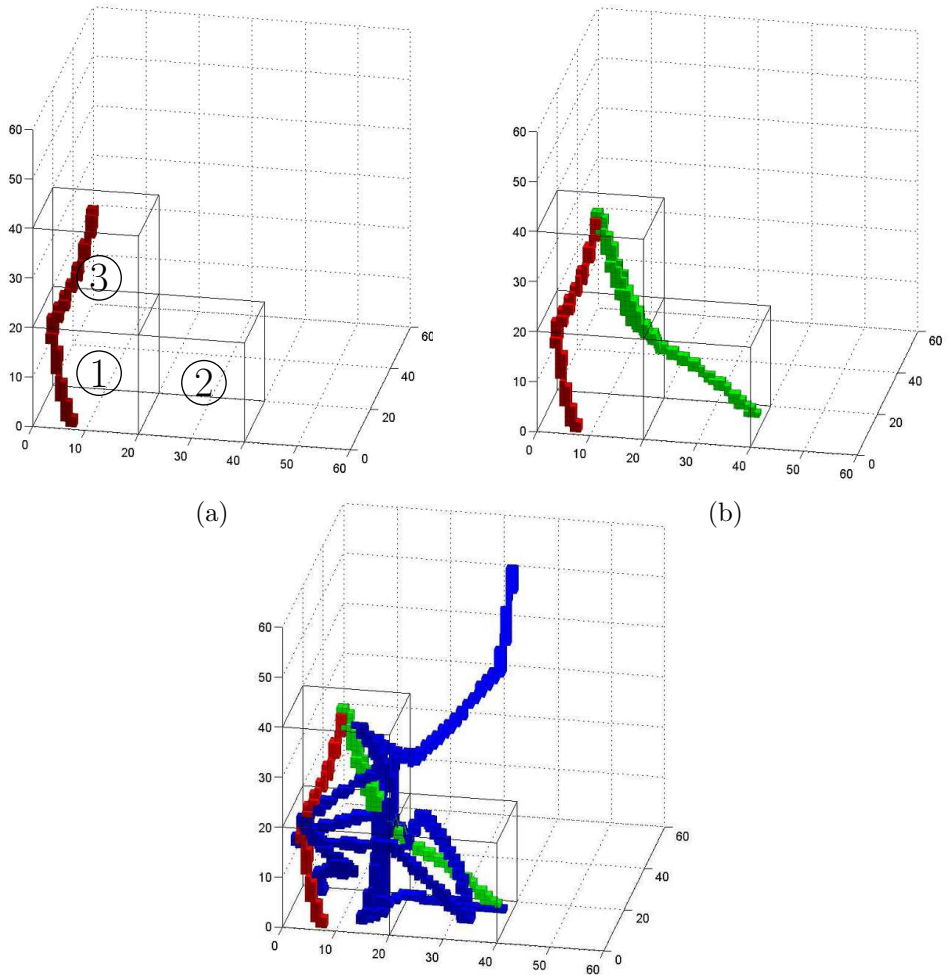

Figure 2-2: Progressive model generation. One trabecula comprised of two trabecular sections (a), an additional trabecula (b) and several further trabeculae, including one which spans the entire model (c). Note axes correspond to the cartesian coordinate system and their values indicate the dimensionless number of element edge lengths in each direction.

Connection points (CPs) are specified on each face of a local region. Each trabecular section originates and terminates at a CP and neighbouring local regions share CPs on their common face. Figure 2.2(a) shows two sections of a single

trabecula. This originates at a CP on the base of region 1, connects through a CP on the common face of regions 1 and 3, and exits the highlighted area at a CP on the top of region 3.

Tb.Th was specified at each CP. All trabecular paths that pass through a particular CP have the values of thickness specified at that point as a number of voxels. The values of trabecular thickness between CPs were varied within these prescribed limits. In this preliminary phase of the study for most examples the trabecular thickness was varied between 1 and 2 voxels (e.g. Fig. 2-1(a–c)), and the thickness was permitted to be higher at intersections. The algorithm was sufficiently general to permit gradual variation in trabecular thickness to any predefined thickness range, i.e. number of voxels. Figure 2-1(d) shows a high resolution virtual model in which the trabecular thickness was varied between 4 and 8 voxels. Some of the high resolution models were used to examine mesh sensitivity.

Tb.Sp was controlled by the size of the local regions and by the number of CPs on each face. Figure 2-3 shows one face of a local region with CPs. In this case the CPs can be of one or two voxel thickness. The algorithm randomised the location of CPs within prescribed limits; here they are shown at their mean positions for a spacing of 6 voxels.

As mentioned earlier, trabeculae were created by the activation of voxels lying on the paths between sequences of CPs. In order to introduce trabecular curvature as observed in natural bone, the path between two CPs was defined as a pair of second order polynomials in the 3D Cartesian coordinate system. Second-order polynomials were arbitrarily selected for their simplicity as they require only two constants (a and b) to be defined in the parametric form: $x = t;\ y = at^2;\ z = bt^2$. The 'height' of the parabolas were varied randomly, and limited to 1/15 of the straight-line distance between CPs. The first CP serves as the origin and the principal axis (x) is arbitrary. When a polynomial passes through a voxel space, that voxel is activated. In this way a set of activated voxels is generated corresponding to the solid phase of the model. This process is illustrated in Figure 2-4 which shows the generation of an individual trabecular section between two CPs, A & B. Each trabeculum is generated in the following way:

a) Start and end seed CPs (A1, A2, A3 & B1, B2) are selected.

b) Three-dimensional parabolic lines of equal central deflection are connected between the primary CP (A1 & B1) and all CPs opposite.

c) Where the lines emanating from A1 pass through a potential element location, an element is activated.

d) Where the lines emanating from B1 pass through a potential element location that has not been previously activated, an element is activated.

Since the voxel dimensions of the generated models were of arbitrary physical size it was not possible to specify Tb.Th and Tb.Sp directly. The values of Tb.Th and Tb.Sp were therefore specified using the dimensionless ratio (Tb.Th)/(Tb.Sp). Realistic values of (Tb.Th)/(Tb.Sp) were derived from data reported by several studies (Hildebrand et al., 1999; Ulrich et al., 1999; Laib et al., 2002; Newitt et al., 2002), an extract of this data is shown in Table 2.1 with the derived values of (Tb.Th)/(Tb.Sp). For the local region face of Fig. 2-3 it can be seen that the (Tb.Th)/(Tb.Sp) ratio will typically vary between $\frac{1}{6}$ and $\frac{2}{6}$ giving a mean of 0.25. Thus, this specification is similar to the femoral head samples analysed by Ulrich et al. (1999) (Table 2.1) with a ratio of 0.244. It should be noted that this parameter was not directly varied between models; the probability of each location and thickness of potential CPs on region faces was kept constant to simplify the analyses required. However, since not all CPs were activated, the value of (Tb.Th)/(Tb.Sp) in each model was varied as a side effect of specified changes in BV/TV.

The required BV/TV was specified as an input to the generation algorithm. After the generation of each trabecula the accumulated BV/TV was evaluated and generation terminated if this was within prescribed limits of the value specified. The incremental addition of BV/TV by generating further trabeculae is illustrated in Fig. 2-2(b,c). In Fig. 2.2(b), the BV/TV is increased by the addition of a trabecula which originates in region 2 and terminates in region three. Figure 2.2(c) represents a considerably progressed model; the BV/TV of the included regions has increased greatly. One trabecula has been continued to its global terminus at the top of the model.

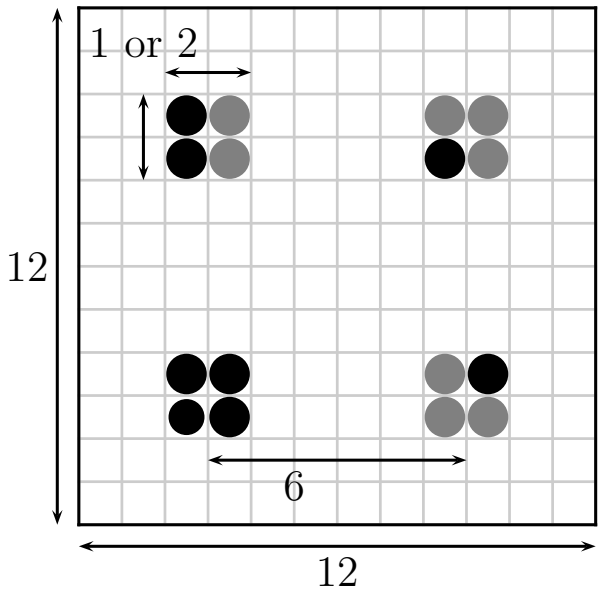

Figure 2-3: Four CPs on the face of a local region. CPs are distributed randomly but shown here in their mean positions for a spacing of 6 voxels. Here thickness was varied between 1 and 2 voxels and spacing is 6 voxels on average.

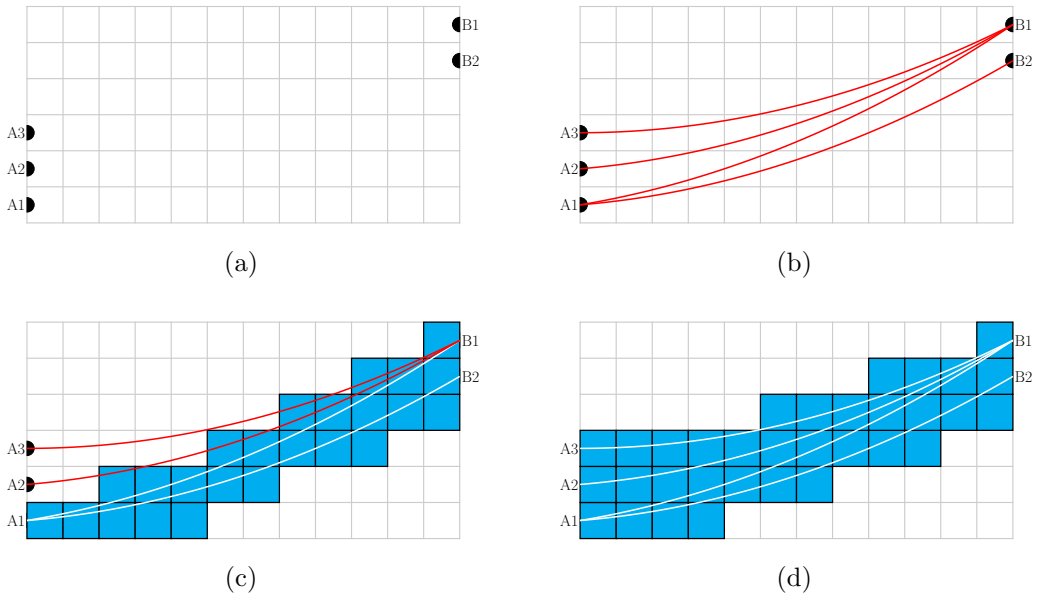

Figure 2-4: Pseudorandom trabecular growth mechanism.

Table 2.1: Microarchitectural indices of trabecular bone (Ulrich et al., 1999; Hildebrand et al., 1999; Laib et al., 2002; Newitt et al., 2002). Note these data are plotted later in Fig. 2.10(c).

Anatomic site	BV/TV	$\frac{Tb.Th}{Tb.Sp}$
Distal Radius (Newitt et al., 2002)	0.370	0.579
Forearm (Laib et al., 2002)	0.347	0.593
Calcaneus samples (Hildebrand et al., 1999)	0.120	0.190
Calcaneus samples (Ulrich et al., 1999)	0.117	0.186
Femoral head samples (Hildebrand et al., 1999)	0.261	0.304
Femoral head samples (Ulrich et al., 1999)	0.207	0.244
Iliac crest samples (Hildebrand et al., 1999)	0.156	0.202
Iliac crest samples (Ulrich et al., 1999)	0.152	0.199
Lumbar spine samples (Hildebrand et al., 1999)	0.085	0.159
Lumbar spine samples (Ulrich et al., 1999)	0.082	0.154

A connection between two trabeculae was created either when their paths overlapped between CPs or when they shared a CP. The generation of trabecular sections between CPs therefore forced connectivity to occur.

Researchers have shown that bone is an anisotropic material which can be well approximated by orthotropy (Cowin and Mehrabadi, 1989). Transverse isotropy also represents bone well (Guo, 2001), this represents a special case of orthotropy with the addition of a further symmetry plane. The DA was controlled by a calibration procedure to produce samples with realistic transverse isotropy. The generation algorithm was calibrated in terms of the probability of connecting any given CP to a neighbouring CP in the axial or transverse direction. This probability is termed the Axial Connectivity Probability (ACP). Variation of this parameter can produce models with approximate apparent-level isotropy or transverse-isotropy. Assigning ACP = 1 results in trabeculae traversing the local region vertically. For ACP=0.5 the probability of trabeculae traversing laterally or vertically is 50 %. The probability of traversing in the two lateral directions was kept equal in order to produce approximate transverse isotropy. Initially, models were generated with a range of ACP. These models were subjected to elastic FE compression tests (discussed later) in the axial and transverse directions. Figure 2-5 shows the results of the calibration procedure (note x and z are the transverse directions). The relative Young's moduli of samples in the three principal directions were compared with properties of natural trabecular bone in the axial and transverse directions (Turner et al., 1999; Wirtz et al., 2000).

An ACP of 40 % was used in all analysis, producing models which exhibited a fair degree of transverse isotropy ($E_x/E_y = 0.45$). Figure 2-5 indicates that any degree of transverse isotropy can be generated by the algorithm.

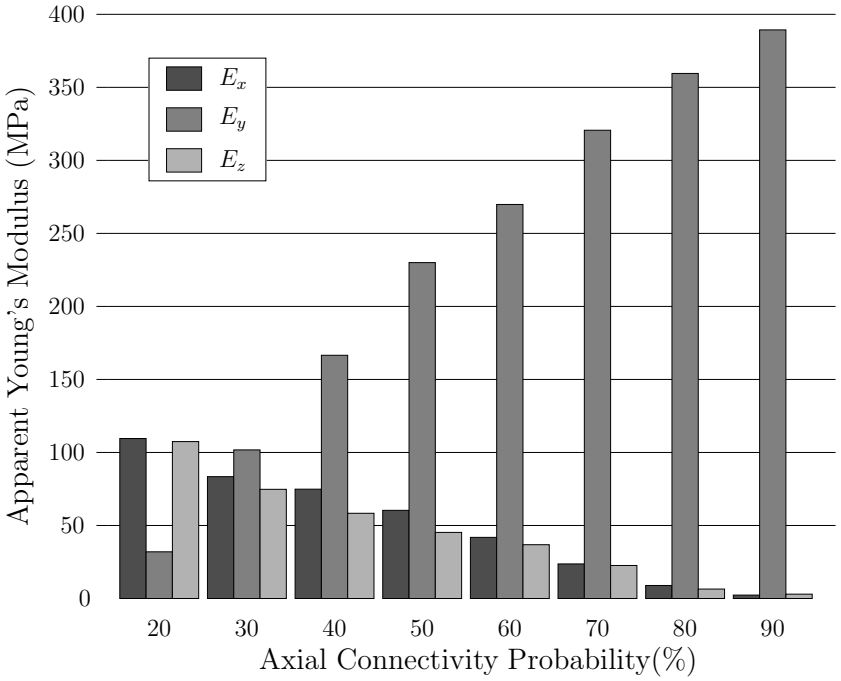

Figure 2-5: The calibration of axial (y) and transverse (x,z) moduli with Axial Connectivity Probability (ACP).

The microarchitectural properties of the generated models were assessed through the measurement of several morphological indices. The indices used were BV/TV, Tb.Th, Tb.Sp, (Tb.Th)/(Tb.Sp), Tb.N, SMI and DA. These parameters were measured in 3D using the CT Analyser 1.7.0.5 software package (Skyscan, Aartselaar, Belgium). Several of the reported morphological indices have units of length, typically reported in mm. To enable comparison with data from studies of real trabecular bone it was necessary to convert the dimensions of each virtual model into mm. The bone generation algorithm is based on rod-like trabeculae, typical of lower density bone, such as BV/TV=12 %. The conversion from voxel to mm units was made using the mean Tb.Th reported by Ulrich et al. (1999) of 0.127 mm which corresponded to a BV/TV of 11.65 %.

2.2.2 Testing procedure

The apparent-level Young's moduli of the generated models were evaluated by subjecting them to uniaxial, strain-controlled, confined compression tests in the three principal directions. Periodic boundary conditions were applied to replicate the effect of neighbouring tissue in-vivo. These conditions were applied by reflecting the models in the three dimensions and tying corresponding nodes on opposite faces. The Young's moduli were calculated as the ratio of mean stress on each face to the applied strain in the orthogonal direction. The mean stress was calculated as the sum of nodal forces orthogonal to each face, divided by the model domain area.

A wide range of elastic trabecular tissue properties have been reported in the literature. A representative selection, highlighting the variability in reported properties, is presented in (Niebur, 2000). The selected values of elastic properties were taken from within the range reported in the literature. There is much evidence for the anisotropy of trabecular tissue properties (Williams and Lewis, 1982; Turner et al., 1999). However, Kabel et al. (1999a) demonstrated the accuracy 'for practical purposes' of assuming isotropic tissue properties. Consistent with Kabel, tissue isotropy was assumed for all analyses. Previous studies have made this assumption and reported high correlation between their μFE and experimental mechanical properties (van Rietbergen et al., 1998b; Kabel et al., 1999b). It can therefore be inferred that apparent-level anisotropy is primarily due to sample microarchitecture. The elastic properties were kept constant for all analyses to allow direct comparison of all results.

The elastic constants were:

Young's Modulus	10 GPa
Poisson's Ratio	0.3

Post-elastic and failure properties of trabecular bone are little understood. Keaveny et al. (1994) reported that trabecular tissue is approximately 30 % stronger in uniaxial compression than in uniaxial tension. Niebur (2000) employed an isotropic yield criterion at the tissue-level, which once again assumes that apparent post-elastic anisotropy is due to microarchitecture. In this study

time independent plasticity with an isotropic Drucker-Prager yield criterion was employed at the tissue-level to model non-linear material (NLM) behaviour. Constitutive models such as Drucker-Prager and Mohr-Coulomb are pressure-dependent plasticity models that have traditionally been extensively employed to describe the behaviour of granular materials such as soil and bone graft (Phillips et al., 2004). More recently they have found application in describing the constitutive behaviour of quasi-brittle materials such as masonry (Addessi et al., 2002), concrete (Pankaj and Lin, 2005) and bone (Keyak and Rossi, 2000; Tai et al., 2006). Both Mohr-Coulomb and Drucker-Prager are based on two parameters: cohesion and friction angle, which can be calibrated using uniaxial tensile and compressive yield strengths. In principal stress space the Mohr-Coulomb criterion is an irregular hexagonal pyramid, in which intersections between surfaces can cause computational difficulties (de Borst et al., 1991). On the other hand, Drucker Prager criterion is a smooth circular cone in the principal stress space. Thus, Drucker Prager is simple both computationally and from the point of view of the number of parameters required. It is applicable to quasi-brittle materials and permits inclusion of strength asymmetry. This criterion was adopted with compressive and tensile tissue yield strains of $-1.01\,\%$ and $0.60\,\%$ respectively as employed by Niebur (2000) and Niebur and Keaveny (2001). Post-elastic behaviour was assumed to be perfectly plastic i.e. no hardening or softening was included.

Separate non-linear geometric (NLG) analyses were conducted on all samples. In NLG analyses the effect of large deformations on structure stiffness are incorporated into the FE integration, this contrasts with linear geometric analyses which assume changes in geometry have negligible influence on the structure stiffness. All analyses were solved with the commercial FE package Abaqus (Dassault Systemes; Simulia, Providence, RI, USA).

2.2.3 Mesh resolution

The effect of model mesh resolution upon both morphology and mechanical response was investigated. Models with 8 times the unrefined (coarse) number of voxels (Tb.Th variation from 2–4 voxels) and 64 times the number of voxels

(Tb.Th variation from 4–8 voxels) were created and analysed. Comparison was made for BV/TV=12 %. In each case the results were evaluated from the mean of four models. Higher resolution models were generated in three ways which are illustrated in Fig. 2-6. In method A) models were generated to an equal BV/TV in the refined model space. In method B) the coarse meshes were refined by dividing each element into eight or sixty-four smaller cubic elements. In method C) the generation algorithm was modified to replicate the skeleton of the coarse meshes but to mesh them at a finer resolution. However, as can be seen in Fig. 2-6(d), method C) resulted in BV/TV loss; this reduced by approximately 34 % between the coarse mesh and one with 64 times the number of voxels.

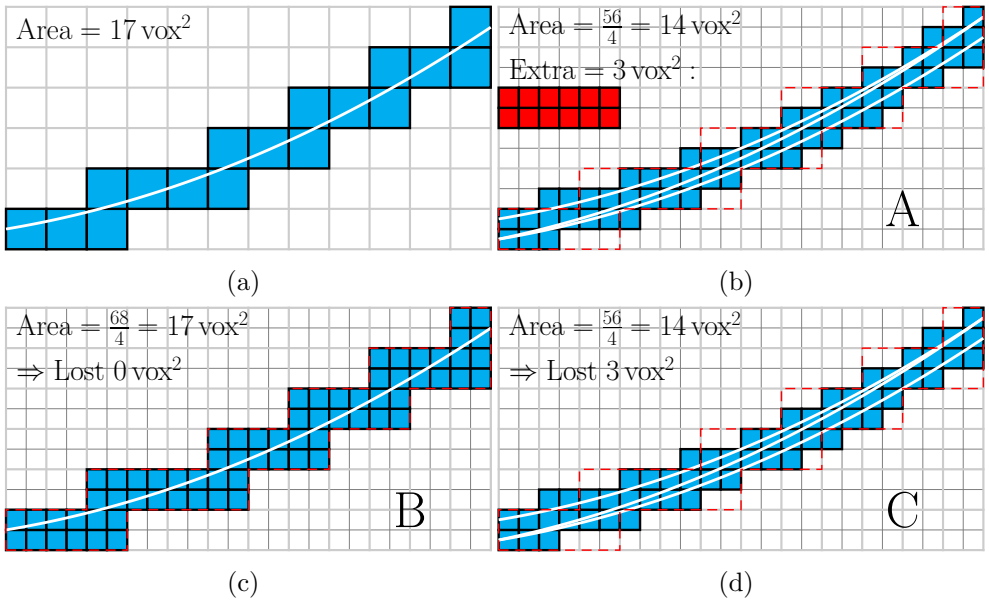

Figure 2-6: The three methods of virtual model mesh refinement. A single trabecula is shown in 2D using different methods of refinement; unrefined resolution (a), method A (b), method B (c) and method C (d). Note, with method A the voxels lost from the present trabecula will contribute to additional trabecula such that BV/TV is maintained (the transferred voxels are shaded red); in method C the lost voxels are not recovered and BV/TV is reduced from the target value. The dashed red line is the outline of the unrefined model (a).

Initial estimates of mesh convergence for E_y were calculated by adjusting the results from method C) by compensating for the lost BV/TV according to the trend evaluated later. The original and adjusted results are labelled C_a) and C_b) respectively. The mesh convergence for all methods of mesh refinement are

presented in Fig. 2-7. Considerable variation in E_y was observed with increasing mesh resolution by all methods. With method A) the coarse meshes were 32 % and 46 % less stiff than the 8 times and 64 times higher resolution models respectively. With method B) the coarse mesh was 13 % and 24 % more stiff than the 8 times and 64 times higher resolution meshes. With method C_a) these values were 56 % and 112 %. When the results from C_b) were adjusted for the lost BV/TV these values became 12 % and 13 % respectively.

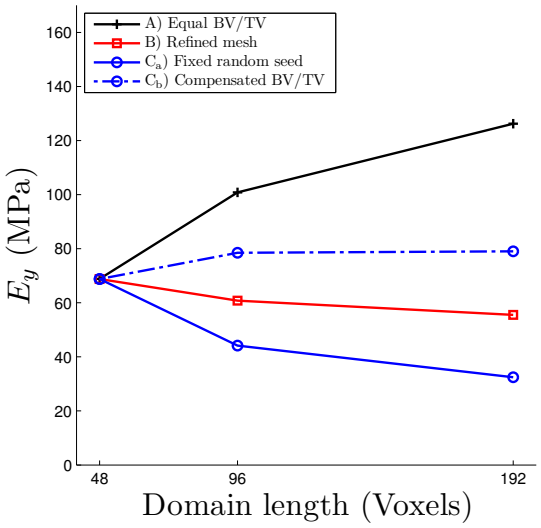

Figure 2-7: The variation of E_y with mesh resolution at a model BV/TV of 12 %. Resolution was adapted in four ways: A) meshes were generated to higher resolution with equalised BV/TV; B) coarse meshes were refined but retained the same surface geometry; C_a) models were generated with the same random seed value to create approximately identical geometry, but loss of BV/TV; C_b) results from C_a) were adjusted to compensate for the loss of BV/TV.

The elastic properties of the virtual models were dependent upon the resolution in which they were defined. In FE studies of specific constructs it is necessary to use a mesh resolution which is sufficiently fine to minimise the numerical error associated with dividing a continuum into discrete elements. In such cases a specific geometry is fixed a priori and results from increasingly fine meshes are studied to identify a convergence point. In the current study each model's geometry and mesh were intrinsically linked; the geometry was defined and limited by the chosen mesh resolution of the modelling space. As a result, any change in mesh resolution incurred a change in the base model geometry and morphology.

The substantial variation of model morphology which resulted from changes in mesh resolution are illustrated in Fig. 2-8 and 2-9. The mechanisms behind the variation of the elastic stiffness with mesh refinement can be identified from these relationships.

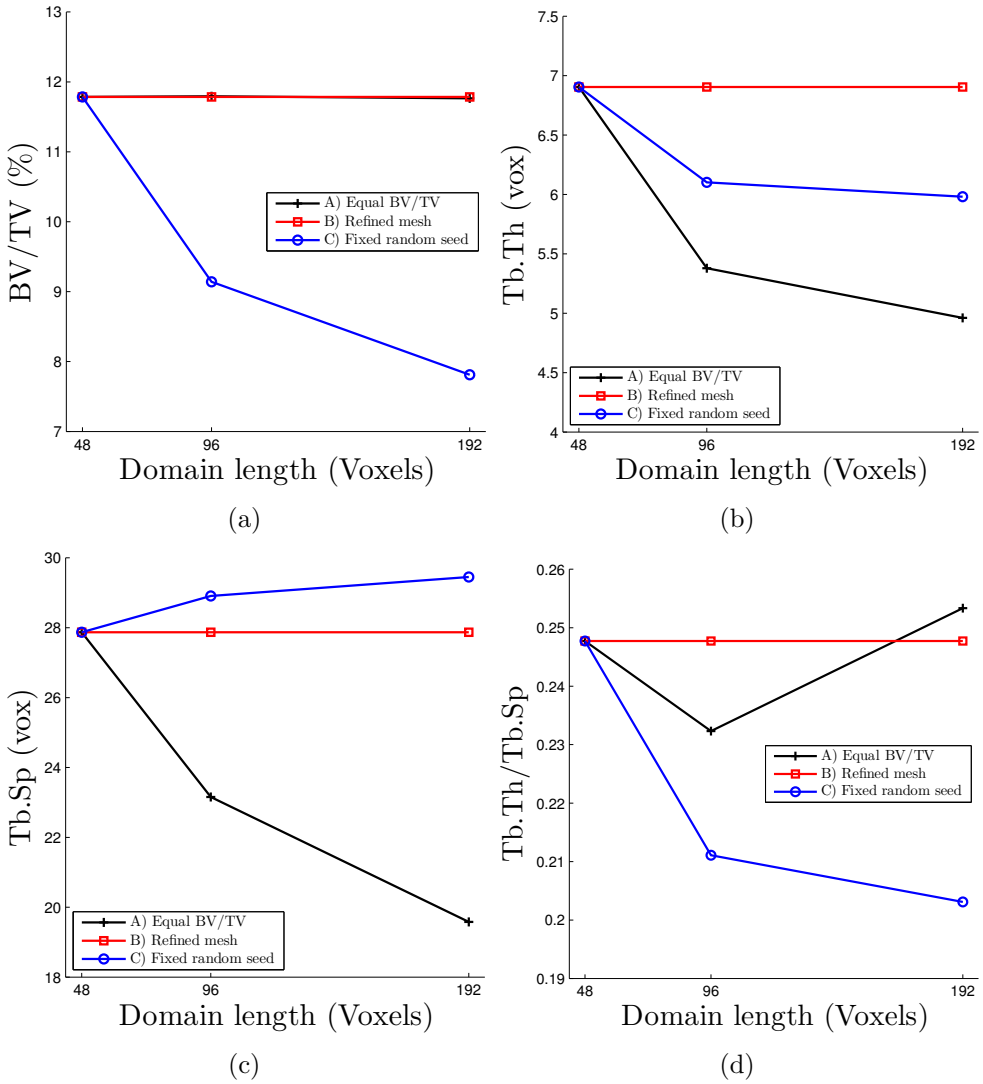

Figure 2-8: The variation of BV/TV (a), Tb.Th (b) and Tb.Sp (c), (Tb.Th)/(Tb.Sp) (d) with mesh resolution for the virtual models. Note the variable range of y-axis values.

Under mesh refinement method A) E_y increased. This coincided with no variation of BV/TV and thus resulted entirely from microarchitectural changes. Tb.Th and Tb.Sp reduced considerably, but the ratio of these parameters indicated that

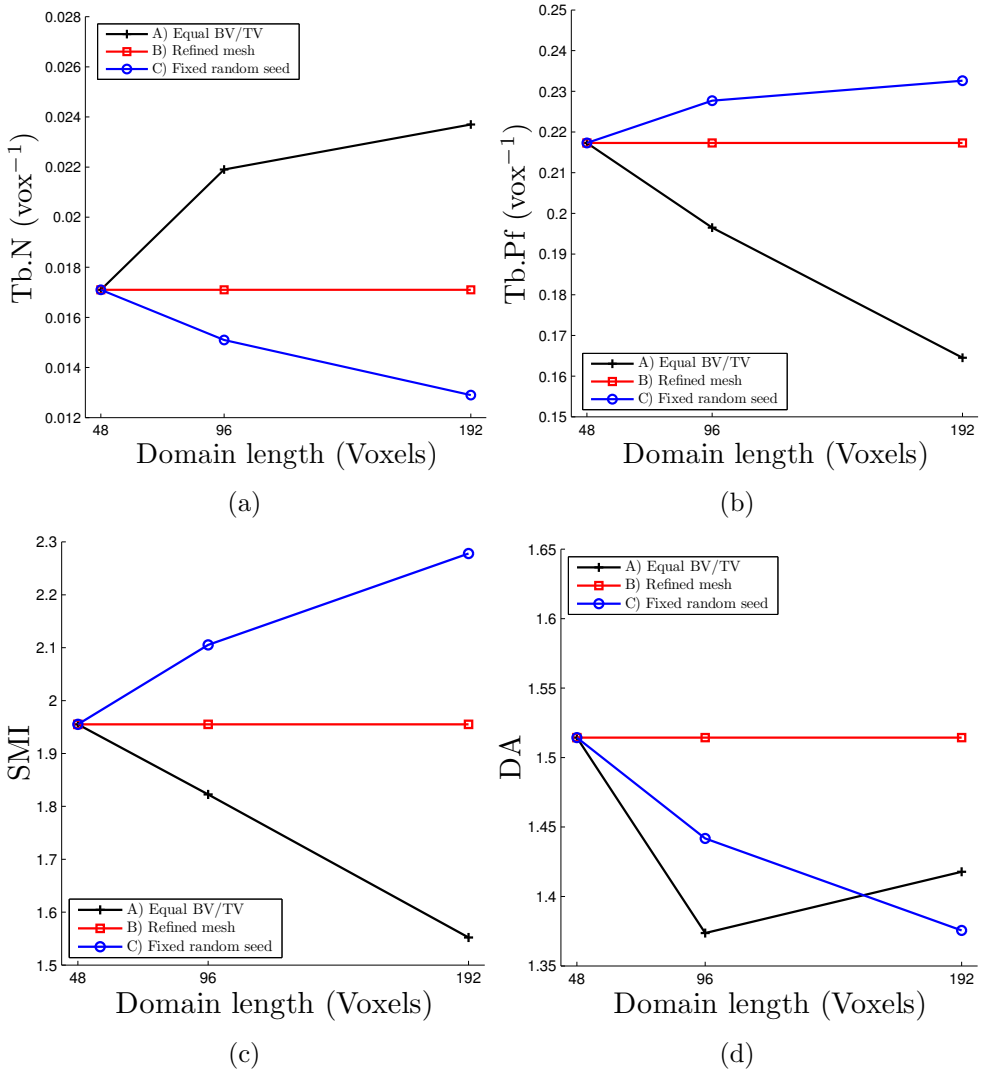

Figure 2-9: The variation of Tb.N (a), Tb.Pf (b), SMI (c), and DA (d) with mesh resolution for the virtual models. Note the variable range of y-axis values.

trabecular slenderness was approximately unchanged with A) refinement; these parameters were therefore not expected to have substantially changed E_y. The variation of Tb.N indicated that considerably more trabeculae were generated at higher mesh resolutions under method A), which was expected to increase E_y. Furthermore, both Tb.Pf and SMI reduced with A) refinement which indicated a transition to more connected, plate-like morphology, also expected to increase E_y. Under mesh refinement method B) E_y reduced although the morphological indices remained unchanged. This was expected since the external surface of the models did not vary with B) refinement. The reduction of E_y therefore resulted from the greater flexibility afforded by the presence of more numerical degrees

of freedom in the FE mesh, reducing the effect of shear locking typical of coarse meshes of hexahedral elements. Under method C_a) mesh refinement E_y reduced substantially. This coincided with a considerable (22 % and 34 %) reduction in BV/TV. This index has been identified as a powerful predictor of trabecular bone elastic properties (Carter and Hayes, 1977; Rice et al., 1988) which motivated the discussed compensation of E_y under method C_b). With C) refinement Tb.Th reduced and Tb.Sp increased, both of which would be expected to reduce E_y since the trabeculae became more slender. Tb.N reduced with C) refinement and Tb.Pf and SMI indicated the formation of less connected and more rod-like morphologies which would further be expected to reduce E_y. In both A) and C) refinement the DA reduced slightly which indicated a less aligned arrangement of the trabeculae which would be expected to reduce the stiffness in the preferred direction slightly (i.e. E_y).

Models generated by refining the geometry represented by coarse meshes (method B), showed no variation in morphological indices. Method B) therefore offered the best estimate of numerical mesh dependency of the methods considered. Using this method it was concluded that the E_y of the coarse models varied by 24 % with mesh refinement. When coupled with variations in model morphology this dependence became 46 %. This was a relatively high degree of mesh dependence which would be considered unacceptable in a typical FE study, with a fixed geometry. In this study, the geometry was intended to be an approximation of trabecular bone. Indeed the microstructure was used as a guide to produce models with mechanical properties that approached those of trabecular bone. Furthermore, a key goal of this study was to produce models with low numerical complexity for use in larger-scale FE simulations. This necessitated a degree of mesh dependency in the resulting models. It is envisaged that in application to larger simulations the tissue-level elastic properties could be scaled to produce the effective elastic properties required. This scaling would therefore take account of the deviation of elastic properties from their fully converged state. Note that tissue property scaling as described would be necessarily variant with BV/TV since (as discussed later) the observed difference between real bone and model elastic stiffness was found to be a function of BV/TV.

2.3 Results

2.3.1 Microarchitectural indices

The microarchitectural properties of the generated trabecular bone models were evaluated using several morphological indices. Tb.Th and Tb.Sp are plotted in Fig. 2-10. As previously noted, the conversion of units from voxels to mm was applied using Tb.Th = 0.127 mm as reported by Ulrich et al. (1999) at BV/TV=12 %. It can be seen that the model Tb.Th is consequently in close agreement with the real bone data at this BV/TV. However, the model value of Tb.Th did not increase as rapidly with BV/TV as real bone; Tb.Th of the models was in general lower than for real bone. Tb.Sp was also found to be lower than in real bone. The values of Tb.Sp reported by Hildebrand et al. (1999) and Ulrich et al. (1999) were greater than 0.6 mm for all BV/TV; in the virtual models, this value reduced considerably with increased BV/TV, and was less than 0.4 mm at BV/TV=24 %.

Since the conversion from voxels to mm was dependent upon the value of BV/TV at which the conversion is made, it was useful to consider the dimensionless parameter (Tb.Th)/(Tb.Sp) as plotted in Fig. 2.10(c). The value of this ratio was found to be greater for the models than for real bone, and increased more rapidly with BV/TV. The variation of Tb.N with BV/TV is plotted in Fig. 2.10(d). At low BV/TV there was a poor match between the Tb.N of the virtual models and data presented by Hildebrand et al. (1999) and Ulrich et al. (1999). It should be noted that these studies both calculated Tb.N as 'the inverse of the mean distance between the middle axes of the structure' (Ulrich et al., 1999), whereas the method employed here calculated the ratio of BV/TV to Tb.Th. This is a possible reason for the poor correlation between the models and real bone, even at the value of BV/TV=12 %, where the conversion was made. It can be seen that in both the real bone and model data, Tb.N increased with BV/TV. The trend of both data were therefore similar.

The SMI is plotted against BV/TV in Fig. 2.10(e). The value of SMI for both the models and real bone data from Hildebrand et al. (1999) reduced with increased BV/TV. The real bone data although similar to the models at low BV/TV, reduced considerably more rapidly with BV/TV. The DA is plotted

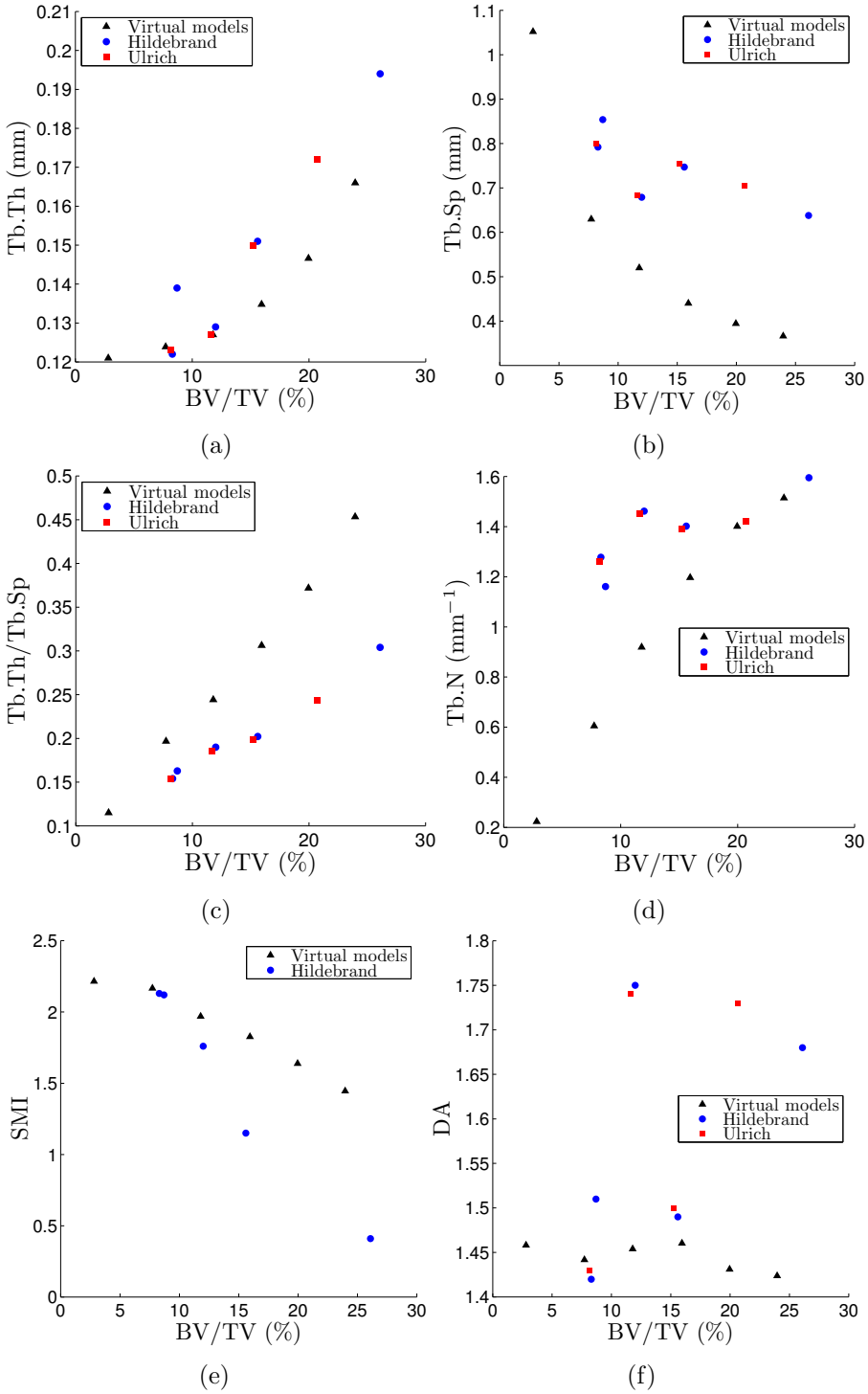

Figure 2-10: The variation of Tb.Th (a), Tb.Sp (b), (Tb.Th)/(Tb.Sp) (c), Tb.N (d), SMI (e), and DA (f) with BV/TV for the virtual models and real bone (Hildebrand et al., 1999; Ulrich et al., 1999).

in Fig. 2.10(f). The DA of the models remained at approximately 1.45 for all BV/TV values. This value was within the lower range reported for real bone.

2.3.2 Elastic response

Prior to conducting detailed analyses it was essential to evaluate the minimum model size required for accurate determination of apparent-level properties. The variation of apparent Young's modulus with model size is shown in Fig. 2-11. Model size is here parameterised as the length of one side of the cubic domain. Lengths are expressed as an equivalent number of pore widths. As the model size was increased, the amount of variance in the Young's modulus reduced. Interestingly, the magnitude of the mean Young's modulus also reduced with increased model size. In particular, with small model sizes the maximum observed Young's modulus was considerably greater than the mean obtained with larger models. It was decided to adopt a standard model size of four pore lengths for all remaining analyses. With reference to Fig. 2-11, it can be seen that little accuracy was lost by so limiting the model size. However, considerable computational efficiency

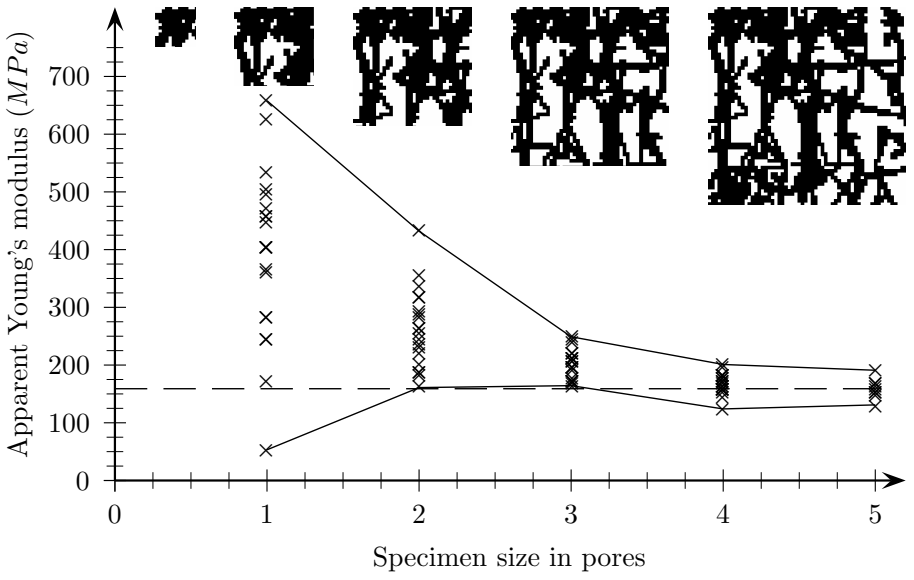

Figure 2-11: The variation of apparent Young's modulus with model size (BV/TV = 16 %). The solid lines are envelopes of maximum and minimum values and the dashed line represents the mean value from a sample size of five pore lengths.

was achieved in this way. Interestingly, a study of trabecular bone identified the same critical sample size from a similar variation of Young's modulus variation with specimen size (Simon et al., 2006).

A direct convex non-linear relationship was observed between the apparent Young's modulus and BV/TV. The trend of Young's modulus with apparent density is shown in Figure 2-12. Data from proximal femoral samples, collated by Wirtz et al. (2000) are plotted for comparison. The data presented by Wirtz et al. correspond to axial tests, for completeness both the axial (y) and transverse (x,z) Young's modulus are shown for the virtual models. A tissue density of 2.2 g/cm^3 (Ding et al., 1997) was assumed for the purposes of this comparison.

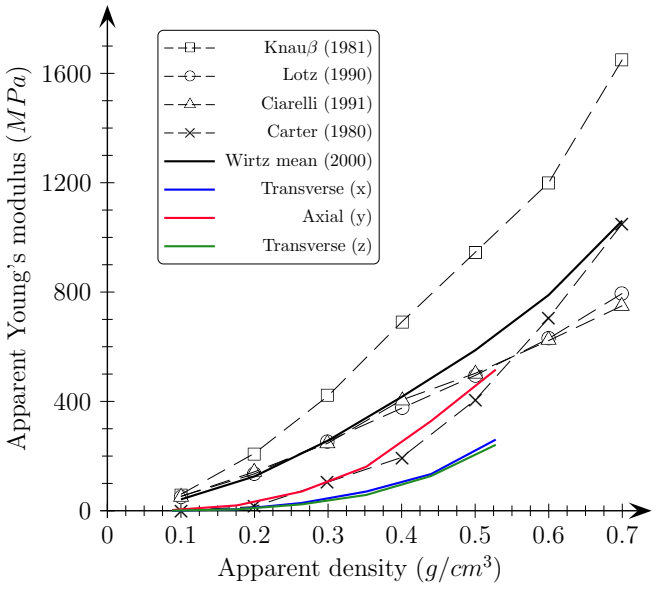

Figure 2-12: Comparison of apparent axial and transverse Young's moduli of the virtual models with the axial modulus of real trabecular bone from the proximal femur reported by Wirtz, (Wirtz et al., 2000).

2.3.3 Post-elastic response

The post-elastic trace of apparent stress with apparent strain at two values of volume fraction are shown in Fig. 2-13. Each trace represents the mean response of three virtual models. Three non-linear analyses of each model were conducted; materially non-linear (NLM), geometrically non-linear (NLG) and

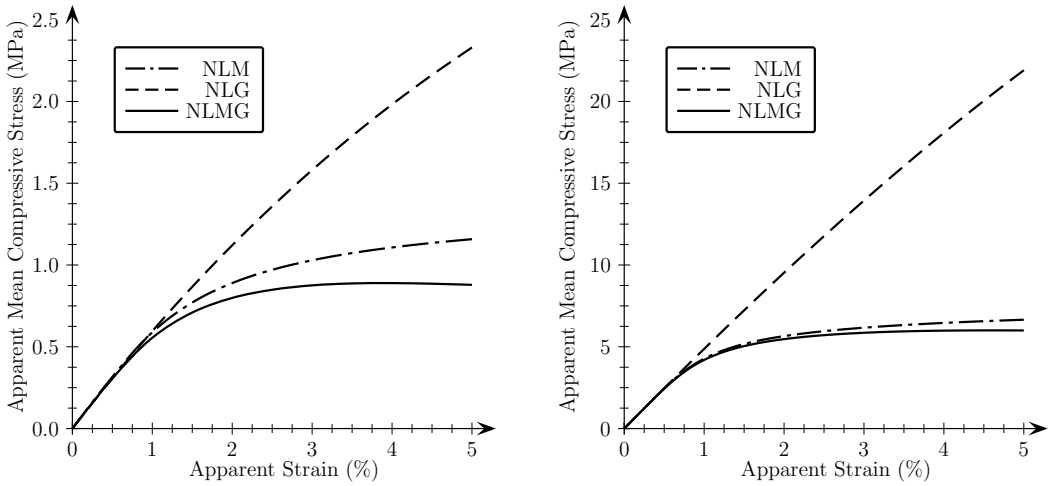

Figure 2-13: Apparent stress-strain response of models under axial compression with NLM, NLG and NLMG assumptions. Samples of BV/TV = 12 % (a) and BV/TV = 24 % (b).

combined material-geometric non-linear (NLMG) analyses. Contour plots of the resulting plastic strain magnitude for two typical NLMG analyses are shown in Fig. 2-14. These plots are at apparent axial compressive strain of 50000 $\mu\epsilon$. Regions shaded black correspond to a plastic strain magnitude of greater than 5000 $\mu\epsilon$. A clear reduction of apparent tangent stiffness was observed with increasing strain. Yield at the apparent-level occurred at approximately 8000 $\mu\epsilon$, which is within the range reported for natural trabecular bone (Evans and Lebow, 1951; Kopperdahl and Keaveny, 1998) and adopted for previous μFE studies (van Rietbergen et al., 2000; Pistoia et al., 2002).

A greater deviation from linear elastic behaviour was found with NLM than with NLG. Indeed, only a relatively slight reduction in tangent stiffness was observed during the NLG analyses. As can be seen in Fig. 2-13, NLM and NLMG traces were very similar.

The relative influence of NLG upon the apparent response was seen to increase with reduced volume fraction. For models of high apparent density (Fig. 2.13(b)), the inclusion of NLG in the NLM analyses altered the response only slightly. For low apparent densities (Fig. 2.13(a)), the combined inclusion of NLM and NLG resulted in apparent-level strain softening at large strains. This was not observed at higher apparent densities.

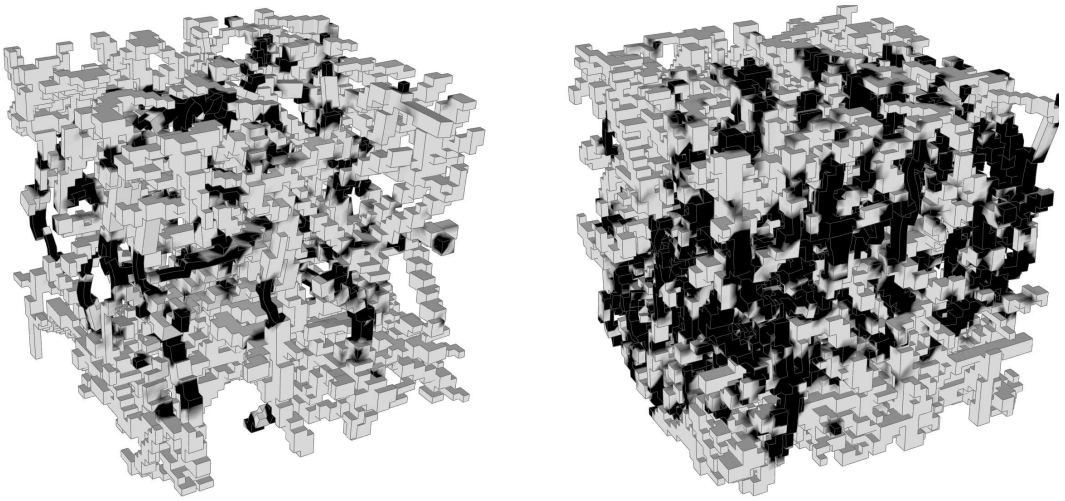

(a) (b)

Figure 2-14: Visualisations of the magnitude of plastic strain in the virtual models of BV/TV = 12 % (a) and BV/TV = 24 % (b). Regions shaded black correspond to a plastic strain greater than 5000 $\mu\epsilon$ magnitude.

2.4 Discussion

2.4.1 Microarchitectural indices

The generated models were examined to assess whether they conformed to the expected microarchitectural indices. It was found that the BV/TV ratio and the axial to transverse elastic modulus ratios closely matched the predicted targets. Since BV/TV was the primary parameter used to control the generation of the models this was expected. The variation of model microarchitecture with BV/TV was assessed using several further morphological indices, as discussed in Section 2.3.1. Tb.Th and Tb.Sp of the virtual models was lower than for real bone. Model Tb.Th followed a similar rising trend to real bone with increasing BV/TV. The difference from real bone varied between approximately 0 % at BV/TV=12 %, to 50 % at BV/TV=16–20 %, and 13 % at BV/TV=25 %. However, model Tb.Sp reduced more rapidly than real bone, with a difference of approximately 20 % at BV/TV=8 %, which increased to 45 % at BV/TV=25 %. The fact that model Tb.Th and Tb.Sp were both lower than real bone lowered the observed error in the normalised measure (Tb.Th)/(Tb.Sp). The results in Fig. 2.10(c) indicated

that this ratio was consistently higher than real bone and increased more rapidly with higher BV/TV. This result followed from the fact that Tb.Sp was relatively lower than Tb.Th compared to real bone values, and was on the denominator of the ratio. From these results it can be inferred that the model generation procedure produced pores which were too small, leading to Tb.Sp which were considerably lower than in real bone. It should be noted that in real bone the presence of rods gives way to more plate-like geometry with increasing BV/TV; yet in the generated models remained rod-based at all values of BV/TV. Indeed, the fact that the error in Tb.Sp became greater at higher BV/TV indicated that the well defined pores which would exist between plates were traversed by trabeculae, which divided the effective pore size. This effect was confirmed by the model SMI values (Fig. 2.10(e), note that values of 0, 3 and 4 correspond to an ideal plate, cylinder and sphere respectively). In real bone (Hildebrand et al., 1999) the value of SMI drops from approximately 2.2 at BV/TV=8 % to 0.4 at BV/TV=25 %; the 81 % drop in SMI corresponds to the transition from cylinder or rod-like morphology to plate-like geometry. In contrast, the virtual models displayed a more limited variation of SMI from 2.1 at BV/TV=8 % to 1.4 at BV/TV=24 %, or a 33 % drop over a similar range of BV/TV. This demonstrated that as BV/TV increased, the models displayed more plate-like geometry but still retained a considerable proportion of rod-like components. Tb.N provides a measure of the number of trabeculae traversing a unit distance within a sample. Figure 2.10(d) indicates that at BV/TV < 20 % the number of trabeculae in the models was considerably lower (by approximately 50–14 % at BV/TV=8–16 %) than expected in real bone; at higher BV/TV the models contained a similar number to real bone. This would be expected to reduce disproportionately the stiffness of low BV/TV models as discussed later in Section 2.4.3. It was noted that the DA of the models remained constant with BV/TV, at the lower range reported for real bone. Indeed, this parameter was not varied during the model generation process since an ACP of 40 % was used in all analyses. This value was selected because it produced a realistic value of mechanical anisotropy. It was not varied with BV/TV to avoid introducing additional independent variables during this study. To generate a more realistic variation of DA it would be possible to increase the ACP with BV/TV with a similar calibration procedure to that illustrated in Fig. 2-5.

2.4.2 Elastic response with model size

Simon et al. (2006) tested cubic FE meshes derived from μCT attenuations of real trabecular bone samples. It was required to know the minimum sample size needed to evaluate the elastic properties of trabecular bone. The variation of apparent Young's modulus with sample size presented by Simon et al. for real bone samples is very similar to that observed in this study for virtual samples (Fig. 2-11). Similar to this study, they also found that for real bone samples the mean apparent elastic Young's modulus and its variance decreased with increased sample size. Furthermore, previous studies of real bone samples have shown (Simon et al., 2006; Harrigan et al., 1988) that a minimum sample size of four or five pore lengths is required for accuracy. Virtual models considered in this study also indicate this.

2.4.3 Elastic response with density

As illustrated in Fig. 2-12, the elastic response of the virtual models was within the range reported for natural trabecular bone (Carter et al., 1980; Knauβ, 1981; Lotz et al., 1990; Ciarelli et al., 1991; Wirtz et al., 2000), and followed a similar trend. At low apparent densities the virtual models were considerably less stiff than the samples considered by Wirtz et al. (2000), with the exception of Carter et al. (1980). This could have resulted from one of the following limitations of this comparison with Wirtz. It has been reported (Carter et al., 1980; Parfitt, 1984; Guo and Kim, 2002) that progressive trabecular thinning, leading to loss of connectivity, is one of the major causes of weakening in osteoporotic bone. Virtual models with low BV/TV were produced by limiting the number of trabeculae generated, without reducing trabecular thickness. While the generation algorithm was capable of producing samples with this link between BV/TV and trabecular thickness, it was not activated as part of this study in order to limit the problem size. The degree of variation within the results presented by Wirtz et al. (2000) is large. It can be inferred that there are significant differences between the samples and methods of the reported studies. It can be hypothesised that the samples from different studies had different microarchitectural indices than those used in the creation of the virtual models of this study. Considering the measured morphological indices of the models in this study, it was not possible to make a direct assessment of Tb.Th at low BV/TV because the conversion from voxel to

physical dimensions was made at a low BV/TV of 12 %. It was noted however that Tb.N was lower than real bone at low BV/TV. Such a disproportionately low number of trabeculae in low BV/TV models likely contributed to their reduced stiffness. As discussed in Section 2.2.3, the coarse mesh resolution adopted for the models is also considered a source of reduced stiffness in low BV/TV models. Indeed, for models generated to the same BV/TV with 8 times and 64 times the domain volume, coarse resolution models were found to be 46 % less stiff than those at the highest resolution. It is therefore likely that had a higher resolution been selected for the modelling space, more realistic values of stiffness would have been produced at low BV/TV. It was found that this variation resulted from microarchitectural changes induced by differences in mesh resolution. This effect should not be confused with numerical mesh dependency which was demonstrated to have the effect of increasing rather than decreasing model stiffness.

2.4.4 Post-elastic response

The results of this study suggest that tissue properties rather than non-linear geometry dominate the post-elastic response of trabecular bone. For regions of high apparent density (Fig. 2.13(b)), large-deformation effects appeared to be negligible. In samples of low apparent density (Fig. 2.13(a)) a small effect was observed; the influence of NLG effects was found to increase with reduced BV/TV.

Guo et al. (1995) analysed idealised trabecular bone models of 'very low structural density'. It was observed that 'elastic buckling occurs at much higher strain levels [than plastic or tissue failure].' Analyses of the virtual models broadly agree with the conclusion of Guo et al. however, their study did not investigate the link between density and large deformation effects.

Bevill et al. (2006) analysed FE models created from μCT attenuations of trabecular bone cores. To assess the importance of large-deformation effects, analyses were conducted first by including, then excluding, large-deformation failure mechanisms. Hard tissue material properties were applied to all analyses. Bevill et al. observed significant reductions in strength predictions with the inclusion of large-deformations. Negligible reductions were observed in samples of high density, however, large-deformation effects induced substantial strength loss at lower densities. The link between apparent density and large-deformation

effects reported by Bevill et al. for real bone samples appears to be similar to that found in this study for virtual samples.

Kopperdahl and Keaveny (1998) investigated the apparent yield strain behaviour of vertebral trabecular bone. Stölken and Kinney (2003) tested an individual trabecula and a low density specimen with and without large-deformation effects. Significant strain softening was observed at strains above 2 % in both studies. The lower density samples tested in this study (Fig. 2.13(a)) showed slight strain softening at large strains. Vertebral trabecular bone forms low density structures relative to other anatomic sites (Ulrich et al., 1999). Indeed the samples tested by Kopperdahl and Keaveny (1998) and Stölken and Kinney (2003) were of lower density than those subjected to non-linear analysis in this study. It is predicted that a similar degree of strain softening would be observed in virtual models of comparable density.

2.4.5 Conclusions

This preliminary study showed that it is possible to create virtual models of trabecular bone with a pseudorandom microarchitecture using microarchitectural indices. The apparent-level mechanical response of the generated models in both the elastic and post-elastic regimes was evaluated. The results showed that the minimum sample size required to determine the elastic response is four to five pore lengths, similar to that reported for real bone. The variation of Young's modulus with density also showed characteristics observed in physical experiments. The post-elastic response was also found to be similar to that reported for natural bone samples.

As well as the described strengths of this study, several limitations should be noted. The model generation algorithm developed in this study was conceptually based upon the creation of rods. Morphological analysis of the generated models indicated that they lacked plate-like components. This issue became more important at high BV/TV which has been shown to correspond with more plate-like architecture in real bone. To improve the ability of virtual models to represent bone it seems essential that plate-like components are incorporated into the model generation algorithm. Indeed, to achieve this it seems sensible to

assign weights to the relative prevalence of rods and plates, coupled with their separated morphological indices, similar to those observed in real bone (Stauber and Müller, 2006b). The variation of both model morphology and resulting elastic stiffness with mesh resolution represents a key limitation of this study. It has been noted that to achieve the goal of generating virtual models of bone microstructure for use in larger FE studies, it was necessary to limit models to relatively low numbers of elements, and thus coarse mesh resolutions. However, in their present form, the use of virtual models in larger FE models would require considerable calibration and adjustment of tissue-level properties to achieve an acceptable balance between realistic microarchitectural and macromechanical properties. This limitation largely resulted from the generation of models in a cubic element grid. To generate a smooth surface geometry, and therefore converged morphology, in such a modelling space requires a restrictively high mesh resolution. This issue could be avoided in future by defining the FE mesh such that it follows the orientation of trabeculae. For example, this would enable rods with elliptical cross-sections to be defined to high accuracy with relatively few elements. In such a scenario, difficulty would be encountered at intersections where FE meshes of different trabeculae would not correspond to one another. A preliminary solution to this issue would be to apply tied constraints to the degrees of freedom of nodes at intersections. Indeed, models could be developed in this way by first creating a 'skeleton' of rods upon which a network of plate-like and rod-like components could be generated. This process would be similar to several studies which have sought to reduce μFE simulation times by first skeletonising μCT images and generating beam element based models from these skeletons (Pothuaud et al., 2004; van Lenthe et al., 2006; Vanderoost et al., 2008).

The virtual modelling technique represents a potentially valuable tool in the study of trabecular bone, mechanical behaviour, mechanics of fracture and response of bone to implants. This study demonstrated the proof of concept that such a methodology could be used to generate models which contain bone microstructure. With refinement of the method presented here, such models could be used to evaluate the variation of the mechanical behaviour of bone with changes in microarchitectural indices. They could also be used in macroscale FE studies where microstructural features are poorly represented by the continuum assumption to simulate bone of varying quality.

Chapter 3

Micro-finite-element modelling of cortical bone

3.1 Introduction

Micro-finite-element (μFE) techniques have been used extensively to assess the elastic constants of trabecular bone structures (Ulrich et al., 1998; Niebur et al., 2000). μFE has proved to be a powerful tool in relating bone microarchitecture to effective orthotropic elastic properties. The typical approach is to convert μCT scans of bone structure into high resolution 3D FE meshes by thresholding on the CT attenuation values. To date, the μFE technique has not been used to assess the elastic constants of cortical bone. Methods commonly employed to study cortical bone elastic properties include direct mechanical testing, nanoindentation, and ultrasonic techniques.

Both trabecular and cortical bone can be considered orthotropic at the apparent level (Knets, 1978; Van Buskirk et al., 1981; Cowin and Mehrabadi, 1989). Mechanical testing techniques are capable of assessing the orthotropic constants of bone but are subject to limitations (Rho, 1996). Bending tests (Choi et al., 1990; Zioupos and Currey, 1998; Cuppone et al., 2004) are capable of evaluating the three Young's moduli with three specimens, and Poisson's ratio. A combination of tension/compression and shear tests can be used to evaluate the full set of engineering constants (Reilly and Burstein, 1975; Knets, 1978; Turner and Burr, 1993) but the results are dependent upon the degree of mechanical symmetry assumed and are also subject to end effects (Odgaard et al., 1989). Furthermore, separate specimens must be machined for different tests so the results are an

amalgamation of the properties of several locations.

Nanoindentation methods provide accurate assessment of the Young's moduli of bone tissue. The assumption of isotropy is required for the application of nanoindentation theory, typically assuming Poisson's ratios $\nu_{ij} = 0.3$ for bone (Rho et al., 1997). It has been demonstrated that this assumption 'does not limit nanoindentation as a technique for measurement of Young's modulus in anisotropic bone' (Turner et al., 1999). However, this method cannot provide the remaining constants that define orthotropic elasticity. More recently, researchers have measured the indentation modulus of anisotropic materials (Swadener and Pharr, 2001; Fan et al., 2002; Franzoso and Zysset, 2010) in different orientations. The limitation of this method is the difficulty of converting the indentation moduli into full elasticity tensors. Franzoso and Zysset (2010) presented a technique for establishing the orthotropic elastic constants of osteons from two, orthogonal indentation measurements. This technique involves mapping a fabric tensor onto an isotropic material model to generate fabric dependent anisotropy. This requires several assumptions regarding the values of isotropic properties and assumes that the eigenvectors of the fabric and principal directions are aligned. While such methods enable accurate measurement of the Young's moduli, it was demonstrated by Franzoso and Zysset (2010) that large variations in the orthotropic shear moduli and Poisson's ratios are coupled with little corresponding variation in the indentation moduli. This suggests that these parameters remain difficult to calculate with indentation methods.

Ultrasonic testing has been widely and successfully used to assess the orthotropic elastic constants of bone tissue (Abendschein and Hyatt, 1970; Yoon and Katz, 1976; Van Buskirk et al., 1981; Rho, 1996). Two significant advantages of ultrasonic techniques over mechanical techniques have been identified (Rho, 1996): a) the ability to use 'smaller, more simply shaped specimens', and b) the measurement of several elastic constants from a single specimen. Ultrasonic methods require that sample sizes are significantly greater than the wavelength used. Cortical specimen sizes larger than 5 mm are required to use ultrasonic techniques. Studies, (Cooper et al., 2007) (femoral midshaft) and (Russo et al., 2006) (tibial midshaft), have observed mean cortical thicknesses of approximately 5 mm in males and 4 mm in females. It is therefore likely that many samples re-

main too small for ultrasonic testing. Consequently, ultrasonic measurement of the periosteal-endosteal variation of properties is prevented by size requirements. Assessment of wave path length can also be a limitation of ultrasonic techniques (Guo, 2001); in cancellous bone it is likely that the path travelled by a sound wave is longer than the edge length of the sample. However, since cortical bone is a relatively dense material, path length should not be as significant a limitation as it is in cancellous bone. Ultrasonic methods require the specification of a mean tissue density to evaluate elastic properties. This can be a source of limitation in that it ignores the heterogeneity of bone tissue (Guo, 2001).

It has been noted in previous studies that age-related porosity variations are greater at the endosteal aspect than at the periosteal aspect at the femoral mid-shaft (Bousson et al., 2000; Cooper et al., 2007). Such variations may lead to differences in elastic constants across the cortical thickness. Variations of elastic constants through the cortex could have a considerable impact on FE simulations. For instance, a fracture fixation pin traversing through a cortex with variable elastic stiffness will encounter variable resistance, which will in turn affect the pattern of load transfer. This may cause stress concentrations and loosening which may not appear without the incorporation of such elastic stiffness variations. Therefore, data which quantify the variation of elastic constants between the periosteum and endosteum are needed. μFE analyses enable the use of sufficiently small samples to study distinct locations across the cortex and thus evaluate associated variations in elastic properties.

This study quantified the variation of cortical bone elastic properties using μFE analyses (Donaldson et al., 2009a;b; 2010a;b). The first aim was to evaluate the variation of apparent-level (homogenised) orthotropic elastic constants of cortical bone with age and indices of bone microarchitecture. The second aim was to quantify the location dependent differences in elastic constants, specifically between periosteal and endosteal sites. Three Young's moduli E_R, E_C, E_L, three shear moduli G_{RC}, G_{RL}, G_{CL} and six Poisson's ratios, $\nu_{RC}, \nu_{CR}, \nu_{RL}, \nu_{LR}, \nu_{CL}, \nu_{LC}$ were evaluated for each sample (R, C, L refer to radial, circumferential and longitudinal directions respectively); only nine of these are independent in orthotropic elasticity.

3.2 Methods

The methods described in the following were implemented using programs written by the author in Matlab (The MathWorks, Inc., Natick, MA, U.S.A.).

3.2.1 Sample acquisition

The specimens used in this study came from the Melbourne Femur Collection (MFC) and were scanned as part of a previous study (Cooper et al., 2007). Full sample details are presented in this previous publication. The previous study considered both male and female samples. The largest variation in architectural properties was observed in female samples. Therefore these were chosen for the study. The 27 female samples ranged from 20–87 years in age (mean age 53.4, $\pm$ 23.6). All samples originated from the anterior femoral midshaft and were scanned using μCT at an isotropic resolution of 7 μm.

3.2.2 Regions of interest

Samples were taken near the periosteal and endosteal aspects. Three samples, separated circumferentially, were taken at each aspect to reduce the possible effect of local structural variations around the circumference of the cortex. This resulted in a total of six sampling locations per specimen, as illustrated in Fig. 3-1. Each of these samples consisted of a $150 \times 150 \times 150$ voxel cube, edge length 1.05 mm. The standard mechanics approach adopted here (discussed later) is dependent on sample size (Hollister and Kikuchi, 1992). The use of bending tests of cortical bone identified that samples deeper than 0.5 mm provided sufficient reliability (Choi et al., 1990). The sample size used here is more than twice this minimum.

3.2.3 Morphological analysis

Morphological analysis was conducted on each of the six samples from the specimens. This was carried out using the CT Analyser 1.7.0.5 software package (Skyscan, Aartselaar, Belgium). The scanning resolution prevented the inclusion of canalicular and lacunar porosity. All pores in the scan images were therefore considered canals, consistent with (Cooper et al., 2007). Parameters assessed included canal volume fraction to tissue volume ratio (Ca.V/TV), canal surface to

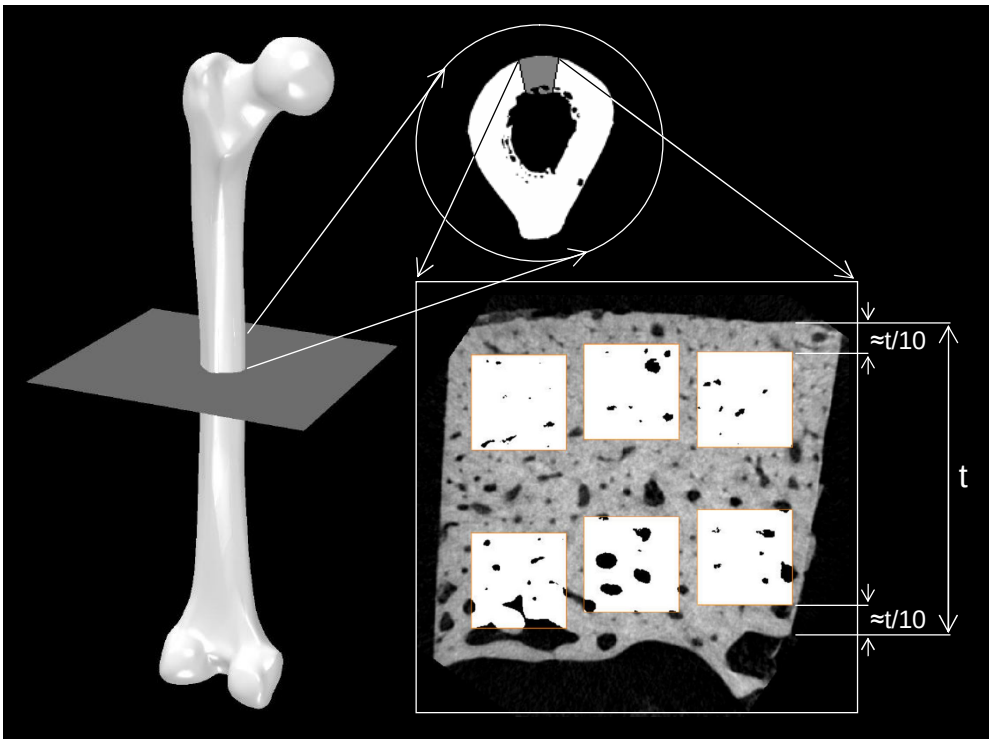

Figure 3-1: The anterior femoral midshaft sampling site, showing periosteal (upper) and endosteal (lower) samples.

tissue volume ratio (Ca.S/TV), mean canal diameter (Ca.Dm) and degree of geometric anisotropy (DA). Ca.V/TV was used throughout this study as a measure of porosity. Ca.V/TV is analogous to trabecular porosity ($1 - \mathrm{BV/TV}$) (Cooper et al., 2003), as the scans did not depict canaliculi and lacunae.

3.2.4 Mesh generation

μCT scan data were converted to FE meshes using the commercial imaging software Amira 5.0 (Visage Imaging, Berlin, Germany). User-defined thresholding was employed to binarize the images into bone and pore phases. Thresholds were constant for the six samples within each specimen but varied between specimens due to scanning differences. Surfaces of approximately $20,000$ triangles were computed from the binarized images. The number of triangles determined the resulting FE mesh resolution which was evaluated using a mesh convergence study. Tetrahedral meshes generated using a surface of approximately $20,000$ triangles were found to predict the orthotropic elastic constants with a difference of less than $1\,\%$ from meshes consisting of greater than 3.5 times more elements.

Meshes comprising tetrahedral elements (illustrated in Fig. 3-2) were generated from the triangular surfaces automatically, these typically comprised 200,000–300,000 elements.

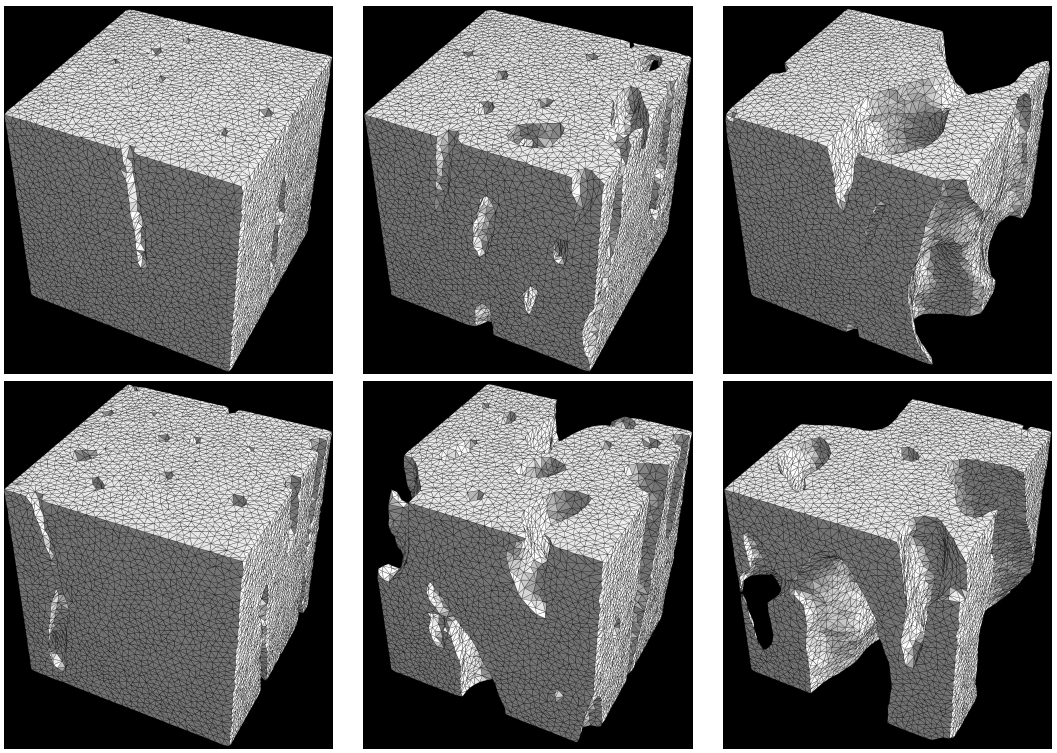

(a) (b) (c)

Figure 3-2: 3D renderings of selected samples at the periosteal and endosteal aspects. The upper row are samples from the periosteal aspect, the lower row shows samples from the endosteal. (a) 20-year-old female, (b) 61-year-old female, (c) 84-year-old female. The periosteal aspect is at the upper-left corner of all images.

3.2.5 Tissue properties

A transversely-isotropic material model was used to account for tissue-level anisotropy. The tissue-level elastic constants were derived from the orthotropic elastic properties of individual lamella (Yoon and Cowin, 2008). These results were ideal for use in this study because they provide the elastic properties of lamella, above the lacuna-canalicular and (crucially) below the osteonal levels. The Young's moduli of Yoon and Cowin compared well with those measured using nanoindentation by others (Rho et al., 1997; Fan et al., 2002; Rho et al., 2002). It

Table 3.1: Elastic constants used to define the transversely-isotropic, homogeneous tissue-level material model (Moduli in GPa). 1,2 refer to the two transverse directions and 3 to the longitudinal.

E_1	E_2	E_3	G_{12}	G_{13}	G_{23}	ν_{12}	ν_{13}	ν_{21}	ν_{23}	ν_{31}	ν_{32}
19.2	19.2	22.8	7.4	7.2	7.2	0.294	0.266	0.294	0.266	0.315	0.315

was assumed that all lamella were aligned in the longitudinal direction. Thus the orthotropic properties presented by Yoon and Cowin were converted into tranversely isotropic properties by rotating the lamellar stiffness tensor into 3600 equally spaced orientations around the longitudinal axis and extracting the average values. The tissue properties used are presented in Table 3.1 in the same format as Yoon and Cowin for ease of comparison.

3.2.6 Numerical tests

Six strain states were computationally applied to each sample; tensile strain in the x, y, z directions and pure shear strain in the xy, xz, yz planes. These tests enabled the evaluation of the full elastic stiffness tensor $\underset{\sim}{D}^e$ using standard mechanics methodology (Hollister and Kikuchi, 1992; van Rietbergen et al., 1996). Periodic boundary conditions were used in the analyses by reflecting the models in the three dimensions and tying corresponding nodes on opposite faces. Periodic conditions have been identified as providing the most realistic predictions, between those of traction and displacement boundary conditions (Hollister and Kikuchi, 1992; Kanit et al., 2003). Using this method the effective stiffness tensor is evaluated as,

$$\underset{\sim}{D}^e = \frac{1}{V} \int \underset{\sim}{D}_t^e \underset{\sim}{M} dV \tag{3.1}$$

where V is the total sample volume and $\underset{\sim}{D}_t^e$ is the tissue-level stiffness tensor. $\underset{\sim}{M}$ is the local structure tensor (Suquet, 1985; Hollister and Kikuchi, 1992), which relates the applied macrostrain $\left(\underset{\sim}{\epsilon}^{app}\right)$ to the local strain at each integration point $\left(\underset{\sim}{\epsilon}^{loc}\right)$, such that $\underset{\sim}{\epsilon}^{loc} = \underset{\sim}{M}\underset{\sim}{\epsilon}^{app}$. Each applied state of strain enabled the evaluation of one column of $\underset{\sim}{M}$, such that $M_{ij} = \epsilon_i^{loc}/\epsilon_j^{app}$.

To account for the potential misalignment of sample and bone orientations, an optimisation routine similar to that of van Rietbergen et al. (1996) was applied to the effective stiffness tensors. This process enabled sample orientations to be found such that the assumption of orthotropy best fit the effective stiffness tensor. The approach involved minimisation of the ratio of the square of 'zero' to 'non-zero' terms in a perfectly orthotropic material. Since specimens and samples were selected in approximately longitudinal, circumferential and radial femoral orientations, only minimal rotations were desirable. To prevent anatomical axes being altered excessively, the rotations were limited to 10°. In practice less than 15 % of optimisations resulted in angles in excess of 1° indicating that femur and sample orientations were generally well aligned. A simple methodology was employed to estimate the error induced by the orthotropy assumption (van Rietbergen et al., 1996). Stress-strain relationships can be expressed as $\underset{\sim}{\sigma} = \underset{\sim}{D}^e \underset{\sim}{\epsilon}$ (where $\underset{\sim}{\sigma}$, $\underset{\sim}{D}^e$ and $\underset{\sim}{\epsilon}$ are the stress, material stiffness and strain tensors respectively). The assumption of orthotropy replaces $\underset{\sim}{D}^e$ with $\underset{\sim}{D}^{e,\mathrm{ORT}}$ in which the appropriate tensor terms of $\underset{\sim}{D}^e$ are set to zero, leading to $\underset{\sim}{\sigma} = \underset{\sim}{D}^{e,\mathrm{ORT}} \underset{\sim}{\epsilon}^{\mathrm{ORT}}$ (with constant stress). The difference between the two predictions of strain is used to estimate the accuracy of the orthotropy assumption, such that

$$\underset{\sim}{\epsilon} - \underset{\sim}{\epsilon}^{\mathrm{ORT}} = \left(\underset{\sim}{I} - \left[\underset{\sim}{D}^{e,\mathrm{ORT}} \right]^{-1} \underset{\sim}{D}^e \right) \underset{\sim}{\epsilon} \tag{3.2}$$

where $\underset{\sim}{I}$ is the identity. The relative error in the strain tensor is contained in the first term of Eq. 3.2. The maximum error induced by the orthotropy assumption can therefore be expressed as

$$\mathrm{Error}^{\mathrm{ORT}} = \frac{\left\| \underset{\sim}{\epsilon} - \underset{\sim}{\epsilon}^{\mathrm{ORT}} \right\|}{\left\| \underset{\sim}{\epsilon} \right\|} = \left\| \left(\underset{\sim}{I} - \left[\underset{\sim}{D}^{e,\mathrm{ORT}} \right]^{-1} \underset{\sim}{D}^e \right) \right\| \tag{3.3}$$

where $\left\| \underset{\sim}{x} \right\|$ denotes the Euclidean norm when applied to vectors ($\sqrt{\underset{\sim}{x}^T \underset{\sim}{x}}$) or the matrix norm when applied to matrices ($\sqrt{\max(\mathrm{eigval}(\underset{\sim}{x}^T \underset{\sim}{x}))}$). Figure 3-3 illustrates the distribution of orthotropy errors in periosteal and endosteal samples using the above methodology. The median errors were 0.15 % and 1.87 % at the periosteal and endosteal sites respectively. The maximum errors at periosteal and endosteal sites were 3.56 % and 9.94 % respectively. It was noted that, in general,

samples with higher porosity exibited greater deviation from the assumption of orthotropy. This may indicate an increase in anisotropy with increased porosity. The indicated errors suggested that orthotropy was a good representation of the material symmetry present. Once the effective stiffness tensors were evaluated, the 12 elastic constants were evaluated algebraically.

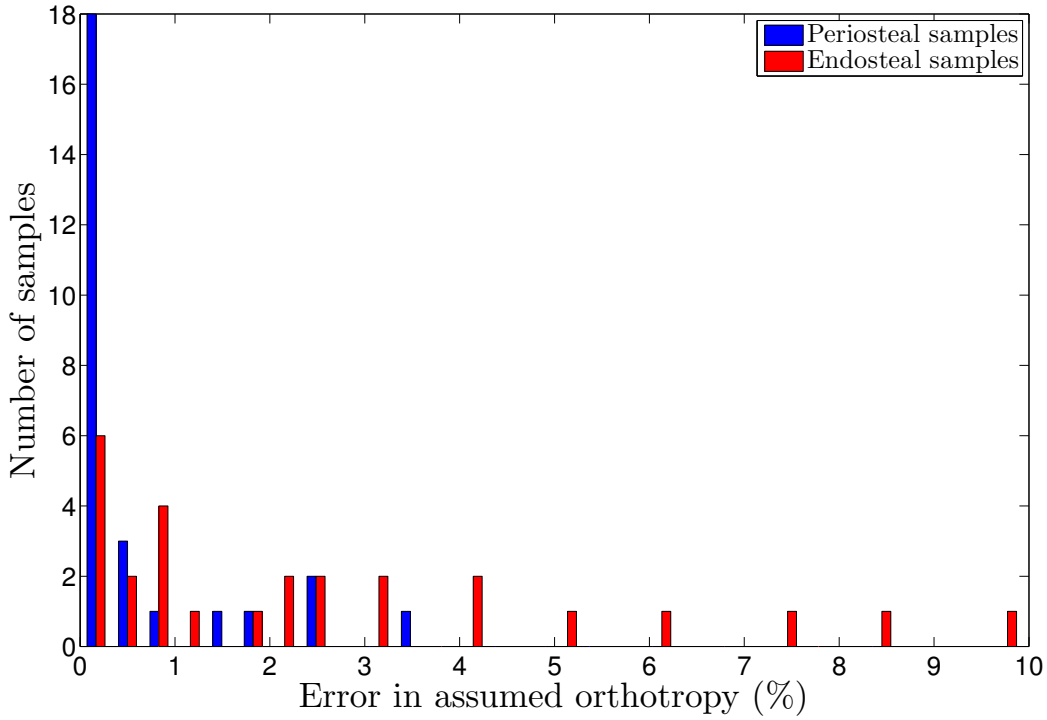

Figure 3-3: The distribution of orthotropy errors in periosteal and endosteal samples.

3.3 Results

3.3.1 Regression with architectural indices

Linear regressions were performed between all considered microarchitectural indices and elastic constants. Ca.V/TV was observed to correlate very well with the three Young's moduli ($r^2 > 0.96$, see Fig. 3.4(a) and Table 3.2). All Young's moduli reduced as Ca.V/TV increased. At low Ca.V/TV the Young's moduli reflected the assigned transversely isotropic tissue properties; E_L was greater than the

two transverse moduli, which were approximately equal. As Ca.V/TV increased the moduli diverged from the assigned tissue properties; at Ca.V/TV=50 %, E_L, E_C and E_R had reduced by approximately 52 %, 68 % and 87 % respectively. The divergence of the two transverse moduli indicated greater anisotropy with increased Ca.V/TV. Figure 3.4(b) shows the variation of effective shear moduli with Ca.V/TV. All shear moduli reduced with increased Ca.V/TV. At Ca.V/TV $>$ 10 %, G_{RC} became less than both G_{RL} and G_{CL}. G_{CL} was also greater than G_{RL} for Ca.V/TV $>$ 10 %.

All Poisson's ratios reduced with increased Ca.V/TV (Fig. 3-5). One Poisson's ratio, ν_{CR} (Fig. 3-5(d)) correlated poorly with Ca.V/TV. Noting that in orthotropy the Poisson's ratios are related in three pairs as $\frac{\nu_{ij}}{E_i} = \frac{\nu_{ji}}{E_j}$, it is only necessary to specify one from each pair. Following linear regression analysis it was observed that the three best correlated ($r^2 > 0.82$) Poisson's ratios (with Ca.V/TV) were each from separate pairs. These values are illustrated in the top row of Figs. 3-5. It was also noted that these Poisson's ratios exhibited the greatest reduction with Ca.V/TV increase; approximately 66 %, 85 % and 44 % for ν_{RC}, ν_{RL} and ν_{CL}. Following from the relationship between orthotropic Poisson's ratios it can be shown that if one Poisson's ratio (and both Young's moduli) are related linearly to Ca.V/TV, then the other must be related non-linearly. This non-linearity appeared to be slight for ν_{LR} and ν_{LC} but is more pronounced in the case of ν_{CR}.

Table 3.2: Linear regression parameters for all elastic constants against Ca.V/TV = x with transversely-isotropic tissue properties (all moduli are in GPa, Ca.V/TV as percentage). ν_{ij} marked * are suggested as independent constants.

Parameter	Equation	r^2	p
E_R (Radial)	$= -0.3898x + 19.2016$	0.959	< 0.001
E_C (Circ.)	$= -0.3024x + 19.1781$	0.983	< 0.001
E_L (Longit.)	$= -0.2620x + 22.9581$	0.996	< 0.001
G_{RC}	$= -0.1334x + 7.4220$	0.974	< 0.001
G_{RL}	$= -0.1165x + 7.1715$	0.982	< 0.001
G_{CL}	$= -0.0954x + 7.1496$	0.992	< 0.001
ν_{RC}^*	$= -0.003691x + 0.2919$	0.825	< 0.001
ν_{CR}	$= -0.000784x + 0.2836$	0.171	< 0.001
ν_{RL}^*	$= -0.004529x + 0.2648$	0.944	< 0.001
ν_{LR}	$= -0.001354x + 0.3106$	0.722	< 0.001
ν_{CL}^*	$= -0.002771x + 0.2633$	0.966	< 0.001
ν_{LC}	$= -0.001316x + 0.3123$	0.880	< 0.001

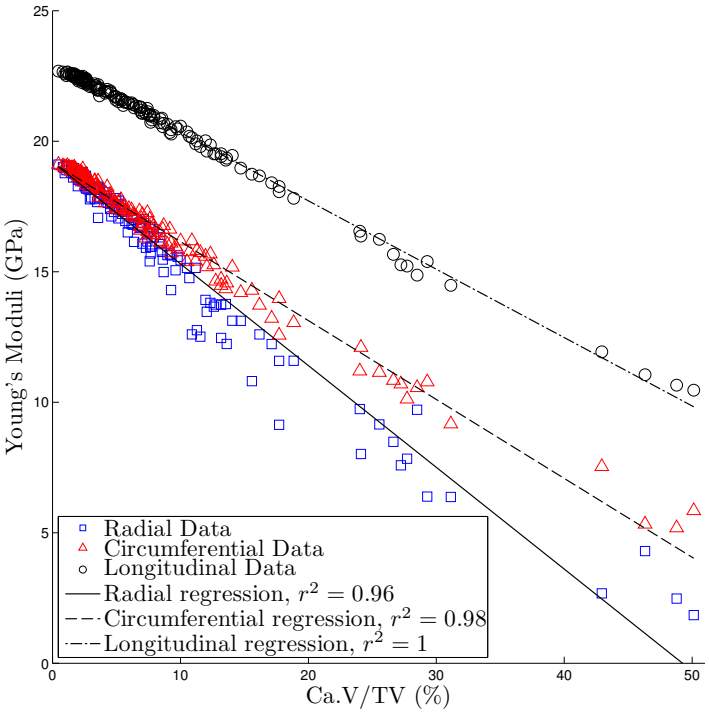

(a)

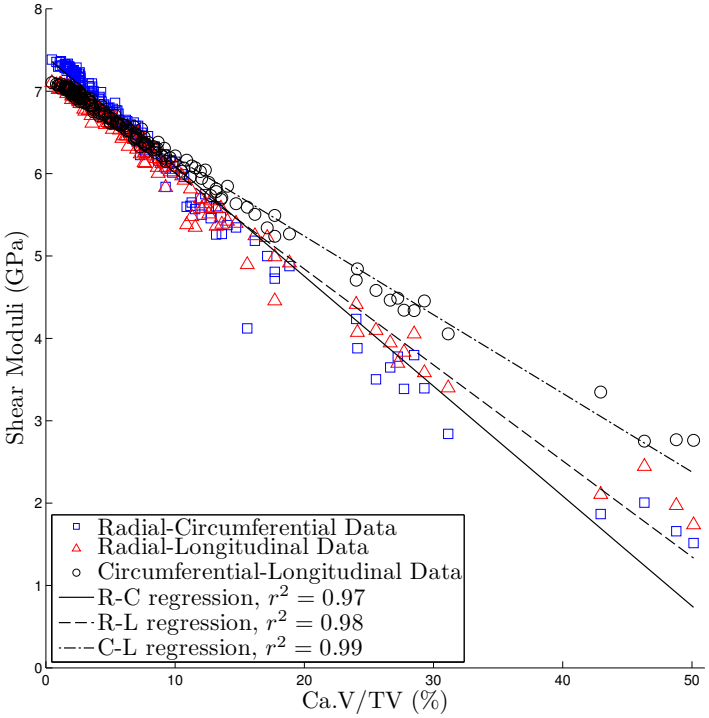

(b)

Figure 3-4: The three Young's moduli (a), and shear moduli (b) plotted against Ca.V/TV.

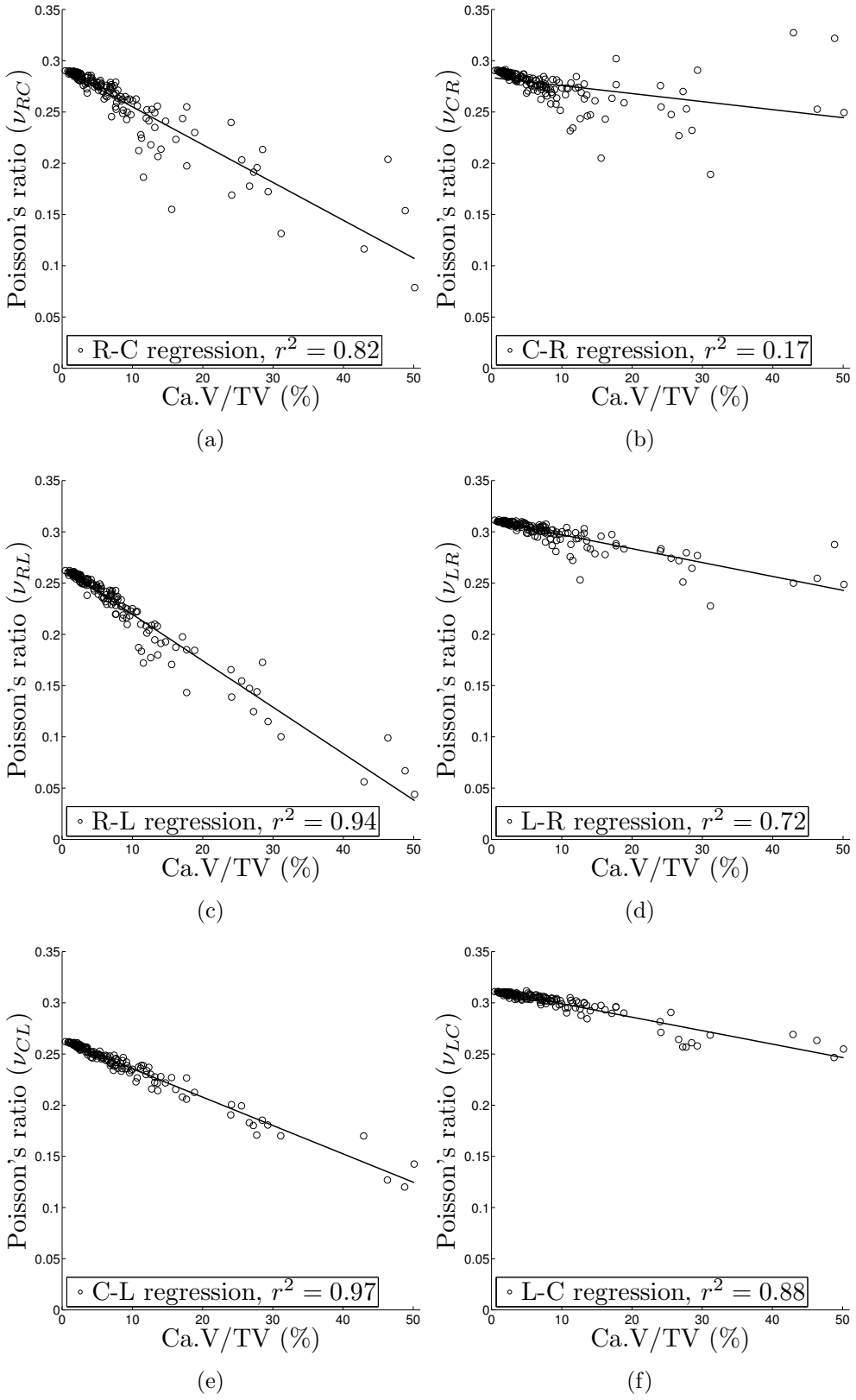

Figure 3-5: Effective orthotropic Poisson's ratios regressed against Ca.V/TV.

Reduction of the three Young's moduli was very strongly predicted ($r^2 > 0.83$) by increased Ca.S/TV (see Table 3.3 and Fig. 3.6(a)). At Ca.S/TV $< 0.007\,\mu\text{m}^{-1}$ little change in Young's moduli was observed with changes in Ca.S/TV. This may suggest a need for a non-linear regression function. However, this deviation was relatively small compared to the scatter at larger Ca.S/TV and a non-linear function was not expected to considerably improve its predictive power. In the interests of simplicity, linear regressions were retained. The source of this behaviour at low Ca.S/TV was expected to be the increased presence of narrow canals which represent a sudden increase in surface area but a less sudden reduction in stiffness. The longitudinal Young's modulus was greater than the two transverse moduli for all Ca.S/TV. At low Ca.S/TV, the two transverse moduli were similar. However, as Ca.S/TV increased the transverse moduli diverged; the circumferential modulus retained higher stiffness than the radial. Reduced shear moduli were very strongly predicted ($r^2 > 0.85$) by increased Ca.S/TV (see Table 3.3 and Fig. 3.6(b)). These also deviated slightly from the linear trend at low Ca.S/TV. The shear moduli were more similar to each other than were the Young's moduli. At Ca.S/TV $< 0.008\,\mu\text{m}^{-1}$, G_{RC} was slightly greater than the other shear moduli. As Ca.S/TV increased they diverged and at Ca.S/TV > 0.012 were ranked $G_{CL} > G_{RL} > G_{RC}$.

Table 3.3: Linear regression parameters for all elastic constants against Ca.S/TV $= x$ with transversely-isotropic tissue properties (all moduli in GPa, Ca.S/TV as μm^{-1}). ν_{ij} marked * are suggested as independent constants.

Parameter	Equation	r^2	p
E_R (Radial)	$= -1532.1x + 30.1094$	0.831	< 0.001
E_C (Circ.)	$= -1212.5x + 27.8595$	0.887	< 0.001
E_L (Longit.)	$= -1031.4x + 30.3044$	0.867	< 0.001
G_{RC}	$= -524.7x + 11.1579$	0.845	< 0.001
G_{RL}	$= -456.4x + 10.4183$	0.846	< 0.001
G_{CL}	$= -379.6x + 9.8610$	0.88	< 0.001
ν_{RC}^*	$= -0.001373x + 0.3881$	0.641	< 0.001
ν_{CR}	$= -0.000300x + 0.3048$	0.141	< 0.001
ν_{RL}^*	$= -0.001748x + 0.3887$	0.789	< 0.001
ν_{LR}	$= -0.000506x + 0.3462$	0.567	< 0.001
ν_{CL}^*	$= -0.001113x + 0.3430$	0.874	< 0.001
ν_{LC}	$= -0.000506x + 0.3481$	0.73	< 0.001

The variation of all Poisson's ratios with Ca.S/TV are plotted in Fig. 3-7. As Ca.S/TV increased, all Poisson's ratios decreased. As described for Ca.V/TV, the Poisson's ratio with the largest coefficient of determination was selected from each

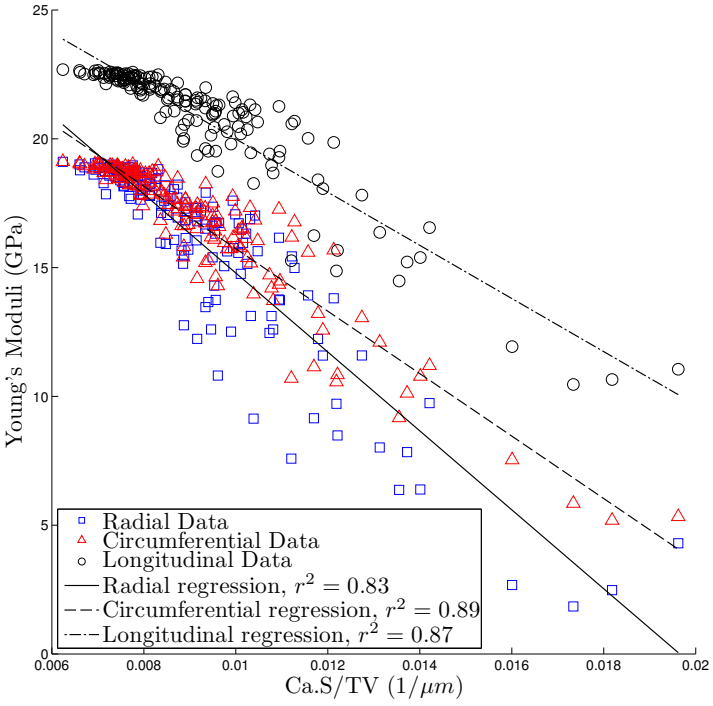

(a)

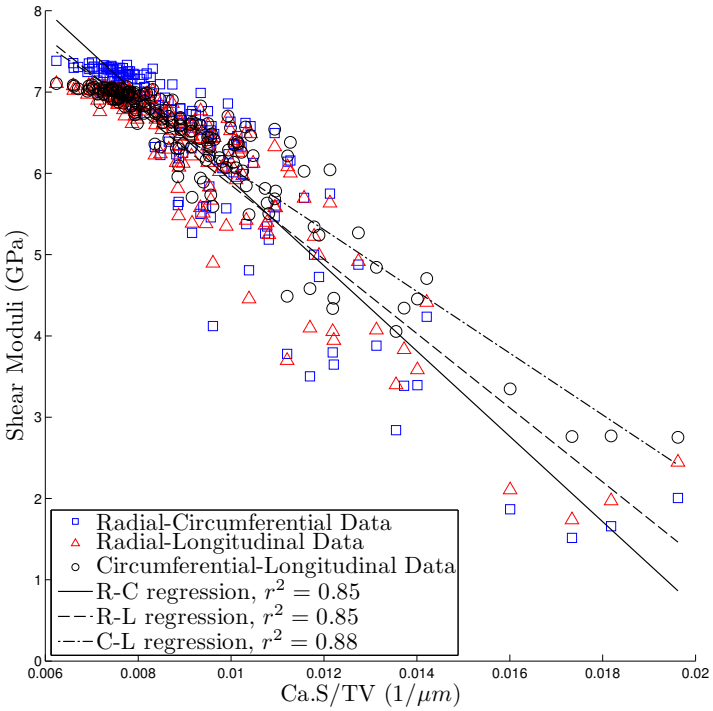

(b)

Figure 3-6: The three Young's moduli (a), and shear moduli (b) plotted against Ca.S/TV.

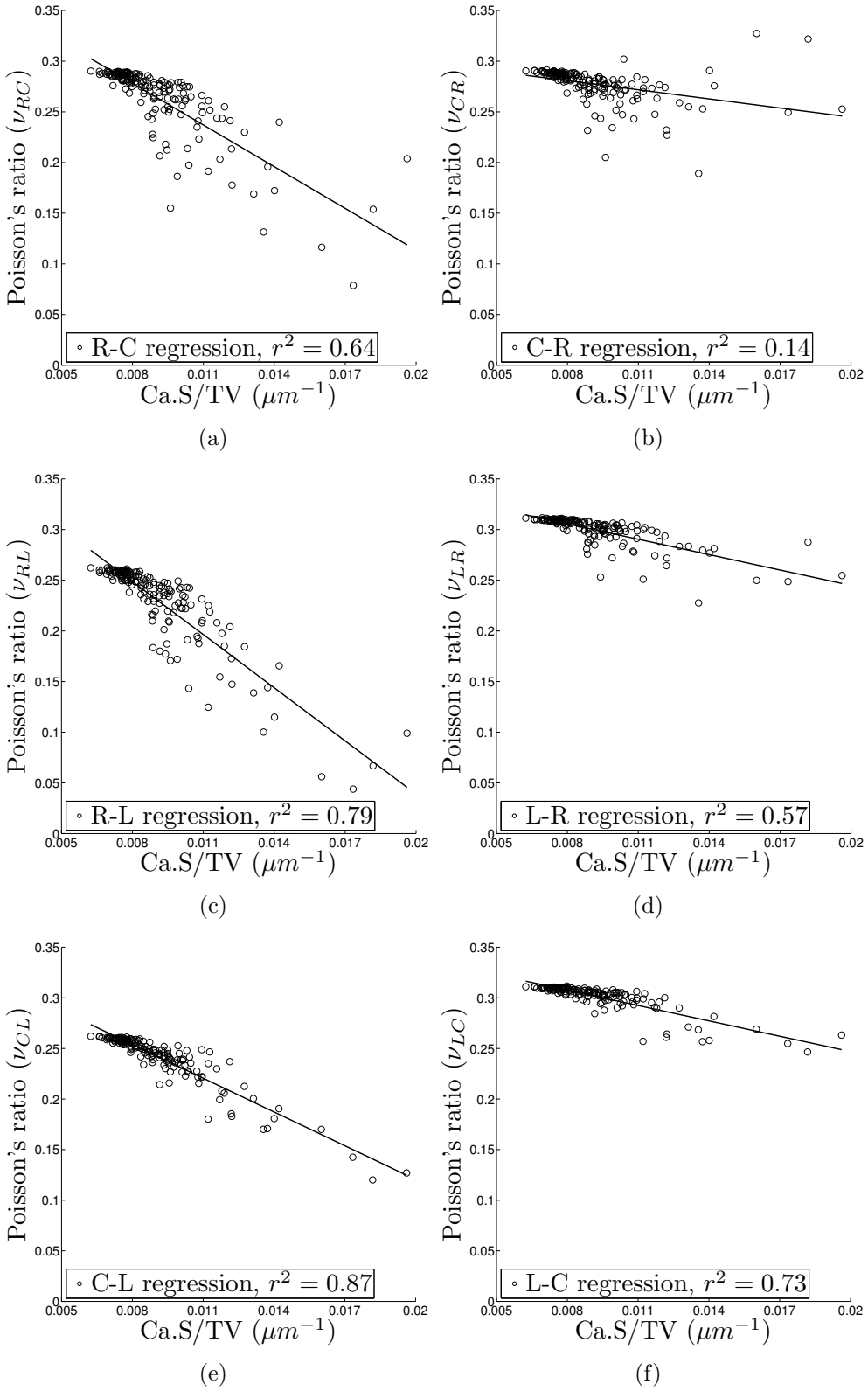

Figure 3-7: Effective orthotropic Poisson's ratios regressed against Ca.S/TV.

pair. These were the same as selected against Ca.V/TV. Ca.S/TV was strongly predictive ($r^2 > 0.64$) of the selected Poisson's ratios. At Ca.S/TV $< 0.008\,\mu\text{m}^{-1}$ slight deviation from the linear trend was observed. This appeared less than observed with the Young's and shear moduli and was minimal in the lesser correlated Poisson's ratio from each pair. ν_{CR} was poorly predicted ($r^2 = 0.14$) by Ca.S/TV.

The Young's moduli were very strongly predicted by Ca.Dm ($r^2 > 0.80$, see Fig. 3.8(a) and Table 3.4). As Ca.Dm increased, the Young's moduli decreased. The scatter in results appeared to increase with Ca.Dm, this suggested that the arrangement of canals became more varied as their size increases. At all values of Ca.Dm, it was observed that E_L was greater than the two transverse moduli. At Ca.Dm $< 125\,\mu$m the two transverse moduli were similar but diverged as Ca.Dm increased; E_C was greater than E_R at Ca.Dm $> 100\,\mu$m. The shear moduli also reduced, and were very strongly predicted ($r^2 > 0.82$) by increased Ca.Dm (see Table 3.4 and Fig. 3.8(b)). At Ca.Dm $< 75\,\mu$m G_{RC} slightly exceeded the other shear moduli. As Ca.Dm increased the shear moduli diverged and became ranked $G_{CL} > G_{RL} > G_{RC}$.

The Poisson's ratios reduced with increased Ca.Dm (see Fig. 3-9 and Table 3.4). The Poisson's ratio from each pair with the greatest coefficient of determination was identical to that indicated for other morphological indices. The minimal coefficient of determination of this set was $r^2 > 0.7$. Similar to other morphological predictors, ν_{CR} was poorly predicted by Ca.Dm ($r^2 = 0.20$).

Table 3.4: Linear regression parameters for all elastic constants against Ca.Dm = x with transversely-isotropic tissue properties (all moduli in GPa, Ca.Dm as μm). ν_{ij} marked * are suggested as independent constants.

Parameter	Equation	r^2	p
E_R (Radial)	$= -0.0556x + 21.2692$	0.801	< 0.001
E_C (Circ.)	$= -0.0431x + 20.7750$	0.818	< 0.001
E_L (Longit.)	$= -0.0370x + 24.3150$	0.817	< 0.001
G_{RC}	$= -0.0193x + 8.1523$	0.835	< 0.001
G_{RL}	$= -0.0166x + 7.7847$	0.815	< 0.001
G_{CL}	$= -0.0136x + 7.6540$	0.826	< 0.001
ν_{RC}^*	$= -0.000530x + 0.3118$	0.698	< 0.001
ν_{CR}	$= -0.000133x + 0.2897$	0.2	< 0.001
ν_{RL}^*	$= -0.000638x + 0.2881$	0.768	< 0.001
ν_{LR}	$= -0.000189x + 0.3174$	0.576	< 0.001
ν_{CL}^*	$= -0.000389x + 0.2774$	0.781	< 0.001
ν_{LC}	$= -0.000183x + 0.3188$	0.696	< 0.001

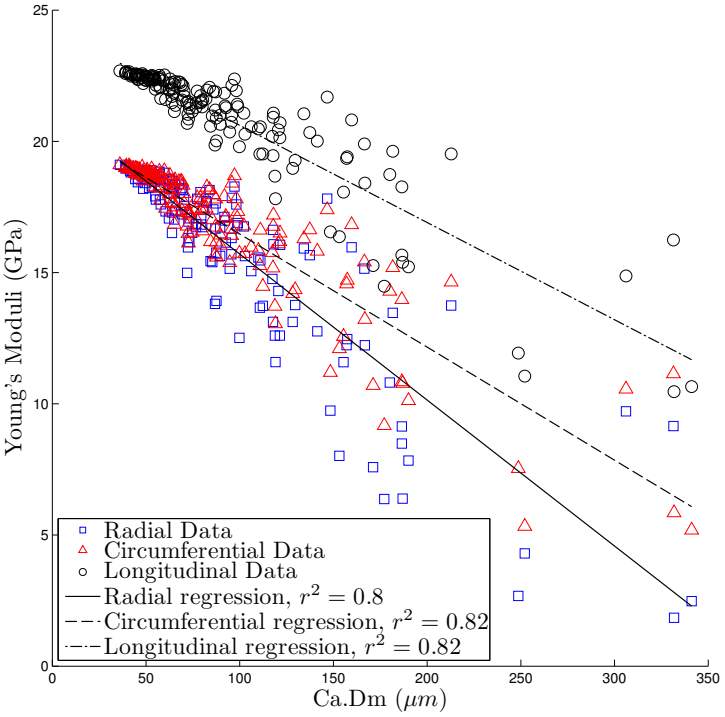

(a)

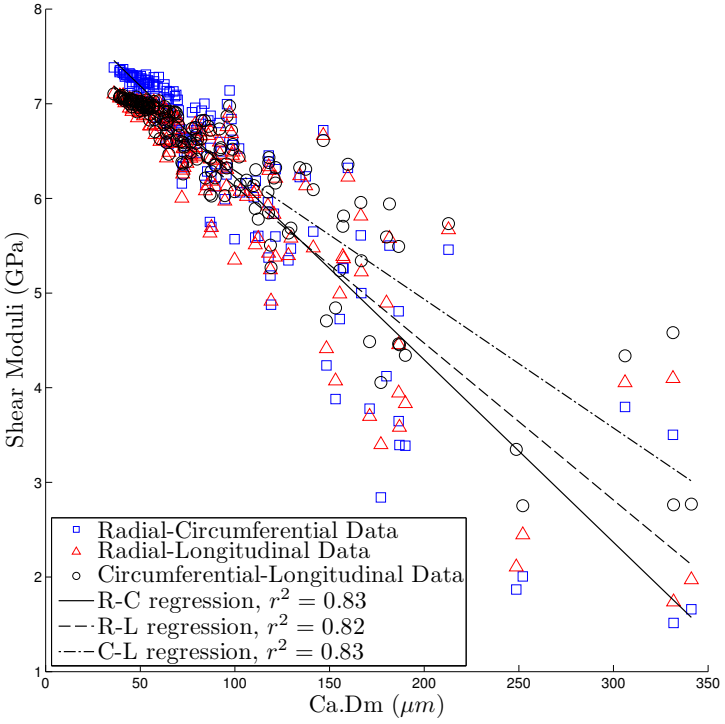

(b)

Figure 3-8: The three Young's moduli (a), and shear moduli (b) plotted against Ca.Dm.

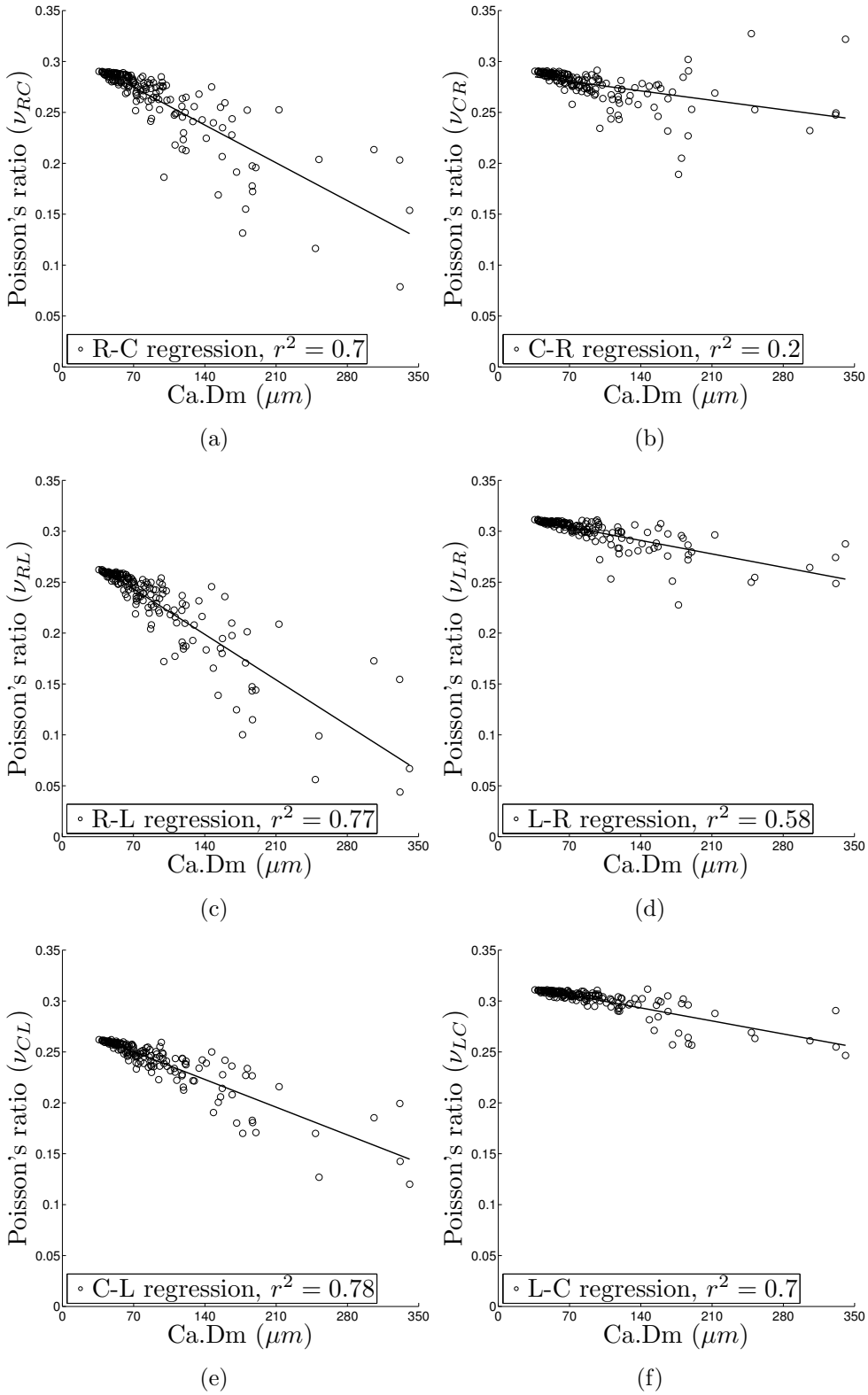

Figure 3-9: Effective orthotropic Poisson's ratios regressed against Ca.Dm.

The DA was measured on a scale of 1 to ∞, where 1 represents canal structural isotropy, and ∞ represents complete anisotropy. The samples were evaluated with a DA between 1.3 and 4.75. This indicated a variation of microstructure from near isotropy to considerable anisotropy. Decreased Young's moduli were strongly predicted ($r^2 > 0.74$) by increased morphological anisotropy (see Table 3.5 and Fig. 3.10(a)). At all DA E_L was greater than the two transverse Young's moduli. At DA < 2.5 the transverse moduli were relatively similar. G_{CL} became greater than G_{RL} as DA increased. The increase in canal morphological anisotropy was accompanied by increased elastic anisotropy. At DA < 1.7 the Young's moduli appeared to depart from the linear trend and showed reduced sensitivity to changes in DA. It is considered likely that this resulted from the presence of numerous narrow canals which would considerably adjust the local structural anisotropy without an equivalent effect on the elastic constants. Since this deviation was relatively small compared to the scatter at higher DA it was not considered necessary to adopt a non-linear regression. The shear moduli (see Fig. 3.10(b)) also reduced with increased DA. The shear moduli were strongly predicted ($r^2 > 0.75$) by DA. At DA < 2.5, G_{RC} was greater than the other shear moduli. As DA increased, the shear moduli became ranked $G_{CL} > G_{RL} > G_{RC}$. Similar to the Young's moduli, the shear moduli appeared to deviate from the linear trend for DA < 1.7. It is expected that this occurred for the same reason as with the Young's moduli.

The Poisson's ratios all reduced with increased canal morphological anisotropy (see Table 3.5 and Fig. 3-11). Since Poisson's ratios determine the interaction of strains in orthogonal directions they play a key role in elastic anisotropy. The observed reducing trend indicated that as canal anisotropy increased, the strain components transferred between orthogonal directions reduced. This implied that the elastic response in one orientation became increasingly independent of the properties in the other orientations. The Poisson's ratios from each pair with the best predictive power were identical to those observed through correlation with other indices. Also similar to previously considered indices, ν_{CR} was poorly predicted ($r^2 = 0.12$) by DA.

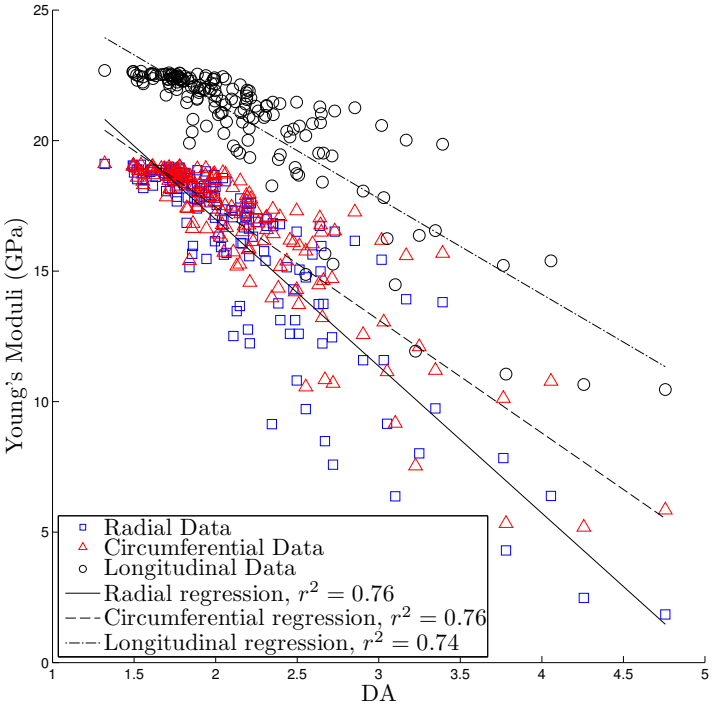

(a)

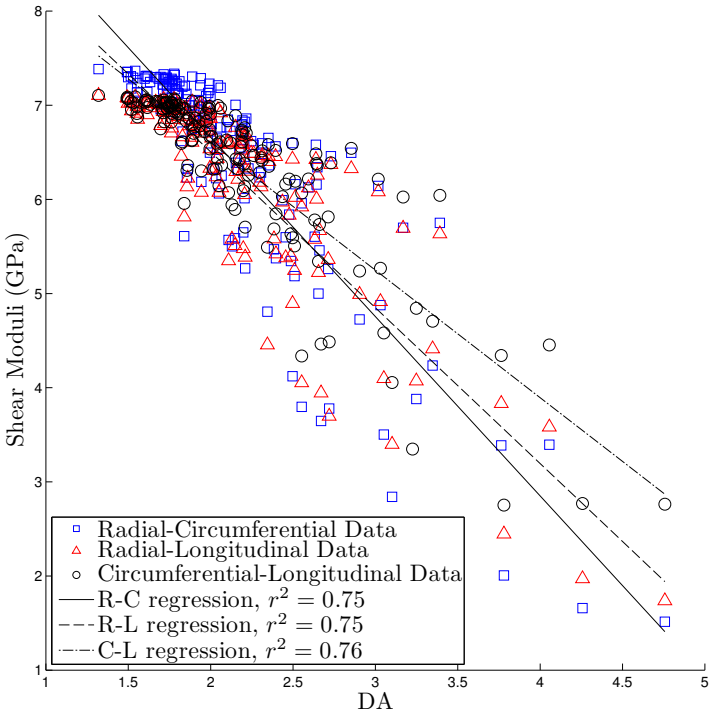

(b)

Figure 3-10: The three Young's moduli (a), and shear moduli (b) plotted against DA.

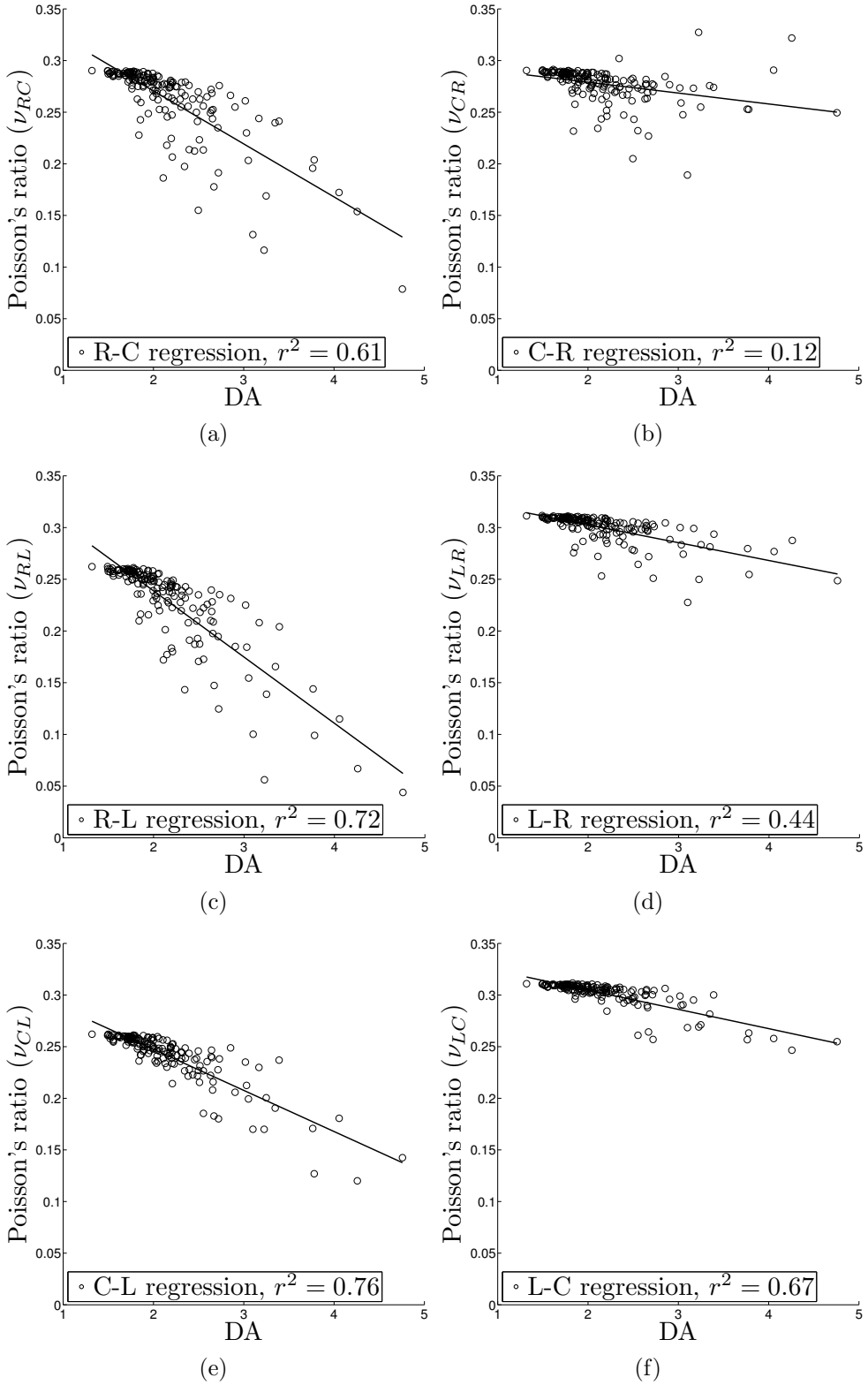

Figure 3-11: Effective orthotropic Poisson's ratios regressed against DA.

Table 3.5: Linear regression parameters for all elastic constants against DA = x with transversely-isotropic tissue properties (all moduli in GPa, DA is dimensionless). ν_{ij} marked * are suggested as independent constants.

Parameter	Equation	r^2	p
E_R (Radial)	$= -5.6270x + 28.2380$	0.758	< 0.001
E_C (Circ.)	$= -4.3276x + 26.1078$	0.764	< 0.001
E_L (Longit.)	$= -3.6681x + 28.7867$	0.741	< 0.001
G_{RC}	$= -1.9045x + 10.4689$	0.753	< 0.001
G_{RL}	$= -1.6553x + 9.8156$	0.752	< 0.001
G_{CL}	$= -1.3544x + 9.3121$	0.758	< 0.001
ν_{RC}	$= -0.0513x + 0.3733$	0.605	< 0.001
ν_{CR}	$= -0.0105x + 0.3001$	0.117	< 0.001
ν_{RL}	$= -0.0641x + 0.3670$	0.716	< 0.001
ν_{LR}	$= -0.0172x + 0.3370$	0.443	< 0.001
ν_{CL}	$= -0.0399x + 0.3272$	0.758	< 0.001
ν_{LC}	$= -0.0187x + 0.3421$	0.671	< 0.001

Multiple regression

The relative predictive power of the four microarchitectural indices for each elastic constant was assessed by stepwise regression. Table 3.6 shows the best predictive equations in terms of coefficients of each of the indices (A_{ind}). Stepwise regression is an iterative process which generates a best fit regression over multiple predictive terms. In this study an initial model containing no predictive terms was employed. Each morphological index was assessed as a predictor of the elastic constants. Predictors were added to the regression if they improved its predictive power, or removed from if they reduced it. If predictors improved the regression

Table 3.6: Stepwise multiple regression parameters for all elastic constants against Ca.V/TV, Ca.S/TV, Ca.Dm and DA (all moduli in GPa, Ca.V/TV, Ca.S/TV and Ca.Dm in %, μm^{-1}, μm respectively). ν_{ij} marked * are suggested as independent constants.

Parameter	r^2	p	intercept	$A_{\text{Ca.V/TV}}$	$A_{\text{Ca.S/TV}}$	$A_{\text{Ca.Dm}}$	A_{DA}	Δr^2
E_R (Radial)	0.965	< 0.001	17.9705	−0.4251	458.9641		−1.245100	0.0054
E_C (Circ.)	0.986	< 0.001	20.7508	−0.2317	−179.4995	−0.005319		0.0027
E_L (Longit.)	0.997	< 0.001	22.4054	−0.2789	42.3870		0.139100	0.0007
G_{RC}	0.978	< 0.001	7.5564	−0.1169		−0.002860		0.0035
G_{RL}	0.984	< 0.001	6.7467	−0.1290	105.1517		−0.202600	0.0027
G_{CL}	0.993	< 0.001	7.3884	−0.0825	−24.0356	−0.001311		0.0012
ν_{RC}^*	0.861	< 0.001	0.2293	−0.005552	13.1540		−0.019872	0.0365
ν_{CR}	0.200	< 0.001	0.2897			−0.000133		0.0293
ν_{RL}^*	0.955	< 0.001	0.2205	−0.006123	8.9698	0.000064	−0.014338	0.0108
ν_{LR}	0.748	< 0.001	0.2958	−0.001816			0.008563	0.0258
ν_{CL}^*	0.967	< 0.001	0.2711	−0.002536	−1.0537			0.0009
ν_{LC}	0.897	< 0.001	0.2948	−0.002007	3.3875	0.000039	−0.005372	0.0174

($p < p_{\text{ent}} = 0.05$) they were included, and removed if they did not improve it ($p > p_{\text{exit}} = 0.1$). The outcome of stepwise regressions are dependent upon both the initial model and the order in which the predictors are added. In this case no initial model was specified and each parameter was added in order of highest significance. It therefore seems a reasonable tool for assessing the relative and combined predictive power of the morphological indices considered. Ca.V/TV was the only predictor seen to significantly predict all orthotropic elastic constants. Indeed, the relative improvement in coefficient of determination from the simple regressions of Ca.V/TV alone (Table 3.2) were small ($\Delta r^2 < 1\,\%$ in the six moduli, and $\Delta r^2 < 4\,\%$ in the Poisson's ratios).

3.3.2 Periosteal-endosteal variation

Following the results presented in Section 3.3.1 it was identified that the variation of elastic constants with Ca.V/TV alone was sufficient to represent the key trends; this Section therefore considers only Ca.V/TV. It is important to note that Ca.V/TV_{ave} used here is the mean of the six samples taken from each donor, this differs from the rest of this study where Ca.V/TV refers to the six samples from each donor individually. Table 3.7 shows the regression equations of the orthotropic constants against Ca.V/TV_{ave}. The linear regression equations found were significant ($p < 0.001$) for all constants except ν_{CR}. The variation of E_L with Ca.V/TV_{ave} is shown in Fig. 3-12(a). At Ca.V/$\text{TV}_{\text{ave}} < 5\,\%$, the

Table 3.7: Periosteal and endosteal linear regression parameters for all elastic constants against Ca.V/$\text{TV}_{\text{ave}} = x$ (all moduli in GPa, Ca.V/TV_{ave} in %). ν_{ij} marked * are suggested as independent constants.

Parameter	Equation - Periosteal	r^2	p	Equation - Endosteal	r^2	p
E_R (Radial)	$= -0.2319x + 19.4293$	0.804	< 0.001	$= -0.5712x + 19.1588$	0.949	< 0.001
E_C (Circ.)	$= -0.1684x + 19.2972$	0.798	< 0.001	$= -0.4520x + 19.1821$	0.975	< 0.001
E_L (Longit.)	$= -0.1280x + 22.8531$	0.818	< 0.001	$= -0.3993x + 23.0896$	0.979	< 0.001
G_{RC}	$= -0.0753x + 7.4703$	0.801	< 0.001	$= -0.1959x + 7.4084$	0.957	< 0.001
G_{RL}	$= -0.0629x + 7.1807$	0.809	< 0.001	$= -0.1737x + 7.191$	0.964	< 0.001
G_{CL}	$= -0.0508x + 7.1584$	0.805	< 0.001	$= -0.1433x + 7.1659$	0.976	< 0.001
ν_{RC}^*	$= -0.002086x + 0.2929$	0.756	< 0.001	$= -0.005155x + 0.2898$	0.868	< 0.001
ν_{CR}	$= -0.000953x + 0.2901$	0.557	< 0.001	$= -0.000659x + 0.2774$	0.1	0.108
ν_{RL}^*	$= -0.002488x + 0.2653$	0.788	< 0.001	$= -0.006690x + 0.2653$	0.948	< 0.001
ν_{LR}	$= -0.000717x + 0.3110$	0.612	< 0.001	$= -0.002006x + 0.3104$	0.846	< 0.001
ν_{CL}^*	$= -0.001452x + 0.2637$	0.799	< 0.001	$= -0.004236x + 0.2641$	0.976	< 0.001
ν_{LC}	$= -0.000621x + 0.3118$	0.82	< 0.001	$= -0.002046x + 0.3131$	0.928	< 0.001

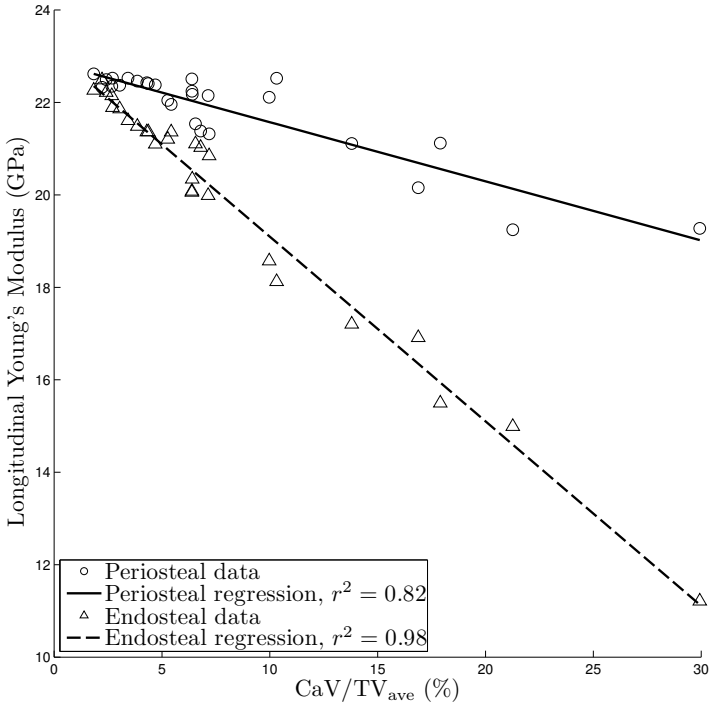

(a)

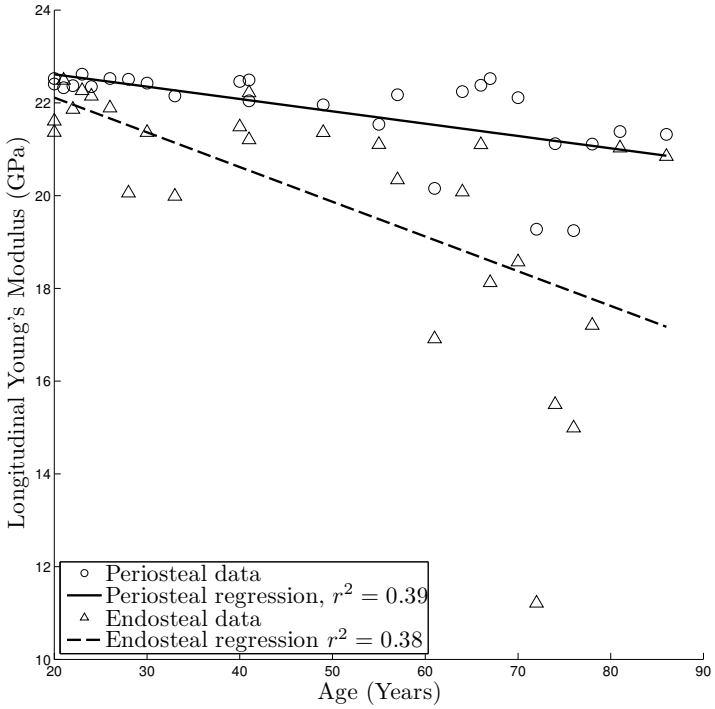

(b)

Figure 3-12: Effective periosteal and endosteal E_L plotted against a) Ca.V/TV$_{ave}$ (six-sample mean Ca.V/TV), b) age.

elastic constants at the periosteal and endosteal aspects were relatively similar. As Ca.V/TV$_{ave}$ increased the orthotropic constants at the endosteal aspects reduced considerably more than at the periosteal aspect. The variation of E_L with age is shown in Fig. 3-12(b), and the corresponding regression data in Table 3.8. E_L was considerably more scattered with age variations than with Ca.V/TV$_{ave}$. A reduction of stiffness with age was apparent at both locations, but was considerably more pronounced at the endosteal aspect.

Table 3.8: Linear regression parameters for all elastic constants against age = x (all moduli in GPa, age in years). ν_{ij} marked * are suggested as independent constants.

Parameter	Equation - Periosteal	r^2	p	Equation - Endosteal	r^2	p
E_R (Radial)	$= -0.0437x + 19.7417$	0.317	< 0.05	$= -0.1109x + 20.0929$	0.398	< 0.001
E_C (Circ.)	$= -0.0361x + 19.7376$	0.407	< 0.001	$= -0.0874x + 19.9053$	0.406	< 0.001
E_L (Longit.)	$= -0.0266x + 23.1477$	0.393	< 0.001	$= -0.0749x + 23.6113$	0.383	< 0.001
G_{RC}	$= -0.0154x + 7.6321$	0.373	< 0.001	$= -0.0376x + 7.7091$	0.393	< 0.001
G_{RL}	$= -0.0123x + 7.2877$	0.344	< 0.05	$= -0.0333x + 7.4529$	0.394	< 0.001
G_{CL}	$= -0.0107x + 7.2829$	0.398	< 0.001	$= -0.0274x + 7.3797$	0.397	< 0.001
ν_{RC}^*	$= -0.000418x + 0.2970$	0.338	< 0.05	$= -0.001017x + 0.2990$	0.376	< 0.001
ν_{CR}	$= -0.000280x + 0.2964$	0.536	< 0.001	$= -0.000283x + 0.2861$	0.206	< 0.05
ν_{RL}	$= -0.000483x + 0.2694$	0.331	< 0.05	$= -0.001273x + 0.2750$	0.382	< 0.001
ν_{LR}^*	$= -0.000199x + 0.3151$	0.522	< 0.001	$= -0.000428x + 0.3155$	0.428	< 0.001
ν_{CL}^*	$= -0.000299x + 0.2669$	0.377	< 0.001	$= -0.000797x + 0.2698$	0.385	< 0.001
ν_{LC}	$= -0.000112x + 0.3124$	0.295	< 0.05	$= -0.000387x + 0.3160$	0.369	< 0.001

3.3.3 Isotropic vs. transversely-isotropic tissue properties

To compare the role of tissue-level elastic constants and canal architecture, analyses were repeated with isotropic tissue properties. In these analyses the anisotropy of the effective properties resulted from the canal architecture alone. The isotropic Young's modulus of the tissue was taken as 20 GPa, which was the approximate mean of the three transversely-isotropic Young's moduli. An isotropic Poisson's ratio of 0.3 was employed at the tissue-level. Table 3.9 contains linear regression equations for the orthotropic elastic constants against Ca.V/TV with assumed isotropic tissue properties. Figure 3-13 shows the linear regression lines for E_L against Ca.V/TV, for both isotropic and transversely-isotropic tissue-level properties. At low Ca.V/TV the two values of E_L were distinct, which reflected their different tissue-level values. As Ca.V/TV increased, the isotropic

and transversely-isotropic moduli converged. This appeared to suggest an increased effect of canal architecture and a decreased role of tissue-level properties in the determination of E_L. Similar behaviour was observed for all elastic constants.

Table 3.9: Linear regression parameters for all elastic constants against $\text{Ca.V/TV}_{\text{ave}} = x$ with isotropic tissue properties (all moduli in GPa, Ca.V/TV as percentage). ν_{ij} marked * are suggested as independent constants.

Parameter	Equation	r^2	p
E_R (Radial)	$= -0.4039x + 19.9742$	0.960	< 0.001
E_C (Circ.)	$= -0.3135x + 19.9407$	0.983	< 0.001
E_L (Longit.)	$= -0.2272x + 20.1550$	0.997	< 0.001
G_{RC}	$= -0.1342x + 7.6893$	0.979	< 0.001
G_{RL}	$= -0.1245x + 7.7152$	0.985	< 0.001
G_{CL}	$= -0.1028x + 7.6918$	0.992	< 0.001
ν_{RC}^*	$= -0.003848x + 0.2978$	0.833	< 0.001
ν_{CR}	$= -0.000963x + 0.2895$	0.227	< 0.001
ν_{RL}^*	$= -0.005090x + 0.2993$	0.944	< 0.001
ν_{LR}	$= -0.001237x + 0.2962$	0.709	< 0.001
ν_{CL}^*	$= -0.003110x + 0.2975$	0.968	< 0.001
ν_{LC}	$= -0.001194x + 0.2979$	0.882	< 0.001

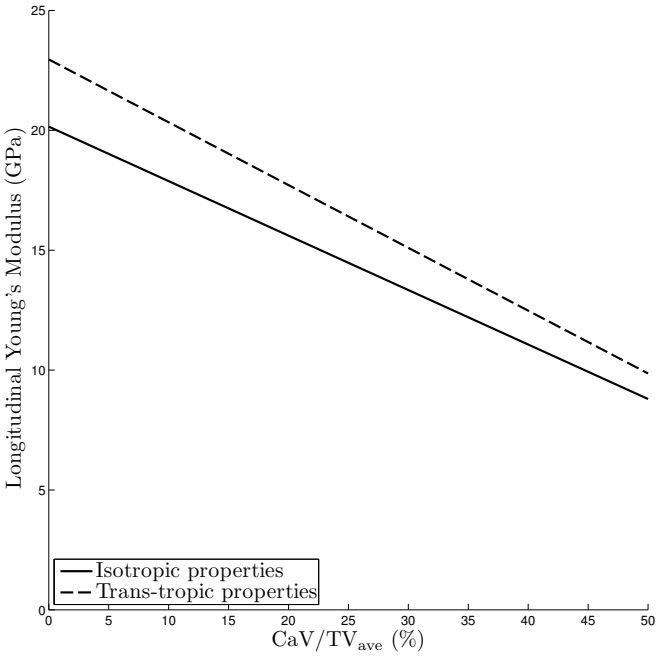

Figure 3-13: Effective E_L (regression) against $\text{Ca.V/TV}_{\text{ave}}$ with isotropic and transversely-isotropic material properties.

3.4 Discussion

The first objective of this study was to assess the predictive power of microarchitectural indices and age for predicting apparent elastic constants. The average coefficient of determination for all elastic constants are shown in Table 3.10. In an average sense it can be seen that Ca.V/TV was the best predictor of elastic constants. Considered individually, the other microarchitectural indices also showed strong predictive power. In a collective sense the stepwise regression procedure also confirmed that Ca.V/TV was the best predictor. Indeed, these results indicated that only Ca.V/TV was necessary to provide a reliable prediction. This is favourable for use in the prediction of elastic constants since Ca.V/TV (closely related to porosity) is the most easily estimated of the indices. For instance, CT has the potential to estimate Ca.V/TV in its volumetric assessment of density (vBMD). This is discussed further later. It is perhaps surprising that Ca.V/TV was so strong a predictor of the elastic constants relative to the other morphological indices considered; since it is a simple measure of the proportion of solid bone tissue within a sample volume but provides no information about how that material is arranged. It can be inferred that cortical bone microstructure at the region considered generates relatively similar morphologies even as canals expand with the loss of bone density. The other indices provide information about the complexity, size and relative orientation of morphological features within the bone volume. The fact that this extra information did not improve the predictive power of regressions of Ca.V/TV alone, further indicates that it is a very strong predictor of such information.

Table 3.10: Mean linear regression parameter r^2_{ave} for all elastic constants with selected microarchitectural indices.

Ca.V/TV	Ca.S/TV	Ca.Dm	DA
0.958	0.829	0.795	0.734

The six elastic moduli were very strongly predicted ($r^2 > 0.974$) by Ca.V/TV and five of the six Poisson's ratios were strongly predicted ($r^2 > 0.72$). Since only 9 of the 12 orthotropic constants are independent, these data provide reliable accuracy to characterise the variation of elastic properties with changes in Ca.V/TV. These results could be of use in the FE analysis of complex whole-bone simulations such as external fracture fixation, studied in Chapters 6 and 7.

The validity of the Young's moduli predicted in this study can be assessed by comparison with values reported by previous researchers. Previous studies of cortical bone stiffness have correlated Young's moduli with apparent density, measured in g/cm^3 (Lotz et al., 1991c; Snyder and Schneider, 1991) and porosity measured in % (Currey, 1988; Schaffler and Burr, 1988; Bayraktar et al., 2004; Dong and Guo, 2004). To enable direct comparison between studies the density of cortical bone 2.2 g/cm^3 (Ding et al., 1997) was used to convert the data to a function of apparent density. Here all porosity is labelled as Ca.V/TV. Figure 3-14 illustrates the variation of E_L against Ca.V/TV for this and previous studies. Considerable variability exists between the previously reported variation of Young's modulus with Ca.V/TV. E_L found in this study lay within the range reported by others. At Ca.V/TV $< 5\,\%$ the prediction of this study was less than that measured by Schaffler and Burr (1988), and greater than that reported by Currey (1988). Between Ca.V/TV of 5–25 % the prediction of this study was slightly larger than those predicted by Snyder and Schneider (1991) and Bayraktar et al. (2004). At Ca.V/TV $> 25\,\%$ the current studies predictions were less than the measurements of Bayraktar et al. (2004) and greater than those of Lotz et al. (1991c). In general the value of E_L found in the current study lies at the upper range of previous data. The slope of E_L found here was most similar to Bayraktar et al. (2004) and was considerably less steep than measured by two others (Currey, 1988; Schaffler and Burr, 1988). Insufficient previous data are available to make similar comparisons of the other elastic constants. Two of the above studies (Lotz et al., 1991c; Dong and Guo, 2004) measured the transverse moduli. The reported values of transverse moduli were as much as 50 % lower than those of this study, although at Ca.V/TV $> 35\,\%$ the data of Lotz et al. (1991c) were similar to E_R found here. However, all values reported by these studies are low compared to the ultrasonic measurments of Rho (1996), who reported mean values of 11.7 GPa and 12.2 GPa for E_C and E_R respectively at the tibial midshaft. These values are closer to the those found in the present study. Furthermore, the predicted values of E_L from both Lotz et al. (1991c) and Dong and Guo (2004) were at the lower end of the spectrum reported by previous researchers which indicates that these may be poor candidates for comparison. Unfortunately, the other studies did not measure the transverse moduli. Measurements of the variation of shear moduli and Poisson's ratios with porosity have only been made by Dong and Guo (2004) using a transversely isotropic

model. Porosity was found to be strongly predictive ($r^2 = 0.72$) of longitudinal shear modulus, but not predictive ($r^2 = 0.01$) for the transverse shear modulus. Only the longitudinal Poisson's ratio was measured, this was also not predicted ($r^2 = 0.02$) by porosity. Similar to this study, the reported variation of all constants was negative with increasing porosity. The value of shear moduli was approximately 18–27 % lower than those found here at equivalent porosity. Since the Young's moduli predicted by Dong and Guo (2004) were lower than other studies it is expected that these data also represent low estimates. The Poisson's ratio found by Dong and Guo (2004) was higher than those found in the current study. However, it is not clear if this is a result of the assumption of transverse isotropy which differs from the orthotropy applied here. In general, it was observed that the orthotropic stiffness coefficients found in this study were at the high end of the measurements of previous researchers. Possible causes for this effect are considered later.

Theoretical predictions of the transversely isotropic Young's and shear moduli with varied porosity and hydroxyapatite mineralization have been made using the theory of porous materials (Sevostianov and Kachanov, 2000). The range of such results corresponds well with those presented here. Their prediction for E_L followed a similar trend to that found in this study; the predicted Young's modulus at 0 and 50 % porosity were 9 % and 25 % lower than those found here. The trends reported for the transverse Young's and shear moduli are non-linear. It is possible that with more data at high Ca.V/TV, a slight non-linear trend could emerge in the present results. The values of transverse Young's modulus predicted by Sevostianov and Kachanov (2000) at 0 and 50 % porosity were approximately 5 % higher and approximately equal to E_R found here. The two shear moduli predicted by Sevostianov and Kachanov were very similar to those found in this study at low porosity (Ca.V/TV < 3 %), at higher porosity their non-linear trend became lower than found in this study. Similar to the previously discussed experimental measurements of elastic properties, the theoretical predictions of Sevostianov and Kachanov (2000) indicate that the current results are realistic, but greater than the mean reported values for cortical bone stiffness.

The decrease of elastic moduli with increased porosity/age is well documented (Bayraktar et al., 2004; Burstein et al., 1976; Zioupos and Currey, 1998) but a

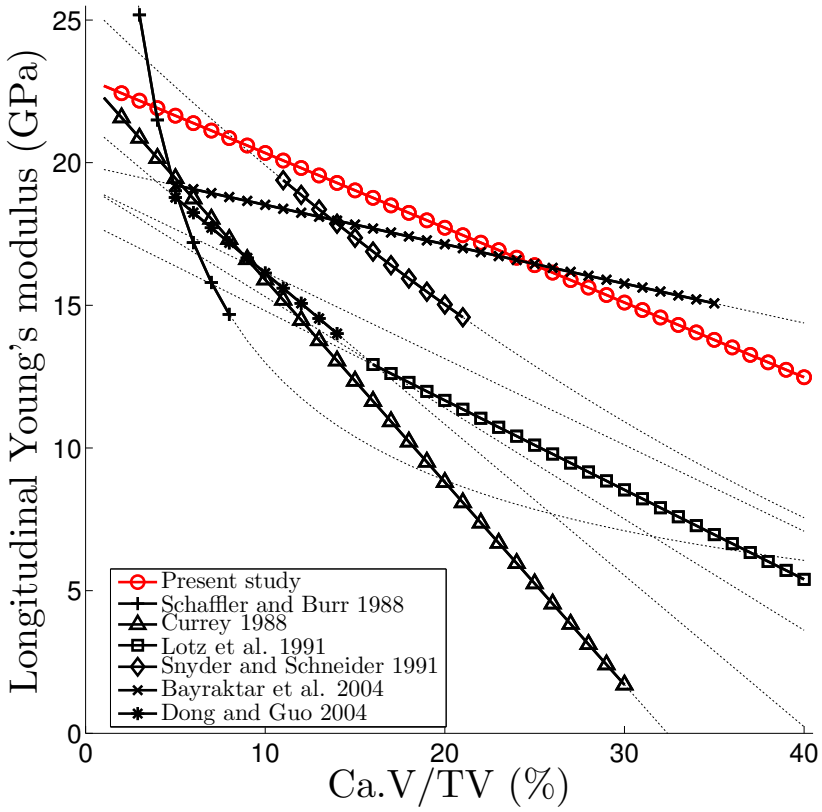

Figure 3-14: Comparison of previous (Currey, 1988; Schaffler and Burr, 1988; Lotz et al., 1991c; Snyder and Schneider, 1991; Bayraktar et al., 2004; Dong and Guo, 2004) experimental and current μFE predictions of E_L in cortical bone. Lines for previous studies are plotted as dashed outside of the reported Ca.V/TV range.

search of the literature revealed little previous data on the variation of the six orthotropic Poisson's ratio with porosity or ageing. A study of cancellous bone (Yang et al., 1999) found very little variation of the six Poisson's ratios with porosity. Some other studies conducted on low porosity materials found a more substantial variation with porosity (Phani and Sanyal, 2007; Ren et al., 2009). In the cortical bone studied here (a low porosity material), considerable variation of the six Poisson's ratios with porosity was observed. It requires further research to confirm and establish the cause of this effect, but it seems reasonable to propose that Poisson's ratios are possibly more variable in low-, as opposed to high-porosity bone. Previous studies report certain Poisson's ratios of cortical bone in excess of those found here; values of approximately 0.4 have been reported commonly (Van Buskirk et al., 1981; Rho, 1996; Dong and Guo, 2004),

and higher than 0.5 in fewer cases (Reilly and Burstein, 1975). In this study the assigned tissue properties appeared to provide an upper limit on the effective Poisson's ratios (i.e. 0.315, Table 3.1). Since increased porosity was predictive of reductions in all Poisson's ratios, these results imply that at least one of the assigned tissue-level Poisson's ratios was lower than in real bone.

Since age was common to both periosteal and endosteal samples from each donor it was not possible to regress it for all samples together as was done for the microarchitectural indices. Regression of age was therefore separated for the periosteal and endosteal aspects. Age was a relatively poor predictor of elastic constants ($r^2_{\text{ave}} = 0.385$). Note age and porosity (Ca.V/TV) have been shown to be correlated for these samples ($r^2 = 0.582$) (Cooper et al., 2007). In the absence of knowledge of indices of bone microarchitecture, age could provide an estimate of elastic constants for macro-FE modelling of general cases. A rate of reduction of 1.5 %/decade ($r^2 = 0.77$) in femoral cortical bone E_L has been observed (Burstein et al., 1976). Another study (Zioupos and Currey, 1998) has reported a 2.2 %/decade ($r^2 = 0.48$) rate of decrease in E_L with ageing. These results compare well with the current study, in which the E_L was found to decrease at between 1.1 %/decade (periosteal) and 3.2 %/decade (endosteal) (Table 3.8).

As mentioned earlier, vBMD obtained from CT has the potential for estimating porosity. vBMD is a combination of tissue mineralization and porosity. Porosity tends to dominate changes in vBMD (Bousson et al., 2000). Some previous studies have attempted to relate CT attenuations of cortical bone directly to elastic constants, and have observed only low correlations (Rho et al., 1995; Lettry et al., 2003; Cuppone et al., 2004). However, the results of this study indicated a strong relationship between elastic constants and porosity (Ca.V/TV). It should be noted that the first study cited (Bousson et al., 2000) employed approximately double the CT resolution of (Cuppone et al., 2004), so poor correlations in the cited studies could be arising from the partial volume effect among others. Indeed since μCT studies (Wachter et al., 2001; Cooper et al., 2007), can accurately identify cortical porosity it can be inferred that scan resolution is the limiting factor for the unsuccessful studies quoted. As discussed later, the models considered here do not include the heterogeneity induced by spatially varied mineralization. This may be a source of deviation of the evaluated elastic

constants from their in-vivo values. Adjustment for mineralization could reduce the measured predictive power of Ca.V/TV but would not be expected to adjust it to the value of $r^2 = 0.12$ reported by Cuppone et al. (2004). The potential of CT in providing porosity requires further investigation; the results of this study indicate that successful development of such a technique would considerably improve patient-specific predictions of orthotropic elastic constants.

The second objective of this study was to investigate the variation of elastic constants through the cortex. In young or low porosity bone the results indicated only small differences in the elastic constants between the periosteal and endosteal aspects (Fig. 3-12 and Table 3.7). As age or porosity increased, differences in all elastic constants were observed between these sites; specifically they were lower at the endosteal aspect ($p < 0.001$). It has been proposed (Russo et al., 2006) that cortical thinning results primarily from increased porosity and bone loss at the endosteal aspect. A further study (Bousson et al., 2000) indicated a pattern of increasing porosity from the periosteal, to the middle, to the endosteal aspect in all age groups. These observations, combined with the previously discussed correlation between Ca.V/TV and elastic constants suggest that the present trend was logical. Accurate evaluation of the stress/strain fields in FE analyses is dependent on accurate elastic constants. The discussed variation of elastic constants through the cortex are therefore considered important for improving macro-FE modelling predictions.

Anisotropy (here orthotropy) is also an important consideration in bone stiffness (Cowin and Mehrabadi, 1989), strength (Reilly and Burstein, 1975) and FE modelling (Au et al., 2005). The present results (Fig. 3-12 and Table 3.7) indicated that the ratio of transverse (averaged radial and circumferential) to longitudinal Young's moduli was 83 % in low porosity bone ($\text{Ca.V/TV}_{\text{ave}} = 0\,\%$). For $\text{Ca.V/TV}_{\text{ave}} = 30\,\%$ this dropped to 74 % and 37 % at the periosteal and endosteal aspects respectively. Elastic anisotropy was more pronounced at the endosteal aspect. This result mirrored the observed variation in morphological anisotropy. The reduction in all elastic constants and divergence of the transverse Young's and shear moduli were all accompanied by increased DA (see Fig. 3.10(a) and 3.10(b)). It is generally accepted that bone structures adapt to their loading (Wolff, 1892; Goldstein, 1987). It follows that as bone density reduces,

the stiffness in the main loading direction(s) is preserved at the expense of others, leaving the tissue vulnerable to failure under loading in the neglected directions. Such behaviour has been directly observed for cancellous bone by Homminga et al. (2004). It seems reasonable to propose that similar behaviour occurs in the cortex, as indicated by the variation of DA noted previously. The described trend has implications for FE modelling of low density bone, particularly under atypical loading, often critical cases for surgical failure.

Several ultrasound studies have reported hierarchies in the orthotropic constants of cortical bone (Knets, 1978; Van Buskirk et al., 1981; Rho, 1996). There is agreement amongst studies (including this one) about the hierarchy in Young's moduli, such that, $E_L > E_C > E_R$. Two studies (Van Buskirk et al., 1981; Rho, 1996) report that $G_{CL} > G_{RL} > G_{RC}$. For Ca.V/TV $> 15\,\%$, the results of this study showed an equivalent hierarchy. At values of Ca.V/TV $< 8\,\%$, however, the hierarchy became $G_{RC} > G_{CL} > G_{RL}$ in the present study. The hierarchies of the six Poisson's ratios reported by another study (Knets, 1978) were ($\nu_{CR} > \nu_{RC} > \nu_{LR} > \nu_{CL} > \nu_{RL}$), and by Rho were ($\nu_{LR}, \nu_{RC}, \nu_{CR} > \nu_{LC} > \nu_{CL}, \nu_{RL}$). A slightly different trend was observed in the results of the present study; $\nu_{LC}, \nu_{LR} > \nu_{CR} > \nu_{CL}, \nu_{RC} > \nu_{RL}$. All studies (including this one) have reported ν_{RL} as the smallest. Similar to Rho it was observed that ν_{LR} was among the largest.

A number of limitations and strengths were common to this study and the previous study of Cooper et al. (2007). The $7\,\mu$m resolution used was not fine enough to visualise all pores. Higher image quality would increase the accuracy of image segmentation between solid and void phases. However, the resolution employed in this study was sufficient to capture both large and medium pores which contribute most to porosity.

As a manual step, user thresholding (employed to binarize images) had the potential to introduce some variability in consistency. However, many of the samples considered in this study have more recently been re-scanned with a new scanner at a consistent threshold. The Ca.V/TV values of samples scanned with both methods were very similar ($r^2 = 0.99$), indicating that the manual thresholding was very robust.

Due to the incomplete nature of the specimens the true midshaft could not be identified exactly. Some variation in the sampling location was therefore unavoidable. Since this study was primarily concerned with relating microarchitecture and elastic properties, the fact that some longitudinal variation in sampling location may have occurred is not expected to have affected the results and observed trends considerably.

It is well recognised that genetic differences between donors can contribute to the observed variations in elastic constants. The ethnic uniformity of the donors in this study minimised this source or error; donors were 'largely of Anglo-Celtic (European) descent' (Cooper et al., 2007). Donors with medical conditions known to affect bone were not included in this study.

This study contained a predominance of low Ca.V/TV samples. This reduced the reliability of the regression equations at large values of Ca.V/TV. This can be seen in the concentration of data points to the left of Figure 3.4(a). Some previous studies (Carter and Hayes, 1977; Keller, 1994; Snyder and Schneider, 1991) have reported higher order expressions between porosity and cortical bone elastic moduli, and it is expected that with more porous specimens such a pattern could emerge here. The linear regression equations using Ca.V/TV provide very strong predictions of the orthotropic elastic constants of bone up to local Ca.V/TV values of 30 %.

In μFE analyses of cancellous bone, it is generally assumed that the solid phase can be represented by an isotropic constitutive law. This is reasonable due to the high porosity and complex orientations of struts in the trabecular microstructures which is the source of apparent-level anisotropy in such analyses. Compared to cancellous tissue, cortical bone is considerably more dense and regular in geometry. It also comprises a hierarchy of organised nano- and microstructures which produce inherently anisotropic macrolevel elastic properties. An elastic tissue model was sought which would better represent the internal microstructure of cortical bone tissue than simple isotropy. More specifically, it was required to assign justifiable orthotropic/transversely-isotropic properties in the absence of sample-specific data of nano-structure, but with knowledge of the geometry of the Haversian canals. The methodology used in this study is an

improvement on the assumption of isotropic tissue properties. It does, however, require a number of assumptions (though fewer than those required for isotropy). First, it assumes that the lamella are principally aligned in the longitudinal direction, in type L (dark-field) osteons or interstitial lamellar bone. Second, it assumes that lamella are oriented equally in all possible directions in the transverse plane, and can thus be considered transversely-isotropic. Third, it assumes that osteonal and interstitial lamellar bone properties can be represented with the same elastic properties. Fourth, it assumes that no deterioration of elastic constants occurs with ageing at the tissue-level. Fifth, it assumes that all solid bone tissue was homogeneous.

With regard to the first assumption, other osteon types (e.g. alternating and transverse (Ascenzi and Bonuuci, 1967)) exist within cortical bone. At the scanning resolution of $7\,\mu$m it was not possible to identify individual osteons, nor their different types. This was therefore a necessary assumption. The choice of longitudinal alignment reflected the primary orientation of lamella around canals and was a better constitutive model than isotropy. In the present case of the femoral midshaft, the direction of the femur axis is aligned with Haversian canals and the typical osteoclast cutting-cone orientation; it was therefore modelled with increased stiffness relative to the radial and circumferential directions. This assumption is perhaps less valid in other regions. In general, assuming longitudinal alignment will increase Young's moduli in the axial direction and decrease them in the transverse directions, as compared to isotropy. Improvement of this assumption could be achieved by skeletonising the canals and extracting local canal orientations from these skeletons. These orientations could be used to assign locally varying stiffness tensors which account for canal-dependent, osteon and lamellar orientations. The second assumption was reasonable in the absence of knowledge about the morphology of the osteons and interstitial lamella in the samples. Other studies have assumed transverse-isotropy at the level of the cortex, e.g. Dong and Guo (2006). In light of the present results, this only seems reasonable at low Ca.V/TV. As Ca.V/TV increased, the deviation from transverse-isotropy to orthotropy became marked at the macro-level (Fig. 3.4(a)). In this study transverse-isotropy was only assumed at the level of the osteon. The third assumption will have contributed some inaccuracy to the results of this study. The Young's moduli of interstitial lamella have been shown to be

greater than osteonal lamella by a factor of approximately 10 % (Fan et al., 2002; Rho et al., 2002). While this difference is not negligible, the properties of the two materials are of a similar order of magnitude. The tissue-level properties assigned here most closely matched those of osteonal lamella. It could be argued that a better approach would have been some averaging process between both interstitial and osteonal lamella properties. The evidence of Rho et al. (2002) suggests that the fourth assumption is valid. Rho et al. found little or no change in nanoindentation moduli with donor age. They observed a slight increase in moduli at the periosteal aspect, and a slight decrease at the endosteal aspect. If their results were applied in this study the effect would be to amplify (slightly) the observed trend that the endosteal aspect deteriorates more rapidly than the periosteal aspect. The fifth assumption (of homogeneity) incorporated variations of the first three assumptions across sample dimensions. It was noted that the effective elastic stiffness coefficients found in this study were at the high end of those reported by previous researchers. The homogeneity of tissue properties may have raised the effective stiffness by representing the mean stiffness within solid cortical tissue, rather than values both above and below the mean stiffness as would naturally occur. This stiffness raising effect of homogeneity can be understood through consideration of two elastic springs in series as illustrated in Fig. 3-15. If the springs have equal stiffness ($k_1 = k_2 = k_o$), the system stiffness ($\hat{K}_o$) will be half of their individual values,

$$\begin{aligned} \hat{K}_o &= \frac{1}{\frac{1}{k_1} + \frac{1}{k_2}} \\ &= \frac{k_o}{2} \end{aligned} \tag{3.4}$$

If however, the stiffness of one spring is raised and the other lowered by an equal amount (αk_o), then the system stiffness ($\hat{K}_{o\pm\alpha}$) will reduce as more strain is concentrated in the lower stiffness spring.

$$\begin{aligned} \hat{K}_{o\pm\alpha} &= \frac{1}{\frac{1}{k_o(1-\alpha)} + \frac{1}{k_o(1+\alpha)}} \\ &= \frac{k_o(1-\alpha^2)}{2} \end{aligned}$$

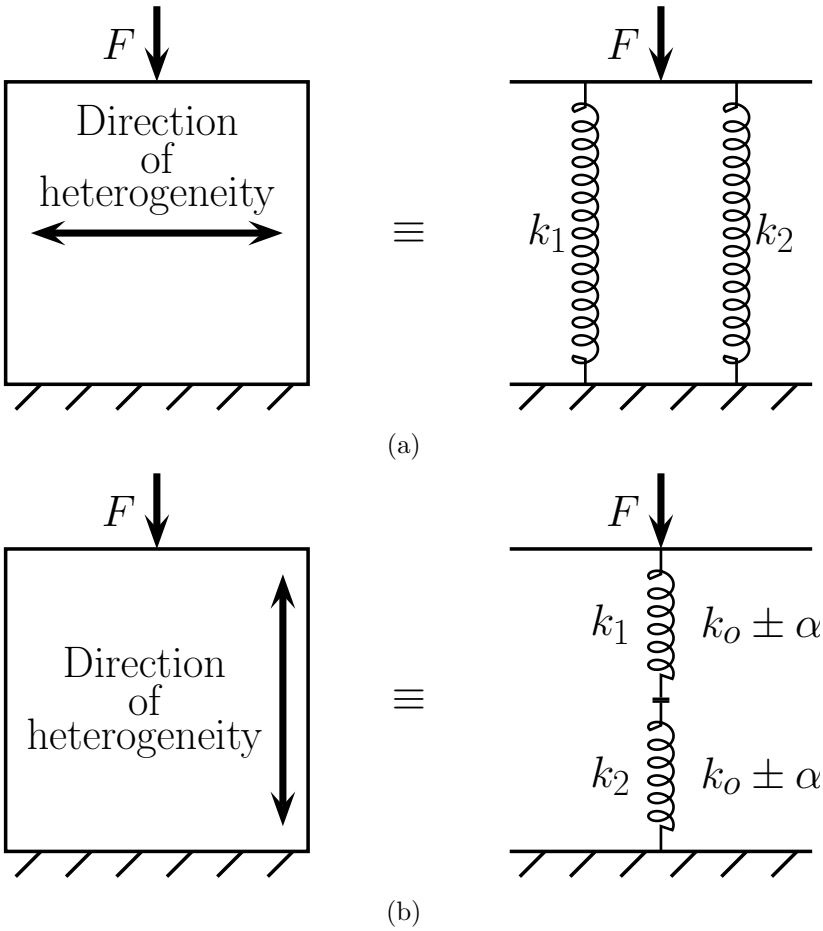

Figure 3-15: Spring representation of heterogeneity. Loading orthogonal to the direction of heterogeneity behaves similarly to springs in series (a), loading aligned with the direction of heterogeneity behaves similarly to springs in parallel (b).

$$\begin{aligned} \Rightarrow \hat{K}_{o\pm\alpha} &= \hat{K}_o(1-\alpha^2) \\ \therefore \hat{K}_{o\pm\alpha} &< \hat{K}_o, \text{ for } \alpha \neq 0 \end{aligned} \tag{3.5}$$

The implication for future development of the present technique would be to assign a homogenised tissue-level stiffness which is lower than the mean values. The problem of such an approach would be establishing an appropriate reduction in the mean stiffness. A superior strategy would be to adopt heterogeneous material properties, either by some randomisation algorithm, or by scaling them from CT attenuation numbers. However, the prediction of Young's moduli from CT attenuation numbers has not been successful for cortical bone to date.

Chapter 4

A nano-finite-element study of cortical bone microcracking

4.1 Introduction

Toughness is arguably one of bone's critical properties. It is well documented that age and disease can have a considerably deleterious effect on the resistance of bone to fracture (Schaffler et al., 1995; Currey et al., 1996; Nalla et al., 2004a). Furthermore, higher rates of fracture can be expected as life expectancy rises and the number of elderly people increases. A comprehensive understanding of bone fracture is required to inform the development of better treatments to combat this increasing fracture risk. However, the complex processes involved in bone fracture resistance remain only partially understood.

Considerable research has identified a variety of mechanisms which act to promote or resist crack propagation and eventual bone fracture. These mechanisms act at several levels of the hierarchical structure of bone such that their interactions are very complex to assess. Indeed mechanisms acting over length scales which vary by over five orders of magnitude have been reported. Viscoplastic flow is a toughening mechanism frequently encountered in polymers. It has been identified in bone at length scales of $\sim$0.01–0.1 μm from 'sacrificial collagen bonds' within the interfibrillar matrix as a so called 'filament glue effect' and the yielding behaviour of mineralized collagen fibrils (Thompson et al., 2001; Fantner et al., 2005; Gupta et al., 2005). Using atomic force microscopy (AFM), Thompson et al. (2001) and Fantner et al. (2005) noted the presence of sacrificial bonds in collagen molecules such as those found in bone. Sacrificial bonds effectively

produce redundant loops within the main collagen chain which, when broken, expose more of the chain length. The exposed length requires further straining, and thus increased energy absorption before the molecule can eventually be broken. If the time between load cycles is increased, greater energy absorption is observed in the collagen. This implied that sacrificial bonds reformed over time, contributing to the time dependent properties of bone (Thompson et al., 2001; Fantner et al., 2005; Gupta et al., 2005). Gupta et al. (2005) employed small angle x-ray scanning (SAXS) to measure both the fibril and tissue strains under applied stress. Under tensile testing the fibrils showed increasing strain at tissue strains below 0.7 %, the tissue-level yield point. Fibril strain did not increase at greater tissue strains. Gupta et al. attributed this behaviour to permanent relative displacement of the mineralized collagen molecules within fibrils to a limiting strain of 0.7 %. Tissue-level strains in excess of this value were predominantly assigned to shear deformations of the interfibrillar matrix and the associated sacrificial bond behaviour noted by Thompson et al. (2001) and Fantner et al. (2005).

The formation of unconnected microcracks in the region surrounding macrocrack tips has been found to act as a toughening mechanism in polymers (Callister, 2003). In ceramics pre-existing microcracks typically act as sources of crack initiation and thus reduce toughness below theoretical values. Both of these behaviours have been observed in bone with microcrack length scales of $\sim 10\,\mu$m (Zioupos and Currey, 1994; Zioupos et al., 1996; Vashishth et al., 1997; 2003; Vashishth, 2004; Nalla et al., 2004b; Peterlik et al., 2006). Preceding propagation of a macrocrack from a critical flaw, the raised stress/strain gradient around the crack tip induces microcrack formation at neighbouring flaws or grain boundaries. Localised straining at surrounding microcracks shields the macrocrack tip from some of the strain (and stress) present in the surrounding tissue. This reduces the stress concentration at the crack tip and thereby reduces potential for further propagation.

Crack bridging is the presence of residual, unbroken material which spans the wake of opened cracks (Nalla et al., 2003; Yeni and Fyhrie, 2003; Nalla et al., 2004b; 2005). This unbroken material retains some load carrying capacity and thereby acts to reduce the stress and strain present to drive propagation at the crack tip. This mechanism is associated with ceramic materials (Sakai and Bradt,

1993). The formation of crack bridges can occur at multiple length scales; collagen fibres have been observed to bridge cracks at the smallest scales ($\sim$1 μm); uncracked 'ligaments' at larger scales ($\sim$10 μm) have been observed where smaller cracks initiate ahead of the main crack tip and the two fail to join up (Nalla et al., 2003; 2004b). Failure to connect can be caused by fibres crossing the region between the two cracks; i.e. where the cracks effectively fall between different plies of the composite. Considerable research has focused on determining whether microcracking or crack bridging is the more dominant mechanism in bone toughening behaviour (Vashishth et al., 1997; Nalla et al., 2003; Vashishth et al., 2003; Vashishth, 2004; Nalla et al., 2004b; 2005). Nalla et al. (2004b) used measurements of the changes in bone compliance to assess the relative effect of microcracking and crack bridging. Since microcracking involves a loss of connectivity it can be expected to increase the compliance (lower the stiffness) from theoretical values that do not incorporate microcracking. Conversely, since crack bridging involves retention of connectivity it can be expected to lower the compliance (raise stiffness). Nalla et al. observed a net reduction in the compliance of cracked bone at different stages of crack propagation, indicating that crack bridging was the dominant mechanism. It should be noted that a crack must be relatively long for substantial crack bridging forces to develop, thus the role of microcracking can be expected to be more important near crack initiation.

The most visible toughening mechanism acting in bone is crack deflection (Liu et al., 1999; Brown et al., 2000; Peterlik et al., 2006; Fratzl et al., 2007). This also occurs in ceramics and composites. Crack deflection is the changing of crack propagation direction induced by the presence of some obstacle to continued cracking. This can take the form of a region of higher crack resistance, or the presence of a plane of lower crack resistance which is not aligned with the crack. Bone is a highly heterogeneous material with variations of materials, mechanical properties and orientations at various length scales. All such forms of heterogeneity influence the path of propagating cracks. The typical source of crack deflection is the penetration of a layer with low crack resistance relative to the surrounding layers (Fratzl et al., 2007), i.e. interlamellar layers or cement lines between osteons (typical length scales $\sim$10 μm). In bone these structures are frequently aligned in preferential orientations, leading to very different crack resistance with changes in orientation (Peterlik et al., 2006; Koester et al., 2008).

A crack driven to propagate in alignment with such structures will tend to follow them, leading to an associated low crack resistance. Conversely, a crack driven orthogonally to such structures will first be required to crack the surrounding collagen fibrils (with higher crack resistance) before reaching the weaker layer. The low crack resistance of these layers results in delamination and crack blunting, reducing the driving force available for further propagation. The blunting of cracks can lead to considerable deviation in crack directions from the plane orthogonal to the maximum tensile stress, further lowering the stress intensity at the crack tip. To propagate out from the weak layers the crack must effectively reinitiate by breaking collagen fibrils on the opposite side of the weak layer. Since the available driving force will be reduced by blunting and deflection, higher applied loads are required to propagate the crack, and thereby increasing crack resistance is developed. Peterlik et al. (2006) observed that cracks driven at more than 50° to the orientation of collagen fibrils required crack extension energies of 5000–9920 Jm^{-2} whereas those driven at smaller angles required only 110–375 Jm^{-2}. Similar results were reported by Koester et al. (2008). Both studies attributed a considerable proportion of the observed orientation dependent toughness to crack deflection. Koester et al. noted a combined effect of microcracking with crack deflection such that microcracks 'are essential to the orientation dependent fracture toughness of cortical bone.' Microcracks were typically observed in the interfibrillar matrix. They were therefore primarily aligned with longitudinal cracks (along the bone axis). For cracks propagating in the longitudinal direction these microcracks were found to be the precursors to crack bridging, leading to eventual toughening behaviour. In the transverse direction microcracks effectively acted to blunt propagating cracks, leading to the discussed increased fracture resistance. The observations of Koester et al. (2008) indicated that microcracking per-se does not act to reduce the crack driving force considerably, but may play an important role in enabling the activation of other toughening mechanisms.

The mechanisms of toughening observed within bone are influenced and in some cases induced by the hierarchical structure of bone. Osteonal bone has the most hierarchical form. Primary osteonal bone develops from a cartilage anlage precursor and thus forms where there was previously no bone. Secondary osteonal bone is generated by remodelling of primary and older secondary osteonal bone. Osteons are themselves built of a series of concentric rings of lamellae sur-

rounding a central Haversian canal. Thin cement layers (1–5 μm) encase osteons within interstitial bone, itself older osteonal bone with reduced blood supply relative to bone neighbouring Haversian canals. Typical osteon diameters measure 200–300 μm, Haversian canals 50–90 μm and individual lamellae 3–7 μm (O'Brien et al., 2005). The large size of Haversian canals has led to osteons being proposed as both sources of stress concentration and barriers to crack propagation (Currey, 2003; O'Brien et al., 2005). It has been observed (Schaffler et al., 1995) that 87 % of microcracks initiate in interstitial bone, 11 % within cement lines and only 2 % within, or partly within, osteons themselves. The greater age, mineralization and reduced remodelling activity within interstitial bone are thought to induce the higher propensity for microcracking. O'Brien et al. (2005) observed that the length of cracks upon first encounter with osteons was found to be critical for determining whether further propagation would occur. If osteons were encountered at cracks lengths less than 100 μm propagation would cease. If crack lengths were approximately 150–300 μm propagation would typically occur with crack deflection around the osteon cement layers. If crack lengths were greater than 300 μm then they would propagate into Haversian canals. It was further observed that once a crack penetrated a Haversian canal the barrier effect of other Haversian systems became insufficient to resist its onward propagation. Apparent level failure was characterised by the propagation of critical cracks which overcame the osteon barrier effect.

In addition to canals, lacuna have been identified as sources of stress concentration and potential microcrack initiation (Prendergast and Huiskes, 1996; Currey, 2003; McNamara et al., 2006; Nicolella et al., 2006; Apostolopoulos and Deligianni, 2009). Stress and strain concentration factors (σCF and ϵCF, the ratio of local to nominal stress or strain respectively) have been used to quantify the local amplification effect of lacuna. A theoretical prediction of the perilacunar σCF was reported as 1.2 (longitudinal loading) and 7 (radial loading) (Currey, 2003). Studies have used FE analyses to identify a mutual stress concentrating effect between neighbouring lacuna and local perilacunar ϵCF as high as 6, including absolute strains as high as 15500 $\mu\epsilon$ (Prendergast and Huiskes, 1996; McNamara et al., 2006; Apostolopoulos and Deligianni, 2009). Digital image correlation (DIC) has been used to measure the local strain around lacuna in polished sections of bovine cortical bone (Nicolella et al., 2006). Perilacunar ϵCF between

1.1 and 3.8 were recorded, with a peak local strain of approximately 35,000 $\mu\epsilon$. Such large, or 'supra-physiological' strains are thought to be continuum representations of localised microcracking around lacuna. Indeed, while macrocracks were observed initiating at canal boundaries in bovine bone (Reilly, 2000), the same study reported frequent initiation of microcracks at lacuna boundaries. It is therefore possible that lacuna influence crack propagation through the initiation of microcracks. As discussed previously, such effects could toughen bone by reducing the driving force available at macrocrack tips, or if formed ahead of macrocracks, perilacunar microcracks could lead to crack bridging when they do not connect. The latter may also suggest a role for perilacunar microcracks in directing macrocracks toward lacuna.

The discussed cracking mechanisms are further complicated by the remodelling processes constantly repairing flaws within bone tissue (Carter, 1984; Hart et al., 1984). The precise nature of remodelling processes in bone is itself an area of considerable ongoing research. The primary biological process involves detection of regions of damaged or over-loaded tissue, coupled with osteoclast activity to resorb bone and osteoblast activity to form new bone. The net effect of this competing relationship between destructive and productive bone cells is the repair and adaptation of bone into modified morphologies. The cells responsible for remodelling occupy osteocyte lacuna. It has been proposed (Qiu et al., 2005) that a local deficiency of lacuna could be associated with greater numbers of cracks, particularly in interstitial bone, since sufficient remodelling cells are not present to repair them. It should therefore be noted that lacuna can act both as stress concentrators to increase cracking, and conversely as hotspots of remodelling activity to minimise the accumulation of fatigue cracks.

Rat and murine bone do not typically display remodelling or microcracks under normal physiological loading (Bentolila et al., 1998). Furthermore, without remodelling, the complexity of osteons is not present. For these reasons such species represent ideal candidates for investigation of the effect of ultrastructural features (canals and lacuna) upon the behaviour of cracks within bone, in isolation from these complicating features.

A comparison of the morphology and basic mechanical properties of bone from two genetically distinct breeds of mice was made by Schneider et al. (2007). The

C57BL/6J (B6) and C3H/HeJ (C3H) breeds have been characterised with different bone mineral density (BMD), bone mineral content (BMC), skeletal characteristics and response to loading (Beamer et al., 1996; Akhter et al., 1998; Kodama et al., 1999; Turner et al., 2000). Assessing the femoral mid-diaphysis, Schneider et al. (2007) observed that C3H mice possessed cortices with significantly greater cortical thickness (Ct.Th), cortical bone volume density (Ct.BV/TV) and canal spacing (Ca.Sp) than B6 mice. C3H mice also possessed fewer, but larger canals than B6 mice. Minimal inter-sex differences were observed in B6 mice. However, female C3H showed significantly greater Ct.Th and Ct.BV/TV than males. Furthermore, the cannular indices showed that female C3H mice possessed significantly more and larger canals than males. These differences influenced the measured mechanical properties. C3H femora recorded significantly higher values of ultimate force and strength than those from B6 mice. Female C3H femora recorded similar values of work to failure as femora from both male and female B6 mice. The work to failure of male C3H femora was more than 20 % higher than in females. Since the femoral cortices of female C3H mice were generally larger than males, the fact that they showed dramatically lower work to failure indicated that the cannular differences between sexes plays a dominant role. The effect of ultrastructure was greater than the macrostructure in determination of the work to failure of C3H femora.

The role of B6 and C3H ultrastructure in crack initiation and propagation was investigated by Voide et al. (2009) by conducting compression tests on notched specimens, and later by Levchuk et al. (2010) and Schneider et al. (2010) through Dynamic Image Guided Failure Assessment (DIGFA). The DIGFA experimental procedure was developed at the Institute for Biomechanics, ETH Zurich (Vogel, 2008). This process enabled the sub-micron visualisation of crack initiation and propagation under dynamic loading. The methodology is summarised in Fig. 4-1. DIGFA experiments were conducted at the Swiss Light Source (SLS) within the Paul Scherer Institute (PSI). The SLS is a 2.4 GeV synchrotron light source which provides 16 high-brightness photon beams for research fields such as materials science, chemistry and biology. The TOMCAT beamline (TOmographic Microscopy and Coherent rAdiology experimenTs) which enables isotropic imaging at resolutions between 0.36 μm and 14.8 μm was used in all analyses. DIGFA scans and experiments were conducted during a previous study (Levchuk et al.,

2010; Schneider et al., 2010) and made available to the author for conducting numerical simulations in the present study. An isotropic resolution of 0.7 μm was used in the present study. The TOMCAT X-ray beam was directed through the bone samples, within the compression device and oriented using a microscope. Images were recorded with a charge-coupled device (CCD) camera. Samples were loaded within a computer-controlled compression device (Fig. 4-1(b)). This consisted of an inner carbon-fibre cylinder to hold the bone samples, a plunger to position the applied load initially, a load cell to measure the applied load and an actuator to apply the compressive force. The device was surrounded in an outer carbon-fibre cylinder for mechanical stability. The cylinders were made from carbon-fibre because of its mechanical performance combined with its x-ray translucency. Murine femora were tested using the DIGFA device. It was necessary to concentrate the applied loading at a known location to guarantee that microcracking would occur within the small x-ray field of view (0.49 mm^2). A notch was therefore cut at the femoral mid-diaphysis to act as a stress-raiser. Compressive loading was applied in the longitudinal direction. The sample ends were embedded in poly-methyl-meth-acrylate (PMMA) to produce repeatable and smooth loading surfaces (Fig. 4-1(c)). The embedded femora had a total length of 18 mm and the exposed length of the mid-diaphysis was 4 mm. Notches were cut to dimensions of 0.76 mm and 0.89 mm in the longitudinal and transverse directions respectively (see dimensions L_n and L_u in Fig. 4-2(a)). Strain-controlled compressive loading was applied in increments of 0.05 % strain to the embedded samples. Loading was maintained between increments, during which samples were scanned. Load increments were continued until sample failure had occurred.

To visualise the interaction between microcracks and the ultrastructural features it was necessary to separate the canals, lacuna and cracks from the bone and the background of the scanned images. Binarized images were separated into these features by applying component labelling which identifies groups of connected voxels with the same value (0 or 1 in the binary case) (Hu et al., 2005). The largest 100 components in each image were then identified as canals, lacunae or cracks by visual inspection; smaller components were assigned as lacunae. The volume of microcracks was calculated as the product of the number of crack voxels and the volume of a single voxel. It was required to know the

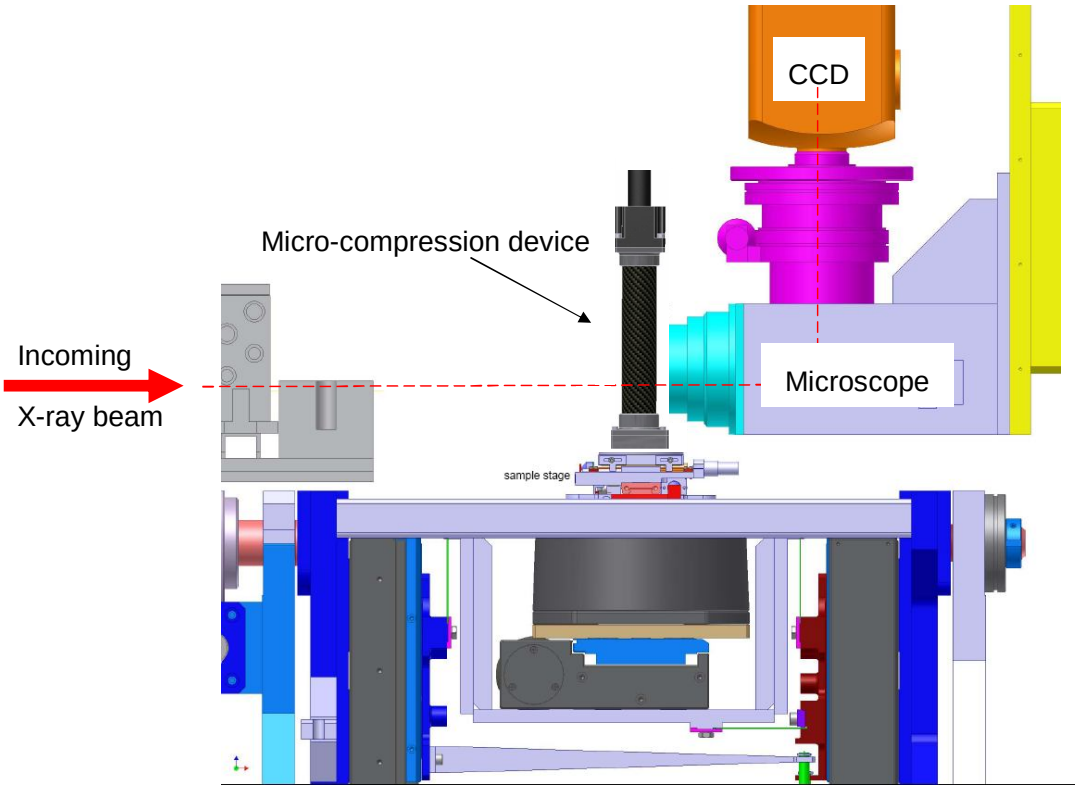

(a)

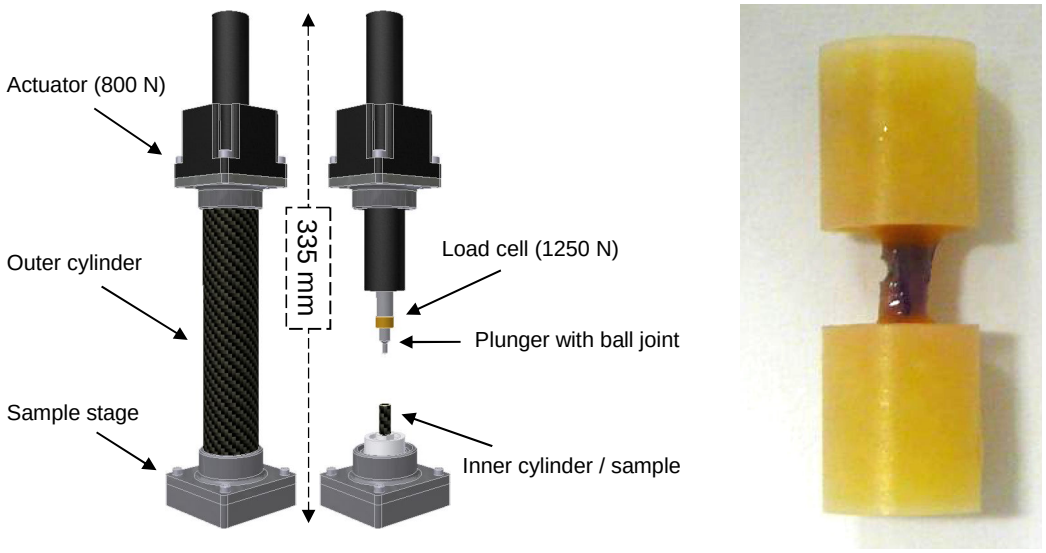

(b) (c)

Figure 4-1: DIGFA experimental setup at the Swiss Light Source (SLS). The global setup (a), the compression device (b), a notched murine femur embedded in PMMA (c). Figures reproduced from Vogel (2008) and Levchuk et al. (2010).

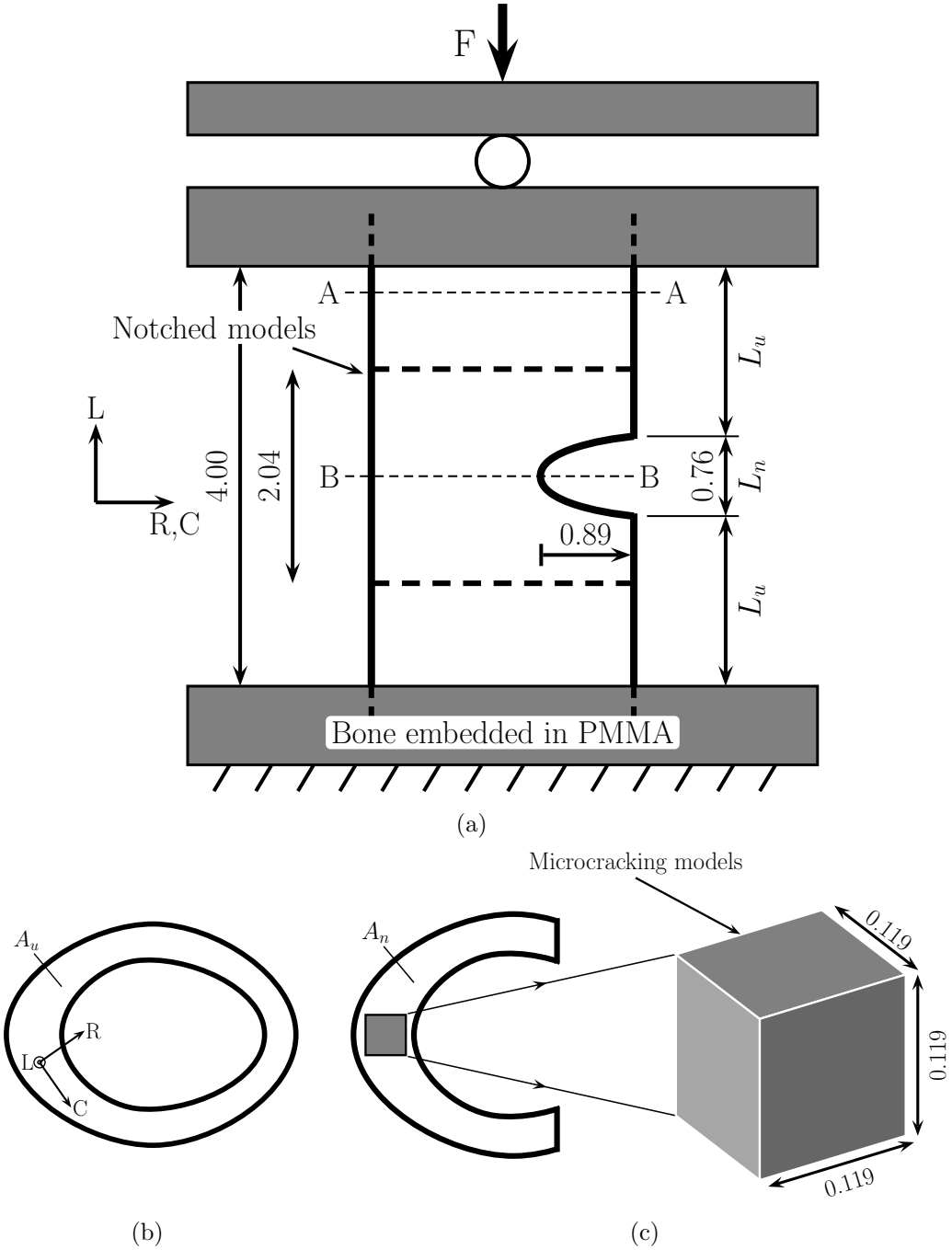

Figure 4-2: Regions modelled in microcracking FE analyses. The DIGFA experimental boundary conditions applied to notched samples (a), unnotched transverse section A-A (b) and notched tranverse section B-B with ROI for microcracking analyses (c). Note that only the region indicated by dashed lines in (a) was modelled, boundary conditions for (c) were taken from the FE analyses of (a), and all dimensions are in mm.

compressive strain across the notched region (ϵ_n) which resulted from the applied strain over the embedded sample (ϵ_{app}). Since there was considerable variation in cross-sectional area between the notched and the unnotched regions of the exposed diaphysis this could not be calculated with a linear relationship. The author derived Equation 4.1 to enable calculation of this value (see Appendix A for derivation). L_n, L_u, A_n and A_u are as indicated in Fig. 4-2.

$$\epsilon_n = \epsilon_{app}\left[\frac{L_n + L_u}{L_n + L_u\frac{A_n}{A_u}}\right] \tag{4.1}$$

Figures 4-3 and 4-4 show the crack paths observed by Voide et al. (2009) for both B6 and C3H mice. It was observed that crack initiation could occur only at

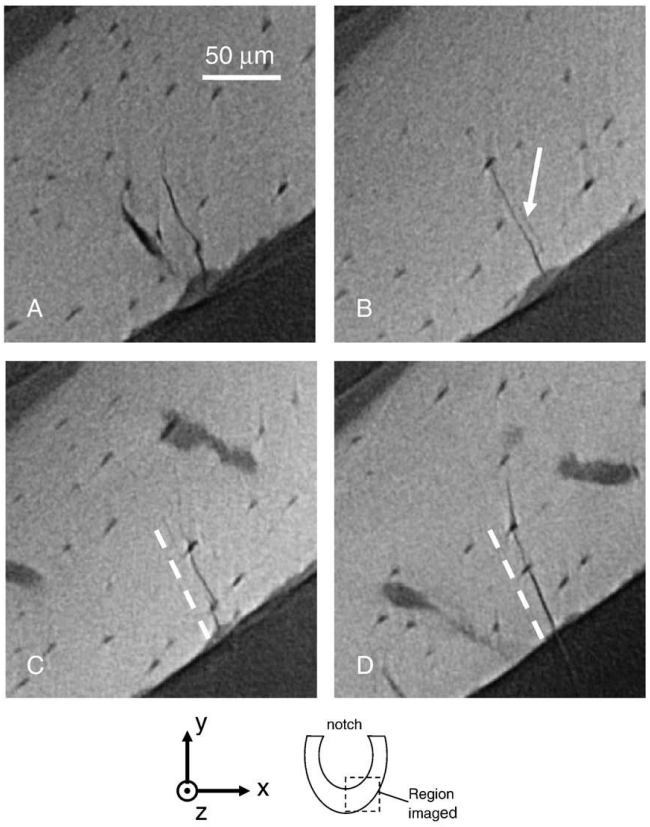

Figure 4-3: Crack propagation in a B6 sample (from Voide et al. (2009)). Slices A–D were taken at 20 μm separation in the longitudinal (z) direction. Note the presence of osteocyte lacuna appeared to deflect the crack path from the original (indicated by the white dashed line).

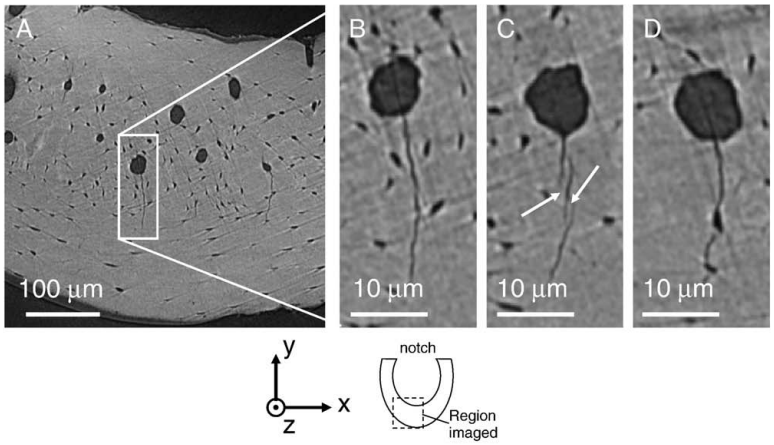

Figure 4-4: Crack propagation in a C3H sample (from Voide et al. (2009)). Crack initiation at canals (large pores)(A,B), crack bridging (C), and crack propagation through osteocyte lacuna (D) can be seen.

the periosteum or endosteum in B6 mice, but also frequently occurred at canal surfaces in C3H mice. This indicated that C3H canals were sufficiently large relative to the Ct.Th to enable initiation. In B6 mice the cortices and were thinner and canals more narrow such that initiation loading was reached on the bone surfaces before it could occur at canals. Lacuna were not able to initiate or arrest crack growth. However, crack paths were guided by the presence of lacuna in both mouse breeds.

The variation of microcrack volume with applied compressive strain found by Levchuk et al. (2010) and Schneider et al. (2010) is presented in Fig. 4-5(a). The initiation strain values and microcrack propagation rates varied considerably between samples of both breeds of mice. The mean compressive strain at initiation was 1.45 % for B6 samples and 3.07 % for C3H samples. The crack-volume data were normalised by setting the initiation strain of each breed to its mean value using the equation 4.1. The normalised data, shown in Fig. 4-5(b), indicated that the microcrack propagation rate of C3H samples was approximately two times that of B6 samples.

Renderings of the ultrastructure and typical DIGFA-induced microcracks within B6 and C3H samples are shown in Fig. 4-6. It can be seen that B6 ultrastructure was characterised by fewer and narrower canals than C3H samples. Cracks were approximately aligned in the longitudinal-radial direction and penetrated the full

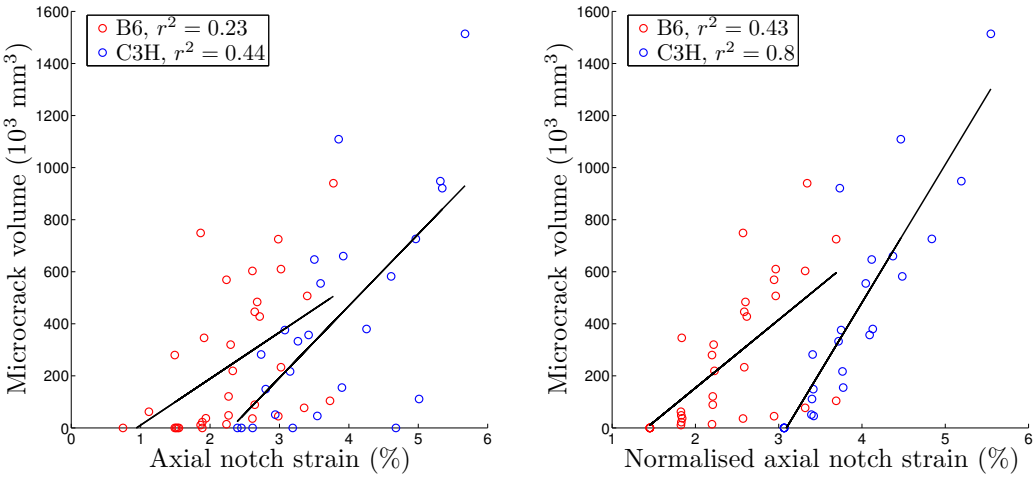

(a) (b)

Figure 4-5: Variation of microcrack volume with strain across the notch (a) and normalised strain across the notch (b). The strain values were normalised in (b) by setting the initiation strain of B6 and C3H samples to their mean in (a).

cortical thickness after propagation (Levchuk et al., 2010; Schneider et al., 2010). Crack initiation was observed at cortical surfaces in both B6 and C3H samples, and was also observed at canal surfaces in C3H samples. Cracks generally followed the canal structure; an example can be seen in Fig. 4-6(f) where the lower half of the crack connected with the large canal in the foreground, but diverted to the smaller canals in the upper half, where the larger canal was not present. In addition, osteocyte lacuna were observed to guide the direction of microcracks but not stop their propagation. The observations of Voide et al. (2009), Levchuk et al. (2010) and Schneider et al. (2010) indicated that ultrastructral features have considerable influence upon crack behaviour. Identification of the precise nature of this influence requires further investigation. The aim of the present study was therefore to improve current understanding of the role of ultrastructure (canals and osteocyte lacuna) to initiate and propagate cracks through the development and use of a computational model.

The fracture resistance of materials is defined using fracture mechanics. Linear-elastic fracture mechanics (LEFM) represents the simplest of these theories. In LEFM it is assumed that a material can be treated as elastic throughout cracking such that the region containing plastic effects at the crack tip remains negligibly

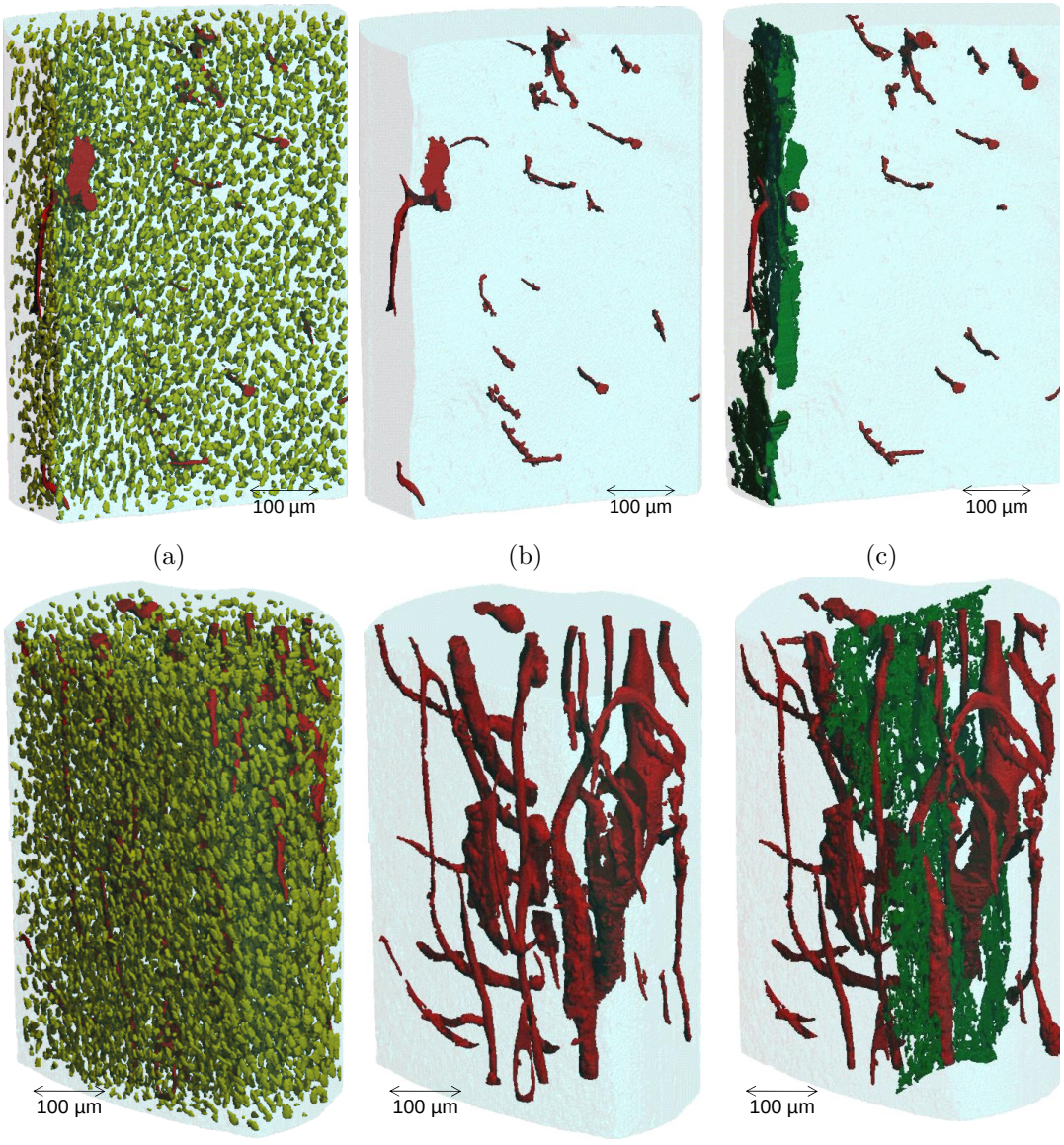

Figure 4-6: 3D microcracks in a B6 (a-c) and C3H (d-f) sample. In all images canals are rendered in red. Light green indicates lacuna in (a,d) and dark green indicates cracks in (c,f). Lacuna are not shown in the middle and right columns to ease visualisation of the canals and cracks. All images provided by Levchuk et al. (2010).

small. Expressions for the local stress intensity surrounding a crack tip can be used to determine stress intensity factors (K). The general form of such factors is

$$K = \sigma\sqrt{\pi a}\, f\left(\frac{a}{w}\right) \tag{4.2}$$

where σ is the apparent stress applied in a direction orthogonal to the crack, a is one half of the length of a critical flaw (crack), and $f(a/w)$ is a dimensionless scaling factor to account for variations in sample geometry. Critical values of stress intensity factors relate crack sizes to the applied stress which would induce instability and complete propagation of the crack. In general, these properties are dependent upon the specimen thickness and cannot be compared directly. However, if the thickness is sufficiently great to justify the assumption of plane strain then geometrical dependence is removed. The critical stress intensity factor in plane strain (K_{IC}) is considered a material constant and can be used for material comparison. Critical values in non-plane strain conditions are labelled K_C. K_C and K_{IC} values can only provide information about the limiting crack size before instability; they cannot indicate or characterise the presence of sub-critical crack growth, i.e. increasing crack length for $K < K_C$. For ideally brittle materials which show no toughening behaviour, a single parameter (such as K_C) can fully characterise the fracture process. For materials which exhibit toughening mechanisms (such as bone) considerable sub-critical cracking can occur. In these cases, crack resistance curves, 'R-curves', can be used to represent the variation of stress intensity factors (K_R or other measures of crack driving force) with crack growth graphically. In these curves stable, sub-critical crack growth occurs while

$$\frac{\Delta K}{\Delta a} < \frac{\Delta K_R}{\Delta a} \tag{4.3}$$

To drive crack growth in this condition, the crack driving force (K here) will have to be increased since the resistance to growth (K_R) will increase more for an equivalent crack extension Δa. Instability can be said to occur when the above inequality becomes an equality. Preparation of such curves requires the experimental determination of K and the corresponding sub-critical crack lengths.

Koester et al. (2008) developed R-curves for short ($< 600\,\mu$m) cracks in human cortical bone. Their results demonstrated that at crack lengths of only $500\,\mu$m the driving force for propagation was more than five time greater in the transverse than the longitudinal direction. Koester et al. (2008) also reported that plasticity effects surrounding the crack tips dominated the observed crack resistance behaviour; elastic components of fracture resistance were found to be only 5–10 % of plastic components in human bone. The presence of such a large plasticity contribution in bone cracking indicated that linear-elastic fracture mechanics are not appropriate for bone studies. The concept of the 'J-integral' from non-linear-elastic fracture mechanics has been proposed to capture such large plastic effects (Koester et al., 2008). The definition of J uses non-linear elasticity to explicitly incorporate plastic effects which are active over a determined plastic zone ahead of the crack tip.

Numerous FE techniques have been developed to simulate cracking processes across the wide variety of materials which exhibit such behaviour. Discrete crack models seek to represent the initiation and propagation of dominant cracks through a medium. Cracks are modelled as a sequential release of nodal connectivity along element boundaries; cracking will split one node into two unconnected nodes. Cracking typically occurs at a node when a tensile criterion is violated. Since the crack path is defined at nodes, discrete cracking models typically suffer from a degree of mesh bias. These effects can be reduced through the use of adaptive remeshing or element-free techniques; however, both of these approaches introduce further modelling difficulties. The method of cohesive surfaces (Needleman, 1987) has been used to model fracture in bone (Ural and Vashishth, 2007; Tomar, 2008; Ural, 2009). This approach requires the placement of cohesive elements on the interfaces of finite elements where cracking can then occur. Cracking is governed by cohesive constitutive laws, distinct from that of the bulk material, which require specification of the tensile strength and work of separation. The cohesive surfaces method can be very effective when a clear interface exists within a model; for example between layers of a composite which can be expected to fail by debonding. It becomes less reliable and also more difficult to identify locations for cohesive surfaces when the material is homogeneous on the scale of the crack length. Several studies of cracking in bone have assumed planar propagation of cracks (Ural and Vashishth, 2007; Ural, 2009) to simplify the meshing and solu-

tion process. However, it is not clear the assumption that cracks will follow such straight paths can be justified with regard to the previously discussed crack deflection mechanisms present in bone. Others (e.g. Xu and Needleman, 1995) have sought to avoid selection of the crack path a-priori by placing cohesive elements on the interfaces of all elements and allowing the crack path to be determined as a function of the solution process. Tomar (2008) employed this technique in modelling of trabecular bone fracture. Problems remain with such an approach since the crack path is necessarily restricted to only a few mesh-dependent directions at each element interface.

Continuum damage techniques seek to represent the deterioration of material load carrying capacity by scaling the elasticity tensor at specific integration points. The various mechanisms of material degradation are collectively represented by a damage variable $0 \leq \omega \leq 1$, such that the stress-strain relation becomes

$$\underset{\sim}{\sigma} = (1 - \omega)\underset{\sim}{\underset{\sim}{D}}^{e}\underset{\sim}{\epsilon} \tag{4.4}$$

where 0 and 1 values of ω correspond to the undamaged and completely damaged cases respectively, and $\underset{\sim}{\underset{\sim}{D}}^{e}$ is the elasticity tensor of the undamaged material. Cracking in particular orientations can be incorporated in damage techniques by scaling terms of the elasticity tensor independently. Continuum damage methods have been demonstrated to suffer from mesh sensitivity leading to theoretically infinite rates of crack propagation for infinitely fine meshes (Peerlings et al., 2002). The continuum damage method has found application in modelling trabecular bone (Zysset and Curnier, 1996), and bone cement (Stolk et al., 2003). Stolk et al. (2003) utilized a 'stress concentration limiter' (SCL) to reduce the mesh dependency of the method by spatially averaging stress components in regions with high stress gradients.

Unification (de Borst et al., 2004) of discrete and damage-based cracking techniques has more recently been achieved by exploiting the 'partition of unity' properties of finite element shape functions (Babuška and Melenk, 1997). The presence of cracks is captured numerically by adding strain 'jumps' or disconti-

nuities to the shape functions used to interpolate within finite elements. These methods involve the activation of cohesive segments (distinct from the cohesive surfaces approach discussed previously) within finite elements at which the partition of unity is modified (Wells and Sluys, 2001; Remmers et al., 2003). A cohesive constitutive law, similar to those used with the cohesive surfaces approach defines the separation process. In its original formulation cohesive segments separated whole elements, such that once a single integration point had cracked, the crack immediately advanced through the entire element. The incorporation of the cohesive segments approach with 'level-sets' (Gravouil et al., 2002; Moës et al., 2002) led to the method known as the extended finite element method (X-FEM). The X-FEM is able to simulate the initiation and propagation of arbitrary cracks in 3D without the need for extensive remeshing.

The aim of the present study was to investigate the role of ultrastructure in the initiation and propagation of cracks in bone. As discussed previously, murine bone represents an ideal candidate for studying these effects since it does not possess many of the features which might obscure them in human bone. The ultrastructural features (canals and lacuna) exist at a scale which requires very high spatial resolution to image and therefore to represent as an FE mesh. It was therefore required to develop a method for the simulation of crack initiation and propagation within nano-FE meshes. To provide meaningful information it is necessary to include a region of bone large enough to include examples of both lacuna and canals. However, this immediately necessitates extreme computational cost even to produce a linear static solution. The simulation of cracking is an inherently non-linear process which further amplifies the computational expense of achieving a solution. The aim of the present study was therefore to develop a simplified method for identifying the role of ultrastructure, specifically as stress raisers to initiate and guide cracking. The use of voxel-based meshes has become commonplace (Ulrich et al., 1998; Niebur, 2000; Newitt et al., 2002; Pistoia et al., 2002) for representing the extremely complex geometries encountered in bone biomechanics. To facilitate rapid solution of these models dedicated parallel solvers have been developed. However, the requirements of domain decomposition for these parallel solvers restrict meshes to hexahedral elements, and consequently 'blocky' geometries. This reality placed a further requirement on the present study: to develop a cracking procedure which functioned over such blocky, hexahedral meshes.

4.2 Methods

The methods described in the following were implemented using programs written by the author in Matlab (The MathWorks, Inc., Natick, MA, U.S.A.), Bash Script and C^{++}.

4.2.1 FE analyses

Throughout this study the method of FE analysis was broadly similar. Images of bone (from μCT or synchrotron radiation based CT (SRCT)) were converted into voxel based FE meshes. These models were solved using the fully parallel FE solver ParFE. ParFE, developed at ETH Zurich, is a linear FE solver which achieves very rapid solutions for large meshes. In this study meshes containing 4,500,000 hexahedral elements were solved in less than 75 seconds, typically distributed over 100–200 processors. All algorithms to model crack propagation were coded for use with ParFE. All FE analyses were run on the Cray XT5 System 'Rosa' at the Swiss National Supercomputing Centre. This resource provides a total of 22,128 compute cores and over 29 terrabytes of memory. Following solution, the FE results were post-processed by deriving output variables and writing them to image files in the original format of the scan images.

Two types of models were considered for FE analysis (Fig. 4-2). The first type, called the *notched models*, included the entire femoral thickness and a longitudinal region that included the notch. The second type, called *microcracking models*, were high resolution meshes comprising a cuboidal sub-domain of the notched models. Analyses of the notched models were required to identify the stress/strain state at the boundary of the microcracking models. These were used as boundary conditions to simulate the microcracking process in sub-domains of interest. To identify the stress/strain state within the notched samples, solid models of these regions were solved and sites of stress/strain concentrations identified. The critical stress/strain states within the notched models were applied to microcracking analyses of cubical regions of interest within the SRCT images of the notched samples. The two types of analyses are described in the following sections.

4.2.2 Notched models

FE models of notched specimens were generated from μCT images of the mid-diaphysis of murine femora scanned at an isotropic resolution of 6 μm. The images contained the full femoral cross-section and extended to a minimum of 2.04 mm in the longitudinal axes when centred upon the notch (Fig. 4-2(a)). Regions of bone were identified by thresholding at a constant attenuation value of 900. This was selected as the approximate inter-peak minimum of all samples and produced a clear identification of the solid and void phases. The images were rotated into consistent orientations such that the medial-lateral and anterior-posterior axes lay in the transverse (x and y-directions) plane and the longitudinal axis lay in the image stacking, or z-direction. 3D rotation angles were determined by user estimation. The sample height of 2.04 mm was less than the 4.00 mm unembedded length of the specimens present in the physical experiments but represented the greatest height available from all of the scan data. In each case the models contained the complete notched region with an unnotched surrounding of 0.5 mm on each side. In the experiments, the samples had an additional 1 mm of exposed bone before they were embedded in stiff PMMA. Since the stiffness of the unnotched cortex can reasonably be expected to be considerably higher than the notched area, its absence in the present models can be considered an approximate representation of the experiment. At the 6 μm scanning resolution some of the larger pores could be perceived. To avoid distortions of the stress/strain field by these features they were removed using a sequence of erosion and dilation image operations. Erosion and dilation are opposite image operations whereby voxels at the solid/void interface are removed or added respectively. In several images it was necessary to remove voxels which were not attached to the main bone fragment since they would cause instability and prevent FE solution. This was achieved by applying component labelling to the eroded images, retaining only the largest component and re-dilating the images. Component labelling is a process whereby groups of connected voxels are identified and ranked by size. The consequent image process was as follows: 1) one erosion step, 2) component label, and retain the largest component, 3) cut the bounding box to enclose only the solid region, 4) append 10 layers of void to each side, 5) dilate the image four times, 6) erode the image three times. Note, the number of erode/dilate operations was equal to avoid any net migration of the outer surfaces of the bone

fragments. The images were converted into cubic hexahedral finite elements containing 8 integration points. Meshes typically included 5.5 million (B6) and 8.5 million (C3H) elements. A constant, isotropic Young's modulus of 20 GPa and Poisson's Ratio of 0.3 were assigned to all solid elements. A longitudinal compressive strain of 1 % was applied to the top surface of the models and the bottom surface was restrained against longitudinal displacements. Nodes were free to translate in transverse directions on the top and bottom surfaces.

4.2.3 Microcracking models

The initial geometry of microcracking models was taken from reference scans of the murine samples, preceeding loading. Regions of interest (ROI) were selected from the images of B6 and C3H mice. A common ROI size was selected to enable a comparison of results between breeds. Images of the C3H samples did not contain the periosteum or endosteum. It was therefore necessary to select ROI entirely from within the cortex. Images of B6 samples did contain the periosteum and endosteum but ROI were restricted to within the cortex to remain consistent with the C3H samples. Since the B6 cortices were thinner than C3H, these placed an upper limit on ROI size. In previous work Voide et al. (2009) the periosteum and endosteum were observed to be the main locations of crack initiation. Their omission in the present ROI can therefore be expected to affect the observed crack initiation behaviour. However, this study was principally concerned with identifying the influence of lacuna and canals on crack propagation behaviour. Since these features are internal to the cortex, the internal ROI used here were expected to be sufficient. Furthermore, it became necessary to apply boundary conditions in the periosteal-endosteal direction. ROI orientations were chosen such that the cube faces were aligned with the radial, circumferential and longitudinal directions. The location of ROI in the circumferential direction was not standardised; ROI were selected at locations with features such as canals or large lacunae which were observed to play a role in crack initiation or propagation during previous experimental work (Voide et al., 2009). In order to select the size of the ROI for further analysis, several cubical ROIs with the same centroid were analysed. ROIs with boundary lengths of 100, 150, 200 and 250 voxels were considered. In each case a voxel represented 0.7 μm. For all analyses the von Mises

stresses within the samples were evaluated. The von Mises stresses in samples of length 100 to 200 voxels were each compared with the same location in the sample of length 250 voxels. The variation relative to the sample centroid is shown in Fig. 4-7. The sample size was found to influence the stress/strain field inside the models. Variations were maximal at the ROI boundaries as indicated in Fig. 4-7. The cause of this size dependency was the boundary effect, or absence of continuity with tissue outside the ROI, in particular the variation of FE gradients which result from the exclusion of pores lying outside the ROI. Indeed, near ROI boundaries the boundary effect remained constant at different sample sizes, and caused a deviation of approximately 7.5 %. However, the deviation at internal locations reduced with increased ROI size; when rounded to the nearest 0.05 % the modal size-dependent deviations were 0.70 %, 0.45 % and 0.30 % with 100, 150, and 200 voxel sample sizes respectively. Cubic ROI of size $170 \times 170 \times 170$ voxels ($119 \times 119 \times 119\,\mu$m) were selected to fit within all B6 cortices. The same ROI size was used in C3H samples. The modal deviation associated with 170 voxel models was approximately 0.39 %.

4.2.4 Microcracking algorithms

Several distinct microcracking algorithms were developed. For all algorithms cracking was simulated by deleting elements and reanalysing the FE system. The algorithms differed in the process used to identify the deleted elements. In all algorithms the value of maximum principal stress (σ_1) was used to identify crack locations. Cracking was dependent upon whether σ_1 exceeded a limiting value σ_{lim}. Constant applied displacements were applied in some analyses and solution dependent (increasing) applied displacements were applied in others. The variation of applied displacement was determined by whether the number of elements deleted in an increment was less than a minimum number, min_{del}. Ideally min_{del} would set to 1 element (i.e. applied displacements would only increase when 0 voxels were deleted in an increment), however a value of 5 voxels per increment was used. This reduced the number of increments in which very little crack propagation occurred. In analyses with constant applied displacements min_{del} was set to 0. When increased, the applied displacements were adjusted to produce 1 % increments of the triaxial strain determined from the notch model analyses under

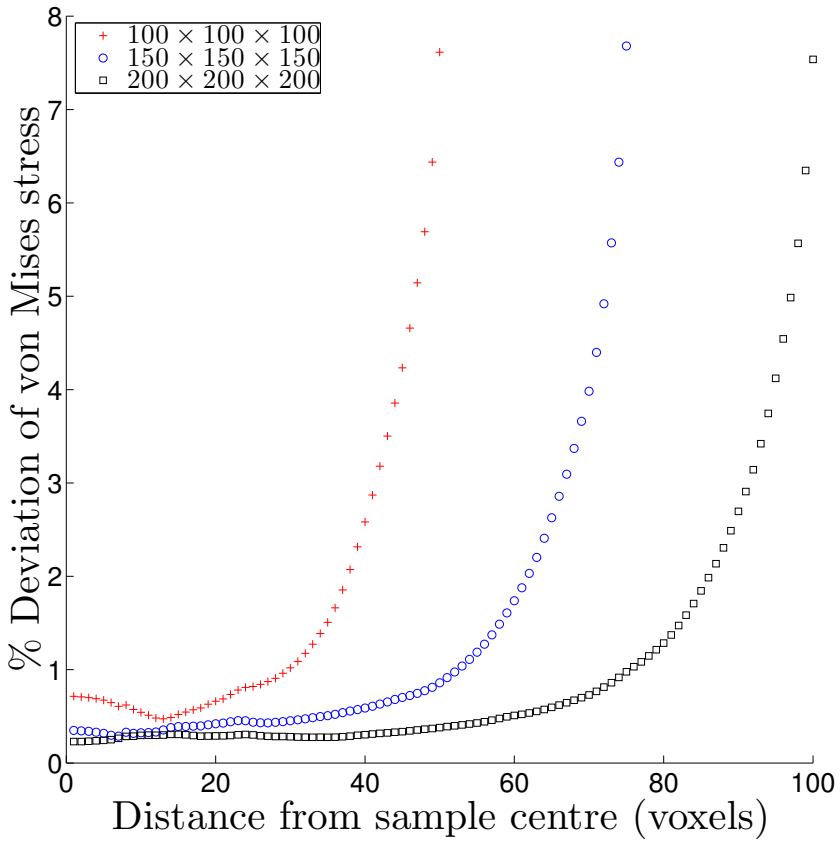

Figure 4-7: The size dependency of FE results within the ROI; deviation from von Mises stress found with a 250 voxel ROI. Note deviations at ROI boundaries are all approximately 7.5 % but larger ROI have smaller internal differences; the modal size-dependent deviations were 0.70 %, 0.45 % and 0.30 % with 100, 150, and 200 voxel sample sizes respectively.

a longitudinal compressive strain of 1 %. The reference (notch model) radial, circumferential and longitudinal strains (ϵ_R, ϵ_C and ϵ_L) were 0.24 %, 0.47 % and -1.03 % respectively. These were selected from the location at which the largest tensile strain component (circumferential) was observed in the previous notch model analyses. The algorithms are discussed in the following Subsections.

σ_{lim} algorithm

In the first algorithm all voxels which were subjected to a maximum principal stress greater than a limiting value Tol.1 = σ_{lim} were deleted. This algorithm is referred to as the σ_{lim} algorithm, and is illustrated by the flowchart in Fig. 4-8.

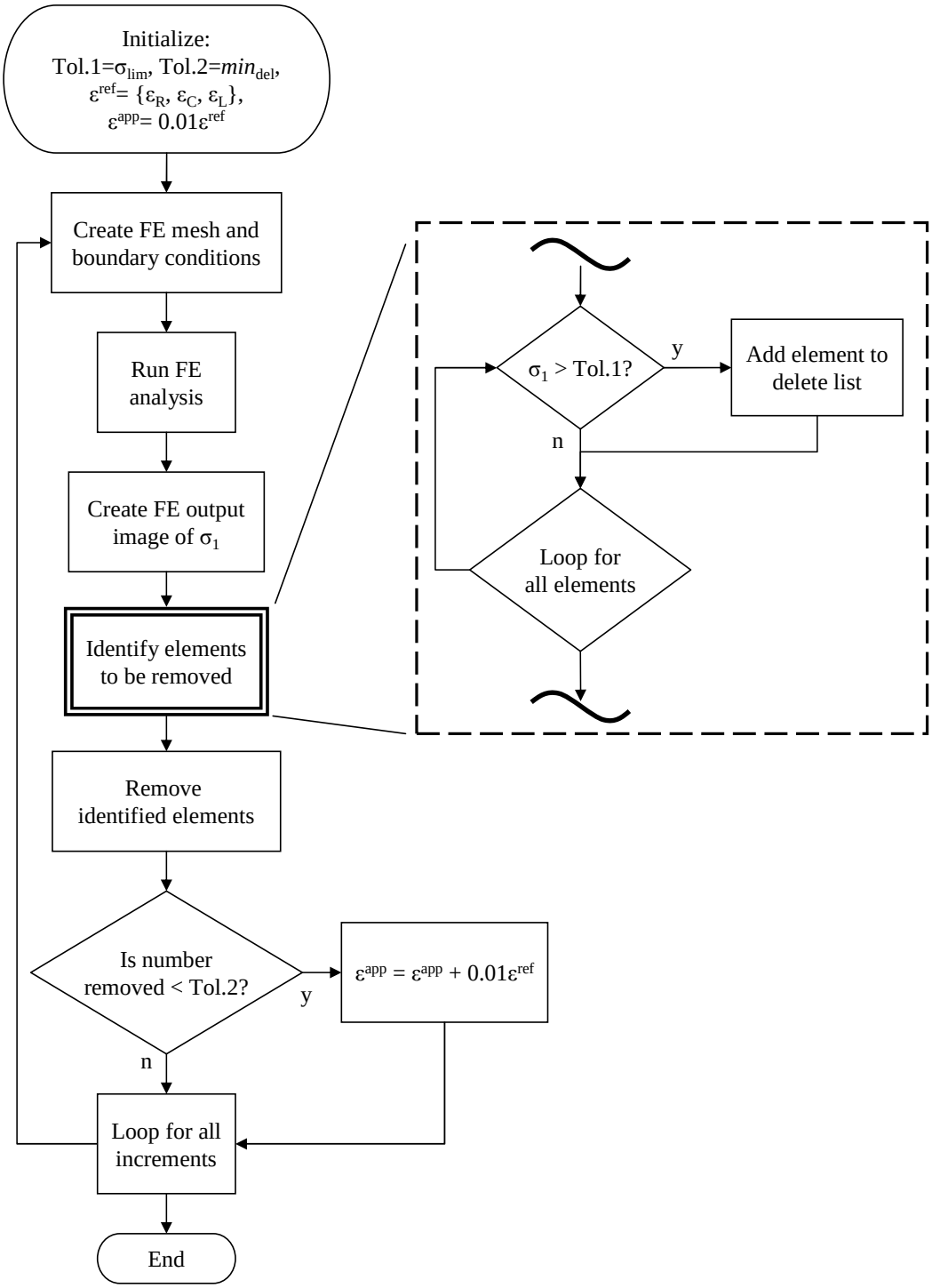

Figure 4-8: Flowchart of the σ_{lim} algorithm. Note Tol.1 and Tol.2 are algorithmic tolerance values, ϵ^{ref} and ϵ^{app} contain the reference and applied displacements (strains).

It was observed that the σ_{lim} algorithm produced very wide crack fronts (e.g. 5–10 voxels). Inspection of the stress gradient around crack tips revealed that the wide crack fronts formed because large regions of voxels were loaded such that $\sigma_1 >$ Tol.1, all of which were deleted in every increment. This algorithm effectively resulted in wide cracks that rapidly spread throughout the specimen.

CL algorithm

To prevent the behaviour observed in the σ_{lim} algorithm it was decided to limit the number of voxels that could be deleted at a crack tip in every increment. Individual crack tips were identified by component labelling only those voxels with $\sigma_1 >$ Tol.1 and separating them into connected groups. From within each connected group a limited number (max_{del}) of voxels could be deleted in each increment. The max_{del} voxels were identified as those with the largest value(s) of σ_1. This algorithm, summarised in Fig. 4-9, will be referred to as the *CL* or component labelled algorithm.

The *CL* algorithm was initially used with a constant applied displacement and successfully prevented the wide crack fronts associated with the σ_{lim} algorithm. However, it was observed that *CL* produced very linear cracks; crack paths typically initiated at the edge of the largest features and propagated orthogonally to the maximum tensile strain direction without deviating to intercept nearby features such as lacuna or canals. This behaviour did not mirror that observed in experimental work in which propagating cracks were observed to be attracted towards neighbouring lacunae and canals (Voide et al., 2009). The straight line cracks produced by the *CL* algorithm could be attributed to mesh dependency. Previous research has shown that when using the smeared crack approach, cracks tend to follow mesh lines (Pankaj, 1990; de Borst et al., 2004) and often produce diffused crack patterns (Pankaj, 1990). Both σ_{lim} and *CL* algorithms are essentially variants of the smeared crack approaches. The smeared crack approaches generally incorporate a gradual reduction of strength (strain softening) rather than a sudden drop that arises in the present methods due to element removal. It should be noted that the discrete crack approaches in their original form also demonstrated similar bias as cracks were required to follow element boundaries. Improvements in this approach through remeshing and use of meshless methods

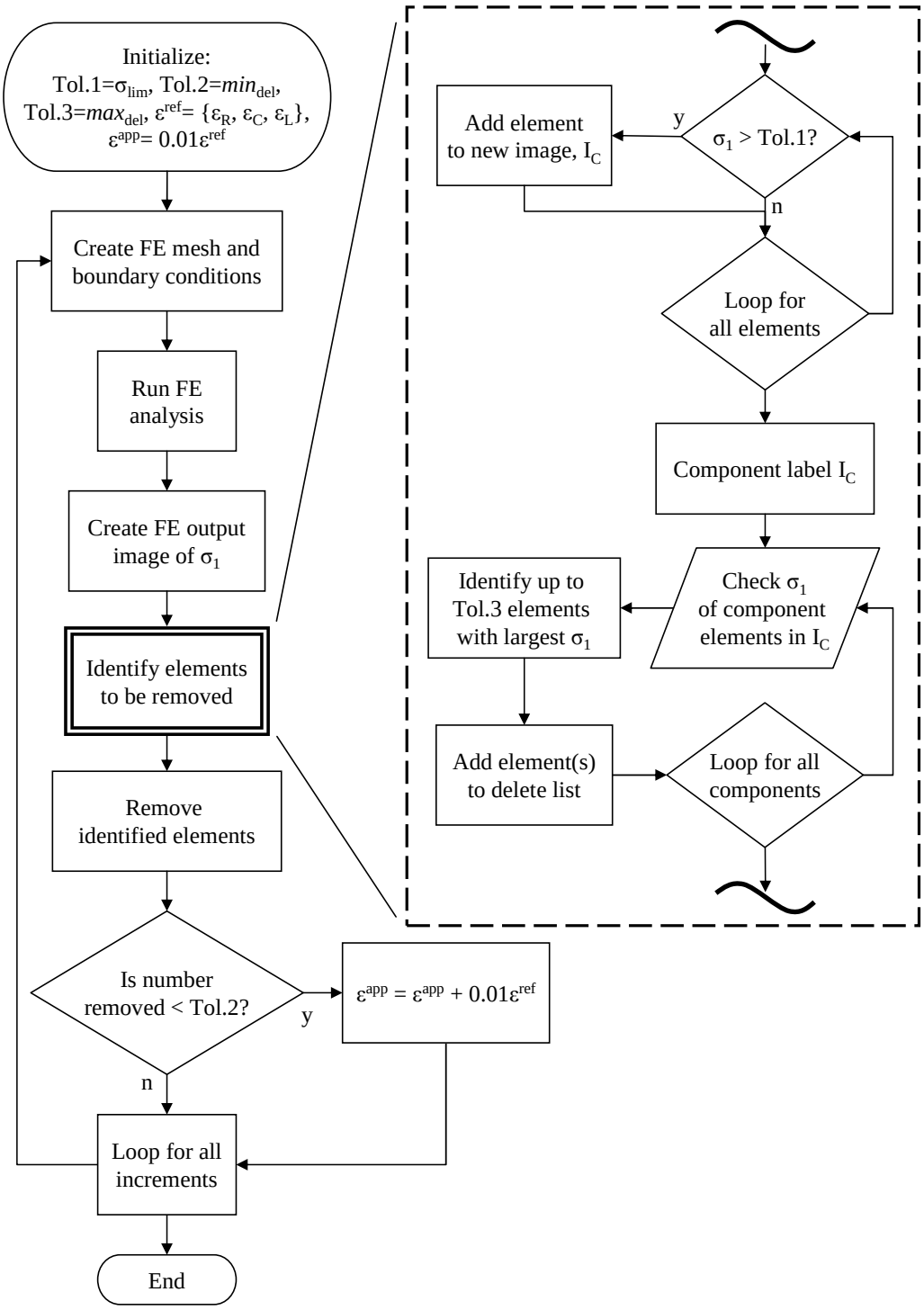

Figure 4-9: Flowchart of the *CL* algorithm. Note Tol.1, Tol.2 and Tol.3 are algorithmic tolerance values, ϵ^{ref} and ϵ^{app} contain the reference and applied displacements (strains), I_C is a temporary image which contains only connected groups of those elements which satisfy $\sigma_1 >$ Tol.1.

introduced additional difficulties for robust three-dimensional implementations (de Borst et al., 2004). The recent development of partition-of-unity properties of finite element shape functions is currently considered the best way to model the coalescence of distributed cracks into one or more dominant cracks (de Borst et al., 2004).

σG algorithm

A new algorithm was developed to minimise mesh dependency and to permit the influence of features such as lacunae and canals in the direction of crack propagation as observed during experiment (Voide et al., 2009). Such features could act as local stress raisers and thereby attract cracks towards them. The algorithm, referred to as the stress gradient (σG) algorithm determined the direction of cracking from the maximum principal stress gradient of a cubic region surrounding the crack tip. Void neighbours of elements with $\sigma_1 >$ Tol.1 were identified as crack tips at which further cracking should occur. Cracking then proceeded from the void voxel crack tips. By this mechanism it was ensured that cracking could only occur from existing pores or cracks. From a void voxel, a surrounding region of size CRS $\times$ CRS $\times$ CRS voxels was identified as were unit vectors pointing towards these voxels. The direction of crack propagation was determined as the sum of the product of these vectors with the corresponding maximum principal stress values and labelled the deletion direction vector (DDV). The weights were assigned a zero value if the maximum principal stress was negative (compressive). The algorithm was implemented in 3D but for the purpose of illustration a 2D representation of the calculation of DDV with a CRS of 3 is shown in Fig. 4-10. In this study a CRS value of 21 was used in most cases. The voxel in the 26 neighbourhood of the crack tip (original void voxel) which corresponded most closely to the determined DDV was deleted. The σG algorithm is summarised in Fig. 4-11.

The σG algorithm produced cracks which were attracted towards nearby features such as canals and lacuna, which acted as stress raisers. The σG cracks did not exhibit the excessive thickness of the σ_{lim} algorithm, or the linearity associated with the CL algorithm.

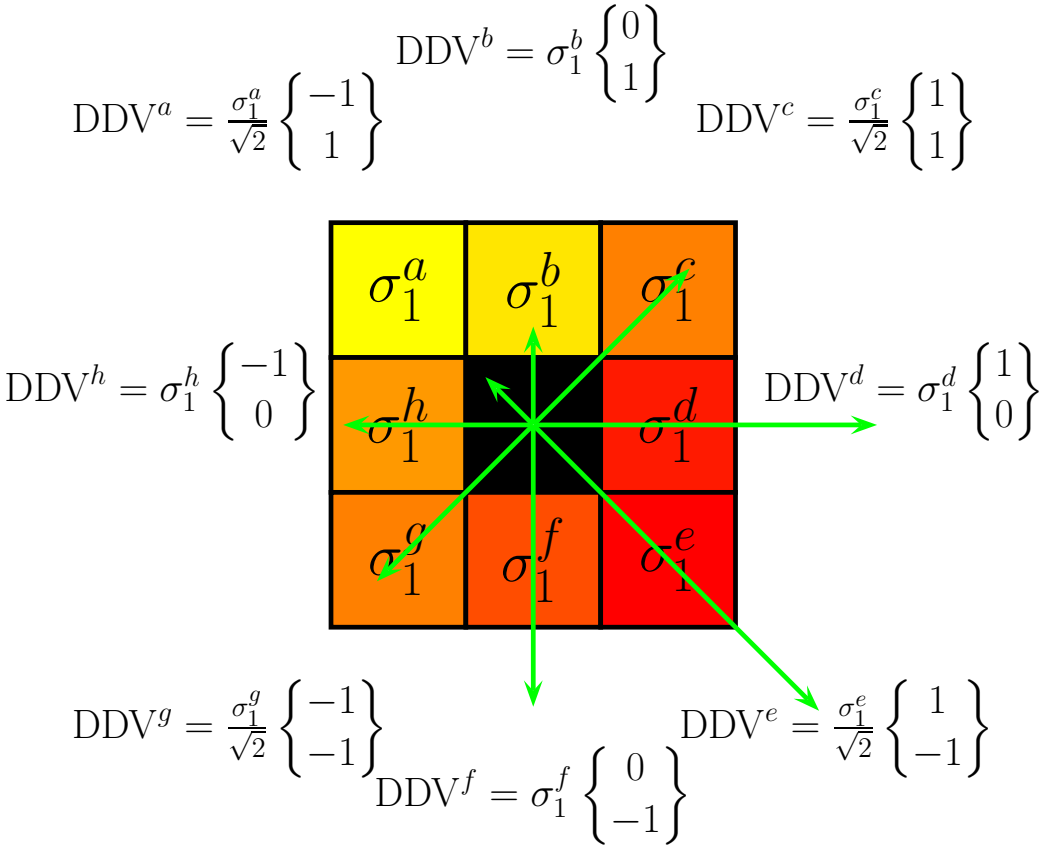

(a)

Figure 4-10: The calculation of the deletion direction vector (DDV) illustrated in 2D for a CRS of 3.

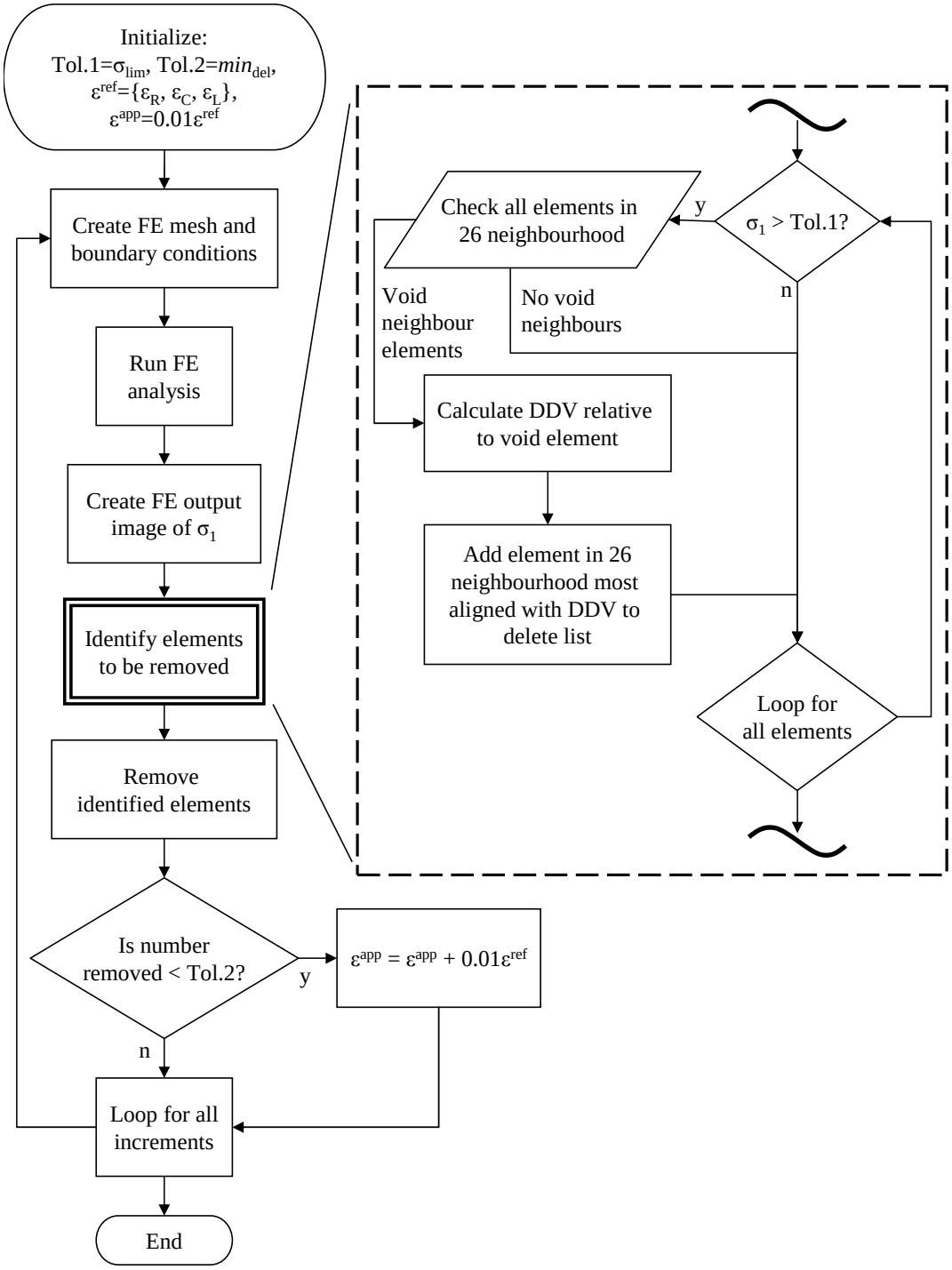

Figure 4-11: Flowchart of the σG algorithm. Note Tol.1 and Tol.2 are algorithmic tolerance values, ϵ^{ref} and ϵ^{app} contain the reference and applied displacements (strains), and the calculation of the DDV is illustrated in Fig. 4-10.

Comparison of algorithms

A comparison of the three algorithms is illustrated in Fig. 4-12. It can be seen that for the same initial crack geometry, the crack propagates in different ways depending upon which algorithm is used. The σ_{lim} algorithm deleted a wide crack front where multiple voxels satisfied $\sigma_1 >$ Tol.1. Further implementation of this algorithm (not shown here) would cause crack widening and tracing of mesh lines. The *CL* algorithm reduced crack widening, but was strongly mesh dependent. The σG algorithm calculated DDV which reflected the presence of the stress raiser and directed crack propagation towards it.

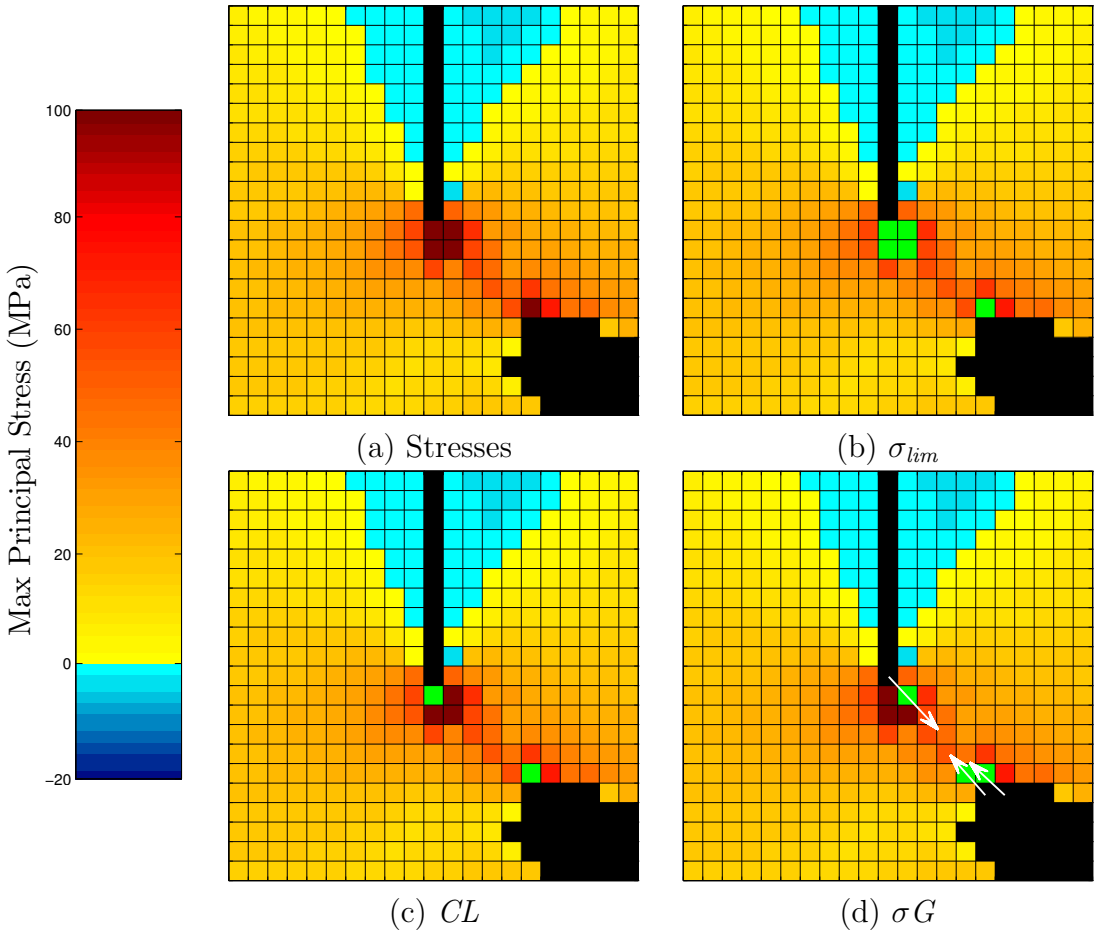

Figure 4-12: Comparison of a single iteration of crack propagation with the three algorithms. Green indicates deleted voxels, the arrows in (d) indicate the deletion direction vectors (DDV) used to determine the direction of propagation. The pore to the bottom right acts as a stress raiser.

4.3 Results

4.3.1 Notched model results

The variation of maximum principal stresses on a typical transverse slice of B6 and C3H mouse strains are shown in Fig. 4-13. B6 samples contained concentrations of tensile (crack inducing) stress at both the periosteum and endosteum. The thicker C3H samples showed tensile stress concentrations at the endosteum only. There were stress concentrations next to the notch (regions A), however under experimental conditions these locations contained very localised cracks. The focus of the current study was on larger cracks located opposite the notch (regions B).

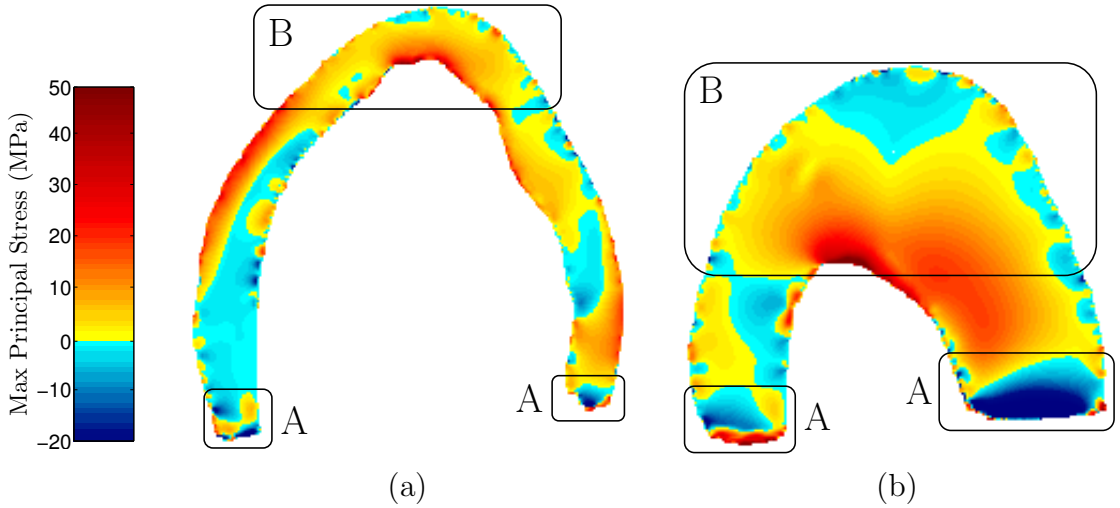

Figure 4-13: Maximum principal stress contours in typical notched B6 (a) and C3H (b) samples. Tensile stress concentrations were observed at both the periosteum and endosteum of B6 samples, but only the periosteum of C3H samples.

Figure 4-14 illustrates the variation of stresses and strains with longitudinal position in the B6 and C3H samples. The data were taken at all longitudinal locations directly opposite the notch; this site contained the greatest stress and strain concentrations. Locations level with the notch showed considerably raised tensile stress and strain in the circumferential direction. Such increases were not observed in the radial or longitudinal direction. A slight reducing trend with longitudinal position can be seen in the B6 stresses and strains; this resulted from the natural variation of cortical thickness in the mouse femurs with longitudi-

nal position and was minimal relative to the effect of the notch. The localised fluctuations of all stress and strain components were caused by small variations of the surface of the femurs, for example where canals terminated and residual depressions existed.

The variation of tensile stresses and strains from the periosteum to the endosteum are illustrated in Fig. 4-15. The circumferential stress and strain increased towards the endosteum to a peak tensile value slightly inside the endosteum. The radial and longitudinal components showed relatively little variation through the cortex. As can be seen in Fig. 4-13(a) the periosteal-endosteal variation of stresses and strains at other locations could be very different, such that periosteal components were greater than endosteal ones. However, in general the location directly opposite the notch contained the largest tensile components.

As noted, the largest tensile components of stress and strain were located at the endosteum directly opposite the notch. These values were therefore selected as the most likely sites for crack initiation and the stress and strain states used in subsequent nano-level cracking simulations. The mean radial, circumferential and longitudinal components at the location of maximum tensile stress and strain are plotted in Fig. 4-16 for B6 and C3H samples. It can be seen that little difference was observed between the local maximum stresses or strains in B6 and C3H samples; in both cases the B6 and C3H results were within one standard deviation of each other. Negligible stress was observed in the radial direction, concurrent with the fact that no loading or structural continuity existed in this direction. However, a tensile strain was observed, which was approximately equal to that predicted by the Poisson effect. The strain in the circumferential direction was greater than the Poisson effect, this indicated that sample geometry could promote cracking in this direction.

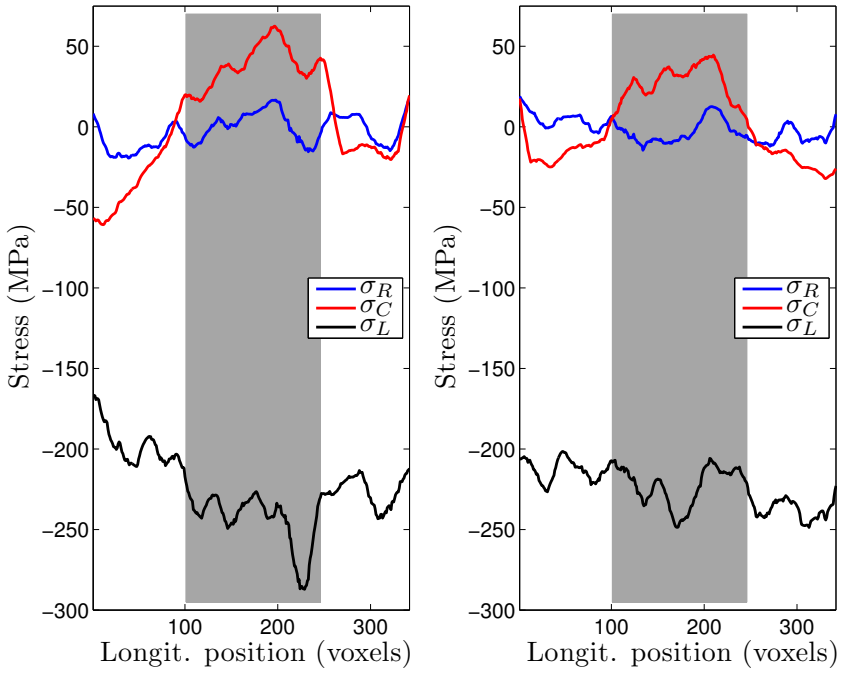

(a) B6, Stress (b) C3H, Stress

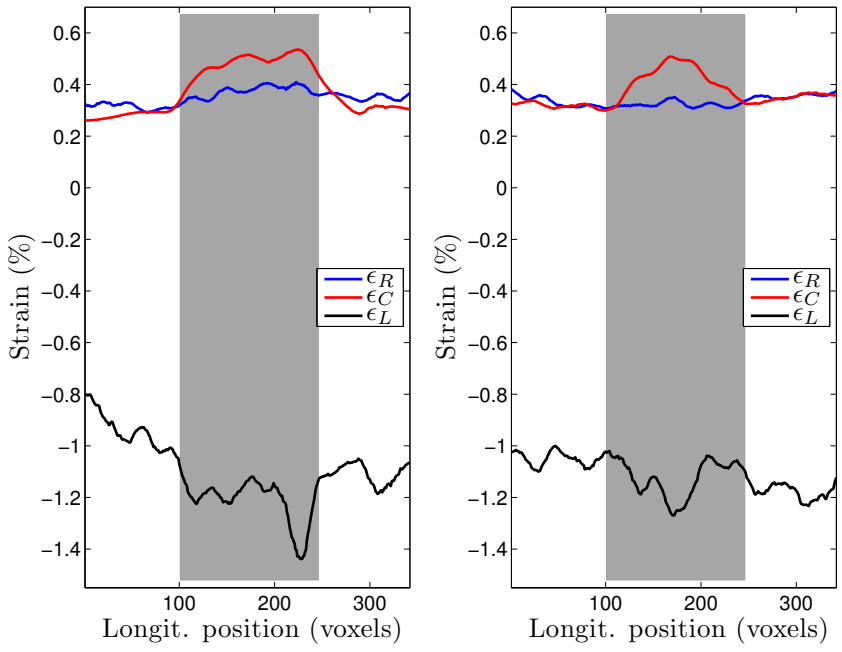

(c) B6, Strain (d) C3H, Strain

Figure 4-14: Variation of stress and strain with longitudinal position in notched B6 and C3H samples. The grey area represents the longitudinal location of the notch. In both B6 and C3H samples large tensile strains were induced opposite the notch in the circumferential direction, but not in the radial or longitudinal directions.

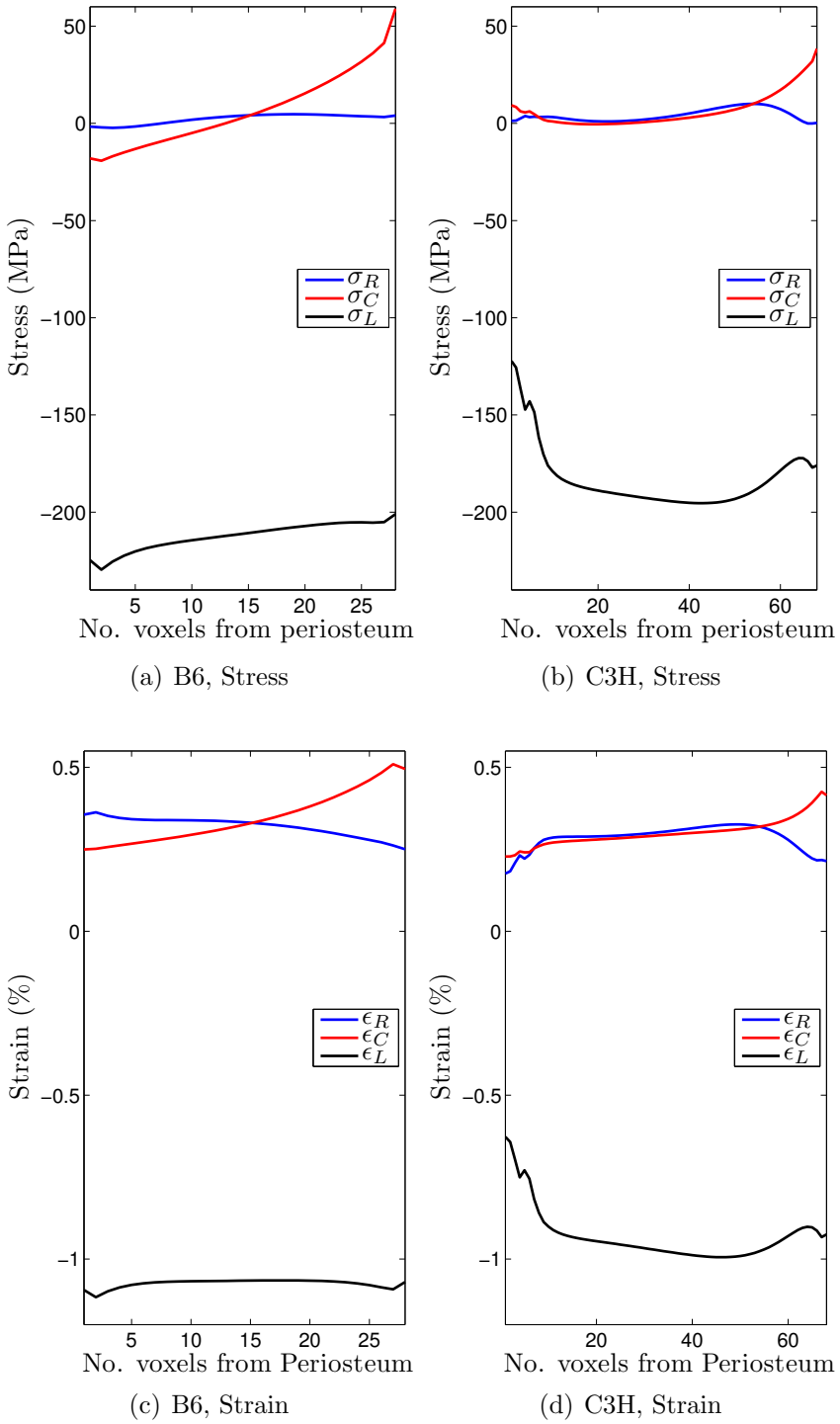

(a) B6, Stress (b) C3H, Stress

(c) B6, Strain (d) C3H, Strain

Figure 4-15: Variation of stress and strain with periosteal-endosteal position in notched B6 and C3H samples. These data were taken from the longitudinally middle slice, directly opposite the notch. Note the periosteum and endosteum lie at the left and right of the figures respectively. At the sampled location both B6 and C3H samples showed large tensile circumferential strains at the endosteum.

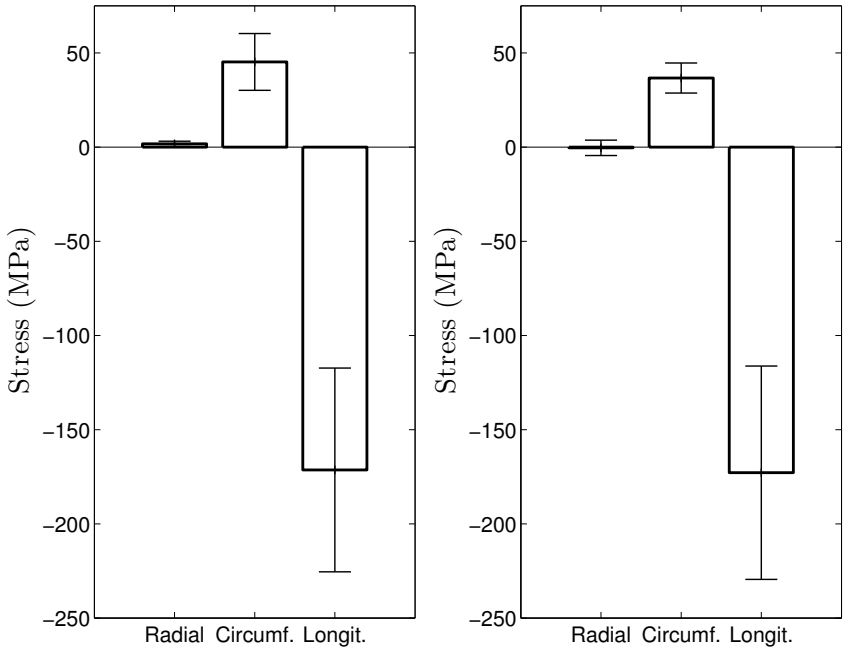

(a) B6, Stress

(b) C3H, Stress

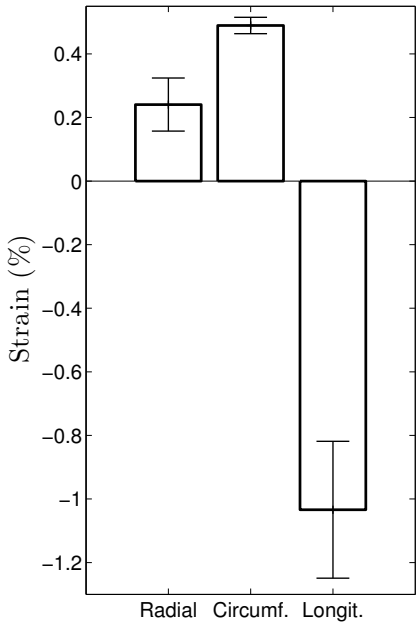

(c) B6, Strain

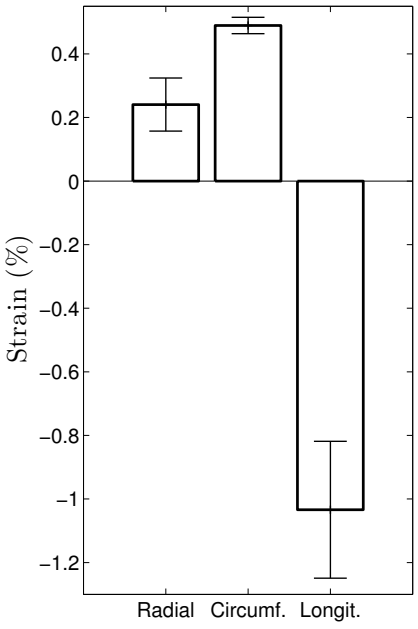

(d) C3H, Strain

Figure 4-16: Maximum stresses and strains opposite notches in B6 and C3H samples. Note whiskers represent one standard deviation. The maximum stress and strain values observed opposite the notch were approximately equal (less than one standard deviation apart) for B6 and C3H mice.

4.3.2 σ_{lim} algorithm results

The σ_{lim} algorithm produced wide cracks as illustrated in Fig. 4-17. A good example of this can be seen between the images of Fig. 4-17 (b) and (c). In (b) a large number of voxels was stressed next to the canal on the left, such that $\sigma_1^v >$ Tol.1 (here Tol.1=100 MPa), in (c) all of these voxels had been deleted, leaving a wide crack.

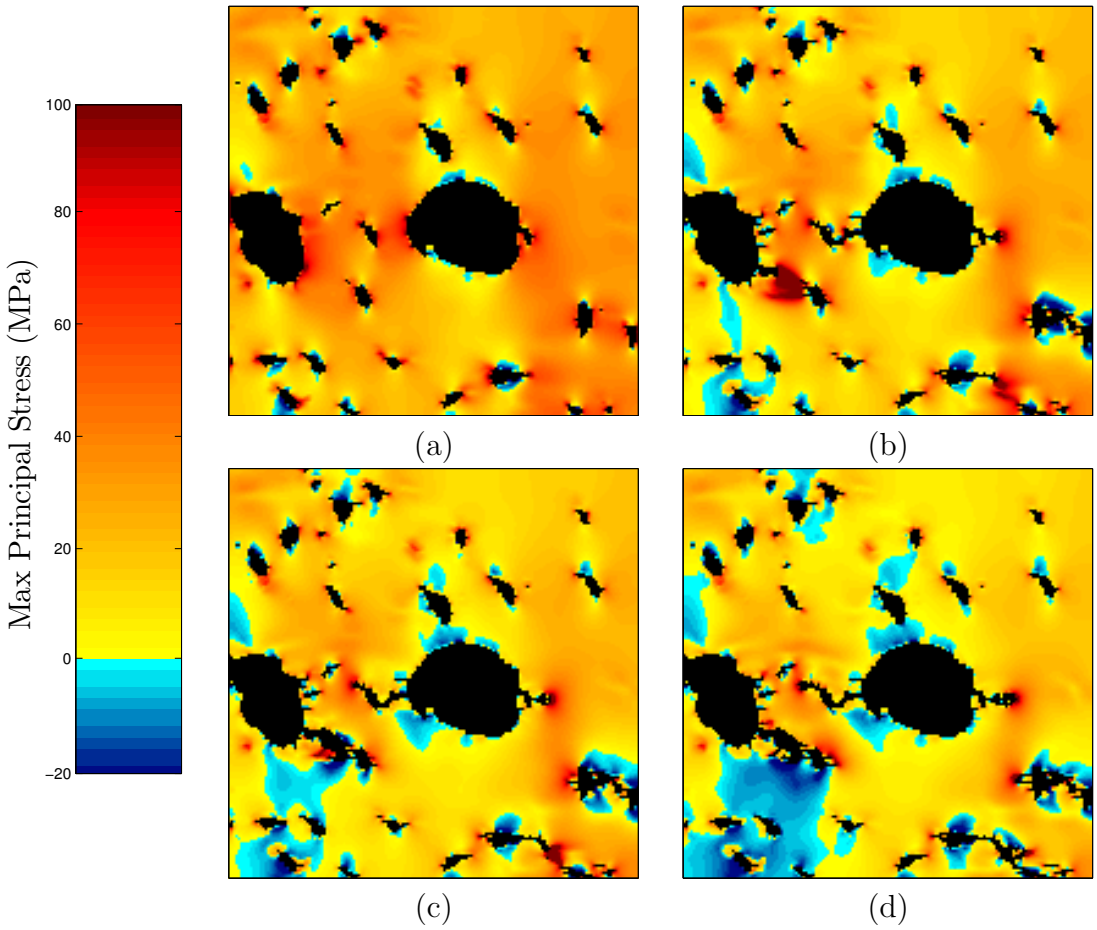

Figure 4-17: Typical crack propagation with the σ_{lim} algorithm within a C3H sample. Intact sample (a), crack propagation (b) to (d). Note the wide crack which propagated between the canal on the left and the lacuna below and to the right; between steps (b) and (c) a large volume of voxels was deleted.

4.3.3 *CL* algorithm results

The *CL* algorithm was developed to prevent the growth of wide cracks as seen with the σ_{lim} algorithm. Typical crack patterns using the *CL* algorithm are illustrated in Fig. 4-18. Many cracks formed under the constant applied displacements. If smaller displacements were applied, fewer cracks would initiate; similar to the σ_{lim} algorithm, a trial and error approach was required to identify appropriate applied displacements. Cracks were thin (typically one voxel wide) reflecting the intended behaviour of the *CL* algorithm. However, it can be seen that the crack paths were very straight, tending to follow the mesh lines rather than deviating towards neighbouring stress concentrations. Cracks therefore appear unaffected by the stress raising effect of nearby lacuna, canals or cracks. An example of this

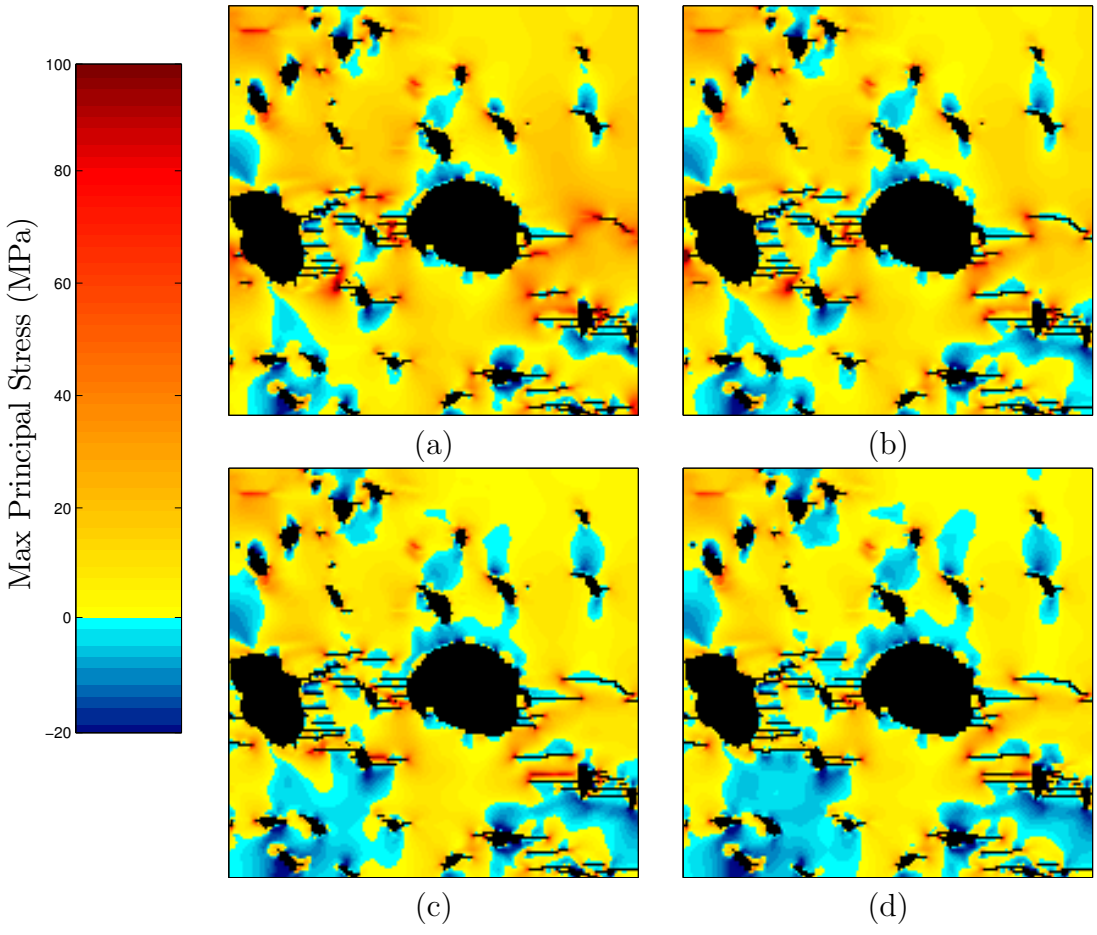

Figure 4-18: Crack propagation with the *CL* algorithm and constant applied displacements within a C3H sample. Crack propagation (a) to (d). Numerous narrow, straight cracks formed. Note, crack propagation direction was unaffected by the stress raising effect of nearby canals or lacuna.

can be seen between two cracks to the right of the central canal in Fig. 4-18; a stress concentration existed between the cracks in (a) and (b) but propagation remained straight in (c) and (d).

Crack propagation with the *CL* algorithm under solution-dependent increasing applied displacements can be seen in Fig. 4-19. Unlike with constant applied displacements, here few cracks developed. Since applied displacements only increased if crack propagation fell below a tolerance this method only produced cracking at the most vulnerable site(s). In the example shown this location was at the bottom right of the left canal. As noted in the case of constant applied

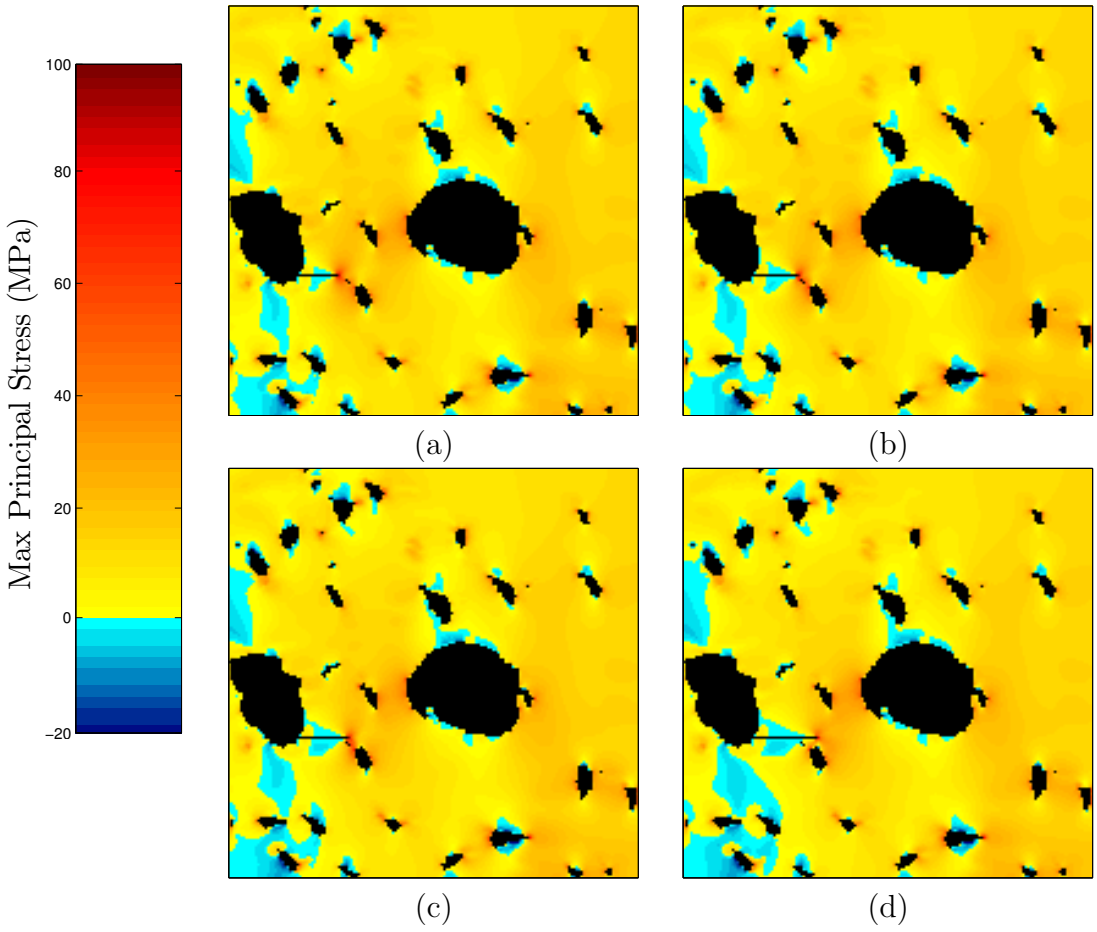

Figure 4-19: Crack propagation with the *CL* algorithm and solution dependent applied displacements within a C3H sample. Crack propagation (a) to (d). A single crack developed since the applied displacements did not increase while propagation occurred anywhere in the sample.

displacements, the *CL* algorithm produced straight cracks which tended to follow the mesh lines. This was also the case with solution dependent applied displacements. It can be seen in Fig. 4-19(a–c) that considerable stress concentration was present between the crack tip and the nearby lacuna. In reality this region would be expected to crack. However, as can be seen in (d) the crack passed the lacuna without deviation from the straight path.

Figure 4-20 illustrates crack propagation in B6 and C3H samples with the *CL* algorithm. The renderings reveal the 3D nature of the cracks. Only the largest features have been rendered to prevent the many lacuna obscuring the view of the cracks. It can be seen that cracks initiated at the edges of the largest features present which were generally canals. The cracks then propagated orthogonally to the maximum tensile applied displacement, to fill the ROI. They therefore appeared square at full size. The slice images were orientated such that the maximum tensile applied displacement direction faced up and down. In these images it can be seen that the cracks formed in straight paths. The crack in (c) appeared to follow the location of two lacuna to the left of the canal. However, in examples (a), (b), (d) and (f) cracks passed very near lacuna without diverting towards them. A shielding effect can be seen in (a) and (e), where the presence of a crack (a) or canal (e) lowered the stress intensity above and below it. In the case of (a) this prevented the crack from the left from propagating across the full ROI, and in (e) crack propagation was stopped above the lower canal until the applied displacements were increased sufficiently to drive further propagation (highlighted in red).

The effect of canal microarchitecture on the strain factor required to achieve propagation (propagation strain factor) was investigated. Canal microarchitectural indices were used to quantify these relationships. From linear elastic fracture mechanics it is known that resistance to fracture is determined by the size of a critical flaw. Canal indices which represented a measure of the canal size were chosen for regression analysis with the propagation strain factor. These indices were the ratio of canal volume to tissue volume (Ca.V/TV), and the mean canal diameter (Ca.Dm). Indices were assessed using the CT Analyser 1.7.0.5 software package (Skyscan, Aartselaar, Belgium).

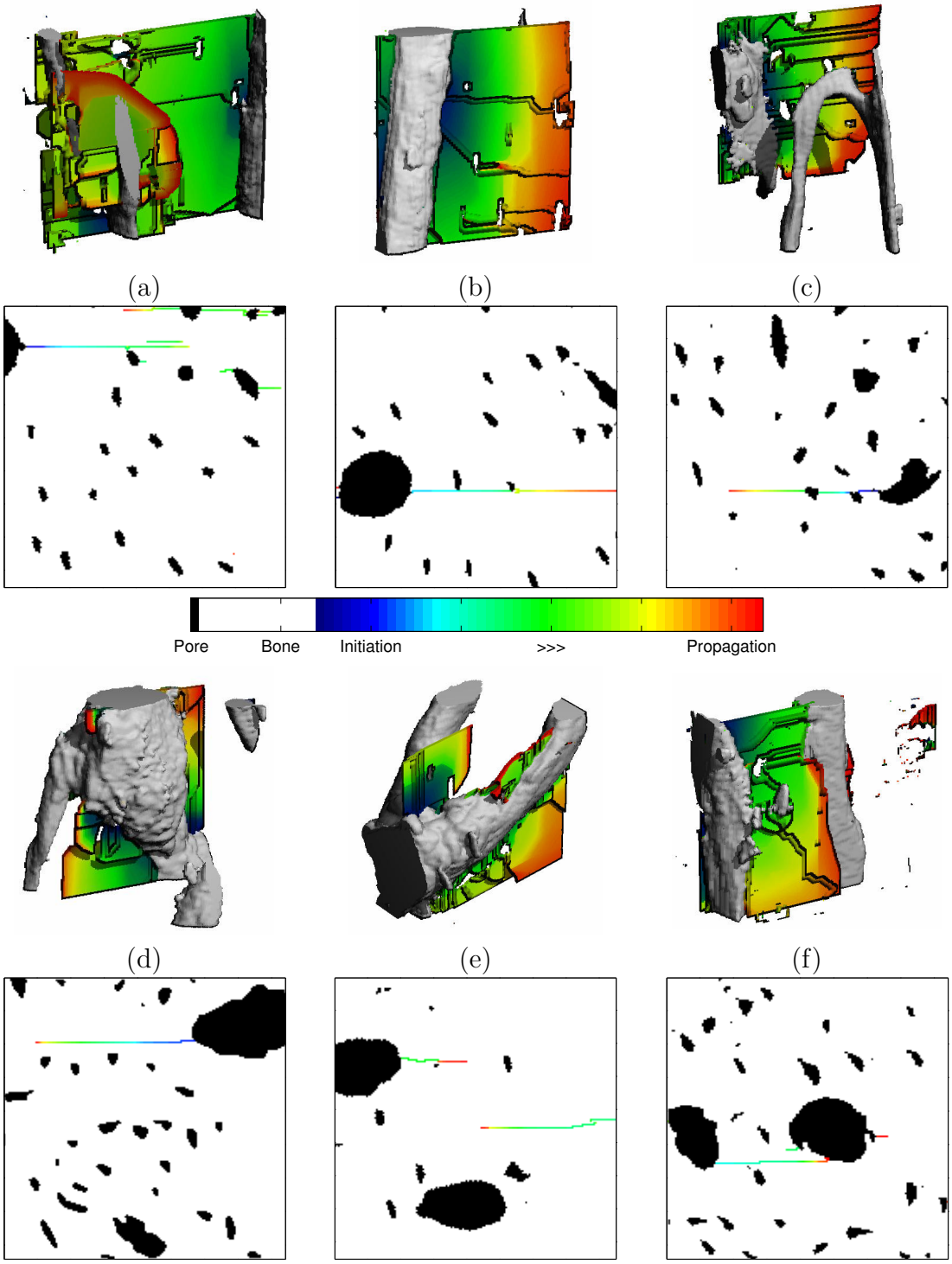

Figure 4-20: Crack progression in B6 (a-c) and C3H (d-f) samples with the *CL* algorithm. The upper row contains renderings of the largest pre-existing pores (canals and attached lacuna) with colour coded voxels representing the crack progression. The lower row contains transverse slices corresponding to the samples in the upper row. Slices were selected which contained features of interest.

With the *CL* algorithm, the mean propagation strain factor in B6 and C3H samples was 47.8 %(±6.5 %) and 39.0 %(±4.7 %) respectively. The propagation strain factor was more than one standard deviation higher for B6 samples than C3H samples, which indicated that under *CL* cracking the B6 samples had a higher resistance to cracking than C3H samples. As noted previously, the ultrastructure of B6 mice typically contains fewer and smaller canals than C3H mice. The variation of propagation strain factor with indices of canal architecture (canal volume to tissue ratio, Ca.V/TV and mean canal diameter, Ca.Dm) are shown in Fig. 4-21. Larger Ca.V/TV and Ca.Dm were associated with lower crack propagation strain factors.

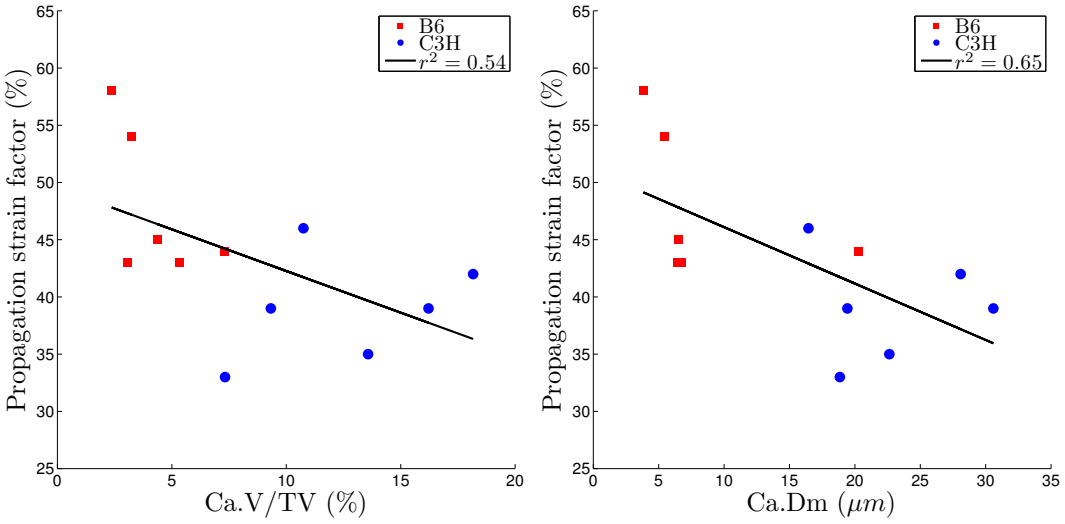

(a) (b)

Figure 4-21: The variation of crack propagation strain factor with Ca.V/TV and Ca.Dm under *CL* cracking.

4.3.4 σG algorithm results

Crack propagation using the σG algorithm is illustrated in Fig. 4-22. The direction of crack propagation was influenced by the presence of stress raisers such as lacuna or canals near the crack tip. In (a) and (b) stress concentrations can be seen between the left canal and a neighbouring lacuna. In (c) and (d) the crack propagated in the direction of this stress concentration. The resulting cracks were not excessively wide as was noted with the σ_{lim} algorithm. Cracks also appeared unrestrained by the mesh lines as was the case with the *CL* algorithm.

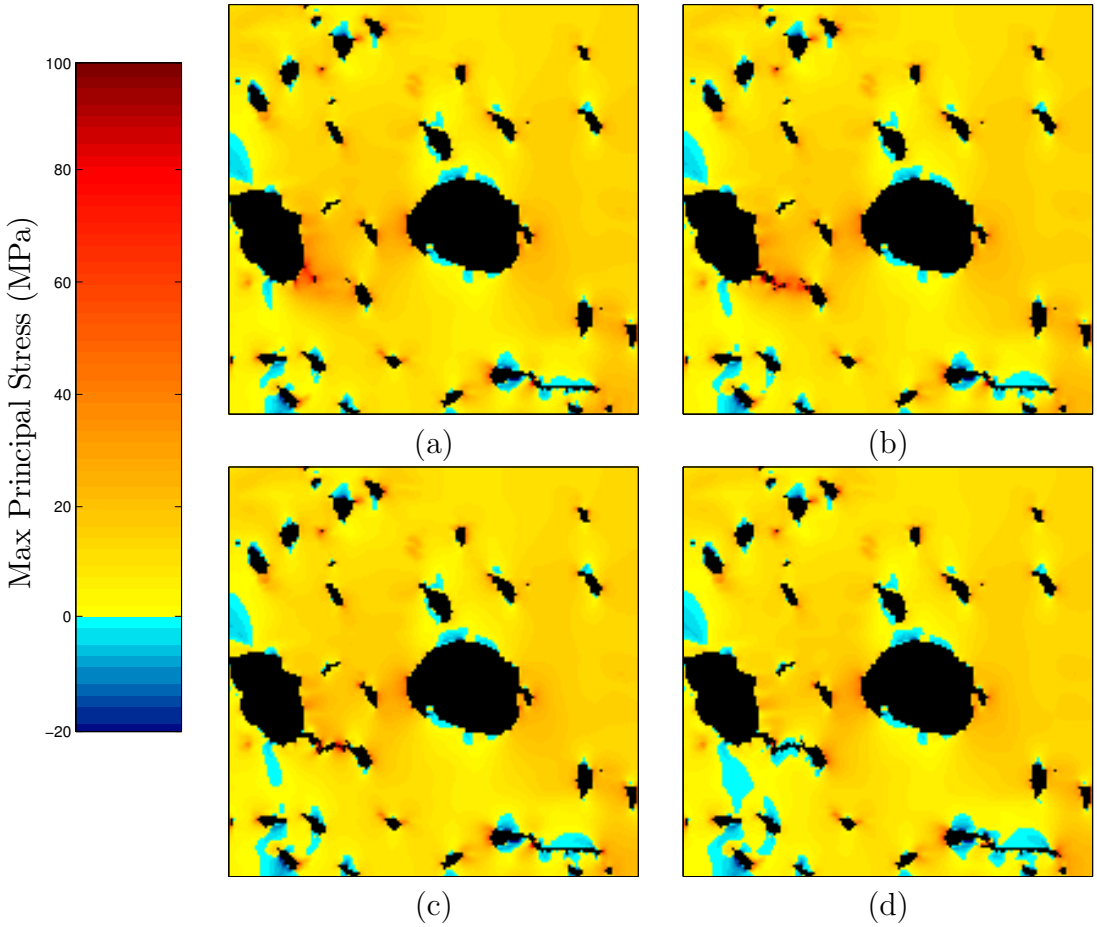

Figure 4-22: Crack propagation with the σG algorithm and solution dependent applied displacements within a C3H sample. Crack propagation (a) to (d). Note the diversion of the crack propagating from the canal on the left to the small pore before proceeding towards the lacuna below and to the right; the crack path is directly influenced by the stress raising effect of the nearby features.

Figure 4-23 illustrates crack propagation with the σG algorithm. The cracks followed lacuna as they propagated. This is not clear in the 3D renderings, but can be seen in the slice images. The 3D location and orientation of cracks can be seen in the renderings. Crack propagation was relatively brittle; the majority of crack formation occurred suddenly, at a single applied strain factor. Cracks typically initiated at the edges of canals; the largest features in the ROI. The general direction of crack propagation was orthogonal to the maximum applied tensile displacement. Cracking was diverted toward features such as lacuna or canals which lay near to this general crack direction. Examples of this behaviour can be seen in Fig. 4-23(a,c,d). In other cases, such as (b), cracks were not di-

verted where neighbouring features were not close enough or large enough to raise stresses sufficiently. Similar to that noted with the *CL* algorithm, shielding can be seen in (e); following initiation the crack rapidly propagated until level with the canal below, at which point propagation ceased until the applied strain factor increased sufficiently for further propagation (red) to occur. Similar behaviour was observed in (f); the crack to the lower right of the image lowered the stress to the right of the middle canal and prevented propagation of the crack on the left.

With the σG algorithm, the mean propagation strain factors in B6 and C3H samples were 40.8 %(±5.7 %) and 36.8 %(±6.7 %) respectively. The propagation strain factor was higher for B6 samples than C3H samples, however the difference was less than one standard deviation. Under the σG cracking algorithm the B6 samples generally displayed a higher resistance to cracking. The effect of canal architecture was investigated by plotting the propagation strain factors against Ca.V/TV and Ca.Dm in Fig. 4-24. A slight trend indicated that increased Ca.V/TV and Ca.Dm was associated with reduced propagation strain factor.

The effect of varying the distance from the crack tip (CRS) on crack propagation was investigated. CRS of 11, 21 and 31 were used with a single sample. The resulting crack geometries are shown in Fig. 4-25. With the smallest CRS (a), cracks appeared less able to divert towards neighbouring features than with larger CRS. In (a) a separate crack propagated from a lacuna, but did not connect with other cracks or features. With CRS = 21 (as used in all other analyses), a crack connected through the same lacuna, to the two neighbouring canals (see (b)). With the largest CRS, cracks appeared to be attracted to features both nearby and further away. For example, in (c) the crack initiated at the left canal and initially propagated towards the nearby lacuna. However, once the crack tip moved nearer to this lacuna, another lacuna fell within the CRS, towards which the crack diverted. A value of CRS = 21 was found to produce approximately realistic crack paths by visual inspection. CRS also appeared to influence crack location. The smallest CRS was associated with a large crack at the bottom right of slice image (a). With the middle CRS value, this crack was reduced in size, and with the largest CRS this crack was replaced with one which propagated from the central canal.

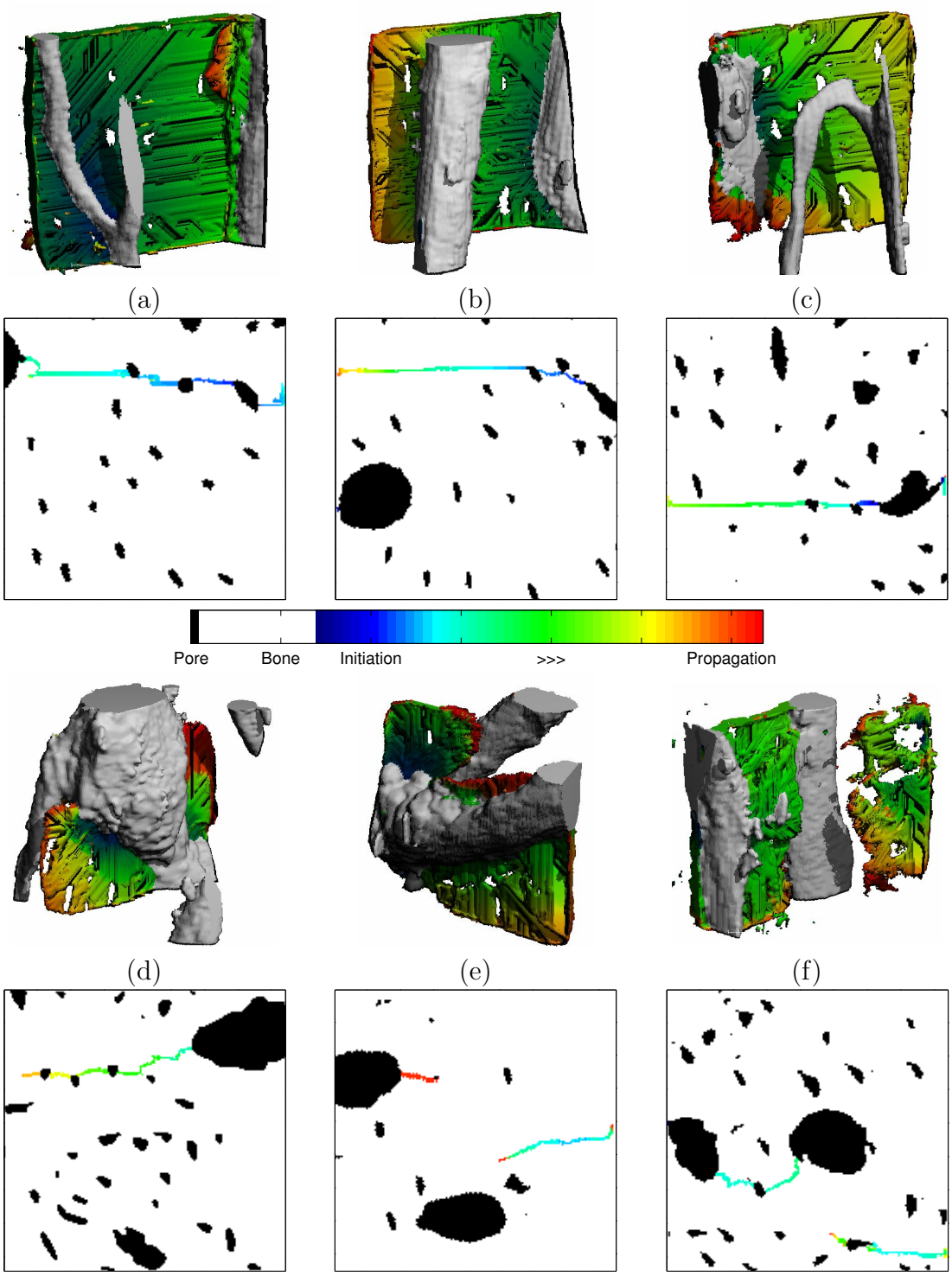

Figure 4-23: Crack progression in B6 (a-c) and C3H (d-f) samples with the σG algorithm. The upper row contains renderings of the largest pre-existing pores with colour coded voxels representing the crack progression. The lower row contains transverse slices corresponding to the samples in the upper row. Slices were selected which contained features of interest.

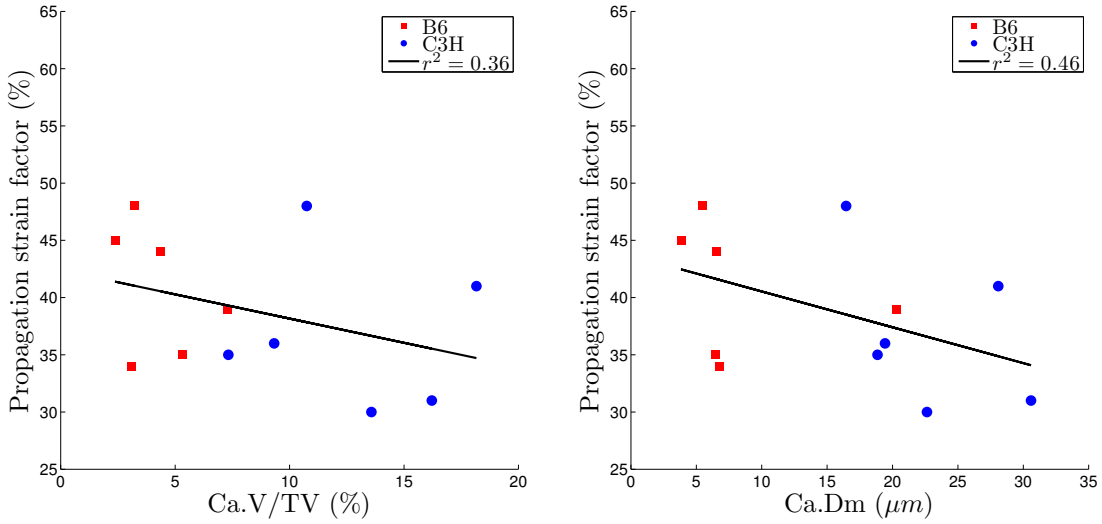

Figure 4-24: The variation of crack propagation strain factor with Ca.V/TV and Ca.Dm under σG cracking.

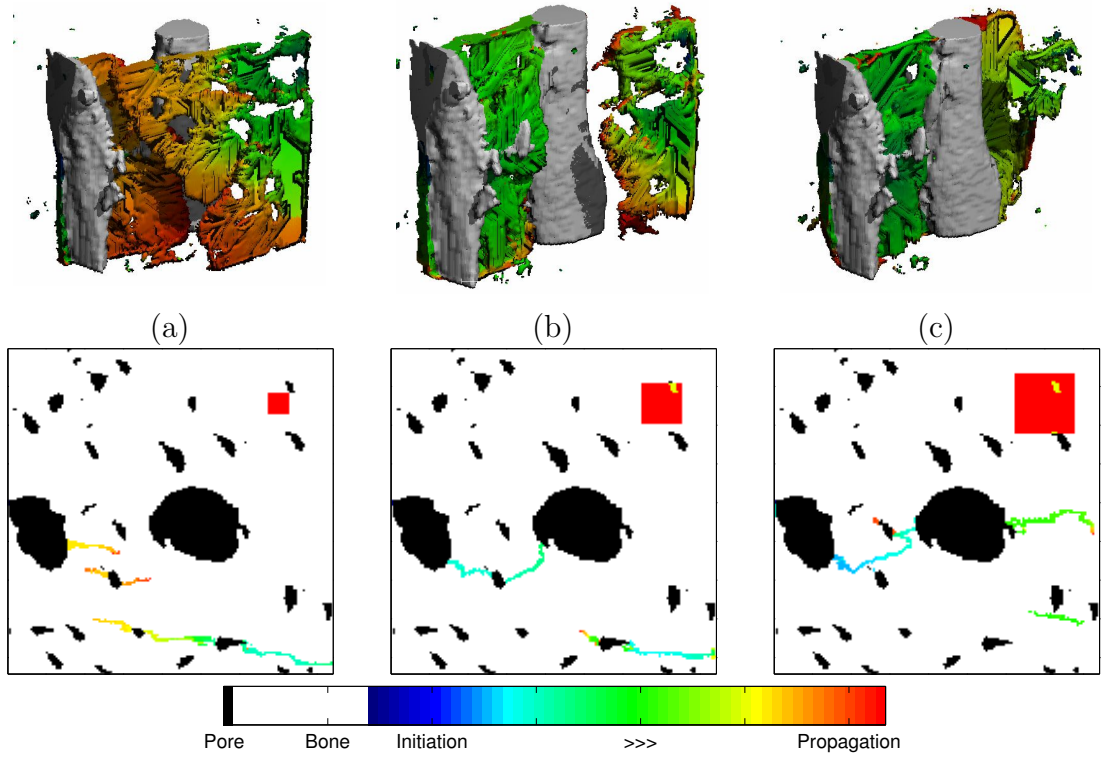

Figure 4-25: The effect of CRS within the σG algorithm. The red squares in the lower row represent the CRS values used. These were 11, 21 and 31 voxels respectively. A CRS of 21 was used in all other analyses.

4.4 Discussion

4.4.1 Notched samples

The aim of the present study was to develop a simplified numerical method for identifying the role of ultrastructure to act as stress raisers to initiate and guide cracking. Several preliminary algorithms were developed which enabled the simulation of cracking through high resolution μFE meshes of murine bone. The methods developed here have the potential to improve our understanding of the interaction of ultrastructural features with crack initiation and propagation but require considerable further development to provide predictive results. As an initial step it was necessary to identify realistic boundary conditions for the microcracking simulations. FE simulations of the notched models were conducted to quantify the local state of stress/strain induced by the DIGFA experiment.

The results of the present study confirmed the stress and strain raising effect of the notches. The variation of stresses and strains with longitudinal position in the notched samples (see Fig. 4-14) showed considerably greater tensile stress and strain in the circumferential direction at notched locations than unnotched locations. This result suggests that the cracking mechanism in the DIGFA experiments was driven by tensile components of stress and strain in the circumferential direction (and to a lesser extent in the radial direction). These tensile components were indirectly induced by the action of the applied compressive longitudinal displacements on the surface geometry of the notched sample cortices.

It was required to identify critical locations and values of tensile components of stress within the notch models which would act to drive cracking. The maximum principal stress and strain values (which represent the most tensile component in any orientation) were greatest near the endosteum, directly opposite the notch for both B6 and C3H samples (see Fig. 4-13). Tensile stress concentrations were also observed at locations near the periosteum of B6 models. Experiments on the same samples (Voide et al., 2009), revealed that crack initiation could occur at the bone surfaces for B6 and C3H samples but the latter also showed initiation at canals. The larger canal size of C3H samples can be expected to raise the potential for crack initiation at canals. Additionally, the present results indicated that the cortical surface geometry of B6 samples exposed them to tensile conditions

on both surfaces of the cortex, which raised the likelihood of crack initiation at a cortical surface.

Since the largest tensile components of stress were located near the endosteal surface of both B6 and C3H samples this location was chosen for evaluating the boundary conditions to apply to the subsequent microcracking simulations. Longitudinal, circumferential and radial boundary conditions were evaluated at the location on the periosteal-endosteal line at which the maximum circumferential stress and strain occurred (see Fig. 4-15). As noted, this location was slightly inside the endosteal surface. The triaxial stresses and strains at this location were similar for B6 and C3H samples (see Fig. 4-16). This indicated that the DIGFA experimental setup was robust in producing similar local loading conditions for both breeds of mice. Furthermore, the similarity of local strains in particular indicated that identical boundary conditions could be applied to both B6 and C3H microcracking analyses.

In the current setup, compressive longitudinal loading was used to induce transverse tensile stresses and strains indirectly, and thus cracking in the murine femora. The present DIGFA experimental design therefore promoted the formation of longitudinal cracks. However, it has been noted (Koester et al., 2008) that transverse cracks are the more physiologically relevant for the breaking (rather than splitting) of bones. The results of the present notch model analyses demonstrate that considerable variation of the tensile components can occur both within and between samples under identical compressive loading conditions. Such variations make evaluation of the local tensile loading responsible for cracking more difficult. Consequently, evaluation of sample crack resistance in terms of fracture mechanics would be a challenge with this experimental setup. The use of loading which applies directly quantifiable tensile conditions (e.g. three point bending or compact tension tests) would avoid such issues. Such an approach would also simplify the identification boundary conditions for any subsequent microcracking analyses.

Several limitations of the notch model analyses should be noted. The tissue-level properties were assumed to be isotropic but bone is known to be approximately orthotropic (Cowin and Mehrabadi, 1989). This simplification could have

adjusted the observed stress and strain distribution in the analyses. Recognising that a significant portion of the strain in the transverse directions was induced by the Poisson effect, it becomes apparent that variation of the orthotropic Poisson's ratios could alter the transverse strains. This limitation was necessitated by the FE package employed in the analyses which only permitted isotropic properties. The effects of tissue anisotropy can be expected to be lesser than the presence of the notch and variations of cortex surface geometry. As such, the present results provide a reasonable approximation of the real notched sample mechanics.

C3H mice have been shown to posses 1.5 times more mineralized bones than B6 (Beamer et al., 1996). Mineralization has been identified as a predictor of bone elastic stiffness (Currey, 1988) which implies that C3H sample have a higher tissue Young's modulus than B6 mice. This effect was not included in the present study. Specification of a higher tissue modulus for C3H models would not affect the strain distribution in the current displacement controlled, materially isotropic analyses. However, it would induce higher stresses in C3H models. In the present results the average peak tensile stress observed in C3H models was 24 % lower than the B6 models. A larger tissue modulus for C3H models would therefore be expected to reduce the inter-species differences in cracking stress.

The homogeneity of tissue properties was also a limitation of these models since bone is a heterogeneous material. Sources of heterogeneity include the variation of mineralization, presence of cement lines and ultrastructural features such as canals and lacuna pores. The greatest variation of mineralization has been identified between osteonal and interstitial bone. Osteons are also the most common location for cement lines. The present study considered murine bone which does not form osteonal structures, so the effects of these features could be neglected. The inclusion of ultrastructral features was prevented by the scanning resolution, at which, only the largest canals were visible. The omission of these features will have affected the observed local elastic response. However, the presence of notches and cortex surface geometry can be expected to dominate the behaviour at the macroscale. Furthermore, the boundary conditions taken from these analyses were applied to the higher resolution microcracking models which did contain the ultrastructure; the heterogeneity of the tissue was therefore included at the appropriate scale.

The final limitation of the notch model analyses was the use of samples with a longitudinal dimension of 2.04 mm which was less than the 4.00 mm of bone which was exposed during the DIGFA experiments. Since the applied strain would vary longitudinally as a function of the local cross-sectional area it was apparent that the omission of the bone between the 4.00 mm and 2.04 mm regions will have influenced the local strain in the models. However, since the surrounding bone was fully fixed in stiff PMMA it was not expected that substantial deformations occurred away from the notched region. Furthermore, the removal of notched tissue will have reduced the local stiffness relative to the intact cross-section such that the majority of the applied displacement can be expected to have occurred in the notched area. This limitation potentially altered the magnitude, but not the pattern of the stress and strain field in the notched models. The local results can therefore be considered a linearly scaled version of those present under experimental conditions.

4.4.2 Microcracking

Three cracking algorithms were developed in the present study. These algorithms were developed sequentially; the limitations of the σ_{lim} and CL algorithms informed the design of the σG algorithm.

It was observed that the σ_{lim} algorithm produced unrealistically wide cracks. This behaviour was dependent upon the magnitude of the applied displacements, which were constant for all analyses with the σ_{lim} algorithm. If large applied displacements were used then wide cracks formed. Conversely, if small displacements were applied then cracking frequently did not occur at all, or followed mesh lines in unrealistically straight cracks. In practice it was difficult to produce realistically narrow cracks with the σ_{lim} algorithm since crack initiation occurred at multiple locations, some of which became wide and others thin, depending on the local stress environment. Also, specification of large displacements was often necessary to produce cracks which deviated from the mesh lines. Selection of appropriate applied displacement magnitudes (and the resulting cracks) therefore became very user dependent, and required a trial and error approach. Moreover, sample differences resulted in variations of the most appropriate applied displacements and therefore required independent evaluation.

Initial (constant applied displacements) use of the *CL* algorithm also resulted in difficulties when selecting the applied displacement magnitudes. It was observed that with large applied displacements many cracks would initiate. Conversely, if smaller displacements were applied then cracking would either not occur, or occur in very few locations. Such behaviour therefore necessitated a trial and error approach, similar to that discussed for the σ_{lim} algorithm. The use of solution-dependent increasing applied displacements was used in subsequent analyses to avoid the user dependency of the number of cracks which initiated.

In both the constant, and the solution-dependent, applied displacement implementations of the *CL* algorithm the generated cracks were observed to be very straight. Crack straightness resulted from the *CL* algorithm which only deleted a single voxel from each connected group with $\sigma_1^v >$ Tol.1. Since the voxel deleted was identified as that with the largest σ_1 in each group, this meant that the voxel immediately in front of a crack was most likely to be deleted because it contained the combined effect of two singularities at the corners of the crack tip. Mesh dependency therefore determined the resultant crack paths with the *CL* algorithm.

The σG algorithm was designed to avoid the mesh dependency of the *CL* algorithm. The σG algorithm successfully enabled cracking to follow local stress gradients without apparent constraint from the defined mesh. This behaviour resulted in the deviation of crack paths from the straight lines of the mesh (see Fig. 4-22 and 4-23).

The avoidance of mesh dependency enabled the role of the ultrastructure in cracking to be investigated using the σG algorithm. The local stress raising effect of canals and lacuna influenced both the initiation and propagation of cracks when the σG algorithm was used. Crack initiation was generally observed at canal surfaces. This observation is in agreement with the cracking behaviour witnessed during experimental testing of other murine samples (Voide et al., 2009). Furthermore, the ability of lacuna and canals to guide the direction of crack propagation was observed both experimentally and in the present study. Since the σG algorithm evaluates the crack direction solely upon the local stress gradient it can be concluded that the crack guiding effect of these features arose from their stress raising effect.

Inhibition of crack propagation was observed with both the CL and σG by a shielding effect. Both neighbouring cracks (Fig. 4-20(a) and 4-23(f)) and canals (Fig. 4-20(e) and 4-23(e)) were observed to inhibit crack propagation. Shielding of crack tips from part of the crack driving force by the presence of surrounding microcracks has previously been noted as a key toughening mechanism in bone (Zioupos and Currey, 1994; Zioupos et al., 1996; Vashishth et al., 1997; 2003; Vashishth, 2004; Nalla et al., 2004b; Peterlik et al., 2006). The present results also indicated that pre-existing canals (and to a lesser extent lacuna) can act to toughen bone when they lie in the vicinity of a propagating crack.

Using both the CL and σG algorithms the propagation strain factor in B6 samples was considerably higher than in C3H samples. These results indicate that, at a local level, C3H bone tissue has a lower crack resistance than B6 bone tissue. Only ultrastructural morphology differed between the two breeds of mice in the present study. Regression of canal microarchitectural indices with the applied strain required for crack propagation was conducted to quantify the role of ultrastructure. It was observed that greater Ca.V/TV and Ca.Dm were associated with lower propagation strain factors. Ca.Dm provided greater predictive power than Ca.V/TV with both the CL and σG algorithms. Ca.Dm was able to explain 65 % of the variation of propagation strain factor with the CL algorithm and 46 % with the σG algorithm. In both cases a substantial degree of the variation could not be explained by the microarchitectural indices, indicating that other mechanisms influenced the propagation strain factor considerably. Such mechanisms may include path dependent behaviour such as the shielding effect discussed previously. Under experimental conditions crack initiation was observed at lower applied strains in B6 than C3H samples (Levchuk et al., 2010). However, the rate of crack propagation in C3H samples was approximately double that observed in B6 samples (Levchuk et al., 2010). The results of the current study indicate similar behaviour to the experiments since the propagation strain factors indicate faster propagation in the C3H samples than the B6 samples.

The results of this preliminary study demonstrated that it is possible to simulate microcracks at a physiologically relevant scale using an image based meshing technique. Of the algorithms developed, the σG algorithm represents the best candidate for the simulation of crack propagation. However, considerable limitations remain that must be resolved for further development of this technique.

It was not possible to include the cortical surfaces in the present analyses; in most cases the cortical surfaces were outside of the field of view of the SRCT device. Since crack initiation was frequently observed at the cortical surfaces in experiments (Voide et al., 2009), this limited the ability of the simulations to capture the true crack initiation behaviour. Consequently, cracks were generally observed to initiate at canals in the present study. Furthermore, the removal of surrounding tissue can be expected to act similarly to a pre-crack which extended from the boundaries of the ROI outwards to the cortical surfaces. This would be expected to lower the crack resistance of the samples. Future cracking simulation should include the cortical surfaces to avoid this limitation.

As noted previously, C3H mice have been shown to have 1.5 times more mineralized bone tissue than B6 mice (Beamer et al., 1996). This would be expected to increase the elastic modulus and strength of C3H relative to B6 bone tissue (Currey, 1988; 2004). A higher tissue modulus in C3H samples would result in greater stress and therefore earlier crack initiation and faster propagation. However, since the strength would also be expected to increase it would be reasonable to increase the critical stress for cracking in these samples which would act to reverse these changes. In the present study the elastic properties of B6 and C3H samples were assumed to be identical to enable a direct comparison of the effect of their ultrastructure in isolation from other effects. It would also be difficult to identify a realistic balance between increased elastic modulus and increased strength at the scale of the crack tip. In future analysis it seems advisable to evaluate the tissue mechanical properties for each breed separately to minimise this limitation.

Mesh dependency was found to dominate the crack path with the *CL* algorithm, and, to a considerably lesser extent, can also be expected to have influenced the results of the σG algorithm. The use of a 'stress concentration limiter' (SCL), similar to Stolk et al. (2003), could avoid some of the observed mesh dependency. This approach is attractive since it could be implemented alongside the FE solver used here, retaining the computational advantages of fully parallel analysis afforded by ParFE. The SCL method of Stolk et al. (2003) minimises the effect of stress singularities by spatially averaging the stress values within a radius of a central element. The averaging process weights the stress values from neigh-

bouring elements as a function of their proximity to the central element. Such an approach would be expected to remove the mesh dependency of the *CL* algorithm. The σG algorithm effectively employs a similar methodology by selecting the deleted voxel as a function of the stress values of surrounding elements. The σG algorithm could be improved by weighting the stress contributions, and using a circular or spherical sampling region, similar to the SCL of Stolk et al. (2003). When the value of CRS was large, it was observed that the crack path could deflect away from nearby stress concentrations towards those further away. The use of a weighting function would be expected to resolve this issue by promoting the attraction of cracks towards nearby stress concentrations over those further away.

The behaviour of the algorithms developed in the present study was dependent upon the chosen values of their various parameters. All algorithms were dependent upon the maximum principal stress value selected for voxel deletion. The *CL* algorithm was dependent upon the number of voxels which could be deleted from each connected set of voxels over the deletion stress ($\sigma_1 >$ Tol.1). The σG algorithm was dependent upon the value of CRS. Further development would require an evaluation of the appropriate values of the algorithmic parameters for bone. The influence of these parameters is difficult to separate from the effect of ultrastructure in the murine samples studied. Calibration of these parameters should therefore be conducted with non-porous samples. Furthermore, the use of a standard fracture test set-up such as three-point bending or the compact tension test would enable calculation of algorithmic K_{IC} values and thus direct comparison with experimentally determined measures of bone toughness.

The applied strain required for crack propagation was considerably lower in the present study than was observed with experiments on the same samples. For example, the mean apparent-level strain for crack propagation of B6 and C3H models was 0.41 % and 0.36 % respectively; the equivalent experimentally determined values were 1.81 % and 3.6 %. The simulation and experimentally determined values differed by as much as a one order of magnitude. The maximum principal stress value for voxel deletion was the primary determinant of the applied strain at which crack initiation and propagation occurred. The present results indicated that the value used was too low. Indeed, the value of 100 MPa used was specified as the apparent-level yield stress of bone based on a tissue

modulus of 20 GPa and a yield strain of 0.5 % in tension. Since apparent level strength is inherently reduced by smaller scale flaws (such as the ultrastructural pores) it seems reasonable to presume that the tissue-level strength is considerably higher than this. If the tissue-level strength was four times higher than as modelled (i.e. 400 MPa) then the applied cracking strain predicted from B6 microcracking models would be of a similar magnitude to those found experimentally. Furthermore, since C3H mouse bones are known to be more mineralized than B6 (Beamer et al., 1996), it is likely that C3H bone could posses a higher tissue-level strength (Currey, 1988; 2004) than B6 which would account for the higher experimental cracking strain of this breed. Since the FE analyses used here were linear elastic it would be possible to scale the deletion stress linearly to produce the most realistic response. The previously discussed absence of cortical surfaces in the present study may also have contributed to the low propagation strains observed. Redistribution of stress to the surrounding tissue following cracking would reduce the remaining crack driving force. However, since the surrounding tissue was removed, the samples were exposed to larger crack driving forces than would necessarily have occurred if modelled with the cortical surfaces.

Bone has been demonstrated to have increasing crack resistance (rising R-curve) with crack propagation (Koester et al., 2008). As discussed previously, this results from the various toughening mechanisms observed in bone. The algorithms developed in the present study produced brittle cracking behaviour; the majority of crack propagation occurred at a single applied strain level. The cause of this brittleness was the absence of several toughening mechanisms resulting from the homogenisation of the bone hierarchical structure. Since mineralized fibrils, lamina and cement lines were not modelled it was not possible for crack bridging or deflection to occur at their interfaces as occurs in bone. Furthermore, the discussed sacrificial bonds in collagen molecules were not present. To produce rising R-curve behaviour a modelling strategy which incorporates these energy dissipating mechanisms would be required. The specification of a 'work of separation' together with a critical tensile stress to determine cracking would enable these energy dissipative effects to be incorporated. This would operate similarly to the constitutive relations employed in cohesive surface methods (Needleman, 1987; Ural and Vashishth, 2007; Tomar, 2008; Ural, 2009). To account for the rising R-curve behaviour the work of separation term could be a rising function of

the crack length. Such an approach would, however, remain homogenised; crack deflection and bridging not only act to toughen bone but also directly influence the crack path. To capture such effects geometrically it would be necessary to represent fibrils, lamina or cement lines directly in the models, for example by introducing layers of elements with differing values of elastic modulus. The realisation of such an approach would be impeded by the difficulty in identifying where such layers should be placed since they cannot be identified in the present bone images.

Chapter 5

A strain-based yield criterion for bone

5.1 Introduction

In the great majority of FE studies involving bone tissue its mechanical properties are restricted to the elastic regime (Brown et al., 1988; Suwito et al., 1992; Pistoia et al., 2002; Chen et al., 2003; Watson et al., 2007). This simplification is acceptable if the questions that are to be answered using such models pertain to their elastic response. Indeed elastic models can also indicate locations of stress or strain concentration from which those regions most at risk of failure can be inferred (Huiskes et al., 1985; Chen et al., 2003; Au et al., 2005; Lennon et al., 2007). Applications of such results can also include the identification of mechanical stimulus for bone remodelling or degeneration (Weinans et al., 1992; Hart et al., 1984; Huiskes et al., 2000). In many studies this is all that is required. However, if the loading takes bone beyond its elastic limit (as in Chapters 6 and 7) it becomes necessary to account for its post-elastic behaviour.

5.1.1 Plasticity and damage

Before progressing to consider numerical treatments of bone post-elasticity, the nature of bone yielding and failure should be considered. Bone inelasticity can be divided into three sources (Jepsen et al., 2001) : 1) plasticity resulting from flow at atomic or ionic level material dislocations; 2) damage accumulation associated with the loss of material continuity from cracking or void creation; 3) time dependent effects, which may include viscous forces or change of stiffness

or strength with loading rate. In this study bone response was assumed to be time independent, i.e. it was assumed the bone response to mechanical forces was instantaneous. Time-dependent models of bone are, therefore, not discussed any further. Both plasticity and damage models can be used to define bone behaviour in the continuum sense. Under maximal loading the difference between plasticity (or elasto-plasticity) and damage models can be described using uniaxial stress-strain behaviour as shown in Fig. 5-1.

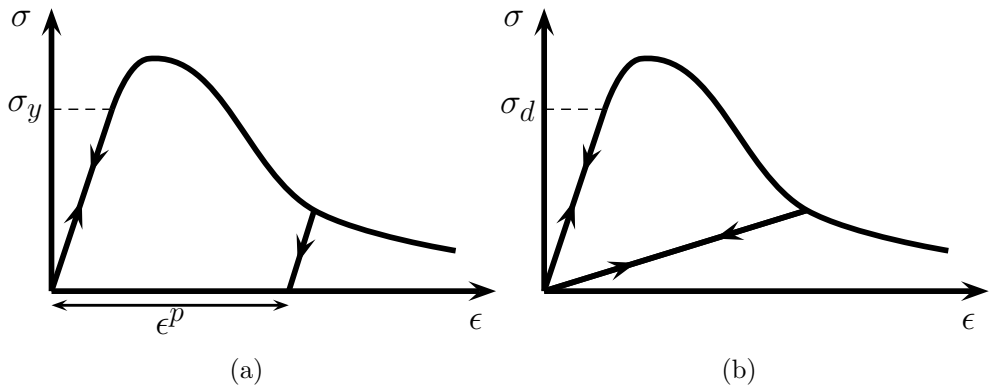

(a) (b)

Figure 5-1: Comparison of stress-strain behaviour with plasticity (a) and damage (b) models. Under plasticity, the irrecoverable plastic strain ϵ^p develops once the material is loaded beyond the yield stress σ_y. In damage models the stiffness of damaged material is reduced once loading proceeds beyond the damage stress σ_d such that all strains are recovered upon removal of loading.

In both models there is an initial elastic regime which can be linear or non-linear. In plasticity, after the yield stress σ_y is reached, further loading causes irrecoverable plastic strains and upon unloading the slope of the stress-strain curve is approximately equal to the slope of the original elastic loading branch (Fig. 5-1(a)). Damage models typically assume that beyond the damage stress σ_d the stiffness degrades such that there are no permanent strains upon unloading (Fig. 5-1(b)). In a monotonic loading cycle it is not possible to distinguish the roles of damage and plasticity which only become apparent upon unloading. Bone response is a combination of the two. Upon unloading from a post-elastic event, bone shows some recovery of the total inelastic strain, but appears to regain the initial elastic modulus (Jepsen et al., 2001). Although it is possible to combine damage and plasticity in simulations, from the modelling perspective it is convenient to use only one of the two theories. In this study the theory of plasticity was adopted. Plasticity has been extensively used for other quasi-brittle

materials (e.g. concrete, rock). Bone's demonstration of irrecoverable strains and regaining of initial modulus indicate plasticity is a better choice. For triaxial stress/strain states plasticity is modelled using the concept of the yield criterion, followed by its evolution. In stress-based plasticity the yield surface expands for hardening materials, contracts for softening and remains unchanged for perfect plasticity.

5.1.2 Yield criteria for bone

Numerous yield criteria have been proposed for bone tissue. Before considering their various details it is worth recalling three mechanical properties of bone: Firstly, bone is an anisotropic material, which can be approximated by orthotropy (Cowin and Mehrabadi, 1989). This is reflected both in its elastic properties and in its strength. Secondly, bone exhibits tension-compression strength asymmetry (Reilly and Burstein, 1975; Keaveny et al., 1994). Thirdly, bone yields at relatively isotropic strains as compared to stresses, and the yield strain is not dependent upon apparent elastic stiffness or density (Vahey et al., 1987; Keaveny et al., 1994; Ford et al., 1996; Bayraktar et al., 2004; Mercer et al., 2006). It seems reasonable to expect that the accuracy of a criterion is related to the degree to which it incorporates these three properties.

The most widely employed yield criterion for bone is von Mises (Lotz et al., 1991a;b; Ford et al., 1996; Voor et al., 1997; Keyak et al., 1998; 2001; Keyak, 2001). This criterion, available in almost all commercial FE codes is typically employed for ductile metals. It is based on the deviatoric stress component and is invariant with hydrostatic stress. It is also isotropic and equivalent in tension and compression which renders it unsuitable for bone which displays considerable anisotropy and yield strength asymmetry.

Keyak and Rossi (2000) conducted an extensive analysis of other criteria over a range of tension-compression strength asymmetry. These included the stress and strain-based Hoffman criterion (Hoffman, 1967), maximum principal stress criterion (Rankine), maximum principal strain criterion (Saint-Venant), maximum shear stress criterion (Tresca), Mohr-Coulomb criterion and modified Mohr

criterion. Their analysis was based on a comparison of a linear FE analyses of a human femur under two loading conditions with identical experiments on real human femurs. The FE models were defined with isotropic, homogeneous elastic properties which represent a significant deviation from the reality. The values of each yield criterion were evaluated for each element using the linear elastic results. These values were scaled up until 15 elements of the bone had exceeded the yield point. The accuracy of each yield criterion was calculated as the degree of correlation of the scaled failure load with that determined experimentally. Several modelling simplifications within the work of Keyak and Rossi (2000) are likely to have affected the calculated yield criteria values. The assumption of elastic isotropy and homogeneity will have influenced the distribution of stress and strain through the model, leading to unpredictable effects upon the 3D stress or strain states from which the criteria were evaluated. The selection of a fracture point as indicated by the load factor at which 15 elements have failed is inherently mesh dependent and could potentially favour one criterion over another. Furthermore, the use of 15 elements is representative of a stage beyond first yield which can only be poorly approximated by the scaled elastic response. In a non-linear treatment, considerable redistribution of stresses will occur in the vicinity of yielded elements. This would have a considerable effect upon the propagation of yielding to other elements, likely to be dependent upon the yield criterion. In spite of these shortcomings, the results of Keyak and Rossi (2000) demonstrate that even with simplified models, various isotropic yield criteria can predict failure with over 80 % accuracy.

Since, as previously noted, bone is anisotropic, the accuracy of all criteria studied by Keyak and Rossi (2000) were limited by their strength isotropy, with the exception of the maximum principal strain criterion, discussed later. Anisotropic yield surfaces, such as the Tsai-Wu (Tsai and Wu, 1971), Kelvin mode (Arramon et al., 2000) and cellular-solid (Fenech and Keaveny, 1999) have been used to overcome this limitation (Fenech and Keaveny, 1999; Pietruszczak et al., 1999; Niebur, 2000). These criteria comprise complex surfaces, requiring numerous input parameters which must all be evaluated with extensive experimental testing. As such, their use requires considerable effort as compared to simpler criteria. To justify their use it is therefore necessary to demonstrate that they afford considerably greater accuracy than the alternatives. Fenech and

Keaveny (1999) compared the validity of the complex Tsai-Wu and cellular-solid anisotropic criterion with the simpler, isotropic maximum principal strain and von Mises criteria. They conducted axial-shear tests on samples of bovine trabecular bone and plotted the experimental data alongside the theoretical yield surfaces. From comparison of the experimental data with the yield surfaces they calculated the accuracy of each yield criterion in compression-shear and tension-shear conditions. The mean error they reported in compression-shear as 7.7 % for the cellular-solid, 19.7 % for the Tsai-Wu, 22.8 % for the maximum principal strain, and 82.4 % for the von Mises criteria respectively. In tension-shear the error was 5.2 %, 14.3 %, 6.9 % and 57.7 % in the same order. While the cellular-solid criterion gave the best agreement with experiment in both cases, it is striking that the relatively simple maximum principal strain criterion performed with equal accuracy to the Tsai-Wu criterion in compression-shear and considerably better than it in tension-shear. It can be inferred that the accuracy of the Tsai-Wu criterion does not justify the additional experimental effort required for determination of its parameters. The low accuracy of the von Mises criterion also confirms that it is inappropriate for modelling bone failure.

5.1.3 Stress vs. strain-based criteria

There has been some debate as to whether stress-based or strain-based criteria are best for representing bone yielding (Doblare et al., 2004). Some studies have indicated that strain-based criteria offer greater accuracy (Keaveny et al., 1994; Ford et al., 1996), whereas the previously discussed results of Keyak and Rossi (2000) indicate that strain-based criteria gave equal or less accuracy than stress-based ones. The discussed limitations of Keyak and Rossi could have affected this conclusion. In particular, their study assumed isotropic elasticity, coupled with isotropic yield behaviour. The reality is that bone properties are well represented by elastic orthotropy (Cowin and Mehrabadi, 1989) and isotropic yield strains (Vahey et al., 1987; Keaveny et al., 1994; Ford et al., 1996). When taken together, these observations necessitate that bone yield strength be orthotropic. Thus, the two available options to include these effects are: elastic orthotropy coupled with either 1) an orthotropic, stress-based yield criterion, or 2) an isotropic, strain-based yield criterion. Theoretically, both strategies can

provide an accurate characterisation of bone elastic and yield properties. The choice of which strategy to adopt is therefore based on which is more readily achievable. An isotropic, strain-based criterion requires relatively few material properties to be evaluated and no a-priori identification of material orientation. Contrastingly, an anisotropic stress-based criterion requires numerous material parameters to be determined and must be oriented with the physical structure of the bone. These issues appear to suggest that a strain-based criterion could be more readily employed in numerical simulation. The advantage of a strain-based criterion can be demonstrated by considering a simple 2D cellular solid as shown in Fig. 5-2a), represented by a homogenised continuum element (Fig. 5-2(b)). The unit dimensions are arbitrarily assigned to ensure stress values equal the load applied. The solid phase of the material is isotropic and follows a Rankine yield criterion as shown in Fig. 5-2(c). If the cellular solid has more vertical columns than horizontal ones then the homgenised continuum element of Fig. 5-2(b) will exhibit different stress-strain slopes when subjected to uniaxial loadings in the 1 and 2 directions (Fig. 5-2(d)), and the yield stress will be different for the two directions. However, the yield strain will be identical, i.e. the stress-based yield criterion is anisotropic (Fig. 5-2(e)), but the strain-based one is isotropic (Fig. 5-2(f)). Furthermore, even under conditions of elastic isotropy a yield surface in strain- and stress-space will not have the same shape (Fig. 5-3). However, the reality is that stress-based criteria are more commonly (if not exclusively) used in FE codes and modellers are much more familiar with these than strain-based criteria. This study sought to partially address this situation through the development of an isotropic strain-based criterion to enable efficient treatment of bone failure in numerical analyses.

5.1.4 Strain-based plasticity

A full treatment of strain-based yield criteria was first provided by Naghdi and Trapp (1975) and developed further by others (Yoder and Iwan, 1981; Youquan, 1986; Mizuno and Hatanaka, 1992; Farahat et al., 1995; Lan et al., 2003). It should be noted that for any static stress-strain state a yield surface formulated in stress-space can be converted into its equivalent in strain-space. However, key differences become apparent as yielding progresses and the stress-strain state

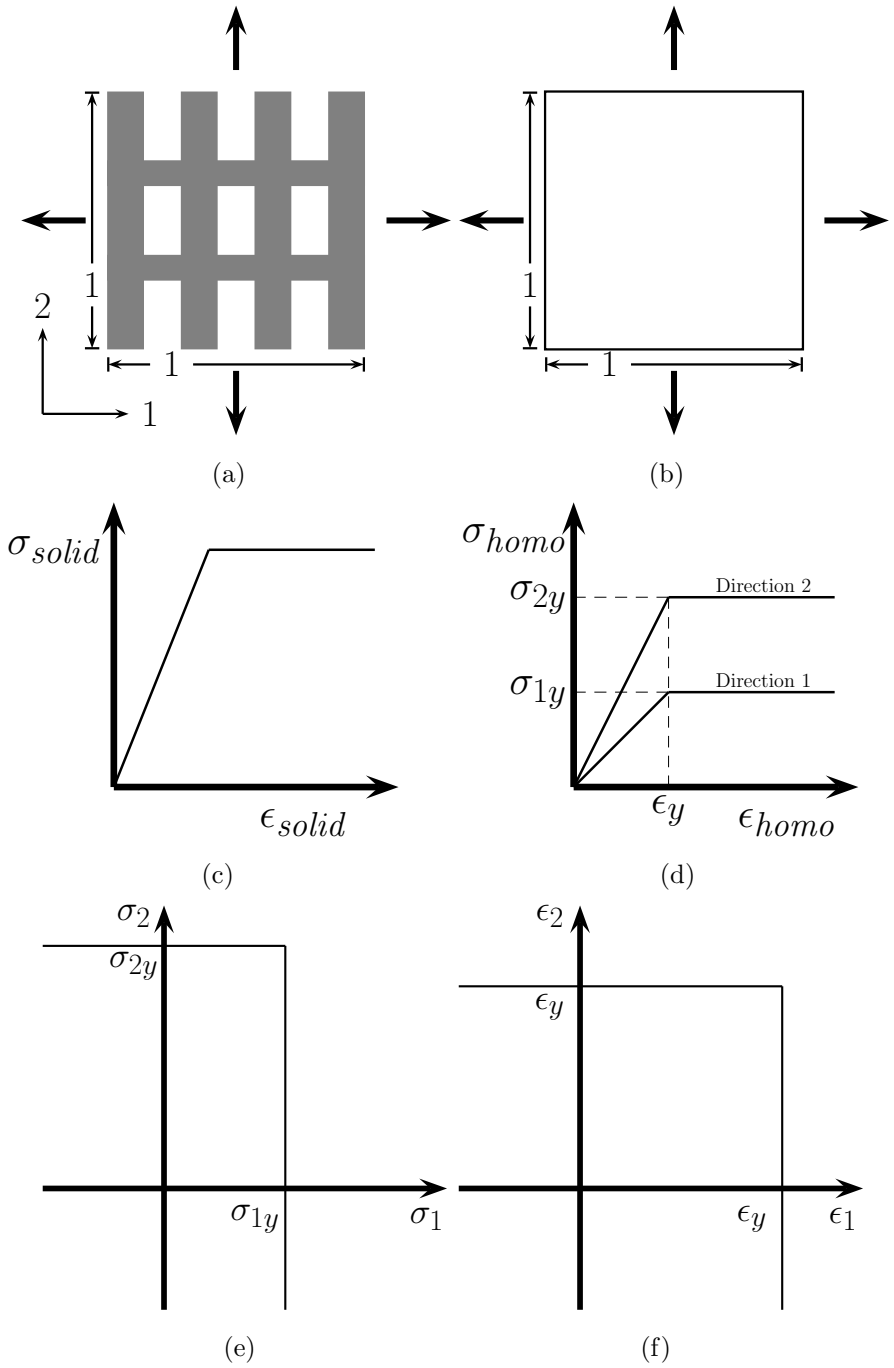

Figure 5-2: Comparison of stress-based and strain-based yield behaviour. The cellular microstructure (a), homogenised representation (b), solid phase constitutive behaviour (c), homogenised constitutive behaviour (d), maximum principal stress yield surface in principal stress-space (e) and maximum principal strain yield surface in principal strain-space (f). Note that the surfaces in (e) and (f) are not equivalent but are used here for illustrative purposes.

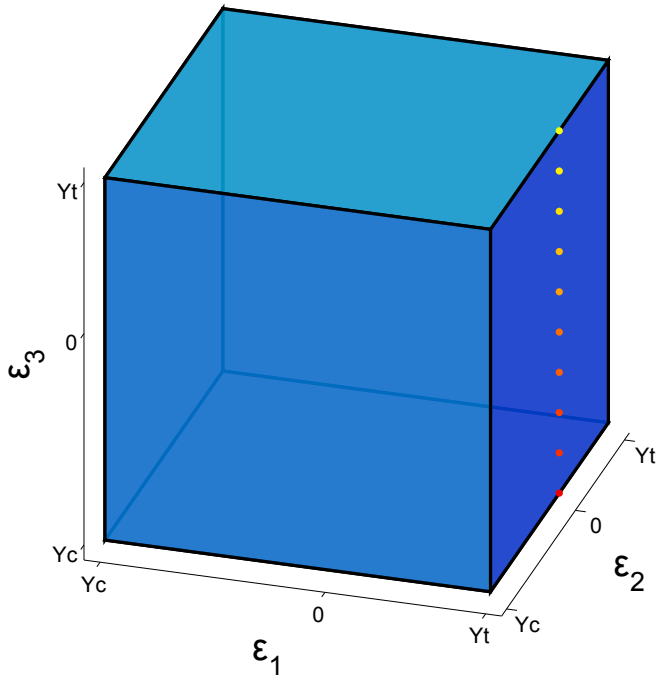

(a)

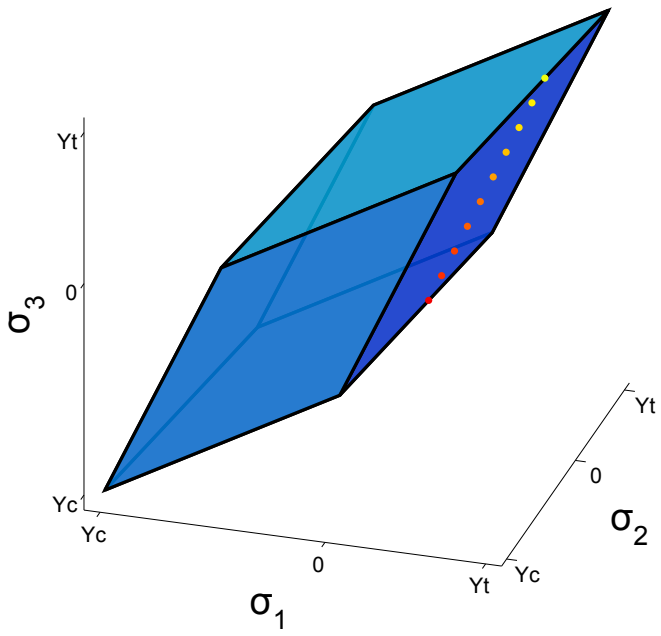

(b)

Figure 5-3: The 3D maximum principal strain criterion (a) and its shape in stress-space (b) under conditions of elastic isotropy. Note the values Y_t and Y_c refer to tensile and compressive yield values of strain and stress respectively. The line of coloured locations indicate equivalent points on the two yield surfaces for $\epsilon_1 = Y_t,\ \epsilon_2 = 0,\ \epsilon_3 = Y_c \rightarrow Y_t$.

adapts (Naghdi and Trapp, 1975; Casey and Naghdi, 1982; 1983). For example, a perfectly plastic material would exhibit a static yield surface in stress-space and an expanding surface in (total) strain-space. These clearly do not remain equivalent with deformation. The major conclusion of the work of Naghdi and Trapp (1975) was that strain-based criteria provide a more robust treatment of post-yield behaviour than stress-based criteria. First identified by Yoder and Iwan (1981), this was illustrated by Lan et al. (2003), who demonstrated that the sign of the derivative of yield surfaces uniquely identifies loading, neutral and unloading conditions in strain-space, but is ambiguous in stress-space (see Table 5.1).

Table 5.1: Comparison of stress-space and strain-space formulations of yield criteria.

		Loading condition				
Formulation	Loading function	Strain hardening	Strain softening	Perfect plasticity	Neutral condition	Unloading condition
Stress-space	$f = 0$	$\frac{\partial f}{\partial \boldsymbol{\sigma}} d\boldsymbol{\sigma} > 0$	$\frac{\partial f}{\partial \boldsymbol{\sigma}} d\boldsymbol{\sigma} < 0$	$\frac{\partial f}{\partial \boldsymbol{\sigma}} d\boldsymbol{\sigma} = 0$	$\frac{\partial f}{\partial \boldsymbol{\sigma}} d\boldsymbol{\sigma} = 0$	$\frac{\partial f}{\partial \boldsymbol{\sigma}} d\boldsymbol{\sigma} < 0$
Strain-space	$g = 0$	$\frac{\partial g}{\partial \boldsymbol{\varepsilon}} d\boldsymbol{\varepsilon} > 0$	$\frac{\partial g}{\partial \boldsymbol{\varepsilon}} d\boldsymbol{\varepsilon} > 0$	$\frac{\partial g}{\partial \boldsymbol{\varepsilon}} d\boldsymbol{\varepsilon} > 0$	$\frac{\partial g}{\partial \boldsymbol{\varepsilon}} d\boldsymbol{\varepsilon} = 0$	$\frac{\partial g}{\partial \boldsymbol{\varepsilon}} d\boldsymbol{\varepsilon} < 0$

5.1.5 Strain-based plasticity in bone

A range of researchers (Vahey et al., 1987; Keaveny et al., 1994; Ford et al., 1996; Fenech and Keaveny, 1999; Oden et al., 1999; Keyak and Rossi, 2000; Bayraktar et al., 2004; Mercer et al., 2006; Gupta et al., 2007; Schileo et al., 2008) have considered strain-based criteria for bone failure. However, of this group only one (Gupta et al., 2007) has formulated a numerical plasticity routine for use in a post-elastic analysis; others (Keyak and Rossi, 2000; Schileo et al., 2008) conducted only elastic analyses and employed functions of the computed strain field to identify regions of failed bone, and Oden et al. (1999) developed a strain-based damage model. Gupta et al. (2007) developed a novel yield criterion for human trabecular bone based upon an isotropic modified super ellipsoid defined in principal strain-space by Bayraktar et al. (2004). They also included both isotropic

and kinematic hardening in the criterion. This yield surface was calibrated to fit experimental data in 3D. Furthermore, the surface was smooth and was therefore free from the issues associated with singularities at sharp corners in piecewise surfaces such as Mohr-Coulomb, Tresca and Rankine criteria.

The modified super ellipsoid yield surface developed by Bayraktar et al. (2004) and Gupta et al. (2007) may be considered the most accurate representation of the yield properties of bone to date. However, regions of high curvature in the yield surface are associated with reduced accuracy and stability (Ortiz 1985). It has been demonstrated by previous researchers (Fenech and Keaveny, 1999; Keyak and Rossi, 2000) that reasonable accuracy can be achieved through the use of a maximum principal strain (Saint Venant) criterion. This yield surface is considerably simpler than the modified super ellipsoid; it can be visualised as a cube in principal strain-space. Indeed, it consists of six planar yield surfaces and requires only two parameters (yield strain in tension and compression) to be defined. Furthermore, it has been shown that accurate returns to such piecewise linear surfaces (in a predictor-corrector algorithm) can be achieved in a single increment (de Borst, 1987; Pankaj and Moin, 1996). This greatly reduces the numerical cost of the overall algorithm, and also improves its stability and accuracy. For these reasons the maximum principal strain (Saint Venant) criterion was selected for this work. While it has previously been used as a limit in studies of bone failure (Oden et al., 1999), it has not previously been developed as a full plasticity algorithm. The remainder of this Chapter details the development and testing of this criterion.

5.2 Methods

The methods described in the following were implemented using programs written by the author in Matlab (The MathWorks, Inc., Natick, MA, U.S.A.) and Fortran.

5.2.1 Definition of the criterion

The failure criterion defined here consists of limiting values of elastic principal strain. The criterion is fully defined by specification of tensile and compressive

yield strains. A strain-based criterion developed previously for bone (Gupta et al., 2007) included both isotropic and kinematic hardening. While hardening rules enable greater flexibility and stability in final usage, it is not clear that bone does exhibit hardening behaviour in the general case. Hardening, particularly kinematic, adds considerable numerical effort to the return mapping process and was avoided in the present implementation in the interests of simplicity and processing speed. The criterion is therefore perfectly plastic, although it is expected that the incorporation of isotropic hardening would be relatively simple. States of stress and strain are represented throughout this study in the Voigt form,

$$\begin{aligned} \underset{\sim}{\sigma} &= [\sigma_x \ \sigma_y \ \sigma_z \ \tau_{xy} \ \tau_{xz} \ \tau_{yz}]^T \\ \underset{\sim}{\epsilon} &= [\epsilon_x \ \epsilon_y \ \epsilon_z \ \gamma_{xy} \ \gamma_{xz} \ \gamma_{yz}]^T = [\epsilon_x \ \epsilon_y \ \epsilon_z \ 2\epsilon_{xy} \ 2\epsilon_{xz} \ 2\epsilon_{yz}]^T \end{aligned} \tag{5.1}$$

The equations of the yield surface (g) are a function of the elastic principal strains

$$g = g(\epsilon_1^e, \epsilon_2^e, \epsilon_3^e) \tag{5.2}$$

The six yield surfaces are of the form

$$\begin{aligned} &g_{1t} = \epsilon_1^e - Y_t \ ; \ g_{2t} = \epsilon_2^e - Y_t \ ; \ g_{3t} = \epsilon_3^e - Y_t \\ &g_{1c} = -\epsilon_1^e + Y_c \ ; \ g_{2c} = -\epsilon_2^e + Y_c \ ; \ g_{3c} = -\epsilon_3^e + Y_c \end{aligned} \tag{5.3}$$

where Y_t and Y_c are the tensile and compressive yield strains, and $\epsilon_1^e, \epsilon_2^e, \epsilon_3^e$ are the principal elastic strains in the order of tensile to compressive components. In principal strain-space this yield criterion can be visualised as a cube with sides $Y_t + |Y_c|$ as illustrated in Fig. 5-4.

5.2.2 Predictor-corrector theory

This Section follows the general arguments of previous studies which used a formulation specific to piecewise linear yield functions Clausen et al. (2006); Huang and Griffiths (2008). For such yield criteria the flow vectors are constant during the corrector phase if it is performed in the principal coordinate system. This

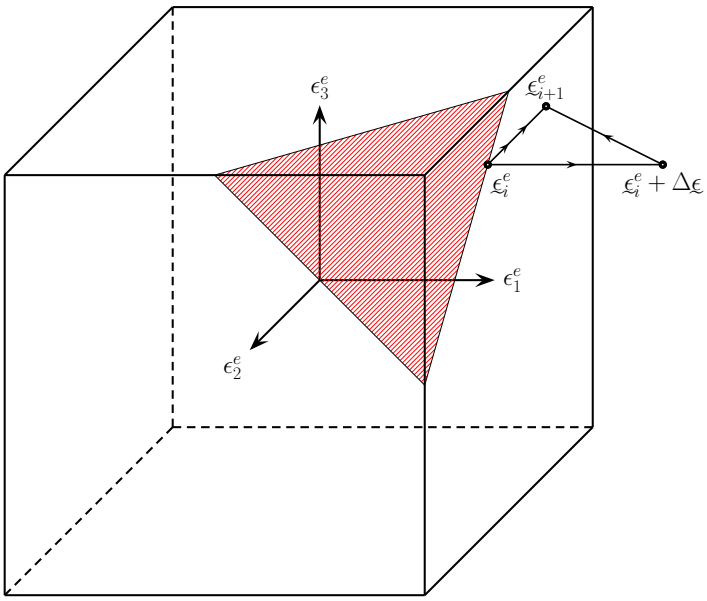

(a)

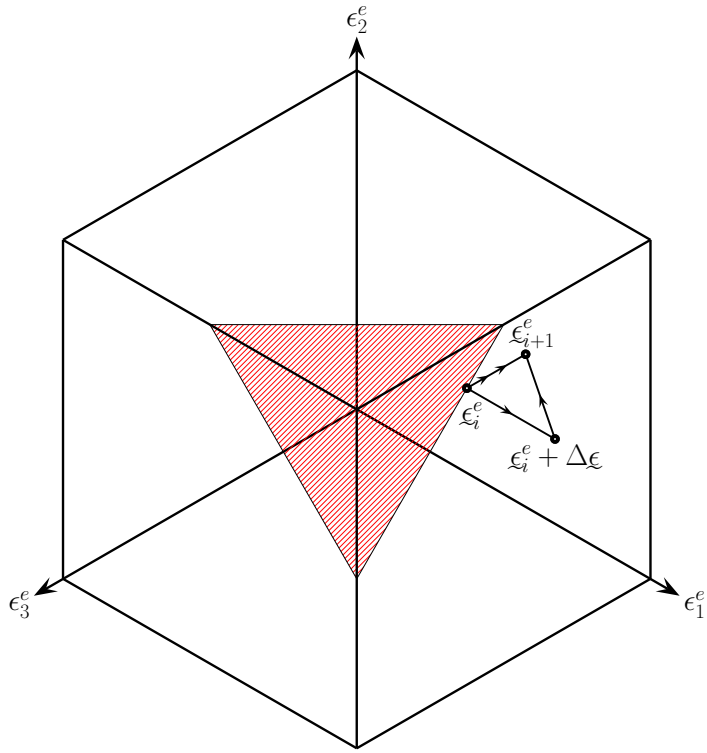

(b)

Figure 5-4: The strain-based yield surface (a) in principal strain-space, (b) π plane representation. A predictor-corrector step is shown between states of strain $\underset{\sim}{\epsilon}_i$ and $\underset{\sim}{\epsilon}_{i+1}$.

fact can be used to greatly simplify the return mapping process, particularly at the intersection of multiple yield surfaces. To realise these simplifications is it necessary to rotate the predictor state into its principal orientation before performing the plastic return. The consistent tangent matrix can then be defined in principal coordinates before it and the returned state are rotated back into general coordinates. In the following, the symbols $\underset{\sim}{x}$ and $\hat{\underset{\sim}{x}}$ denote the same term in general and principal coordinate systems. The rotation of strain and stress vectors in Voigt notation can be expressed as

$$\hat{\underset{\sim}{\epsilon}} = \underset{\sim}{A}\underset{\sim}{\epsilon} \quad \text{or} \quad \underset{\sim}{\epsilon} = \underset{\sim}{A}^{-1}\hat{\underset{\sim}{\epsilon}} \tag{5.4}$$

$$\hat{\underset{\sim}{\sigma}} = \underset{\sim}{A}^{-T}\underset{\sim}{\sigma} \quad \text{or} \quad \underset{\sim}{\sigma} = \underset{\sim}{A}^{T}\hat{\underset{\sim}{\sigma}} \tag{5.5}$$

and elasticity and compliance tensors as

$$\hat{\underset{\sim}{D}}^{e} = \underset{\sim}{A}^{-T}\underset{\sim}{D}^{e}\underset{\sim}{A}^{-1} \quad \text{or} \quad \underset{\sim}{D}^{e} = \underset{\sim}{A}^{T}\hat{\underset{\sim}{D}}^{e}\underset{\sim}{A} \tag{5.6}$$

$$\hat{\underset{\sim}{C}}^{e} = \underset{\sim}{A}\underset{\sim}{C}^{e}\underset{\sim}{A}^{T} \quad \text{or} \quad \underset{\sim}{C}^{e} = \underset{\sim}{A}^{-1}\hat{\underset{\sim}{C}}^{e}\underset{\sim}{A}^{-T} \tag{5.7}$$

where $\underset{\sim}{A}$ is the 6×6 rotation matrix A (see Appendix B for details). Hooke's law can be written in terms of the elastic and plastic parts of the total strain as

$$\hat{\underset{\sim}{\sigma}} = \hat{\underset{\sim}{D}}^{e}(\hat{\underset{\sim}{\epsilon}} - \hat{\underset{\sim}{\epsilon}}^{p}) = \hat{\underset{\sim}{D}}^{e}\hat{\underset{\sim}{\epsilon}}^{e} \tag{5.8}$$

where $\hat{\underset{\sim}{D}}^{e}$ is the elasticity matrix in principal strain orientations. The associative plastic flow rule for stress-based criterion, f, and equivalent strain-based criterion, g, can be expressed in rate form as

$$\dot{\hat{\underset{\sim}{\epsilon}}}^{p} = d\lambda\frac{\partial f}{\partial \hat{\underset{\sim}{\sigma}}} = d\lambda\hat{\underset{\sim}{C}}^{e}\frac{\partial g}{\partial \hat{\underset{\sim}{\epsilon}}^{e}} \tag{5.9}$$

where $\hat{\underset{\sim}{C}}^{e} = (\hat{\underset{\sim}{D}}^{e})^{-1}$, is the compliance matrix in principal strain orientations and $d\lambda$ is the plastic multiplier. The presence of $\hat{\underset{\sim}{C}}^{e}$ in equation 5.9 is required to satisfy Il'iushin's postulate (Il'iushin, 1961). This postulate requires that the work done by external forces during a closed cycle of deformation of an elasto-plastic

material must be non-negative. This is illustrated in the context of strain-space plasticity by Lan et al. (2003). The predictor-corrector phase can be written in terms of stress (Eq. 5.10), and strain (Eq. 5.11) as

$$\hat{\underset{\sim}{\sigma}} = \hat{\underset{\sim}{\sigma}}_T - d\lambda \hat{\underset{\sim}{D}}^e \frac{\partial f}{\partial \hat{\underset{\sim}{\sigma}}} \tag{5.10}$$

$$\hat{\underset{\sim}{D}}^e \hat{\underset{\sim}{\epsilon}}^e = \hat{\underset{\sim}{D}}^e \hat{\underset{\sim}{\epsilon}}^e_T - d\lambda \frac{\partial g}{\partial \hat{\underset{\sim}{\epsilon}}^e} \tag{5.11}$$

where $\hat{\underset{\sim}{\sigma}}_T$ and $\hat{\underset{\sim}{\epsilon}}^e_T$ are the trial or predictor states of stress and elastic strain. Rearranging Eq. 5.11 and premultiplying by C^e, we have

$$d\lambda \hat{\underset{\sim}{C}}^e \frac{\partial g}{\partial \hat{\underset{\sim}{\epsilon}}^e} = \hat{\underset{\sim}{\epsilon}}^e_T - \hat{\underset{\sim}{\epsilon}}^e \tag{5.12}$$

Premultiplying Eq. 5.12 by $\left(\frac{\partial g}{\partial \hat{\underset{\sim}{\epsilon}}^e}\right)^T$ and alternatively $\left(\frac{\partial g}{\partial \hat{\underset{\sim}{\epsilon}}^e_T}\right)^T$ gives

$$d\lambda \left\{\frac{\partial g}{\partial \hat{\underset{\sim}{\epsilon}}^e}\right\}^T \hat{\underset{\sim}{C}}^e \frac{\partial g}{\partial \hat{\underset{\sim}{\epsilon}}^e} = \left\{\frac{\partial g}{\partial \hat{\underset{\sim}{\epsilon}}^e}\right\}^T (\hat{\underset{\sim}{\epsilon}}^e_T - \hat{\underset{\sim}{\epsilon}}^e) \tag{5.13}$$

$$\text{and} \quad d\lambda \left\{\frac{\partial g}{\partial \hat{\underset{\sim}{\epsilon}}^e_T}\right\}^T \hat{\underset{\sim}{C}}^e \frac{\partial g}{\partial \hat{\underset{\sim}{\epsilon}}^e} = \left\{\frac{\partial g}{\partial \hat{\underset{\sim}{\epsilon}}^e_T}\right\}^T (\hat{\underset{\sim}{\epsilon}}^e_T - \hat{\underset{\sim}{\epsilon}}^e) \tag{5.14}$$

respectively. Following the analysis of convex surfaces by (Hiriart-Urruty and Lemarechal, 1993) and yield surfaces by (Huang and Griffiths, 2008), we can write

$$\left\{\frac{\partial f}{\partial \hat{\underset{\sim}{\sigma}}}\right\}^T (\hat{\underset{\sim}{\sigma}}_T - \hat{\underset{\sim}{\sigma}}) \leq f(\hat{\underset{\sim}{\sigma}}_T) \leq \left\{\frac{\partial f}{\partial \hat{\underset{\sim}{\sigma}}_T}\right\}^T (\hat{\underset{\sim}{\sigma}}_T - \hat{\underset{\sim}{\sigma}}) \tag{5.15}$$

$$\text{and} \quad \left\{\frac{\partial g}{\partial \hat{\underset{\sim}{\epsilon}}^e}\right\}^T (\hat{\underset{\sim}{\epsilon}}^e_T - \hat{\underset{\sim}{\epsilon}}^e) \leq g(\hat{\underset{\sim}{\epsilon}}^e_T) \leq \left\{\frac{\partial g}{\partial \hat{\underset{\sim}{\epsilon}}^e_T}\right\}^T (\hat{\underset{\sim}{\epsilon}}^e_T - \hat{\underset{\sim}{\epsilon}}^e) \tag{5.16}$$

Substituting the left hand sides of Eqs. 5.13 and 5.14 into Eq. 5.16 we get

$$\left\{\frac{\partial g}{\partial \hat{\underset{\sim}{\epsilon}}^e}\right\}^T \hat{\underset{\sim}{C}}^e \frac{\partial g}{\partial \hat{\underset{\sim}{\epsilon}}^e} \leq \frac{g(\hat{\underset{\sim}{\epsilon}}^e_T)}{d\lambda} \leq \left\{\frac{\partial g}{\partial \hat{\underset{\sim}{\epsilon}}^e_T}\right\}^T \hat{\underset{\sim}{C}}^e \frac{\partial g}{\partial \hat{\underset{\sim}{\epsilon}}^e} \tag{5.17}$$

If the yield surface is piecewise linear and the return is to a single surface then $\frac{\partial g}{\partial \hat{\underset{\sim}{\epsilon}}^e} = \frac{\partial g}{\partial \hat{\underset{\sim}{\epsilon}}^e_T}$ will remain constant throughout the return in principal coordinates. Therefore 5.17 becomes

$$\begin{aligned} \left\{\frac{\partial g}{\partial \hat{\underset{\sim}{\epsilon}}^e}\right\}^T \hat{\underset{\sim}{C}}^e \frac{\partial g}{\partial \hat{\underset{\sim}{\epsilon}}^e} &= \frac{g(\hat{\underset{\sim}{\epsilon}}^e_T)}{d\lambda} = \left\{\frac{\partial g}{\partial \hat{\underset{\sim}{\epsilon}}^e_T}\right\}^T \hat{\underset{\sim}{C}}^e \frac{\partial g}{\partial \hat{\underset{\sim}{\epsilon}}^e} \\ \text{giving } d\lambda &= \frac{g(\hat{\underset{\sim}{\epsilon}}^e_T)}{\left\{\frac{\partial g}{\partial \hat{\underset{\sim}{\epsilon}}^e}\right\}^T \hat{\underset{\sim}{C}}^e \frac{\partial g}{\partial \hat{\underset{\sim}{\epsilon}}^e}} = \frac{g(\hat{\underset{\sim}{\epsilon}}^e_T)}{\left\{\frac{\partial g}{\partial \hat{\underset{\sim}{\epsilon}}^e_T}\right\}^T \hat{\underset{\sim}{C}}^e \frac{\partial g}{\partial \hat{\underset{\sim}{\epsilon}}^e_T}} \end{aligned} \tag{5.18}$$

Substituting Eq. 5.18 into Eq. 5.11 we have

$$\begin{aligned} \hat{\underset{\sim}{D}}^e \hat{\underset{\sim}{\epsilon}}^e &= \hat{\underset{\sim}{D}}^e \hat{\underset{\sim}{\epsilon}}^e_T - \left[\frac{g(\hat{\underset{\sim}{\epsilon}}^e_T)}{\left\{\frac{\partial g}{\partial \hat{\underset{\sim}{\epsilon}}^e_T}\right\}^T \hat{\underset{\sim}{C}}^e \frac{\partial g}{\partial \hat{\underset{\sim}{\epsilon}}^e_T}}\right] \frac{\partial g}{\partial \hat{\underset{\sim}{\epsilon}}^e_T} \\ \hat{\underset{\sim}{\epsilon}}^e &= \hat{\underset{\sim}{\epsilon}}^e_T - \left[\frac{g(\hat{\underset{\sim}{\epsilon}}^e_T)}{\left\{\frac{\partial g}{\partial \hat{\underset{\sim}{\epsilon}}^e_T}\right\}^T \hat{\underset{\sim}{C}}^e \frac{\partial g}{\partial \hat{\underset{\sim}{\epsilon}}^e_T}}\right] \hat{\underset{\sim}{C}}^e \frac{\partial g}{\partial \hat{\underset{\sim}{\epsilon}}^e_T} \end{aligned} \tag{5.19}$$

Return to a line

Equation 5.19 represents the core return mapping process for returns to a plane. In the present yield criterion it is also necessary to return states of strain that lie in singular regions to lines (intersection of two yield planes) and points (intersections of three yield planes). The equation of a line on the yield surface can be expressed as the parametric equation

$$\hat{\underset{\sim}{\epsilon}}^e = t\hat{\underset{\sim}{r}}^l + \hat{\underset{\sim}{\epsilon}}^l \tag{5.20}$$

where t is a scalar parameter, $\hat{\underset{\sim}{r}}^l$ is a vector parallel to the line and $\hat{\underset{\sim}{\epsilon}}^l$ is an arbitrary point on the line. An infinite number of predictor states may require a return to a given point on a line, therefore the direction of $\Delta\hat{\underset{\sim}{\epsilon}}^p$ is unknown. However, the fact that the first derivatives of the yield surfaces are orthogonal to the line can be used to derive a closed form expression for the corrected state. Substitution of Eq. 5.20 into Eq. 5.12 gives

$$d\hat{\underset{\sim}{\epsilon}}^p = d\lambda \hat{\underset{\sim}{C}}^e \frac{\partial g}{\partial \hat{\underset{\sim}{\epsilon}}^e} = \left[\hat{\underset{\sim}{\epsilon}}^e_T - \left(t\hat{\underset{\sim}{r}}^l + \hat{\underset{\sim}{\epsilon}}^l\right)\right] \tag{5.21}$$

which premultiplied by $\hat{\underset{\sim}{D}}^e$ gives

$$d\lambda \frac{\partial g}{\partial \hat{\underset{\sim}{\epsilon}}^e} = \hat{\underset{\sim}{D}}^e \left[\left(\hat{\underset{\sim}{\epsilon}}^e_T - \hat{\underset{\sim}{\epsilon}}^l\right) - t\hat{\underset{\sim}{r}}^l\right] \tag{5.22}$$

rearranging Eq. 5.22 and premultiplying by $\left(\hat{\underset{\sim}{r}}^l\right)^T$ produces

$$d\lambda \left(\hat{\underset{\sim}{r}}^l\right)^T \frac{\partial g}{\partial \hat{\underset{\sim}{\epsilon}}^e} + t\left(\hat{\underset{\sim}{r}}^l\right)^T \hat{\underset{\sim}{D}}^e \hat{\underset{\sim}{r}}^l = \left(\hat{\underset{\sim}{r}}^l\right)^T \hat{\underset{\sim}{D}}^e \left(\hat{\underset{\sim}{\epsilon}}^e_T - \hat{\underset{\sim}{\epsilon}}^l\right) \tag{5.23}$$

Noting that

$$\left(\hat{\underset{\sim}{r}}^l\right)^T \frac{\partial g}{\partial \hat{\underset{\sim}{\epsilon}}^e} = 0 \tag{5.24}$$

due to the orthogonality condition, the parameter t can be evaluated as

$$t = \frac{\left(\hat{\underset{\sim}{r}}^l\right)^T \hat{\underset{\sim}{D}}^e \left(\hat{\underset{\sim}{\epsilon}}^e_T - \hat{\underset{\sim}{\epsilon}}^l\right)}{\left(\hat{\underset{\sim}{r}}^l\right)^T \hat{\underset{\sim}{D}}^e \hat{\underset{\sim}{r}}^l} \tag{5.25}$$

Substitution of Eq. 5.25 into Eq. 5.20 gives the corrected state as

$$\hat{\underset{\sim}{\epsilon}}^e = \left[\frac{\left(\hat{\underset{\sim}{r}}^l\right)^T \hat{\underset{\sim}{D}}^e \left(\hat{\underset{\sim}{\epsilon}}_T^e - \hat{\underset{\sim}{\epsilon}}^l\right)}{\left(\hat{\underset{\sim}{r}}^l\right)^T \hat{\underset{\sim}{D}}^e \hat{\underset{\sim}{r}}^l} \right] \hat{\underset{\sim}{r}}^l + \hat{\underset{\sim}{\epsilon}}^l \tag{5.26}$$

Return to a point

In the case of a return to a point, in principal space the corrected state can simply be written down as the coordinates of the point. In the present criterion these solutions take the following form

$$\hat{\underset{\sim}{\epsilon}}^e = \left[Y_{t/c}\ Y_{t/c}\ Y_{t/c}\ 0\ 0\ 0\right]^T \tag{5.27}$$

where $Y_{t/c}$ represents the yield strain in tension or compression as appropriate.

5.2.3 Derivations of the singularity indicators

The equations derived in Section 5.2.2 can be used to return any predictor state of strain to the yield surface developed here (see Fig. 5-4). It remains to identify which states of strain require to be returned to a plane, a line or a point. This problem is confounded by the fact that the return vectors in strain-space are not orthogonal to the yield surface (e.g. the predictor-corrector line plotted in Fig. 5-4). Note that while $\frac{\partial g}{\partial \hat{\underset{\sim}{\epsilon}}^e}$ is orthogonal to g, the term $\hat{\underset{\sim}{C}}^e \frac{\partial g}{\partial \hat{\underset{\sim}{\epsilon}}^e}$ is not. Predictor states of strain therefore exist which are in violation of only one yield surface, yet when corrected are in violation of another. Such strain states are a subset of the singular states. To overcome this obstacle we require the derivation of 'singularity indicators' similar to those derived by Pankaj (1990) and Pankaj and Bicanic (1997) for the Mohr-Coulomb yield criterion.

Following an argument similar to that of Pankaj, we continue in principal strain-space which simplifies the algebra required. The process used here effectively checks whether the elastic principal strains have changed order following a return(s) to the yield surface(s). By definition the predictor principal strains, are ranked $\epsilon^e_{T1} \geq \epsilon^e_{T2} \geq \epsilon^e_{T3}$. A singular predictor state must exist if, following a return(s), the final elastic principal strains are ranked other than $\epsilon^e_1 \geq \epsilon^e_2 \geq \epsilon^e_3$.

Writing the plastic corrector to a plane in principal strain-space (Eq. 5.19), we have

$$\hat{\underset{\sim}{\epsilon}}^e = \hat{\underset{\sim}{\epsilon}}^e_T - d\hat{\underset{\sim}{\epsilon}}^p = \hat{\underset{\sim}{\epsilon}}^e_T - \left[\frac{g(\hat{\underset{\sim}{\epsilon}}^e)}{\left\{\frac{\partial g}{\partial \hat{\underset{\sim}{\epsilon}}^e}\right\}^T \hat{\underset{\sim}{C}}^e \frac{\partial g}{\partial \hat{\underset{\sim}{\epsilon}}^e}}\right] \hat{\underset{\sim}{C}}^e \frac{\partial g}{\partial \hat{\underset{\sim}{\epsilon}}^e} \tag{5.28}$$

In principal strain-space the first derivatives of the yield functions (Eq. 5.3) are

$$\begin{aligned}
\frac{\partial g_{1t}}{\partial \hat{\underset{\sim}{\epsilon}}^e} &= \begin{Bmatrix} 1 \\ 0 \\ 0 \end{Bmatrix}; \frac{\partial g_{2t}}{\partial \hat{\underset{\sim}{\epsilon}}^e} = \begin{Bmatrix} 0 \\ 1 \\ 0 \end{Bmatrix}; \frac{\partial g_{3t}}{\partial \hat{\underset{\sim}{\epsilon}}^e} = \begin{Bmatrix} 0 \\ 0 \\ 1 \end{Bmatrix} \\
\frac{\partial g_{1c}}{\partial \hat{\underset{\sim}{\epsilon}}^e} &= -\begin{Bmatrix} 1 \\ 0 \\ 0 \end{Bmatrix}; \frac{\partial g_{2c}}{\partial \hat{\underset{\sim}{\epsilon}}^e} = -\begin{Bmatrix} 0 \\ 1 \\ 0 \end{Bmatrix}; \frac{\partial g_{3c}}{\partial \hat{\underset{\sim}{\epsilon}}^e} = -\begin{Bmatrix} 0 \\ 0 \\ 1 \end{Bmatrix}
\end{aligned} \tag{5.29}$$

if we neglect the shear terms which are all zero in principal space. Writing Eq. 5.28 in vector form we therefore get one of the following

$$\begin{Bmatrix} \epsilon^e_1 \\ \epsilon^e_2 \\ \epsilon^e_3 \end{Bmatrix} = \begin{Bmatrix} \epsilon^e_{T1} \\ \epsilon^e_{T2} \\ \epsilon^e_{T3} \end{Bmatrix} - \frac{g_{it}}{\hat{C}^e_{ii}} \begin{Bmatrix} \hat{C}^e_{1i} \\ \hat{C}^e_{2i} \\ \hat{C}^e_{3i} \end{Bmatrix} \tag{5.30}$$

$$\begin{Bmatrix} \epsilon^e_1 \\ \epsilon^e_2 \\ \epsilon^e_3 \end{Bmatrix} = \begin{Bmatrix} \epsilon^e_{T1} \\ \epsilon^e_{T2} \\ \epsilon^e_{T3} \end{Bmatrix} + \frac{g_{ic}}{\hat{C}^e_{ii}} \begin{Bmatrix} \hat{C}^e_{1i} \\ \hat{C}^e_{2i} \\ \hat{C}^e_{3i} \end{Bmatrix} \tag{5.31}$$

where $i = 1, 2, 3$. From these expressions we can evaluate the corrected principal strains, check whether they remain ranked appropriately and derive singularity indicators. The full derivation of singularity indicators is given in Appendix C. A typical example to show how they work is discussed in the following Subsection.

Example 1 - Singular in tension-tension region

Consider violation of the yield surface g_{1t}. A single return to this yield surface (Eq. 5.30) results in

$$\epsilon_1^e = \epsilon_{T1}^e - g_{1t} \tag{5.32}$$

$$\epsilon_2^e = \epsilon_{T2}^e - g_{1t}\frac{\hat{C}_{21}^e}{\hat{C}_{11}^e} \tag{5.33}$$

If this return results in $\epsilon_2^e > \epsilon_1^e$ then the predictor strain state is in a singular regime and we can define a singularity indicator such that

$$\begin{aligned} \mu_{tt} &= \epsilon_2^e - \epsilon_1^e > 0 \\ \text{or } \mu_{tt} &= \left\{\epsilon_{T2}^e - g_{1t}\frac{\hat{C}_{21}^e}{\hat{C}_{11}^e}\right\} - \{\epsilon_{T1}^e - g_{1t}\} \end{aligned} \tag{5.34}$$

A value of $\mu_{tt} > 0$ would therefore indicate the need for a return to the line at the intersection of the yield surfaces g_{1t} and g_{2t}.

Example 2 - Singular in tension-tension-tension region

In the present yield criterion a singularity could also occur during a return to a line. This would indicate the need to return to a point at the intersection of three yield surfaces. Consider violation of g_{1t} and g_{2t}. A return to the line marking their intersection leads to

$$\begin{aligned} \hat{\underset{\sim}{\epsilon}}^e &= t\hat{\underset{\sim}{r}}^l + \hat{\underset{\sim}{\epsilon}}^l \\ \begin{Bmatrix}\epsilon_1^e \\ \epsilon_2^e \\ \epsilon_3^e\end{Bmatrix} &= t\begin{Bmatrix}0 \\ 0 \\ 1\end{Bmatrix} + \begin{Bmatrix}Y_t \\ Y_t \\ 0\end{Bmatrix} \end{aligned} \tag{5.35}$$

from Eq. 5.20 (note only terms relating to the principal directions are shown - all others are 0). The parameter t is defined as in Eq. 5.25, such that in the present example

$$t = \frac{\hat{D}_{31}^e\left(\epsilon_{T1} - Y_t\right) + \hat{D}_{32}^e\left(\epsilon_{T2} - Y_t\right) + \hat{D}_{33}^e\epsilon_{T3}}{\hat{D}_{33}^e} \tag{5.36}$$

If this return results in $\epsilon_3^e > \epsilon_1^e$ then the predictor state is in a singular region which requires a return to a point. We can then define a singularity indicator as

$$\begin{aligned} \mu_{ttt} &= \epsilon_3^e - \epsilon_1^e > 0 \\ \text{or } \mu_{ttt} &= t - Y_t \\ &= \left\{ \frac{\hat{D}_{31}^e \left(\epsilon_{T1} - Y_t\right) + \hat{D}_{32}^e \left(\epsilon_{T2} - Y_t\right) + \hat{D}_{33}^e \epsilon_{T3}}{\hat{D}_{33}^e} \right\} - Y_t \end{aligned} \tag{5.37}$$

5.2.4 Elasto-plastic tangential modulus matrix

The FE solution of an elasto-plastic problem involves iterative solution of linear increments. This is typically governed by a Newton-Raphson scheme which requires the evaluation of a tangential modulus matrix $\hat{\underset{\sim}{D}}^{ep}$ which relates the incremental change in stress induced by an increment of strain. An increment of stress can be expressed as

$$\begin{aligned} d\hat{\underset{\sim}{\sigma}} &= \hat{\underset{\sim}{D}}^e d\hat{\underset{\sim}{\epsilon}}^e \\ &= \hat{\underset{\sim}{D}}^e \left(d\hat{\underset{\sim}{\epsilon}} - d\hat{\underset{\sim}{\epsilon}}^p\right) \\ &= \hat{\underset{\sim}{D}}^e d\hat{\underset{\sim}{\epsilon}} - d\lambda \frac{\partial g}{\partial \hat{\underset{\sim}{\epsilon}}^e} \end{aligned} \tag{5.38}$$

and an elastic strain increment as

$$d\hat{\underset{\sim}{\epsilon}}^e = d\hat{\underset{\sim}{\epsilon}} - d\lambda \hat{\underset{\sim}{C}}^e \frac{\partial g}{\partial \hat{\underset{\sim}{\epsilon}}^e} \tag{5.39}$$

Tangential modulus matrix - strain state on a plane

In the absence of hardening the consistency equation can be written as

$$dg = \left(\frac{\partial g}{\partial \hat{\underset{\sim}{\epsilon}}^e}\right)^T d\hat{\underset{\sim}{\epsilon}}^e = 0 \tag{5.40}$$

substituting from Eq. 5.39 for $d\hat{\underset{\sim}{\epsilon}}^e$ in Eq. 5.40 gives

$$dg = \left(\frac{\partial g}{\partial \underset{\sim}{\hat{\epsilon}}^e}\right)^T \left[d\underset{\sim}{\hat{\epsilon}} - d\lambda \underset{\sim}{\hat{C}}^e \frac{\partial g}{\partial \underset{\sim}{\hat{\epsilon}}^e}\right] = 0 \tag{5.41}$$

Rearranging Eq. 5.41 gives

$$\left(\frac{\partial g}{\partial \underset{\sim}{\hat{\epsilon}}^e}\right)^T d\underset{\sim}{\hat{\epsilon}} = d\lambda \left(\frac{\partial g}{\partial \underset{\sim}{\hat{\epsilon}}^e}\right)^T \underset{\sim}{\hat{C}}^e \frac{\partial g}{\partial \underset{\sim}{\hat{\epsilon}}^e} \tag{5.42}$$

and

$$d\lambda = \frac{\left(\frac{\partial g}{\partial \underset{\sim}{\hat{\epsilon}}^e}\right)^T d\underset{\sim}{\hat{\epsilon}}}{\left(\frac{\partial g}{\partial \underset{\sim}{\hat{\epsilon}}^e}\right)^T \underset{\sim}{\hat{C}}^e \frac{\partial g}{\partial \underset{\sim}{\hat{\epsilon}}^e}} \tag{5.43}$$

which can be substituted into Eq. 5.38 to produce

$$\begin{aligned} d\underset{\sim}{\hat{\sigma}} &= \left[\underset{\sim}{\hat{D}}^e - \frac{\frac{\partial g}{\partial \underset{\sim}{\hat{\epsilon}}^e}\left(\frac{\partial g}{\partial \underset{\sim}{\hat{\epsilon}}^e}\right)^T}{\left(\frac{\partial g}{\partial \underset{\sim}{\hat{\epsilon}}^e}\right)^T \underset{\sim}{\hat{C}}^e \frac{\partial g}{\partial \underset{\sim}{\hat{\epsilon}}^e}}\right] d\underset{\sim}{\hat{\epsilon}} \\ d\underset{\sim}{\hat{\sigma}} &= \underset{\sim}{\hat{D}}^{ep} d\underset{\sim}{\hat{\epsilon}} \end{aligned} \tag{5.44}$$

Tangential modulus matrix - strain state on a line

In the case of a strain state on a line or a point at the intersection of multiple yield surfaces $\underset{\sim}{\hat{D}}^{ep}$ can be evaluated as the summation of two 6×6 matrices in the form adopted by Clausen et al. (2006) for isotropic stress-based yield criteria in principal space

$$\underset{\sim}{\hat{D}}^{ep} = \langle \underset{\sim}{\hat{D}} \rangle^{ep} + \underset{\sim}{\hat{G}} \tag{5.45}$$

where $\langle \underset{\sim}{\hat{D}} \rangle^{ep}$ contains elements relating only to normal strain components and is thus non-zero only in the first three rows and columns, and $\underset{\sim}{\hat{G}}$ contains only the shear stiffness terms rotated into principal directions (following Eq. 5.6), i.e.

$$\hat{\underset{\sim}{G}} = \underset{\sim}{A}^{-T} \begin{bmatrix} \underset{3\times3}{0} & \underset{3\times3}{0} \\ \underset{3\times3}{0} & \underset{3\times3}{D^e_{ij}} \end{bmatrix} \underset{\sim}{A}^{-1}, \text{ for } i,j = 4,5,6 \tag{5.46}$$

For a line the direction of the elastic strain increment, defined in principal strain space, must be parallel to the line. Therefore

$$d\hat{\underset{\sim}{\epsilon}}^e = d\eta \hat{\underset{\sim}{r}}^l \tag{5.47}$$

where $d\eta$ is a scalar multiple. The corresponding increment of stress must be defined as

$$d\hat{\underset{\sim}{\sigma}} = d\eta \hat{\underset{\sim}{D}}^e \hat{\underset{\sim}{r}}^l \tag{5.48}$$

and $\hat{\underset{\sim}{D}}^{ep}$ must be singular with respect to any vector orthogonal to $\hat{\underset{\sim}{D}}^e \hat{\underset{\sim}{r}}^l$. Hence from Eq. 5.38 and its definition in Eq. 5.44, $\hat{\underset{\sim}{D}}^{ep}$ can be written as

$$\hat{\underset{\sim}{D}}^{ep} d\hat{\underset{\sim}{\epsilon}}^e = \hat{\underset{\sim}{D}}^e d\hat{\underset{\sim}{\epsilon}}^e \tag{5.49}$$

and therefore

$$\begin{aligned} \langle \hat{\underset{\sim}{D}} \rangle^{ep} \hat{\underset{\sim}{r}}^l &= \hat{\underset{\sim}{D}}^e \hat{\underset{\sim}{r}}^l \\ \langle \hat{\underset{\sim}{D}} \rangle^{ep} \hat{\underset{\sim}{r}}^l \left[\left(\hat{\underset{\sim}{r}}^l \right)^T \hat{\underset{\sim}{D}}^e \right] &= \hat{\underset{\sim}{D}}^e \hat{\underset{\sim}{r}}^l \left[\left(\hat{\underset{\sim}{r}}^l \right)^T \hat{\underset{\sim}{D}}^e \right] \\ \langle \hat{\underset{\sim}{D}} \rangle^{ep} &= \frac{\hat{\underset{\sim}{D}}^e \hat{\underset{\sim}{r}}^l \left(\hat{\underset{\sim}{r}}^l \right)^T \hat{\underset{\sim}{D}}^e}{\left(\hat{\underset{\sim}{r}}^l \right)^T \hat{\underset{\sim}{D}}^e \hat{\underset{\sim}{r}}^l} \end{aligned} \tag{5.50}$$

Tangential modulus matrix - strain state at a point

In the present yield criterion only points defined by the intersection of three yield surfaces exist. Following the arguments of (Clausen et al., 2006), at such a point the tangent modulus matrix is singular with respect to any direction in principal

space but not with respect to the shear directions. Hence,

$$\hat{\underset{\sim}{D}}^{ep} = \hat{\underset{\sim}{G}} \tag{5.51}$$

where $\hat{\underset{\sim}{G}}$ is defined in Eq. 5.46.

5.2.5 Consistent tangent matrix

Use of the tangent modulus matrix $\hat{\underset{\sim}{D}}^{ep}$ derived in Section 5.2.4 has been shown to impair the quadratic rate of convergence of the global iteration scheme (Nagtegaal, 1982). Simo and Taylor (1985) developed a consistent tangent matrix to restore the quadratic convergence of the global Newton scheme. This can be expressed as

$$\hat{\underset{\sim}{D}}^{epc} = \underset{\sim}{T}\hat{\underset{\sim}{D}}^{ep} \tag{5.52}$$

where $\underset{\sim}{T}$ is a modification matrix generally defined as

$$\underset{\sim}{T} = \left(\underset{\sim}{I} + \Delta\lambda \underset{\sim}{D}^{e} \frac{d\left(\frac{df}{d\underset{\sim}{\sigma}}\right)}{d\underset{\sim}{\sigma}} \right)^{-1} \tag{5.53}$$

in which the derivative is taken at the corrected state and $\underset{\sim}{I}$ is the identity matrix. In the case of linear yield criteria (such as the present one) it has been established that $\underset{\sim}{T}$ can be evaluated at the predictor state as

$$\underset{\sim}{T} = \underset{\sim}{I} - \Delta\lambda \underset{\sim}{D}^{e} \frac{d\left(\frac{df}{d\underset{\sim}{\sigma}}\right)}{d\underset{\sim}{\sigma}} \tag{5.54}$$

thus avoiding the inversion required in Eq. 5.53 (Crisfield, 1997). Conversion of Eq. 5.54 for a yield surface defined in strain space gives

$$\underset{\sim}{T} = \underset{\sim}{I} - \Delta\lambda \underset{\sim}{C}^e \frac{d\left(\frac{dg}{d\underset{\sim}{\epsilon}^e}\right)}{d\underset{\sim}{\epsilon}^e} = \underset{\sim}{I} - \frac{d\left(\Delta\lambda \underset{\sim}{C}^e \frac{dg}{d\underset{\sim}{\epsilon}^e}\right)}{d\underset{\sim}{\epsilon}^e} = \underset{\sim}{I} - \frac{d\Delta\underset{\sim}{\epsilon}^p}{d\underset{\sim}{\epsilon}^e} \tag{5.55}$$

where the plastic corrector in general strain-space, $\Delta\underset{\sim}{\epsilon}^p$ can be expressed in terms of its representation in principal strain-space, using Eq. 5.4 and Appendix B, as

$$\underset{\sim}{T} = \underset{\sim}{I} - \frac{d\Delta\underset{\sim}{\epsilon}^p}{d\underset{\sim}{\epsilon}^e} = \underset{\sim}{I} - \frac{d\left(\underset{\sim}{A}^{-1}\Delta\hat{\underset{\sim}{\epsilon}}^p\right)}{d\underset{\sim}{\epsilon}^e} \tag{5.56}$$

which can be expanded, noting the matrix identity $\frac{d\underset{\sim}{A}^{-1}}{dx} = -\underset{\sim}{A}^{-1}\frac{d\underset{\sim}{A}}{dx}\underset{\sim}{A}^{-1}$ (Selby, 1974; Petersen and Pedersen, 2008), with the substitution

$$\underset{\sim}{\Gamma}_i = -\underset{\sim}{A}^{-1}\frac{d\underset{\sim}{A}}{d\underset{\sim}{\epsilon}^e_i}\underset{\sim}{A}^{-1}\Delta\hat{\underset{\sim}{\epsilon}}^p$$

such that

$$\underset{\sim}{T} = \underset{\sim}{I} - \begin{bmatrix}\Gamma_x & \Gamma_y & \Gamma_z & \Gamma_{xy} & \Gamma_{xz} & \Gamma_{yz}\end{bmatrix} \tag{5.57}$$

The term $\frac{d\underset{\sim}{A}}{d\underset{\sim}{\epsilon}^e_i}$ represents the rate of change of the principal strain axes which can be expressed using the following geometrical arguments, similar to Clausen et al. (2006) for principal stress axes. Expanding $\frac{d\underset{\sim}{A}}{d\underset{\sim}{\epsilon}^e_i}$ with the chain rule gives

$$\frac{d\underset{\sim}{A}}{d\underset{\sim}{\epsilon}^e_i} = \frac{\partial\underset{\sim}{A}}{\partial\psi^x}\frac{d\psi^x}{d\underset{\sim}{\epsilon}^e_i} + \frac{\partial\underset{\sim}{A}}{\partial\psi^y}\frac{d\psi^y}{d\underset{\sim}{\epsilon}^e_i} + \frac{\partial\underset{\sim}{A}}{\partial\psi^z}\frac{d\psi^z}{d\underset{\sim}{\epsilon}^e_i} \tag{5.58}$$

where $d\psi^x$, $d\psi^y$, and $d\psi^z$ are infinitesimal rotation angles about the x-, y- and z-axis. In the case that the principal $(\hat{x}\hat{y}\hat{z})$ and general (xyz) axes are aligned, the angles between them can be represented as the tensor

$$\underset{\sim}{\psi}^0 = \begin{bmatrix} \psi^x_{\hat{x}} & \psi^x_{\hat{y}} & \psi^x_{\hat{z}} \\ \psi^y_{\hat{x}} & \psi^y_{\hat{y}} & \psi^y_{\hat{z}} \\ \psi^z_{\hat{x}} & \psi^z_{\hat{y}} & \psi^z_{\hat{z}} \end{bmatrix} = \begin{bmatrix} 0 & \frac{\pi}{2} & \frac{\pi}{2} \\ \frac{\pi}{2} & 0 & \frac{\pi}{2} \\ \frac{\pi}{2} & \frac{\pi}{2} & 0 \end{bmatrix} \tag{5.59}$$

from which the corresponding transformation tensor can be derived

$$\underset{\sim}{\Omega}^0 = \cos \underset{\sim}{\psi}^0 = \begin{bmatrix} 1 & 0 & 0 \\ 0 & 1 & 0 \\ 0 & 0 & 1 \end{bmatrix} \tag{5.60}$$

Infinitesimal rotations of the coordinate system about each of the axes are illustrated in Fig. 5-5 and produce the transformation tensors

$$\underset{\sim}{\Omega}^x = \cos \begin{bmatrix} 0 & \frac{\pi}{2} & \frac{\pi}{2} \\ \frac{\pi}{2} & d\psi^x & \frac{\pi}{2} - d\psi^x \\ \frac{\pi}{2} & \frac{\pi}{2} + d\psi^x & d\psi^x \end{bmatrix} = \begin{bmatrix} 1 & 0 & 0 \\ 0 & 1 & d\psi^x \\ 0 & -d\psi^x & 1 \end{bmatrix} \tag{5.61}$$

$$\underset{\sim}{\Omega}^y = \cos \begin{bmatrix} d\psi^y & \frac{\pi}{2} & \frac{\pi}{2} + d\psi^y \\ \frac{\pi}{2} & 0 & \frac{\pi}{2} \\ \frac{\pi}{2} - d\psi^y & \frac{\pi}{2} & d\psi^y \end{bmatrix} = \begin{bmatrix} 1 & 0 & -d\psi^y \\ 0 & 1 & 0 \\ d\psi^y & 0 & 1 \end{bmatrix} \tag{5.62}$$

and

$$\underset{\sim}{\Omega}^z = \cos \begin{bmatrix} d\psi^z & \frac{\pi}{2} - d\psi^z & \frac{\pi}{2} \\ \frac{\pi}{2} + d\psi^z & d\psi^z & \frac{\pi}{2} \\ \frac{\pi}{2} & \frac{\pi}{2} & 0 \end{bmatrix} = \begin{bmatrix} 1 & d\psi^z & 0 \\ -d\psi^z & 1 & 0 \\ 0 & 0 & 1 \end{bmatrix} \tag{5.63}$$

respectively. It may be noted that the above equations are slightly different from those obtained by Clausen et al. (2006). From Eqs. 5.60 to 5.63 the change in transformation matrix $\underset{\sim}{A}$ resulting from a rotation around each axis (see Appendix B) can be expressed as

$$\frac{\partial \underset{\sim}{\underset{\sim}{A}}}{\partial \psi^x} d\psi^x = \underset{\sim}{\underset{\sim}{A}}\left(\underset{\sim}{\underset{\sim}{\Omega}}^x\right) - \underset{\sim}{\underset{\sim}{A}}\left(\underset{\sim}{\underset{\sim}{\Omega}}^0\right) = \begin{bmatrix} & & & 0 & 0 & 0 \\ & \underset{\sim}{\underset{\sim}{0}}_{3\times 3} & & 0 & 0 & -d\psi^x \\ & & & 0 & 0 & d\psi^x \\ 0 & 0 & 0 & 0 & -d\psi^x & 0 \\ 0 & 0 & 0 & d\psi^x & 0 & 0 \\ 0 & 2d\psi^x & -2d\psi^x & 0 & 0 & 0 \end{bmatrix} \tag{5.64}$$

$$\frac{\partial \underset{\sim}{\underset{\sim}{A}}}{\partial \psi^y} d\psi^y = \underset{\sim}{\underset{\sim}{A}}\left(\underset{\sim}{\underset{\sim}{\Omega}}^y\right) - \underset{\sim}{\underset{\sim}{A}}\left(\underset{\sim}{\underset{\sim}{\Omega}}^0\right) = \begin{bmatrix} & & & 0 & d\psi^y & 0 \\ & \underset{\sim}{\underset{\sim}{0}}_{3\times 3} & & 0 & 0 & 0 \\ & & & 0 & -d\psi^y & 0 \\ 0 & 0 & 0 & 0 & 0 & d\psi^y \\ -2d\psi^y & 0 & 2d\psi^y & 0 & 0 & 0 \\ 0 & 0 & 0 & -d\psi^y & 0 & 0 \end{bmatrix} \tag{5.65}$$

and

$$\frac{\partial \underset{\sim}{\underset{\sim}{A}}}{\partial \psi^z} d\psi^z = \underset{\sim}{\underset{\sim}{A}}\left(\underset{\sim}{\underset{\sim}{\Omega}}^z\right) - \underset{\sim}{\underset{\sim}{A}}\left(\underset{\sim}{\underset{\sim}{\Omega}}^0\right) = \begin{bmatrix} & & & -d\psi^z & 0 & 0 \\ & \underset{\sim}{\underset{\sim}{0}}_{3\times 3} & & d\psi^z & 0 & 0 \\ & & & 0 & 0 & 0 \\ 2d\psi^z & -2d\psi^z & 0 & 0 & 0 & 0 \\ 0 & 0 & 0 & 0 & 0 & -d\psi^z \\ 0 & 0 & 0 & 0 & d\psi^z & 0 \end{bmatrix} \tag{5.66}$$

when quadratic terms are neglected. To evaluate Eq. 5.58 it is also necessary to calculate $\frac{d\psi^x}{d\underset{\sim}{\epsilon}_i^e}$, $\frac{d\psi^y}{d\underset{\sim}{\epsilon}_i^e}$ and $\frac{d\psi^z}{d\underset{\sim}{\epsilon}_i^e}$. Infinitesimal changes in the normal strains do not affect the orientation of the principal strain directions, hence

$$\frac{d\psi^i}{d\epsilon_j^e} = \underset{\sim}{0} \;\Rightarrow\; \frac{d\underset{\sim}{\underset{\sim}{A}}}{d\epsilon_j^e} = \underset{\sim}{\underset{\sim}{0}} \;\Rightarrow\; \underset{\sim}{\Gamma}_j = \underset{\sim}{0} \;\text{ , for } i,j = x,y,z \tag{5.67}$$

Through consideration of the strain Mohr's circles illustrated in Fig. 5-6 the rate of change of the rotation angles with the shear strains γ_{xy}^e, γ_{xz}^e and γ_{yz}^e can be found as

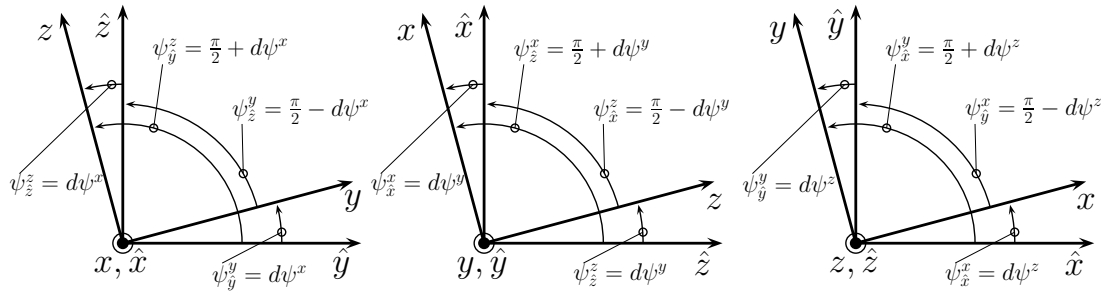

(a) (b) (c)

Figure 5-5: Infinitesimal rotation angles about the three coordinate axes; angle $d\psi^x$ about the x-axis (a), angle $d\psi^y$ about the y-axis (b), angle $d\psi^z$ about the z-axis (c).

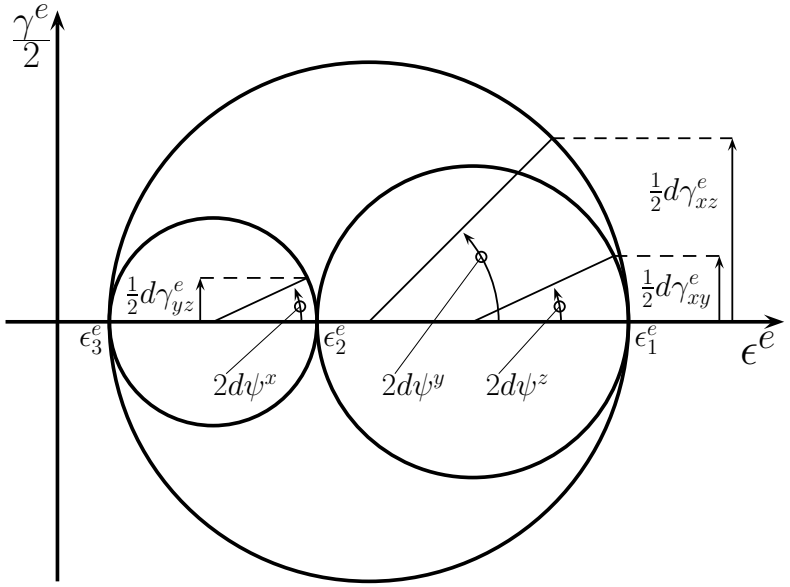

Figure 5-6: Mohr's circles of strain for infinitesimal rotation angles $d\psi^x$, $d\psi^y$ and $d\psi^z$.

$$\sin\left(2d\psi^x\right) = \frac{\frac{1}{2}d\gamma^e_{yz}}{\frac{1}{2}\left(\epsilon^e_2 - \epsilon^e_3\right)} \quad \Leftrightarrow \quad \frac{d\psi^x}{d\gamma^e_{yz}} = \frac{1}{2\left(\epsilon^e_2 - \epsilon^e_3\right)} \tag{5.68}$$

$$\sin\left(2d\psi^y\right) = \frac{\frac{1}{2}d\gamma^e_{xz}}{\frac{1}{2}\left(\epsilon^e_1 - \epsilon^e_3\right)} \quad \Leftrightarrow \quad \frac{d\psi^y}{d\gamma^e_{xz}} = \frac{1}{2\left(\epsilon^e_1 - \epsilon^e_3\right)} \tag{5.69}$$

$$\sin\left(2d\psi^z\right) = \frac{\frac{1}{2}d\gamma^e_{xy}}{\frac{1}{2}\left(\epsilon^e_1 - \epsilon^e_2\right)} \quad \Leftrightarrow \quad \frac{d\psi^z}{d\gamma^e_{xy}} = \frac{1}{2\left(\epsilon^e_1 - \epsilon^e_2\right)} \tag{5.70}$$

noting that for infinitesimal angles, $\sin\theta \approx \theta$. Substitution of Eq. 5.68 into Eq. 5.64 gives

$$\frac{\partial \underset{\sim}{A}}{\partial \gamma_{yz}^e} = \frac{1}{2\left(\epsilon_2^e - \epsilon_3^e\right)} \begin{bmatrix} & & & 0 & 0 & 0 \\ & \underset{\sim}{0}_{3\times3} & & 0 & 0 & -1 \\ & & & 0 & 0 & 1 \\ 0 & 0 & 0 & 0 & -1 & 0 \\ 0 & 0 & 0 & 1 & 0 & 0 \\ 0 & 2 & -2 & 0 & 0 & 0 \end{bmatrix} \tag{5.71}$$

and similarly from Eq. 5.69 and Eq. 5.65

$$\frac{\partial \underset{\sim}{A}}{\partial \gamma_{xz}^e} = \frac{1}{2\left(\epsilon_1^e - \epsilon_3^e\right)} \begin{bmatrix} & & & 0 & 1 & 0 \\ & \underset{\sim}{0}_{3\times3} & & 0 & 0 & 0 \\ & & & 0 & -1 & 0 \\ 0 & 0 & 0 & 0 & 0 & 1 \\ -2 & 0 & 2 & 0 & 0 & 0 \\ 0 & 0 & 0 & -1 & 0 & 0 \end{bmatrix} \tag{5.72}$$

and Eq. 5.70 into Eq. 5.66

$$\frac{\partial \underset{\sim}{A}}{\partial \gamma_{xy}^e} = \frac{1}{2\left(\epsilon_1^e - \epsilon_2^e\right)} \begin{bmatrix} & & & -1 & 0 & 0 \\ & \underset{\sim}{0}_{3\times3} & & 1 & 0 & 0 \\ & & & 0 & 0 & 0 \\ 2 & -2 & 0 & 0 & 0 & 0 \\ 0 & 0 & 0 & 0 & 0 & -1 \\ 0 & 0 & 0 & 0 & 1 & 0 \end{bmatrix} \tag{5.73}$$

The the consistent modifier $\underset{\sim}{T}$ can be calculated by inserting Eqs. 5.67 and 5.71–5.73 into Eq. 5.57 such that

$$\underset{\sim}{T} = \underset{\sim}{I} - \begin{bmatrix} 0 & 0 & 0 & \Gamma_{xy} & \Gamma_{xz} & \Gamma_{yz} \end{bmatrix} \tag{5.74}$$

5.2.6 Overview of the algorithm

1. Initialisation:
   Pass in, $d\underset{\sim}{\varepsilon}, \underset{\sim}{\varepsilon}^e, \underset{\sim}{\varepsilon}^p$
   Set, $Y_t, Y_c, \underset{\sim}{D}^e, \underset{\sim}{C}^e = (\underset{\sim}{D}^e)^{-1}$, $\underset{\sim}{\varepsilon}^e_T = \underset{\sim}{\varepsilon}^e + d\underset{\sim}{\varepsilon}$
2. Transform $\underset{\sim}{\varepsilon}^e_T$, $\underset{\sim}{D}^e$ and $\underset{\sim}{C}^e$ into principal coordinates $\hat{\underset{\sim}{\varepsilon}}^e_T$, $\hat{\underset{\sim}{D}}^e$ and $\hat{\underset{\sim}{C}}^e$ using Eqs. 5.4, 5.6 and 5.7
3. Check yield conditions
   IF all $g(\hat{\underset{\sim}{\varepsilon}}^e) \leq 0$: no return required,
   $\hat{\underset{\sim}{\varepsilon}}^e = \hat{\underset{\sim}{\varepsilon}}^e_T$, $\hat{\underset{\sim}{D}}^{epc} = \hat{\underset{\sim}{D}}^e$ GOTO 5
   ELSE: strain return required,
   GOTO 4
4. Check singularity indicators to identify type of return
   IF return to a plane:
   Calculate $d\hat{\underset{\sim}{\varepsilon}}^p$ from Eq. 5.19 and $\hat{\underset{\sim}{D}}^{ep}$ from Eq. 5.44
   $\hat{\underset{\sim}{\varepsilon}}^e = \hat{\underset{\sim}{\varepsilon}}^e_T - d\hat{\underset{\sim}{\varepsilon}}^p$
   ELSE IF return to a line:
   Calculate $\hat{\underset{\sim}{\varepsilon}}^e$ from Eq. 5.26 and $\hat{\underset{\sim}{D}}^{ep}$ from Eqs. 5.45 and 5.50
   ELSE IF return to a point:
   Calculate $\hat{\underset{\sim}{\varepsilon}}^e$ from Eq. 5.27 and $\hat{\underset{\sim}{D}}^{ep}$ from Eq. 5.51
   END IF
   Calculate $\underset{\sim}{T}$ from Eq. 5.74
   $\hat{\underset{\sim}{D}}^{epc} = \underset{\sim}{T}\hat{\underset{\sim}{D}}^{ep}$
5. Rotate $\hat{\underset{\sim}{\varepsilon}}^e$ and $\hat{\underset{\sim}{D}}^{epc}$ back into general coordinates $\underset{\sim}{\varepsilon}^e$ and $\underset{\sim}{D}^{epc}$ using Eqs. 5.4, 5.6
6. Update stress and state variables
   $\underset{\sim}{\sigma} = \underset{\sim}{D}^e\underset{\sim}{\varepsilon}^e$, $\underset{\sim}{\varepsilon}^p = \underset{\sim}{\varepsilon} - \underset{\sim}{\varepsilon}^e$
7. Return $\underset{\sim}{\sigma}$, $\underset{\sim}{D}^{epc}$, $\underset{\sim}{\varepsilon}^e$ and $\underset{\sim}{\varepsilon}^p$

5.3 Benchmark tests

Following the development of the described maximum/minimum principal strain yield criterion, its performance was evaluated. It was necessary to verify that it functioned as intended, and did so with sufficient accuracy. The algorithm was coded as an Abaqus user subroutine in Fortran and tested under a range of critical boundary conditions using hexahedral, single element models. These cases were simulated using the implicit solver of the FE software Abaqus (ABAQUS, Inc., Providence, Rhode Island, USA), coupled with a user subroutine containing the yield criterion. The applied conditions were uniaxial tension and compression; hydrostatic tension and compression; triaxial combinations of tension and compression; and planar and triaxial pure shear. Uniaxial tests (see Fig. 5-7(a,b)) were applied by fixing all nodes on one face in the z direction and one of these also in the x and y directions, equal displacement was applied to the remaining nodes in the z direction. In hydrostatic tests (see Fig. 5-7(c,d)) one node was fixed in all directions and all nodes with a common face were restrained against translation orthogonally to that face, equal displacements were applied orthogonally to nodes on the unrestrained faces. In triaxial tension and compression tests (see Fig. 5-7(e,f)) nodes were restrained identically to the hydrostatic case but the displacements were applied such that the ratio of tensile to compressive strain was Y_t/Y_c. In the planar shear test (see Fig. 5-7(g)) one node was fully fixed and other nodes were displaced to produce a symmetrical diamond shape within the testing plane, without restraint to displacement out of that plane. In the triaxial shear test (see Fig. 5-7(h)) one node was fully fixed and all others were displaced to produced a symmetrical diamond in 3D. All tests were applied as displacement boundary conditions to guarantee a solution with the assumption of perfect plasticity. The tests were performed using tensile and compressive yield strains of 0.5 % and 0.7 % respectively. These values are arbitrary here but were subsequently used for bone and are discussed in Chapters 6 and 7. In the following, the results shown are the three principal strain components. Their elastic and plastic components are plotted against the largest principal component of applied total strain in each case.

Results of uniaxial tests are illustrated in Fig. 5.8(a) (compression) and Fig. 5.8(b) (tension). Under uniaxial compression, the elastic strain increased linearly

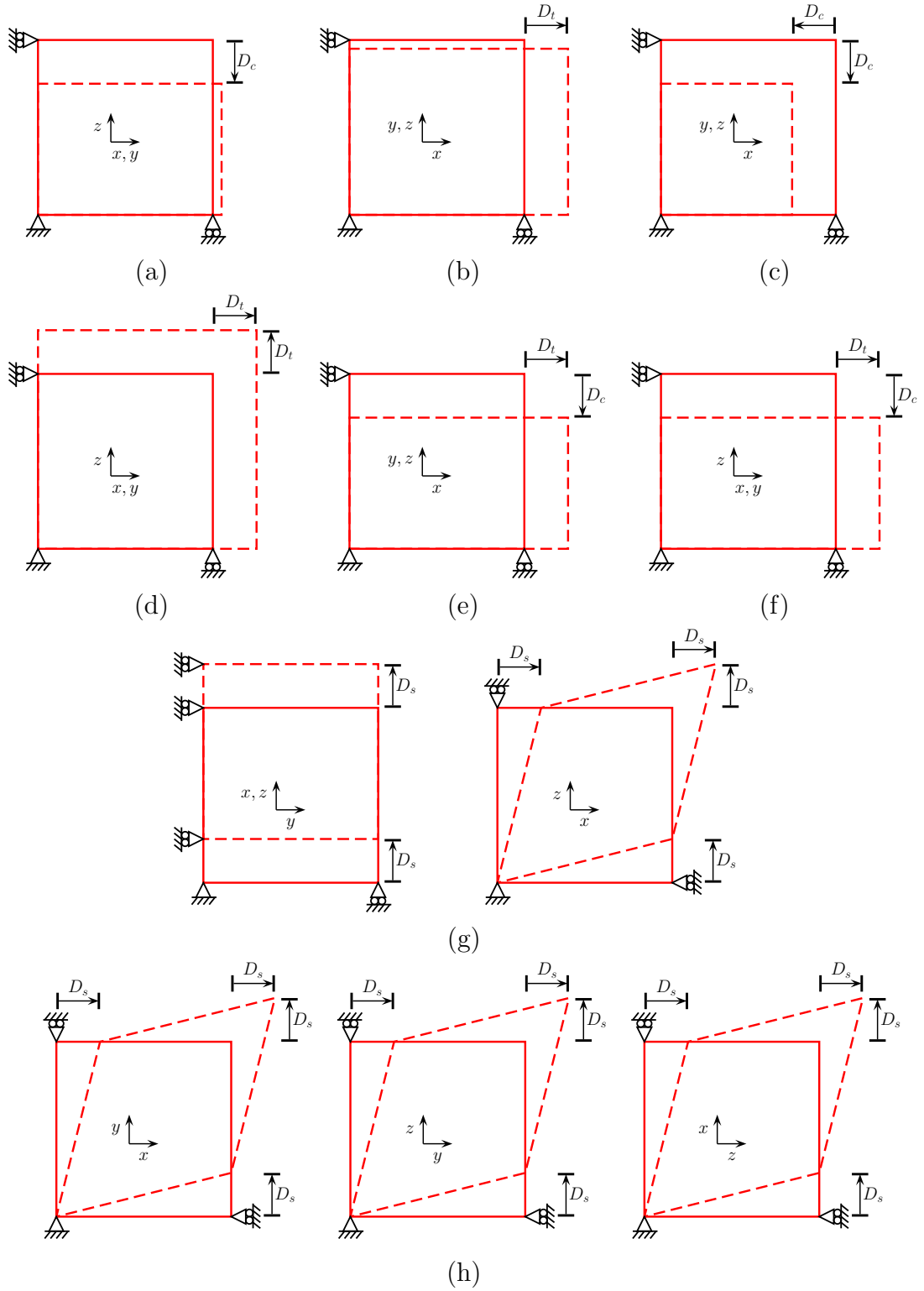

Figure 5-7: Single element benchmark test boundary conditions for uniaxial compression(a), uniaxial tension (b), hydrostatic compression (c), hydrostatic tension (d), compressive-compressive-tensile (e), tensile-tensile-compressive (f), plane pure shear (g), and triaxial pure shear (h). Note D_t, D_c and D_s are the applied tensile, compressive and shear displacements respectively.

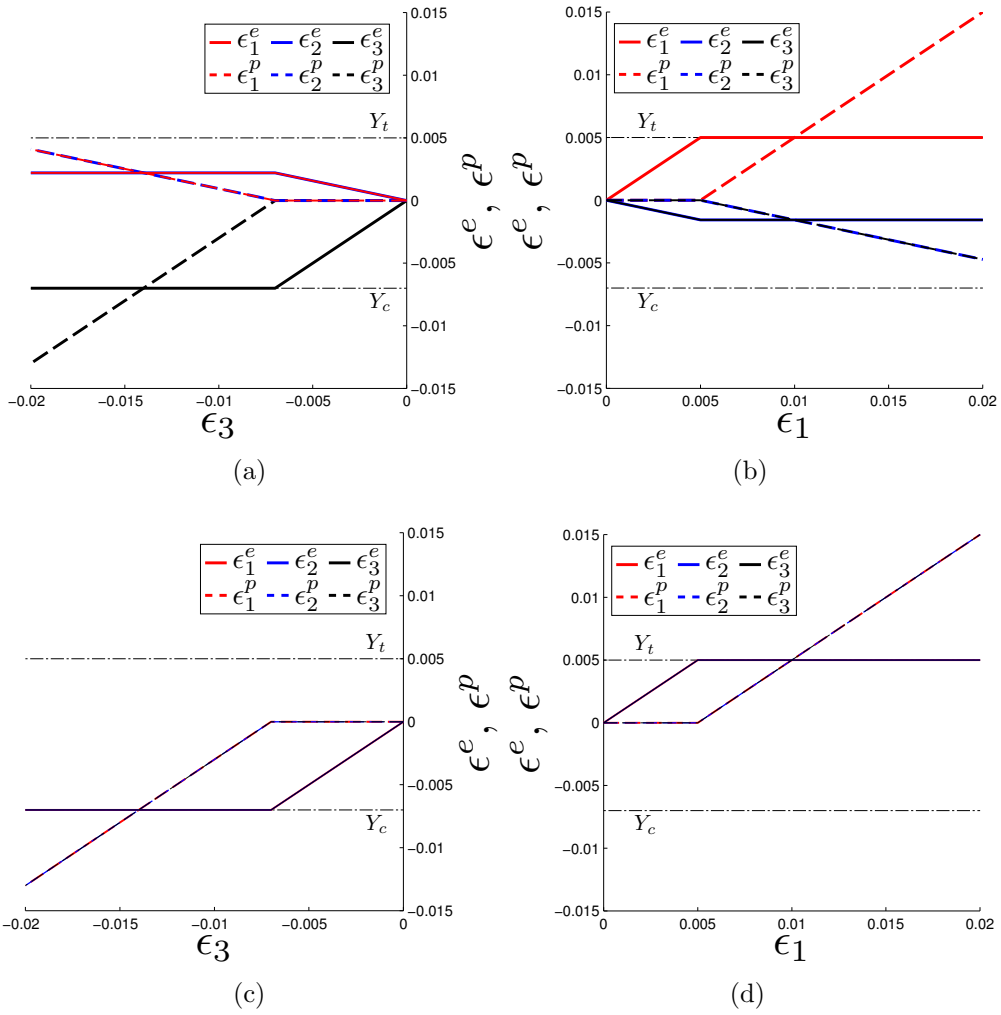

Figure 5-8: Single element uniaxial and hydrostatic tests of the strain-based yield criterion under uniaxial compressive (a), uniaxial tensile (b), hydrostatic compressive (c) and hydrostatic tensile (d) displacements.

until the yield strain in compression was reached. Initial plastic returns were made to a single yield surface. Following first yield no further elastic strain occurred. The minimum elastic principal strain component remained at a constant value of -0.7 %. All further applied strain became plastic strain. A similar pattern of yielding occurred in tension; first yield occurred when the maximum elastic principal strain reached the tensile yield strain, and remained at a constant value of 0.5 % thereafter. In both cases, it was noted that once first yield occurred in one direction, the elastic strain in other, unyielded, directions did not increase.

The results of hydrostatic tests are illustrated in Fig. 5.8(c) (compression) and Fig. 5.8(d) (tension). The plastic strain remained at zero until the compres-

sive yield surface was reached. Plastic returns were to three yield surfaces. This occurred simultaneously in all principal directions. Under further displacement, the elastic strain remained constant at a value of -0.7 %, and all additional strain became plastic. Equivalent behaviour was observed under conditions of hydrostatic tension. The elastic strain reached the tensile yield strain simultaneously in all principal directions, further strain became plastic. The limiting strain was 0.5 %.

Under compression-compression-tension conditions, the single element response was as shown in Fig. 5.9(a). The ratio of tensile to compressive applied displacements was Y_t/Y_c. The principal elastic strains increased until first yield occurred; in this case at two compressive and one tensile yield surface simultaneously. Further strain induced plastic strain in all principal directions. Once yielded, the elastic strain components remained constant at their respective yield values. Further applied strain became plastic. Similar behaviour was observed under tension-tension-compression conditions, illustrated in Fig. 5.9(b). In this case tensile yield occurred for both the maximum and middle principal strain component and compressive yield for the minimum. Post-yield, the principal elastic strains remained at the yield strain values.

Figure 5.9(c) shows the response of a single element under pure shear displacements in a single plane. Under these conditions the applied shear strain, γ^{app} can be resolved into principal strains of $\epsilon_1 = \frac{\gamma^{app}}{2}$, $\epsilon_2 = 0$, and $\epsilon_3 = -\frac{\gamma^{app}}{2}$. Therefore, since the yield strain was lower in tension, it was the mode of first yield. Following first yield, a component of plastic strain was induced in all principal directions due to the Poisson effect. This reduced the rate of increase of the elastic minimum principal strain component (see kink between points A and B in Fig. 5.9(c)), and induced an equal and opposite component of elastic strain in the direction of the middle principal strain to satisfy the boundary condition $\epsilon_2 = 0$. The minimum principal elastic strain then increased until the compressive yield strain was reached. At this point no further elastic strain accumulated; further displacement induced only plastic strain. The principal elastic strains in yielded directions remained at the yield values.

The results of a triaxial state of pure shear are presented in Fig. 5.9(d). The applied shear strains of $\gamma_{12} = \gamma_{23} = \gamma_{31} = \gamma^{app}$ resulted in applied principal

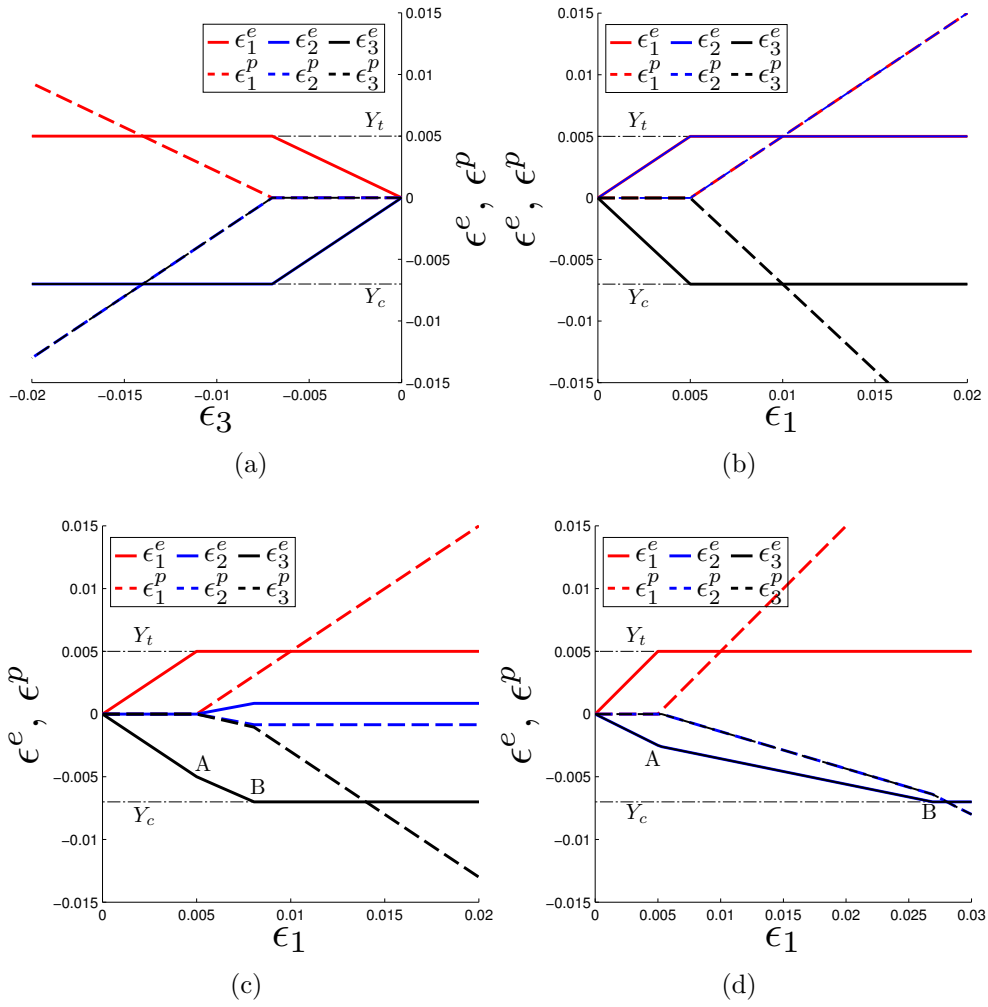

Figure 5-9: Single element triaxial and shear tests of the strain-based yield criterion. Applied boundary conditions were compressive-compressive-tensile (a), tensile-tensile-compressive (b), plane pure shear (c) and triaxial pure shear (d) displacements.

strains of $\epsilon_1 = \gamma^{app}$, and $\epsilon_2 = \epsilon_3 = -\frac{\gamma^{app}}{2}$. The elastic strains increased until first yield occurred in tension. Further straining induced plastic strain in all principal directions. This reduced the rate of accumulation of elastic strain in the unyielded middle and minimum principal directions (see kink between points A and B in Fig. 5.9(c)). Elastic strain accumulated in the unyielded directions until the compressive yield strain was reached. Following yield, all elastic principal strain components remained at their respective yield strains.

The elastic and plastic strain components which developed in a single element tested by several cycles of uniaxial tensile and compressive displacements

are plotted in Fig. 5-10(a,b). Under the initial tensile conditions the behaviour was linear until it reached the tensile yield strain Y_t. Yielding then progressed for 0.1% plastic strain at which point the applied displacements were reduced. The elastic strain returned along the pre-yield gradient with a non-zero total strain component where the elastic strain was reduced to zero. Additional compressive strain was applied until yield occurred on the compressive yield surface. This was encountered at a total strain value of -0.6%, 0.1% higher than the assigned yield strain as a result of the preceding tensile plastic strain in the z direction. Compressive yielding continued for 0.3% plastic strain. Two further loops of tensile followed by compressive loading were applied and produced similar behaviour. The principal elastic strain components remained within the assigned yield strains throughout all cycles.

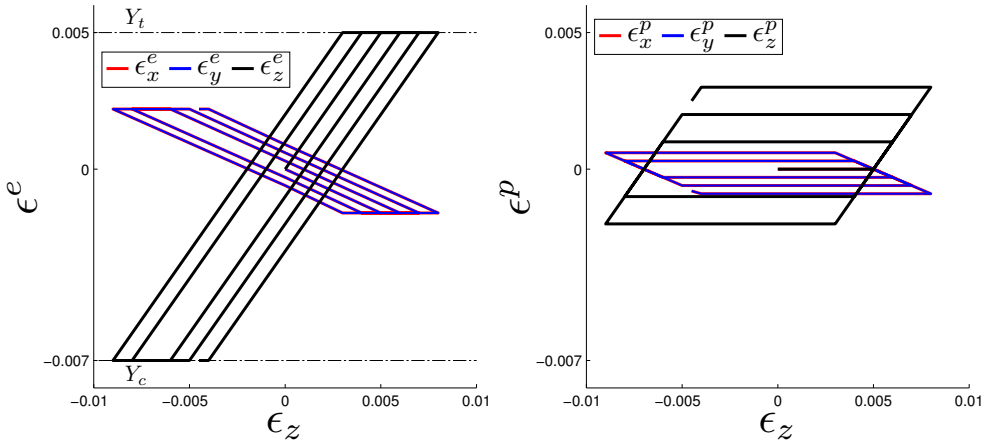

Figure 5-10: Single element test under cycles of uniaxial tensile and compressive applied strain in the z direction. Elastic (a) and plastic (c) strain components.

5.4 Discussion of benchmark tests

It was necessary to evaluate the performance of the maximum/minimum principal strain yield criterion and related algorithm developed earlier in this Chapter. It was specifically required to check that it restrained the elastic principal strain components to values less than, or equal to the specified yield strains. The results of a range of single element tests under critical boundary conditions demonstrated that the algorithm functioned properly; at no point did the elastic strain

components exceed the specified yield strains of 0.5 % and 0.7 % in tension and compression respectively.

Under uniaxial tension and compression it was demonstrated that the elastic predictor - plastic corrector algorithm worked correctly for non-singular states of strain. The various tests under hydrostatic and combinations of tension and compression involved singular strain states in violation of both two and three yield surfaces. In every case the algorithm was seen to achieve a valid plastic return to the yield surface. The planar and triaxial pure shear conditions involved the greatest possible rotation of the principal strain state from the model coordinate system. This represents an additional test for the developed algorithm. Under these conditions the singular strain states were resolved successfully. Under repeated cyclical uniaxial tensile and compressive strains the algorithm correctly resolved the elastic and plastic strain components. These results indicate that the developed algorithm is able to accurately model the maximum/minimum principal strain yield criterion in general FE analyses, including loading, unloading and reverse loading conditions.

5.4.1 Yielding and the Poisson effect

In the results of uniaxial, single element tests it was observed that following yielding in one direction, the elastic Poisson effect in other directions ceased. More specifically, the component of elastic strain induced by Poisson's effect was replaced by an equivalent plastic strain. For example, this behaviour can be seen in Fig. 5.8(a) with uniaxial compression. Preceding first yield, the elastic compressive strain increased and was accompanied by associated tensile Poisson strains in the orthogonal directions. Following first yield, both the compressive and tensile elastic strain components remained constant, although only the former had exceeded the yield surface. This behaviour was accompanied by the accumulation of plastic strains at an equivalent rate to the pre-yield state. It is important to note that the Poisson effect is related to elastic strain and once the elastic strain becomes constant in the principal loading direction there will be no additional elastic strain due to the Poisson effect in the orthogonal directions.

In the case of multiaxial and shear tests, similar behaviour was observed. However, following first yield in these cases the rate of increase of elastic strain reduced, but did not cease, in the unyielded, orthogonal directions. Since the applied loading at the element boundary continued to increase at the same rate both pre- and post yield, the fact that the rate of increase of elastic strain reduced in the unyielded directions requires explanation.

To explain this we first consider the uniaxial case in more detail. Consider an isotropic solid with elastic compliance tensor $\hat{\underset{\sim}{C}}^e$. If we assume an initial state of strain which lies on the tensile yield surface and apply an additional tensile unit stress $d\hat{\underset{\sim}{\sigma}}$, the elastic predictor, or trial strain increment in principal space is

$$\begin{aligned} d\hat{\underset{\sim}{\epsilon}}^e_T &= \hat{\underset{\sim}{C}}^e d\hat{\underset{\sim}{\sigma}} \\ &= \frac{1}{E}\begin{bmatrix} 1 & -\nu & -\nu \\ -\nu & 1 & -\nu \\ -\nu & -\nu & 1 \end{bmatrix}\begin{Bmatrix} 1 \\ 0 \\ 0 \end{Bmatrix} \\ &= \frac{1}{E}\begin{Bmatrix} 1 \\ -\nu \\ -\nu \end{Bmatrix} \end{aligned} \tag{5.75}$$

From equation 5.12 the plastic strain is

$$\begin{aligned} \Delta\hat{\underset{\sim}{\epsilon}}^p &= d\lambda \hat{\underset{\sim}{C}}^e \frac{\partial g}{\partial \hat{\underset{\sim}{\epsilon}}^e} \\ &= d\lambda \hat{\underset{\sim}{C}}^e \begin{Bmatrix} 1 \\ 0 \\ 0 \end{Bmatrix} \\ &= \frac{d\lambda}{E}\begin{Bmatrix} 1 \\ -\nu \\ -\nu \end{Bmatrix} \end{aligned} \tag{5.76}$$

The increment of elastic principal strain following the plastic return will therefore be

$$\begin{aligned}
\Delta\hat{\underset{\sim}{\epsilon}}^e &= \Delta\hat{\underset{\sim}{\epsilon}}^e_T - \Delta\hat{\underset{\sim}{\epsilon}}^p \\
&= \frac{1}{E}\begin{Bmatrix} 1 \\ -\nu \\ -\nu \end{Bmatrix} - \frac{d\lambda}{E}\begin{Bmatrix} 1 \\ -\nu \\ -\nu \end{Bmatrix} \\
&= \frac{1-d\lambda}{E}\begin{Bmatrix} 1 \\ -\nu \\ -\nu \end{Bmatrix}
\end{aligned} \tag{5.77}$$

Since the initial state lay on the tensile yield surface it follows that the increment of maximum elastic principal strain must be zero ($\Delta\epsilon^e_1 = 0$). Therefore $d\lambda = 1$ and the plastic increment exactly matches, and eliminates the elastic trial strain. This process effectively converts all components of the trial strain state into identical plastic strain components, even if only one of them is in violation of the yield surface. It should be noted that this behaviour is induced by the presence of the elastic compliance tensor $\hat{\underset{\sim}{C}}^e$ in the flow vector; which is necessary to make a return in strain-space physically valid (Il'iushin, 1961).

Following the above discussion it becomes possible to understand the observed reduction in the rate of elastic strain for unyielded directions in multiaxial loading conditions. Following first yield, the associated Poisson strain in the orthogonal directions becomes plastic. Since the apparent strain increases as the same rate, to retain equilibrium, the elastic component of strain in the unyielded directions must be reduced by the amount of plastic strain induced by the Poisson effect. To illustrate this consider the case of a planar pure shear boundary condition on an isotropic material (Fig. 5.9(c)). As previously noted, an applied shear strain of γ^{app} resolves into principal strains of $\epsilon_1 = \frac{\gamma^{app}}{2}$, $\epsilon_2 = 0$, and $\epsilon_3 = -\frac{\gamma^{app}}{2}$. The initial state lies upon the tensile yield surface and an additional stress $d\hat{\underset{\sim}{\sigma}}$ is applied

$$\Delta\hat{\underset{\sim}{\epsilon}}^e_T = \hat{\underset{\sim}{C}}^e \Delta\hat{\underset{\sim}{\sigma}}$$

$$= \frac{1}{E}\begin{bmatrix} 1 & -\nu & -\nu \\ -\nu & 1 & -\nu \\ -\nu & -\nu & 1 \end{bmatrix}\begin{Bmatrix} 1 \\ 0 \\ -1 \end{Bmatrix}$$

$$= \frac{1}{E}\begin{Bmatrix} 1+\nu \\ 0 \\ -1-\nu \end{Bmatrix} \tag{5.78}$$

Using equation 5.76 the increment of elastic principal strain following the plastic return will therefore be

$$\begin{aligned} \Delta\hat{\underset{\sim}{\epsilon}}^e &= \Delta\hat{\underset{\sim}{\epsilon}}^e_T - \Delta\hat{\underset{\sim}{\epsilon}}^p \\ &= \frac{1}{E}\begin{Bmatrix} 1+\nu \\ 0 \\ -1-\nu \end{Bmatrix} - \frac{d\lambda}{E}\begin{Bmatrix} 1 \\ -\nu \\ -\nu \end{Bmatrix} \end{aligned} \tag{5.79}$$

To achieve a return to the tensile yield surface ($\Delta\epsilon^e_1 = 0$), this implies $d\lambda = 1+\nu$. Therefore

$$\Delta\hat{\underset{\sim}{\epsilon}}^e = \frac{1}{E}\begin{Bmatrix} 0 \\ \nu(1+\nu) \\ (\nu+1)(\nu-1) \end{Bmatrix} \tag{5.80}$$

Here the discussed plastic Poisson effect changed the value of ϵ^e_2 from zero in the elastic regime, to proportional to $\nu(1+\nu)$ following first yield. Furthermore, the absolute rate of increase in ϵ^e_3 was reduced by the same effect. This proportional reduction can be calculated as

$$\frac{\Delta\epsilon^e_3}{\Delta\epsilon^e_{T3}} = \frac{\frac{1}{E}(1+\nu)(\nu-1)}{-\frac{1}{E}(1+\nu)} = 1-\nu \tag{5.81}$$

It can similarly be demonstrated that under triaxial shear conditions (Fig. 5.9(d)) the proportional reduction of the rate of increase in elastic strain following yield in another, orthogonal direction is $1-2\nu$. These results demonstrate that the observed behaviour results entirely from the Poisson effect, which is only present because of the requirements of Il'iushins's postulate (Il'iushin, 1961).

Chapter 6

Half-pin fixation of tibial midshaft fractures

6.1 Introduction

Musculoskeletal injuries contribute a large proportion of all human injuries globally (Weinstein, 2000). Within this group, a considerable number a injuries require the treatment of bone fractures; for example, in the USA alone over 490,000 fractures of the tibia and fibula occur every year (Praemer et al., 1992; Bhandari et al., 2001). While many bone fractures can be treated nonoperatively, satisfactory outcomes in many cases can only be achieved through the use of operative techniques, such as fixation. In the UK, more than 225,000 operations involving fixation of bone were conducted in the year 2008–2009 (HES, 2010). It is well established that global populations are ageing, particularly in western countries, and that fracture risk increases exponentially with age (Weinstein, 2000). Bone fixation in older patients can, therefore, be expected to become more common. Loss of bone competence through ageing and disease (such as osteoporosis) will place additional demands on the behaviour and design of fixators.

In addition to treating fractures, fixation is commonly used to extend limbs (De Bastiani et al., 1987; Ilizarov, 1989a;b). The process involves breaking the bone by osteotomy, using fixation to hold the bone fragments in position, and gradually extending the healing fracture (known as callus distraction or callotasis) (De Bastiani et al., 1987). Callus distraction enables the extension of the leg by 10 % (or more) of its original length (Kenwright and Simpson, 2000). The rate of limb lengthening must be slow enough to prevent separation of the callus,

but fast enough so that premature healing does not occur; a rate of 1 mm per day is typical (De Bastiani et al., 1987; Simpson et al., 1999). Limb lengthening is used in cases where considerable deformity is present. Causes of deformity include congenital conditions, diseases such as osteomyelitis and polio, and fractures which heal too short or out of alignment (Simpson et al., 1996; 1999).

Two strategies of healing are typically induced at fracture sites; 'direct' ('primary' or 'cutting cone') and 'indirect' ('secondary' or 'external callus') healing (Goodship et al., 1998). With direct healing the bone fragments are brought very close together and rigidly held in position using fixation. This is termed a '100 % reduction' of the fracture gap, to separations of less than 200 μm. The natural processes of bone remodelling can operate over such small distances and the fracture is repaired in the same way as non-critical microcracks. Direct healing is slow because it progresses at the natural rate of bone turnover rather than the accelerated rates of bone formation associated with the presence of callus. The method of fixation used with direct healing must be very stiff to prevent substantial movement at the fracture site which can disturb the remodelling process. Contrastingly, indirect healing seeks to maximise the stimulation of bone generation within the callus. A fracture gap is often left; the fracture is said to be incompletely reduced. Displacement across the fracture gap is promoted through the use of less stiff fixation methods to excite the formation of new bone. The method requires patients to load the limb in order to stimulate new bone growth. Rates of fracture healing are dependent upon the mechanical environment formed in the callus which can be modulated by varying the fixation settings. Healing is generally more rapid under indirect than direct healing (Goodship et al., 1998).

Internal methods of fixation with plates and screws generally provide rigid support and are therefore used to provide direct healing. Methods of internal fixation which target direct healing include the use of interfragmentary screws, plates with screws and intervertebral 'cages' (Rüedi and Murphy, 2000; Tencer, 2002; Solomon et al., 2005). Interfragmentary screws are used to fix small fragments to the main bone. Plates provide very stiff fixation and therefore target direct healing. These are frequently used in metaphyseal fractures in the legs, diaphyseal fractures in the forearms, as well as applications in hip and spinal fixation. Locking plates use threaded screw heads to fix screws rigidly to the plate

(in addition to the bone), which enables them to be used without plate-bone contact, and nonsubcutaneously (Ramotowski and Granowski, 1991; Kowalski et al., 1996). Dynamic compression plates achieve compression of the fracture using oval holes in the plate which force the plate to slide as the screw is driven into the plate (Cordey et al., 1980; Tencer, 2002). Cage fixation is one method used to fuse vertebrae at a fixed separation (Tencer et al., 1995; Tencer, 2002). Other internal fixation implants are used to target indirect healing such as Kirschner wires and intramedullary (IM) nails (Solomon et al., 2005). Fragments can be held together with Kirschner wires where rapid healing and no concentrated loads are expected. IM nails are inserted down the medullary canals of the long bones with 'locking screws' (screws orthogonal to the nail) used to prevent rotation occurring at the fracture site. Additionally, reaming of the medullary canal prior to IM nail installation can be used to improve the achieved fit, but at the cost of increased damage to the blood supply (Bhandari et al., 2001; Solomon et al., 2005). IM nailing is the accepted method for fixation at the femoral diaphysis.

External fixation enables more displacement at the fracture gap than internal methods and therefore promotes indirect healing. External fixation comprises the use of screws (pins) or wires to restrain the bone above and below the fracture site. These are attached to an external frame made of stiff rings or bars. Pins can either be supported on both sides of the bone (transfixion pins) or unilaterally (half-pins). Wires always transfix the bone and are pre-tensioned to increase their stiffness. External fixation using wires is considered further in Chapter 7. A wide variety of individual component designs are available, these typically comprise modular systems that can be combined in different configurations to suit specific installations. This also enables considerable variation of the fixator stiffness to provide the required mechanical environment at the callus site; external fixator stiffness can be varied by as much as three orders of magnitude (Huiskes and Chao, 1986).

The choice of internal or external fixation methods can vary considerably with surgeon preference and geographical location (Bhandari et al., 2001). There is general agreement that closed fractures and open fractures with a small wound (type I), should be treated with internal fixation. Open fractures with severe soft-tissue damage (type III) (Bhandari et al., 2001; Solomon et al., 2005) are

more frequently treated with external fixation. Unstable and comminuted fractures are also sometimes treated with external fixation (Solomon et al., 2005). Open fractures increase the risk of infection which can be difficult to control with internal fixation methods. Contrastingly, external methods enable the wound to be left open, providing access for inspection and dressing (Solomon et al., 2005). Limb lengthening procedures typically employ external fixation methods because they enable manipulation of misaligned bone fragments and adjustment of the distraction rate during extension (De Bastiani et al., 1987; Ilizarov, 1989a;b). IM nailing can also be used in leg extension, both on its own (Guichet et al., 2003) or in combination with external fixation components (Simpson et al., 1999). External methods also offer the advantage of being able to stabilise injuries which span joints (Goslings, 2002).

The present study considered loosening of half-pins as used in external fixation of the tibial midshaft. Tissue failure at the pin-bone interface and associated loosening are serious complications of external fixation (Chao and Hein, 1988; Behrens, 1989; Aro et al., 1993; Pettine et al., 1993; Wikenheiser et al., 1995; Goslings, 2002; Moroni et al., 2002). Sterile loosening occurs when bone at the interface is subjected to stresses beyond its strength (Behrens, 1989). Pin design, placement and thermal injury during pre-drilling have all been shown to promote loosening (Wikenheiser et al., 1995). Dynamic loading, induced by daily activity, also increases the risk of pin loosening by the repeated action of alternating loads (Pettine et al., 1993). Infection of pin sites can act in combination with mechanical loosening to destabilise fixation (Moroni et al., 2002); pin-track loosening or infection has been reported in 10 % of tibial and femoral cases (Lewallen and Edwards, 1994). Infection can lower bone strength and promote pin loosening under lower loading, and sterile loosening can disturb the soft-tissues, promoting contamination and infection (Huiskes et al., 1985; Chao and Hein, 1988; Aro et al., 1993; Moroni et al., 2002; Parameswaran et al., 2003). Serious infection of pin sites can necessitate movement of the pin or abandonment of external fixation (Goslings, 2002; Moroni et al., 2002).

Silver (Collinge et al., 1994) and hydroxyapatite (Arciola et al., 1999) pin coatings can be used to reduce infections rates. In addition, hydroxyapatite coatings promote osseointegration at the pin-bone interface, reducing the risk of pin

loosening (Campbell et al., 2000; Moroni et al., 2002; Parameswaran et al., 2003). However, osseointegration requires the action of bone remodelling and hence takes time to develop. The initial stability of coated pins is therefore identical to uncoated pins (Moroni et al., 2002).

Ageing and diseases such as osteoporosis and osteomalacia can lead to a reduction in bone strength and increased risk of pin loosening (Behrens, 1989; Goslings, 2002; Tencer, 2002). Since global populations are ageing (Weinstein, 2000), treatment of patients with reduced bone mechanical properties will become increasingly common. In trabecular bone structures increased porosity lowers interconnectivity and strength, reducing its resistance to screw pullout (Weaver and Chalmers, 1966; Rice et al., 1988; Perilli et al., 2008). The periosteal and endosteal profiles of cortical bone also migrate with ageing, leading to a reduction of cortical thickness (Inoue and Chao, 2002; Russo et al., 2006). Smaller interfacial contact areas therefore induce higher stresses and increased potential for local bone failure and pin loosening. Furthermore, cortical thinning leads to reduced buttressing at the exit cortex and therefore lower resistance to pin bending (Tencer, 2002). Changes in microstructure (as studied in Chapter 3), and mineralization (Currey, 1979; Currey et al., 1996) also reduce the stiffness and strength of remaining cortical bone, further lowering its resistance to pin loosening.

Analytical and FE techniques have been used to investigate the mechanical behaviour of pin fixators in the past. Initial studies used parametric analyses to investigate the effect of fixator settings on overall stiffness. Key parameters to increase fixator stiffness were: the use of more pins, increased pin diameter, reduced exposed pin length, increased longitudinal pin separation, pin material (Chao et al., 1982; Huiskes et al., 1985; Huiskes and Chao, 1986; Juan et al., 1992; Oni et al., 1993). One study observed that the pins nearest the fracture gap were critical to providing fixator stability (Oni et al., 1993). The methods found to increase fixator stiffness were also found to reduce the stresses at the pin-bone interface (Huiskes et al., 1985). The stiffness and length of the fracture callus were found to affect the load transferred through the fixator considerably for 70–80 % of the installed life of a fixator (Juan et al., 1992). The addition of articulated and diagonal connection bars to bilateral frames was found to increase fixator

stiffness considerably without increasing the pin-bone interfacial stress (Lauer et al., 2000). The combined use of IM nails with unilateral fixation was found to provide greater axial stiffness than bilateral external fixation alone (Shahar and Shani, 2004). However, the same study observed substantially higher strains in the fracture gap under torsional loading with IM nail fixation. It was also noted by Shahar and Shani (2004) that the focus of previous studies on maximising fixator stiffness was misplaced since strains across the callus are required to stimulate bone growth (Goodship et al., 1998; Lacroix and Prendergast, 2002). More recently, the use of appropriate contact conditions was found to be critical to FE predictions of fixator behaviour (Karunratanakul et al., 2010). However, all previous studies had employed either tied (Chao et al., 1982; Huiskes et al., 1985; Huiskes and Chao, 1986; Juan et al., 1992; Oni et al., 1993; Lauer et al., 2000; Shahar and Shani, 2004) or sliding (Huiskes et al., 1985) pin-bone contact conditions which unrealistically enabled tensile stresses to be transferred at the interface. Such simplified contact conditions would therefore be expected to reduce the reliability of previous predictions, particularly regarding the mechanical environment at the pin-bone interface. All previous studies were limited by further modelling simplifications. The geometry of bone fragments and fixator components have been simplified to 1D, 2D or idealised cylindrical representations in 3D (Chao et al., 1982; Huiskes et al., 1985; Huiskes and Chao, 1986; Juan et al., 1992; Oni et al., 1993; Lauer et al., 2000; Shahar and Shani, 2004; Karunratanakul et al., 2010). The mechanical properties of bone and fixator components have been restricted to elastic behaviour (Chao et al., 1982; Huiskes et al., 1985; Huiskes and Chao, 1986; Juan et al., 1992; Oni et al., 1993; Lauer et al., 2000; Shahar and Shani, 2004; Karunratanakul et al., 2010), but the high stresses observed at the pin-bone interface and pin supports would be expected to approach and possibly exceed the elastic limit of these materials. Bone tissue has been modelled as isotropic and homogeneous (Chao et al., 1982; Huiskes et al., 1985; Huiskes and Chao, 1986; Juan et al., 1992; Oni et al., 1993; Lauer et al., 2000; Shahar and Shani, 2004; Karunratanakul et al., 2010). However, bone microstructural variations have been found to produce orthotropic elastic properties (Cowin and Mehrabadi, 1989) which vary considerably with location (see Chapter 3). Furthermore, the reduced cortical thickness and bone density which result from age and disease related bone loss have not been included in previous FE studies of fixation. The aim of the present study was to address the

noted limitations of previous FE studies of fixation, and specifically investigate the effect of bone loss on half-pin loosening.

6.2 Methods

The methods described in the following were implemented using programs written by the author in Matlab (The MathWorks, Inc., Natick, MA, U.S.A.) and Fortran.

The FE method was used to study the mechanical aspects of half-pin loosening in fracture fixation. The configuration of half-pins used in fracture fixation can vary widely, even at a single site. Two factors that can affect configuration complexity include the number of bone fragments that require stabilising and proximity to bone joints. This study considered a single fracture of the tibial midshaft. This location avoided the complications encountered near joints and simplified the modelling process by eliminating the presence of cancellous bone. The long bones of the leg represent an ideal case for numerical study since the static loading they experience during standing can be reasonably approximated by body weight. The standard method of fracture fixation in the femur has become intramedullary nailing. The tibia however, is still frequently fixed with external fixation (Behrens and Searls, 1986; Bhandari et al., 2001) and was therefore a suitable location for the present study. The methodology of the present study involved FE analyses of an externally fixed fracture of the tibial midshaft. Models consisted of a longitudinal midshaft section of the left female tibia under an applied vertical load. The tibia was supported by fixation implants to an unmodelled external frame. The simulations exploited the symmetry of fixation devices around the fracture gap; only one half of the fixation construct was modelled.

6.2.1 Tibial fragment definition

To produce directly applicable results it was necessary to generate a realistic geometrical representation of the tibial midshaft. Surface profiles of an 'average'

tibia were sourced from the open-access online BEL repository via BiomedTown (http://www.biomedtown.org/). These profiles were generated from CT scans of an artificial composite tibiae (SawBones, Vashon, WA, USA), and designed to represent the average geometrical properties of human bones. 3D tibial bone fragments were generated by longitudinally extruding the periosteal and endosteal cross-sectional profiles at the midshaft. The extrusion length was 80 mm in all cases. This process is summarised in Fig. 6-1. Bone fragments therefore did not possess the cross-sectional variations in the longitudinal direction present in real bone. This was desirable in the present study because it simplified the modelling process and made the simulation representative of a general position on the diaphysis rather than specific to the local variations within a single selected region.

Variations in the thickness and area of tibial cortical bone have been observed with ageing (Russo et al., 2006). Substantial bone loss occurs in the average female but the average male undergoes lesser changes. Since one of the aims of the present study was to investigate the effect of bone loss on fixation implant stability, it was desirable to consider the largest variation of cortical bone mass possible. This study therefore modelled only female bone geometries. It has been observed that females posses relatively similar cortical thickness and area between the ages of 20 and 60. However, average values of both of these properties reduce dramatically with increased age (Russo et al., 2006). Two cortical profiles were created to capture the noted variations in the present study; one to represent both young and middle-aged women, and one to represent old-aged women. These profiles were generated by offsetting the 'average' tibial endosteal and periosteal profiles to match the reported (Russo et al., 2006) radially averaged thickness and area at these ages. It should be noted that the data of Russo et al. were measured at a section located at 38 % of the tibial length from the tibio-talar joint cleft. These data were adjusted to be representative of the values at the midshaft (50 % length). This was achieved by multiplying them by the ratio of their values measured on the 'average' tibia at 50 % and 38 % of the tibial length. The resulting area and radially averaged thickness of the modelled bone fragments are listed in Table 6.1. The percentage difference of these values from those reported by Russo et al. was acceptably small (≤ 2 %).

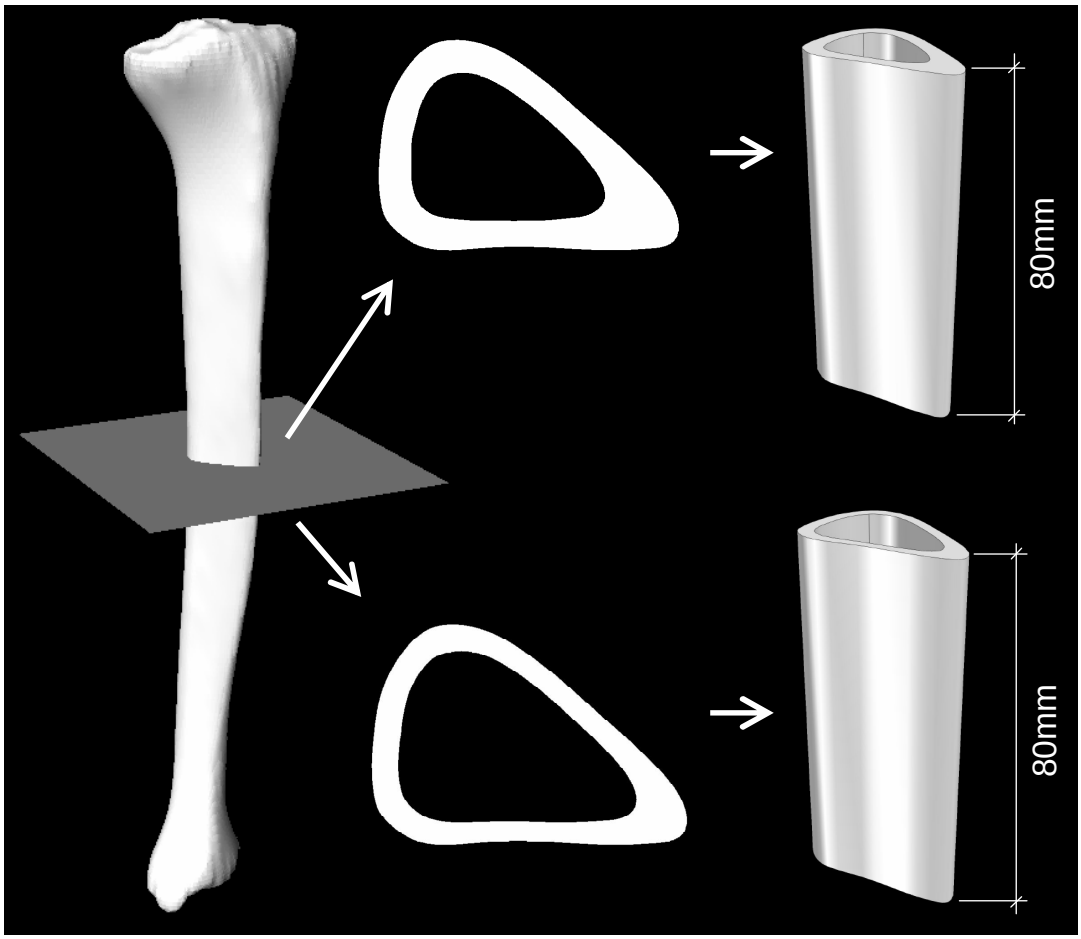

Figure 6-1: Creation of tibial midshaft fragments. An 'average' tibia was used to provide the midshaft cross-sections. This was adjusted to represent each age group, and extruded to a longitudinal length of 80 mm. The geometry of the young/middle-aged bone fragment is shown above the old bone fragment.

In addition to the geometry of young, middle-aged and old models, it was necessary to specify material properties which captured the effects of age and disease related bone loss on the mechanical properties of cortical bone tissue. To this end, results obtained in Chapter 3 for the elastic properties of female cortical bone from the anterior femoral midshaft were employed. This enabled the considerable variation of elastic constants between the periosteum and endosteum (Fig. 3-12(a,b)) to be included in the present study. Negligible heterogeneity was observed in longitudinal or circumferential directions within the tibia (Rho (1996)). Accordingly, the assigned properties were defined as homogeneous in these directions in the present study.

Table 6.1: Geometrical properties of the cortices of modelled bone fragments. The percentage deviation from the (scaled) data of Russo et al. (2006) are indicated in parentheses.

Sample description	Area (mm^2)	Thickness (mm)
Young/Middle-aged	319 (0.6 %)	5.10 (2.0%)
Old-aged	265 (1.9 %)	3.64 (1.6 %)

The use of an orthotropic material definition necessitated the specification of material orientations within the modelled bone fragments to identify the radial, circumferential, and longitudinal directions. Since bone fragments were formed by extruding a section in the longitudinal direction, all locations shared the orientation of the longitudinal axis. The circumferential and radial axes varied with position around the cortex and required definition as a distribution over the bone fragment. This was achieved by partitioning the bone fragment into regions which had similar surface curvature and assigning rectangular Cartesian (edge) or cylindrical (corner) material coordinate systems to them as appropriate. The resulting orientation of the radial axes in the young/middle-aged bone fragment is illustrated in Fig. 6-2. The circumferential axes was therefore uniquely defined; i.e. orthogonal to the determined radial and longitudinal axes.

The elastic constants in Chapter 3 were evaluated at two radial positions. These were located 10 % of the cortical thickness from the periosteal and endosteal surfaces respectively. Table 6.2 contains the elastic constants at these locations for the three age groups modelled in the present study. It was necessary to interpolate the elastic properties between these locations in a numerically consistent fashion such that realistic properties were applied at intermediate regions which retained the orthotropic symmetry of the source data. It should be noted that linear interpolation of each term of the material tensors can cause considerable error in the intermediate tensor terms, and can lead to loss of material symmetry. This is demonstrated in the following example originally presented by Rapoff and Haftka (2005).

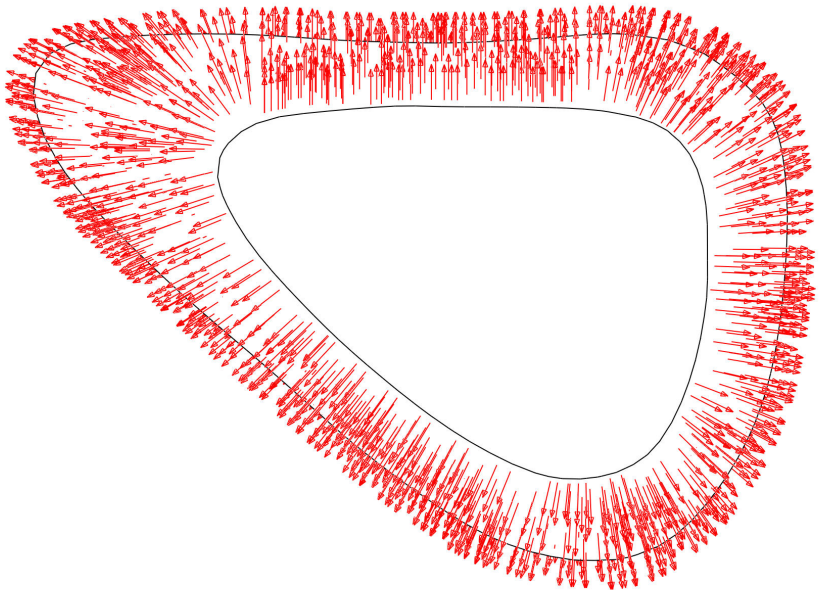

Figure 6-2: Orientation of the radial axis in tibial bone fragments, the circumferential and longitudinal axes were orthogonal in-plane, and out-of-plane respectively.

Considering a 2D situation in which isotropic elastic constants are known at two points; we seek an expression for the interpolated terms. If the Young's moduli and Poisson's ratios at the two locations are $E^{(1)}$, $E^{(2)}$, $\nu^{(1)}$, $\nu^{(2)}$ respectively, the shear moduli are

$$G^{(1)} = \frac{E^{(1)}}{2(1+\nu^{(1)})} \qquad G^{(2)} = \frac{E^{(2)}}{2(1+\nu^{(2)})} \tag{6.1}$$

Using a linear interpolation function with fractional variable β, the constants at the interpolated location can be calculated as

$$E^{(\beta)} = (1-\beta)E^{(1)} + \beta E^{(2)} \qquad \nu^{(\beta)} = (1-\beta)\nu^{(1)} + \beta\nu^{(2)}$$
$$G^{(\beta)} = (1-\beta)G^{(1)} + \beta G^{(2)} \tag{6.2}$$

If this produces a valid interpolation we would expect $G^{(\beta)}$ defined in 6.2 to

Table 6.2: Periosteal and endosteal orthotropic elastic constants specified in the tibial bone fragments. Note values were tensor interpolated at intermediate locations. Subscripts L, C, and R correspond to the longitudinal, circumferential and radial directions respectively. All moduli are in GPa.

	Young/healthy		Middle-aged/osteoporotic		Old/osteoporotic	
	Periosteum	Endosteum	Periosteum	Endosteum	Periosteum	Endosteum
E_R	18.552	16.602	16.219	8.492	12.865	3.151
E_C	18.752	17.086	17.142	10.690	14.584	6.017
E_L	22.409	21.366	21.121	15.496	19.276	11.213
G_{RC}	7.210	6.569	6.468	3.718	5.356	1.844
G_{RL}	6.947	6.430	6.315	3.885	5.395	2.174
G_{CL}	6.986	6.529	6.502	4.418	5.730	2.957
ν_{RC}	0.285	0.272	0.262	0.173	0.237	0.158
ν_{RL}	0.256	0.235	0.228	0.138	0.198	0.074
ν_{CL}	0.259	0.244	0.247	0.183	0.222	0.139

be equivalent to the shear modulus calculated using the interpolated Young's modulus and Poisson's ratio, $G^{(E\nu\beta)}$, defined as

$$G^{(E\nu\beta)} = \frac{(1-\beta)E^{(1)} + \beta E^{(2)}}{2(1 + (1-\beta)\nu^{(1)} + \beta\nu^{(2)})} \tag{6.3}$$

The difference between $G^{(\beta)}$ and $G^{(E\nu\beta)}$ is generally only zero when $\nu^{(1)} = \nu^{(2)}$. The error can be seen to increase as the Poisson's ratios diverge. This interpolation therefore produces intermediate material properties that do not, in general, preserve the degree of symmetry at the known locations. Furthermore, this method can lead to material properties that are not physically possible and can induce numerical errors when employed. This approach was particularly inappropriate for the current study since the Poisson's ratios differ considerably between some pairs of samples.

A more suitable interpolation in elastic constants can be achieved using the eigenvalues and eigenvectors of the original material elasticity (or compliance) tensors (Cowin and Yang, 1997; Yang et al., 1999; Rapoff and Haftka, 2005). The process is summarised here from Yang et al. (1999). This approach utilises a form of the elasticity tensor, originally expressed by Lord Kelvin (Thomson, 1856). The Kelvin form is best understood in relation to the more familiar Voigt

form of the elasticity tensor $\underset{\sim}{C}_V$, expressed as a 6×6 matrix. Using the Voigt form, Hookes law can be expressed as

$$\begin{aligned} \underset{\sim}{\sigma} &= \underset{\sim}{C}_V \underset{\sim}{\epsilon} \\ \begin{Bmatrix} \sigma_{11} \\ \sigma_{22} \\ \sigma_{33} \\ \sigma_{12} \\ \sigma_{23} \\ \sigma_{31} \end{Bmatrix} &= \begin{bmatrix} c_{11} & c_{12} & c_{13} & c_{14} & c_{15} & c_{16} \\ c_{21} & c_{22} & c_{23} & c_{24} & c_{25} & c_{26} \\ c_{31} & c_{32} & c_{33} & c_{34} & c_{35} & c_{36} \\ c_{41} & c_{42} & c_{43} & c_{44} & c_{45} & c_{46} \\ c_{51} & c_{52} & c_{53} & c_{54} & c_{55} & c_{56} \\ c_{61} & c_{62} & c_{63} & c_{64} & c_{65} & c_{66} \end{bmatrix} \begin{Bmatrix} \epsilon_{11} \\ \epsilon_{22} \\ \epsilon_{33} \\ 2\epsilon_{12} \\ 2\epsilon_{23} \\ 2\epsilon_{31} \end{Bmatrix} \end{aligned} \tag{6.4}$$

Re-writing 6.4 in the Kelvin form, the elasticity tensor becomes $\underset{\sim}{C}_K$

$$\begin{Bmatrix} \sigma_{11} \\ \sigma_{22} \\ \sigma_{33} \\ \sqrt{2}\sigma_{12} \\ \sqrt{2}\sigma_{23} \\ \sqrt{2}\sigma_{31} \end{Bmatrix} = \begin{bmatrix} c_{11} & c_{12} & c_{13} & \sqrt{2}c_{14} & \sqrt{2}c_{15} & \sqrt{2}c_{16} \\ c_{21} & c_{22} & c_{23} & \sqrt{2}c_{24} & \sqrt{2}c_{25} & \sqrt{2}c_{26} \\ c_{31} & c_{32} & c_{33} & \sqrt{2}c_{34} & \sqrt{2}c_{35} & \sqrt{2}c_{36} \\ \sqrt{2}c_{41} & \sqrt{2}c_{42} & \sqrt{2}c_{43} & 2c_{44} & 2c_{45} & 2c_{46} \\ \sqrt{2}c_{51} & \sqrt{2}c_{52} & \sqrt{2}c_{53} & 2c_{54} & 2c_{55} & 2c_{56} \\ \sqrt{2}c_{61} & \sqrt{2}c_{62} & \sqrt{2}c_{63} & 2c_{64} & 2c_{65} & 2c_{66} \end{bmatrix} \begin{Bmatrix} \epsilon_{11} \\ \epsilon_{22} \\ \epsilon_{33} \\ \sqrt{2}\epsilon_{12} \\ \sqrt{2}\epsilon_{23} \\ \sqrt{2}\epsilon_{31} \end{Bmatrix} \tag{6.5}$$

Following conversion of $\underset{\sim}{C}_V$ to $\underset{\sim}{C}_K$, the method of Rapoff and Haftka (2005) is used to interpolate between two known elasticity tensors. The nominal weighted average eigenvectors $\underset{\sim}{V}_i^{(na)}$ from the eigenvectors of the two known tensors $\underset{\sim}{V}_i^{(1)}, \underset{\sim}{V}_i^{(2)}$ (here $i = 1, 2, \ldots, 6$ and refers to the six eigenvectors or eigenvalues of $\underset{\sim}{C}_K$) are

$$\underset{\sim}{V}_i^{(na)} = (1 - \beta)\underset{\sim}{V}_i^{(1)} + \beta \underset{\sim}{V}_i^{(2)} \tag{6.6}$$

Where β is the interpolation variable. It has been demonstrated Cowin and Yang (1997) that the optimal average eigenvector can be found by minimising the distance between each eigenvector and the set of corresponding eigenvectors of the original elasticity tensors

$$\underset{\sim}{V}_i^{(avg)} = \left(\sum_{j=1}^{6} \underset{\sim}{V}_j^{(na)} \underset{\sim}{V}_j^{(na)^T} \right)^{-\frac{1}{2}} \underset{\sim}{V}_i^{(na)} \tag{6.7}$$

Denoting the six eigenvalues of the known elasticity tensors (in the form of equation 6.5) as $\Lambda_i^{(1)}$ and $\Lambda_i^{(2)}$, interpolated eigenvalues referred to the average eigenvectors can then be generated as

$$\Lambda_j^{(avg)} = (1-\beta) \sum_{i=1}^{6} \Lambda_i^{(1)} \left[\underset{\sim}{V}_i^{(1)} \underset{\sim}{V}_j^{(avg)} \right]^2 + \beta \sum_{i=1}^{6} \Lambda_i^{(2)} \left[\underset{\sim}{V}_i^{(2)} \underset{\sim}{V}_j^{(avg)} \right]^2 \tag{6.8}$$

The interpolated elasticity tensor, still in Kelvin notation, is therefore

$$\underset{\sim}{C}_K = \sum_{i=1}^{6} \Lambda_i^{(avg)} \left(\underset{\sim}{V}_i^{(avg)} \underset{\sim}{V}_i^{(avg)^T} \right) \tag{6.9}$$

Upon conversion of $\underset{\sim}{C}_K$ to Voigt notation, appropriately interpolated elastic constants can be extracted. This method was used in the present study because it preserved the orthotropic symmetry of the source data and produced material properties that made sense from a mechanics viewpoint.

It should be noted that the source data was measured at locations 10 % of the cortical thickness from the endosteum and periosteum. The interpolation algorithm detailed by equations 6.4–6.9 was therefore used to interpolate between these locations. It was not appropriate to extrapolate the data outside of this region since this would produce elastic constants both larger and smaller than those observed in Chapter 3. Locations between the endosteum and the 10 % sub-endosteal sampling site were assigned identical values equal to those at the 10 % sampling site. Locations between the periosteum and the 10 % sub-periosteal sampling site were assigned properties similarly. To interpolate between the two sites it was necessary to calculate the position of intermediate locations normalised with respect to the position of the sampling sites.

The initial strategy to calculate the normalised locations was to run a nom-

inal 'heat transfer' analysis on the geometry of the tibial section. This could be contrived effectively to assign a 'temperature' at each integration point which varied from 1 at the periosteal aspect to 0 at the endosteal. The value of temperature (between 0 and 1) could thus be used to calculate the normalised position through the cortex (β in the preceding equations). This method was successfully implemented but was abandoned due to several limitations. The first was that this approach required the creation of an extra, possibly unnecessary FE analysis which was time consuming. In particular, holes for implants had to be 'filled' for the heat transfer analysis to avoid local non-linearities in the temperature gradient. More serious was the fact that this approach required the interpolation, at runtime, of temperatures from the mesh used in the heat transfer analysis to that used in the mechanical analysis. This was unexpectedly computationally expensive, e.g. it added 3 hours to the initialisation stage of a typical analysis. Furthermore, the temperature gradient was considerably non-linear at corners of the tibial sections, which induced distortions in the resulting variation of elasticity tensor components.

To avoid the discussed limitations associated with the initial 'heat transfer' approach, the following geometrical methodology was applied in the remainder of the study. Since the tibial profiles were generated from one 2D cross-section (extruded in the longitudinal direction), it was possible simply to assign the position using the 2D coordinates of all integration points in the model. A map was required which contained the proportional position of points within the cortex. This map could be used to interpolate the values at each integration point. Since there were only two distinct profiles in use (young/middle-aged and old), this was relatively inexpensive to achieve. The following process was followed:

a. Generate binary inner and outer profiles of the tibial cross-section to enable interpretation by analysis program (Fig. 6-3(a,b)).

b. Calculate the Euclidean distance transform (EDT) of each profile to provide the distance from each point (i) in the cortex to the periosteal and endosteal aspects; i.e. EDT_p^i and EDT_e^i (p and e refer to the periosteal and endosteal profiles respectively).

c. Define the thickness at i as $\mathrm{Th}^i = \mathrm{EDT}_p^i + \mathrm{EDT}_e^i$ (Fig. 6-3(c)). This is the sum of the minimal distance from i to the periosteal and endosteal aspects.

d. Evaluate the normalised position at i as $\beta = \left[\mathrm{EDT}_p^i + (\mathrm{Th}^i - \mathrm{EDT}_e^i)\right] / 2\mathrm{Th}^i$ by linear interpolation, and set β to 0 or 1 if i lies outside the 10% sub-periosteal or 10% sub-endosteal aspects respectively (Fig. 6-3(d)).

e. Write the generated 2D matrix to the material subroutine and use as a lookup table during FE analysis.

The generated lookup table was defined at a considerably higher resolution than the FE mesh to ensure a good approximation was achieved. Indeed, the minimum number of grid points through the cortex was 60 which corresponded to 18 integration points over the same distance. Under these conditions, the maximum positional interpolation error was calculated as 0.79 %, indicating that the method was very robust.

In Chapter 5 the development of a strain-based plasticity algorithm was described. This algorithm was used in the present study to represent the post-elastic properties of bone. It represented the ideal candidate for several reasons. Primarily, it ensured that the present analyses reflected the realistic isotropic strain- (not stress) based failure properties of bone (Keyak and Rossi, 2000; Fenech and Keaveny, 1999; Vahey et al., 1987; Keaveny et al., 1994; Ford et al., 1996; Bayraktar et al., 2004; Gupta et al., 2007; Mercer et al., 2006; Ebacher et al., 2007; Schileo et al., 2008; Oden et al., 1999). The algorithm also simplified the modelling process since its isotropic yield surface did not require orientation with tissue directions which would be necessary with anisotropic yield surfaces. Furthermore, the algorithm was numerically efficient; only a single plastic return to the yield surface was required for any elastic predictor state, avoiding the iterative return mapping required with non-linear surfaces. Bone post-elastic behaviour in the present study was fully defined by two parameters: the tensile and compressive yield strains. It has been demonstrated that a maximum principal strain criterion was able to predict failure risk and fracture location (Schileo et al., 2008). A range of yield strain values have been reported, some of which are listed in Table 6.3. This study employed yield strains of 0.5% and 0.7% in tension and compression respectively. These values represent the lower bound of reported values and can therefore be considered conservative.

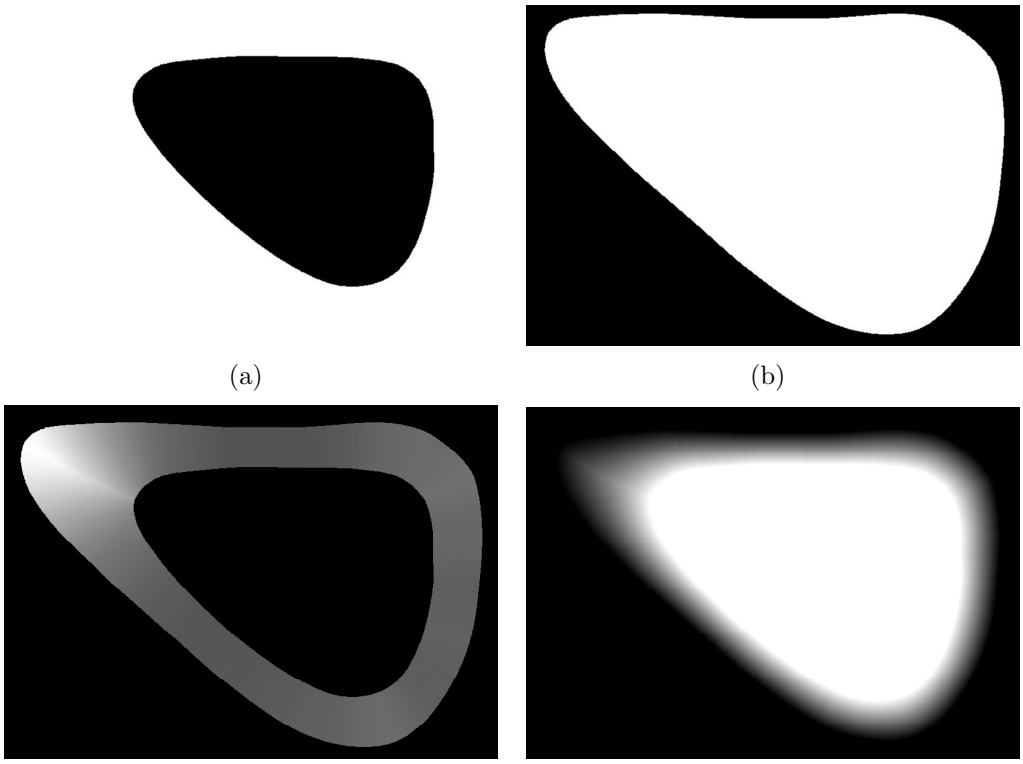

Figure 6-3: Evaluation of the normalised position through the cortex for interpolation of elastic constants. a) binary endosteal profile, b) binary periosteal profile, c) local thickness from EDT (lighter shaded areas indicate greater thickness), d) proportional position - black areas have periosteal properties, white - endosteal, grey-scale-proportional in -between.

6.2.2 Half-pin definition

Numerous designs of external fixation half-pins are available from various manufacturers of orthopaedic implants. The present study sought to model a general case. In the preliminary stage it was thought that modelling of the pin threads was not required to capture the overall behaviour of the fixed bone fragment. Idealised, smooth cylindrical pins were modelled instead. In these simplified models the anchoring of the pins in the bone was achieved using an arbitrarily large coefficient of friction between the pins and bone. It was intended to prevent movement of the pins along their tracks. This approach greatly simplified both the modelling and the analysis phases. However, errors frequently occurred in these analyses since frictional stresses tended to be large (resulting from the artificially high friction coefficient) and to become concentrated at individual nodes

Table 6.3: Yield strains of bone reported in the literature.

	Trabecular		Cortical	
Study	Tensile	Compressive	Tensile	Compressive
Bayraktar et al. (2004)	0.64%	1.04%	0.73%	-
Mercer et al. (2006)	-	-	0.6%	1.1%
Ebacher et al. (2007)[a]	-	-	0.5%	0.7%
Courtney et al. (1996)	-	-	0.38%	-

[a] estimated from Figure 3.

on the pin-bone interfaces. This often lead to distorted elements. It was also possible for the pins to displace along their tracks where they were not in contact, or where normal contact stresses were low; this was unrealistic since the pin threads would resist such displacements in reality. The pin-bone displacements were not considered sufficiently realistic to capture the interfacial conditions accurately. It was therefore decided to incorporate the pin threads into further analyses.

The geometry of a typical 6 mm half-pin was measured using callipers and a silhouette-enlarging light-box. A photograph of the original is shown in Fig. 6-4(a). The pin comprised an unthreaded section of 6 mm diameter, which tapered into a threaded section. The threaded section consisted of a tapered core with threads wound helically around it. The core diameter varied from 4.05 mm to 3.63 mm at the tip. The threads protruded from the core to produce a constant (non-tapered) outer diameter of 4.50 mm. The separation between threads was 1.4 mm. The thickness of each thread at the join with the core was 0.7 mm.

The described geometry was idealised in the generated models in order to simplify the meshing process and produce good quality elements. The idealised geometry did not include the tapered core and did not have rounded thread tips. It was also decided not to model the threads as wound helically around the core; helically wound threads were found to produce 'slivers' of cortex that were difficult or impossible to mesh robustly. The idealised half-pin is illustrated with dimensions in Figure 6-4(b,c). To reduce mesh complexity only those threads that made contact with bone fragments were retained in each model.

Stainless steel half-pins are used most widely in fracture fixation. In addition less stiff materials such as titanium are thought to be beneficial for reducing

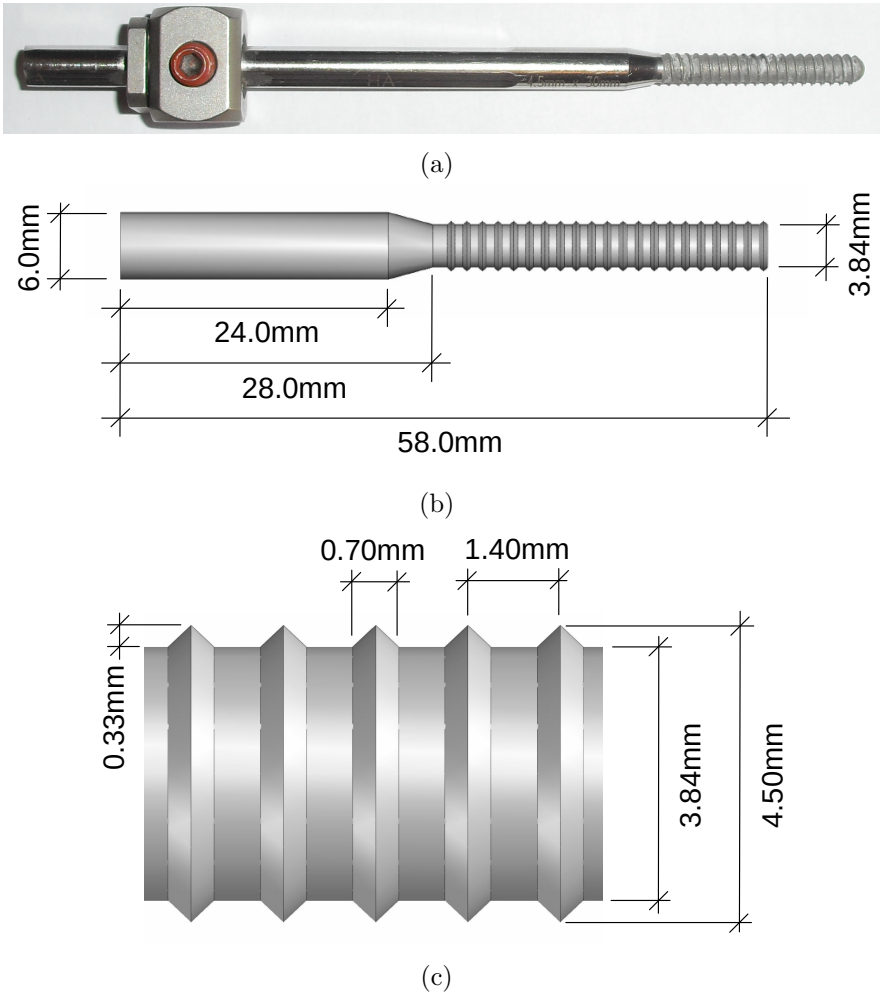

Figure 6-4: Clinical (a) and idealised (b) external fixation half-pins, threaded region expanded (c).

bone damage associated with stress-shielding at the implant interface (Gefen, 2002; Zanetti et al., 2009). All models were analysed using stainless steel elastic properties for the half-pins. Analysis of the old-aged model was repeated with titanium properties to investigate the effect of using half-pins of a lower stiffness material. Both metals were modelled as isotropic and limited to the elastic regime. The Young's modulus was assigned as 180 GPa and 105 GPa for stainless steel and titanium respectively, Poisson's ratio was 0.3 in both materials (Lim et al., 1996; Chen et al., 2003; Zanetti et al., 2009).

External fixation implant insertion sites are restricted to 'safe corridors' to avoid causing damage, discomfort or reduced function to the soft tissues (blood

vessels, muscles). Behrens and Searls (1986) noted that half-pin placement should be limited to the subcutaneous (close to the skin) regions of the tibia wherever possible. In the tibial midshaft the safe corridor is limited to 140°, centred on the transverse medial face. In the present study half-pins were oriented such that they entered orthogonally to the transverse medial face of the tibia and fully penetrated the tibia to emerge on the transverse lateral face. This orientation represents the approximate mid-point of the 'safe corridor' and can therefore be considered a general case for the tibial midshaft. The half-pin length was determined by the bone thickness and the requirement to typically leave a 30 mm gap between the skin and the external fixator. This gap was necessary to enable access for cleaning, dressing and identification of infection at the entrance site. The total half-pin length as modelled was therefore 58 mm. This included an assumed 3 mm of skin and other tissues at the entrance site. The half-pin installation geometry is illustrated in Fig. 6-5. Half-pins nearest to and furthest from the fracture site will be referred to as the near and far pins respectively throughout this study. Half-pins were equally spaced in the longitudinal direction; the far and near pins were separated by 40 mm. The half-pins were centred on the midpoint of the 80 mm tibial bone fragments, such that the fracture gap was separated from the nearest half-pin by 20 mm in the longitudinal direction.

6.2.3 FE analyses

Implicit integration was initially used in the present study. However, a stable solution required the restraint of all degrees of freedom for a least a single node of both the bone fragment and half-pins. This represented an over-restraint compared to reality. Therefore, all analyses were solved using explicit integration. Its robust treatment of contact mechanics, coupled with the ability to model free-bodies, enabled the specification of realistic boundary conditions. In previous FE studies it has generally been assumed that the interactions between half-pins and bone can be captured with fully tied constraints (Huiskes et al., 1985; Juan et al., 1992; Oni et al., 1993; Prat et al., 1994; Lauer et al., 2000; Shahar and Shani, 2004). In fact, this represents an over-simplification, enabling the possibility of tensile stresses being transferred across the pin-bone interface. In reality load could only be transmitted by compressive stresses or surface tractions. Such

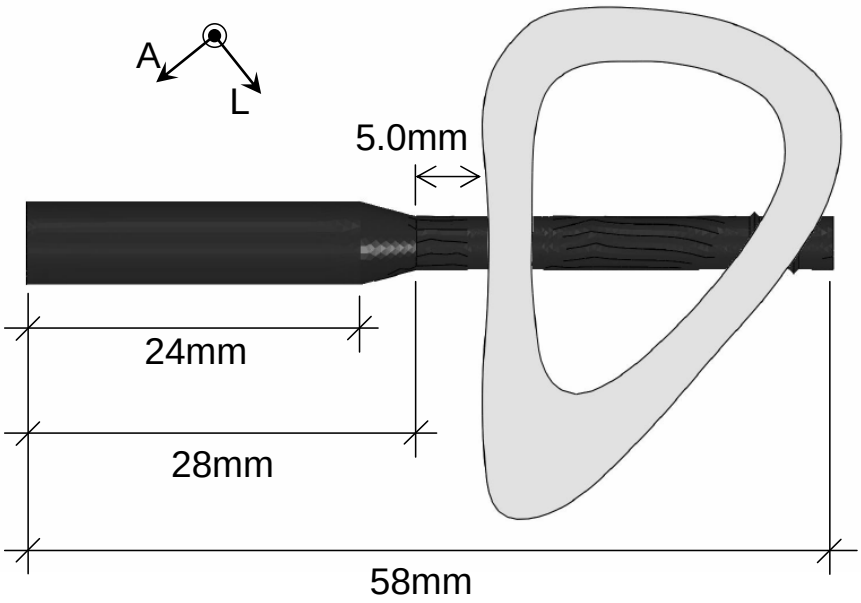

Figure 6-5: Half-pin insertion dimensions as modelled. Note the 33 mm of exposed half-pin comprises 3 mm of skin and tissue and 30 mm for external access. Axes indicate the anterior (A) and left-lateral (L) anatomical directions.

.

effects would be expected to produce unrealistic distributions of load between tensile and compressive regions. The present use of contact mechanics enabled surface separation and therefore represented an improvement on previous FE studies of fracture fixation. General contact was specified; all surfaces that came into contact resisted penetration and transferred stresses across their interface. Zero friction was assumed at all interfaces. All analyses were solved with the commercial FE package Abaqus (Dassault Systemes; Simulia, Providence, RI, USA).

Vertical loading of 700 N was applied as a pressure on the superior face of the tibial bone fragment to represent 100 % of body weight. No other boundary conditions were assigned to the bone fragments; they were solely restrained by the fixation half-pins. The half-pins were fully fixed against all displacement degrees of freedom at their far ends, where they were considered to meet the longitudinal fixator component. It was considered reasonable to assume that external fixator frames or bars were considerably stiffer than the implanted half-pins, and thus provide effectively rigid restraints.

It was necessary to assess the relative risk of half-pin loosening both between implants in the different fixator setups, and when applied to different age groups. After loading, the volume of yielded bone observed around implants was used as an indicator of loosening risk. This volume was calculated by summation of the element volume represented by the integration points which had non-zero plastic strain.

The inclusion of material property heterogeneity, tissue plasticity, large deformation theory and contact mechanics were all expected to induce localised non-linearity. To ensure accurate (second-order) numerical integration, ten-noded tetrahedral elements were used for all components in the present study. The presence of a mid-side node on these elements also provided the geometrical advantage of being able to conform to complex surfaces at the pin-bone interface better than linear elements. The FE meshes were complex; they comprised approximately 100,000 elements, with 1,200,000 degrees of freedom. Mesh design required considerable effort to ensure that they were optimized for computational efficiency but were not an excessive source of numerical error (defined here as more than 5 %). The critical region for the present models was at the pin-bone interface. Mesh optimization therefore focused on this location. It was important to keep the element quality and size high enough to ensure accurate integration. Conversely, a high mesh resolution was required to enable a numerical solution to be found; at lower resolutions contact surfaces became 'jagged', leading to unrealistic interactions. The selected mesh resolution was arrived at by a trial-and-error approach. The average element edge length at the pin-bone interface was 0.5 mm. It was necessary to check whether the results were mesh-dependent at the selected mesh resolution. An analysis was conducted of a model using elements of half the average edge length used for other analyses. The difference in the volume of yielded bone and bone fragment displacement were 0.4 % and 1.6 % respectively, which indicated that the selected mesh resolution provided robust numerical analysis.

6.3 Results

Renderings of the old bone fragments, loaded while under fixation with two and three half-pins are presented in Fig. 6-6. Regions with non-zero plastic strain are highlighted in red. Bone yielding was concentrated at the pin entrance sites; peri-implant yielding at the opposite cortex was only observed with the old bone fragments illustrated, and in these cases only small volumes were observed. The unscaled images show the relatively small fragment displacements which were observed; it was necessary to scale the deformations by 30 times to illustrate the deformation mode (see Fig. 6-6(c,f)). The half-pins deformed in contra-flexure; typical cantilever displacements were resisted by the structural continuity derived from the presence of the bone fragment. It was also observed that a couple was generated between the far and near half-pins such that they applied tensile and compressive axial forces respectively, to resist the rigid body rotation of the bone fragment. This resulted in considerable load transfer in the radial direction of the bone fragment and induced the shearing deformations observed in the bone fragment between the far and near half-pins.

The pattern of yielded bone was compared between age-groups at the entrance site of the lowest half-pin. Close-up images at this location are presented in Fig. 6-7 with two-pin (a–c) and three-pin (d–f) fixation. It was observed that peri-implant yielding only occurred on the superior side of the half-pins. Bone yielding initiated on the periosteal side of the half-pin threads. In the case of young and middle-aged groups yielding was confined to the periosteal half of the cortex. In the old group however, yielding propagated through the entire cortical thickness in both two and three-pin fixation.

The variation of minimum principal stress and minimum principal total strain at the entrant cortex of the near pin is presented in Fig. 6-8. At the pin site shown, the minimum principal stresses and strains were approximately oriented in the longitudinal direction. The largest compressive stresses were concentrated at the periosteum. A similar variation of minimum principal stress and total strain with distance from the pin was observed in all age-groups. At distances greater than 1 mm from the pin, the stresses and total strains were slightly greater in the old group. Near to the pin however, the tissue strains exceeded the compressive

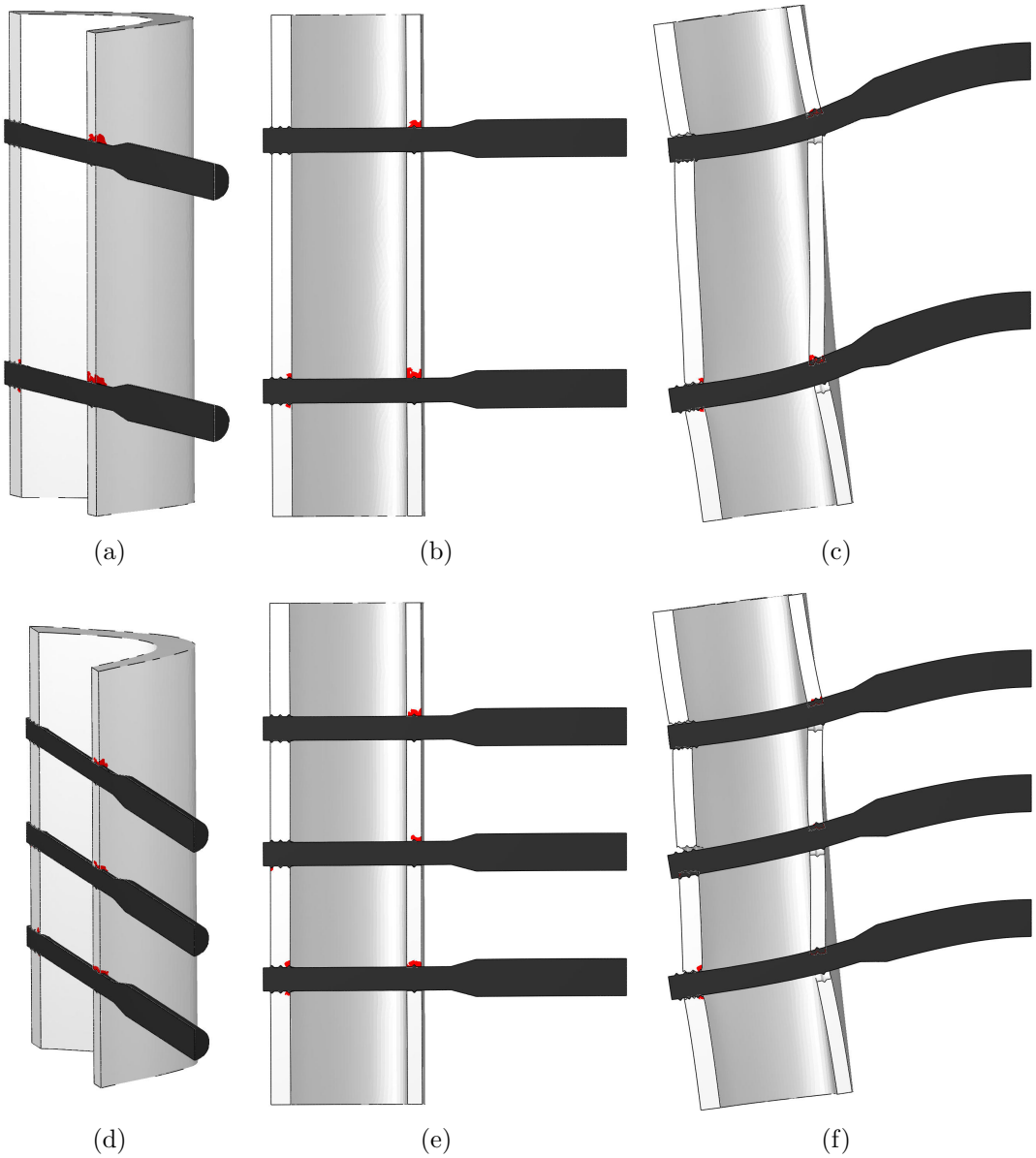

Figure 6-6: Renderings of the old group in two and three-pin fixation, under the applied vertical loading. Unscaled perspective view (a,d), unscaled elevation view (b,e), 30 times deformation, elevation view (c,f). Note: images are cut-through at the midpoint of the half-pins, regions of yielded bone are highlighted in red.

yield strain and the stresses decreased with increased age corresponding to their stiffness in the longitudinal direction (see Table 6.2).

A couple was formed between the far and near pins in all analyses. This behaviour can be seen in the action of the radial stresses at the pin thread sites

in Fig. 6-9. Pull-out stresses were observed at the superior cortex (far pin) and push-in stress at the inferior cortex (near pin).

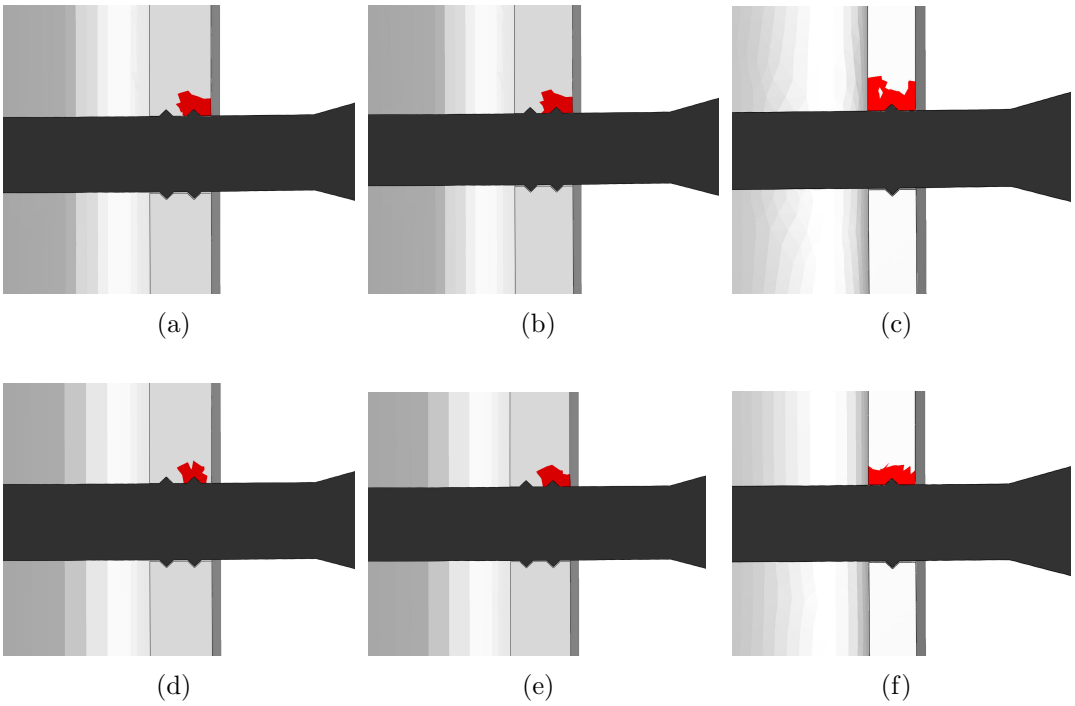

Figure 6-7: Peri-implant yielded bone (highlighted in red) in two and three-pin fixation of young (a,d), middle-aged (b,e) and old (c,f) bone fragments. The upper and lower rows contain images from two and three-pin fixation respectively. All images correspond to the near half-pin, which was nearest to the fracture gap.

The volume of peri-implant yielded bone was evaluated for all half-pins; these are plotted in Fig. 6-10 for two-pin and three-pin fixation. It was observed that greater proximity to the fracture gap resulted in greater volumes of peri-implant yielded bone. Indeed, in two-pin fixation approximately 2.0 times the volume of yielded bone was observed at the near pin site than at the far pin site. Similarly, the pin nearest the fracture in three-pin fixation produced approximately 1.3–2.0 times and 2.0–7.0 times more yielded bone than at the middle and far sites respectively. Ageing was also associated with a greater volume of peri-implant yielded bone in both two and three-pin fixation; approximately 3 times the volume of yielded bone was observed in the old group than was observed in the young group. The efficacy of employing additional half-pins to increase fixation implant stability was investigated. By comparing Fig. 6-10(a) and (b) it was observed that the use of a third half-pin substantially reduced the volume of

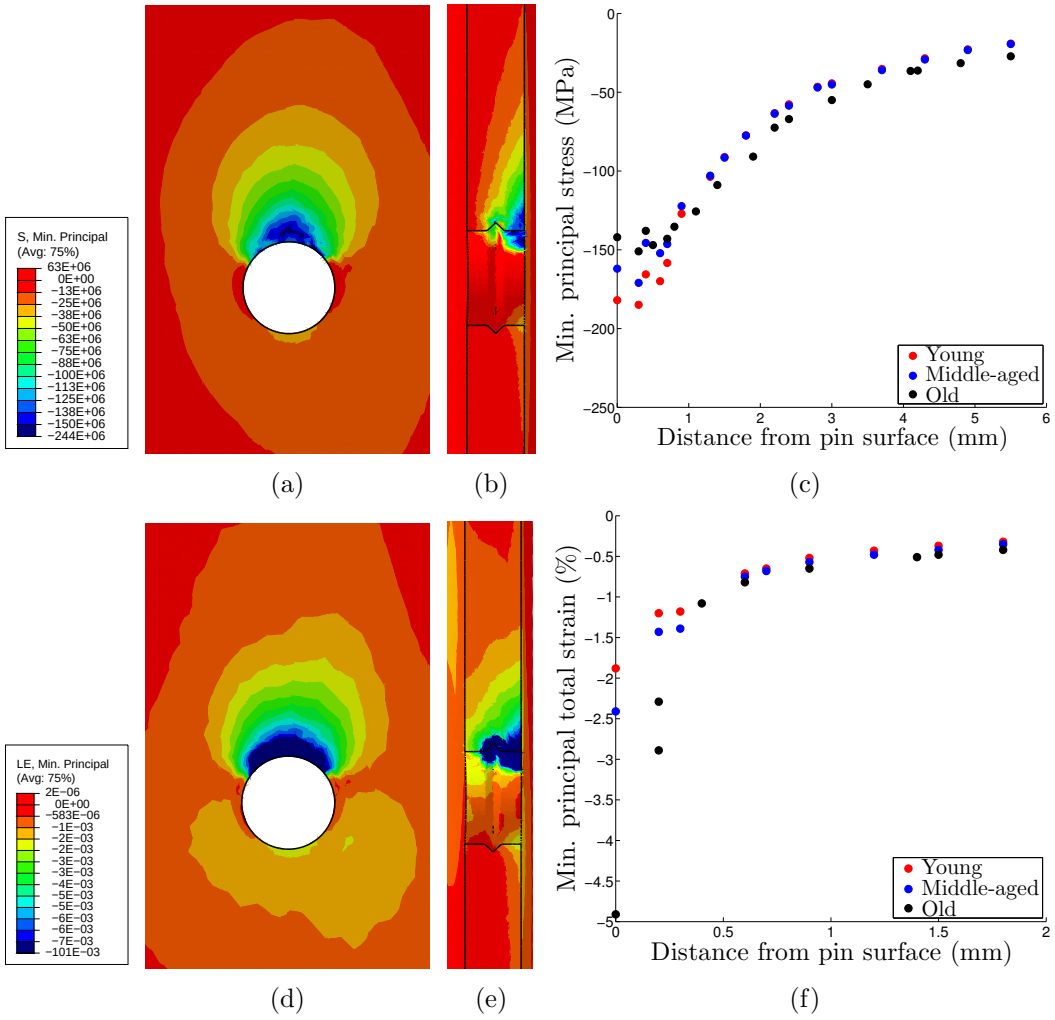

Figure 6-8: Minimum principal stress (a-c) and total strain (d-f) at the pin-bone interface of the near pin entrant cortex in the old group with two-pin fixation. Contours on elevation views (a,d) and cut-through views (b,e). The variation with distance from the pin surface (along the periosteum) for all age groups (c,f). Note the stress contours of (a,b) are in Pa.

peri-implant yielded bone; yielded volumes reduced by 66–75 % from the two to three-pin analyses. However, it can be seen in Fig. 6-11(a) that the use of a third half-pin did not prevent yielding of the full cortical thickness at the lowest pin site. Furthermore, only minimal reduction in the yielded proportion of the cortical thickness was observed at other insertion sites. The effect of ageing on bone fragment displacements can be observed in Fig. 6-11(b). It was found that ageing was associated with increased displacements; the old bone fragments displaced by approximately 21–25 % more than the young bone fragments.

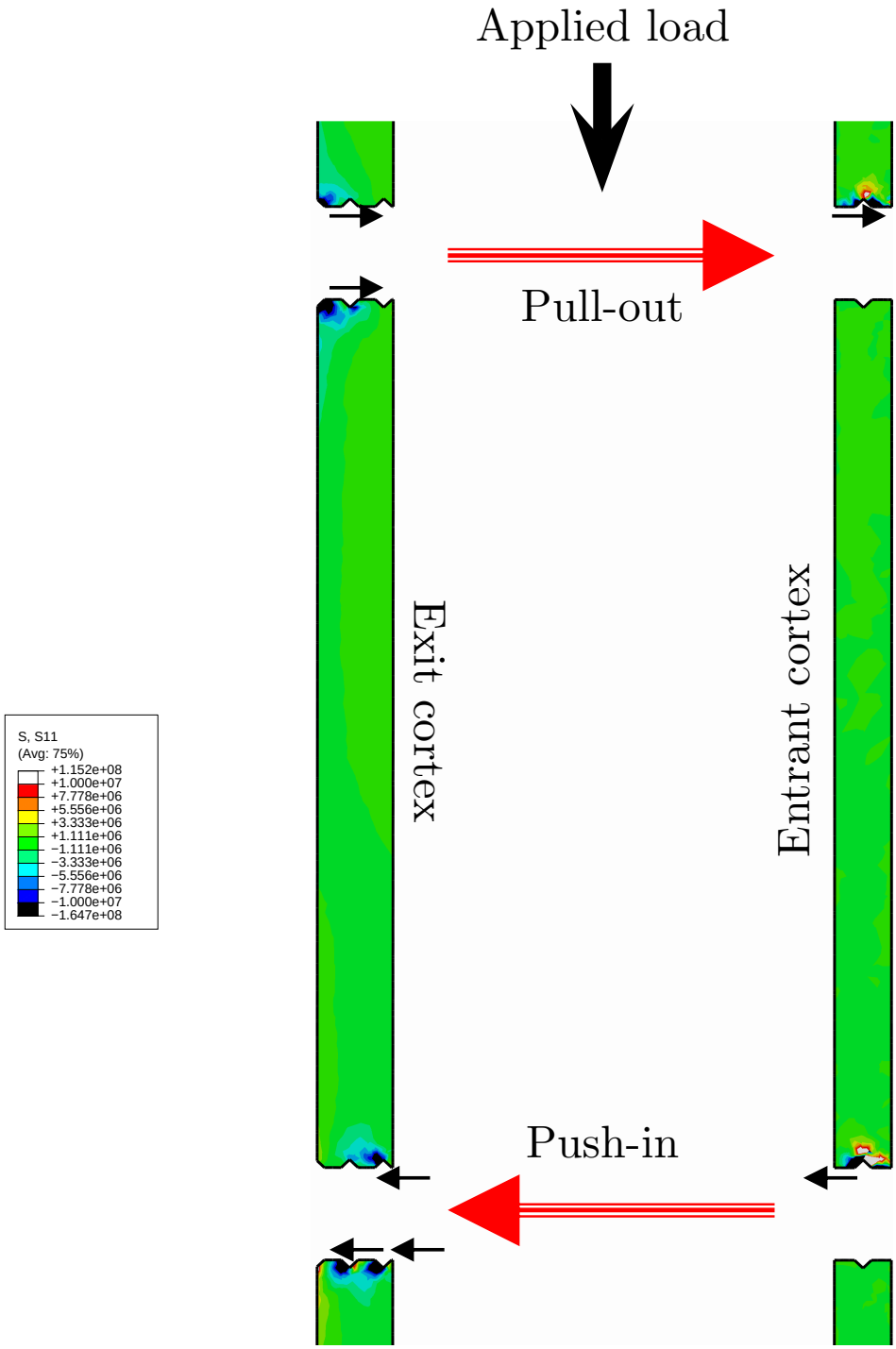

Figure 6-9: Radial stresses at the pin-bone interfaces at the far and near sites. The pin threads applied pull-out stresses at the far pin and push-in stresses at the near pin. The direction of thread forces are indicated by black arrows. Note, stresses are in Pa, the external fixator lies to the right of the image and half-pins have not been drawn.

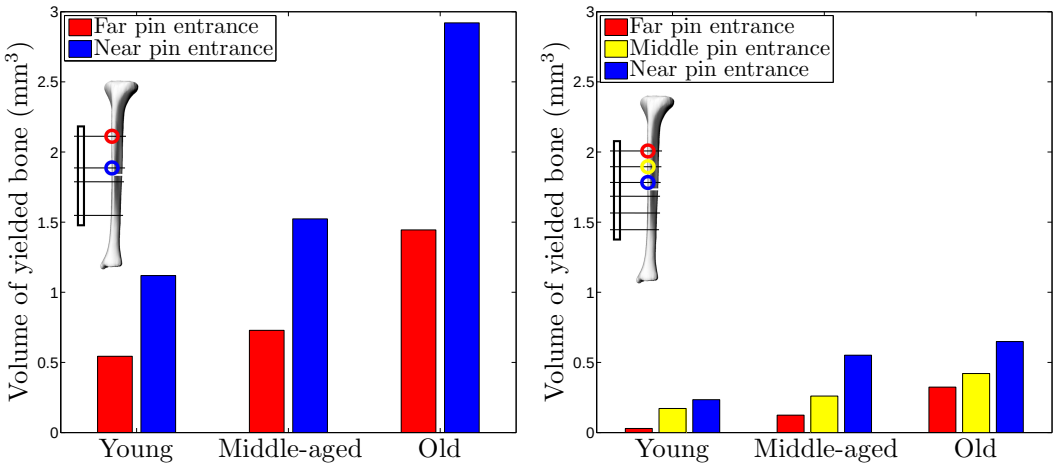

Figure 6-10: Peri-implant yielded bone volume in two and three-pin fixation of young, middle-aged and old bone fragments. The volume of yielded bone increased with ageing. The volume of yielded bone increased with greater proximity to the fracture gap.

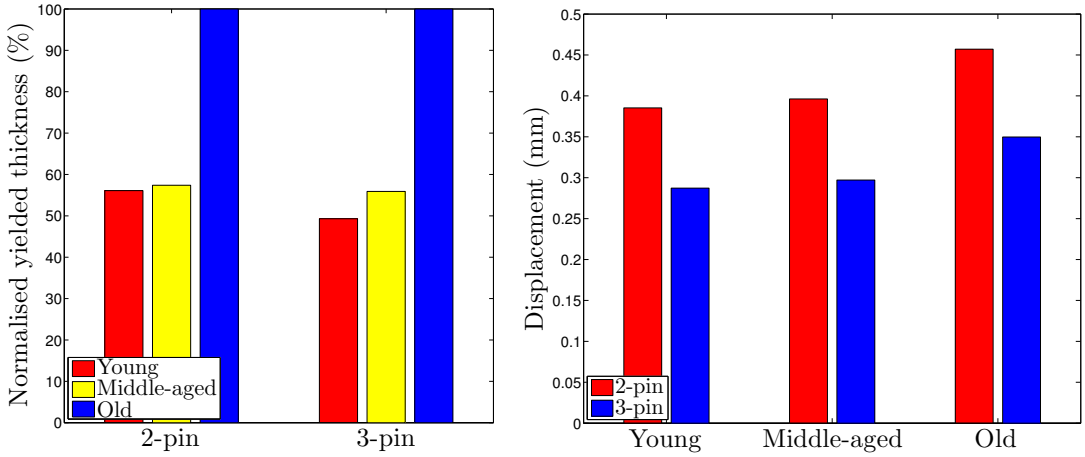

(a) (b)

Figure 6-11: Normalised thickness of yielded bone (a), and bone fragment displacements (b) in half-pin fixation. The full cortical thickness was yielded in the old bone fragment with both two and three-pin fixation. Ageing produced a relatively small increase in bone fragment displacement.

The effect of half-pins with reduced Young's modulus on implant stability was investigated. The volume of peri-implant yielded bone in the old bone fragment fixed with 2 stainless steel and (lower modulus) titanium pins is presented in Fig. 6-12. It was found that the use of lower stiffness titanium half-pins resulted in approximately 60–65 % greater volumes of peri-implant yielded bone.

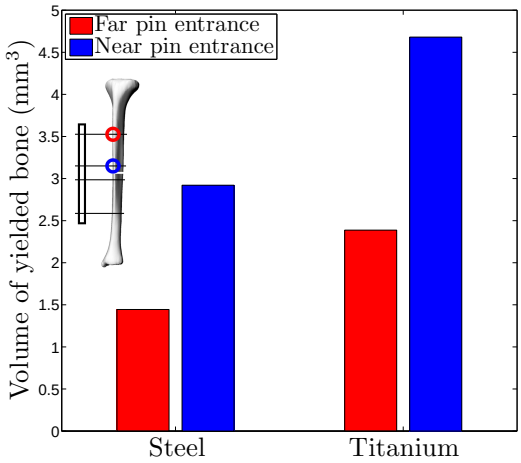

Figure 6-12: Comparison of peri-implant yielded bone volume with stainless steel and titanium half-pins. The plotted volumes correspond to two-pin fixation of the old bone fragment. Titanium half-pins induced a substantially greater volume of yielded bone than stainless steel half-pins.

6.4 Discussion

The aim of this study was to provide insight into the mechanical cause of half-pin loosening through detailed FE analyses by including appropriate bone-implant interaction and the elastic and post-elastic properties of bone. Of particular interest was the effect of age-related bone degradation on the risk of half-pin loosening. A number of conclusions of relevance to clinical practice can be postulated from the results presented.

In this study bone yielding was used as a predictor of half-pin loosening. The relationship between yielding and loosening is briefly considered before the specific results are discussed. Where bone yielding occurred, this indicated that irrecoverable strains had developed. In real bone tissue such irrecoverable strains

would take the form of localised displacements at discontinuities such as microcracks, which would also reduce the material stiffness (George and Vashishth, 2005). If the level of loading continued, damage would increase faster than natural healing could repair it and tissue failure would eventually occur. If a sufficiently large region was to fail then the pin anchorage provided by the remaining bone would reduce to a level where loosening became likely. It therefore seemed reasonable to consider a larger volume of yielded bone as indicative of an increased risk of half-pin loosening. It was also necessary to take into account the location of the yielded bone; for example, if bone yielded around a half-pin to a distance greater than the thread length through the full cortex, this would be more likely to result in pin instability than the same volume of yielded bone located exclusively at the periosteum. Furthermore, the ability of bone to absorb energy through post-elastic deformation before ultimate failure, and its ultimate strain are both known to reduce substantially with ageing (Currey, 1979; McCalden et al., 1993). Such effects were (at least partially) accounted for through the present combination of age-varied elastic properties and the strain-based yield criterion. However, the plastic strain was not constrained to an ultimate value. In the present study it can be inferred that an equivalent volume of yielded bone would represent a higher likelihood of failure in the old model than in the two younger models since the ultimate strain of the former would be reached earlier.

It was observed that the minimum principal stresses were concentrated at the periosteum of the entrant cortex. This was similar to the observation of a previous study (Huiskes et al., 1985). However, the same study also reported considerable tensile stresses at the endosteum of the pin-bone interface. In the absence of osseointegration (as is the case in the first weeks post-op) tensile stresses could not exist at the pin-bone interface. Another study identified large stresses at the entrant site of a half-pin installed in a block of cancellous bone under vertical loading (Board et al., 2007). However, unlike the present study, the highest stresses were observed as much as 15 mm to the side of the pin site at a vertical distance of 3 mm from the pin. It was not clear why the largest stresses were observed at such a large lateral distance from the pin in that study. In this study, the variation of minimum principal stress with longitudinal position was found to be considerable (see Fig. 6-8(c)). The 3 mm vertical offset, at which Board et al. (2007) took their measurements, was associated with a reduction of peak stresses of approximately 66 %.

The volume of yielded bone increased considerably with ageing; approximately 3 times the yielded volume was observed in old cases than young cases. The distribution of yielded bone also changed with ageing; in young and middle-aged cases the yielded bone was concentrated near to the periosteum; in old cases bone yielding progressed through the full cortex, to a depth greater than the thread height. These results indicated that age-related bone degradation can substantially increase the likelihood of half-pin loosening. Similar to clinical experience (Tencer, 2002), achieving stable fixation of older groups would appear to be a greater challenge than with younger groups. It should be noted that age-related changes were included in the present model in two ways, both of which contributed to the reduced resistance of older bone to yielding around half-pins. Firstly, the cortical thickness of old models was reduced from the younger cases. Since there was less pin-bone intersection area for the same load to be transferred, the stresses transferred to the bone necessarily increased. This can be seen in the higher stresses in the old group than the young and middle-aged groups at locations more than 1 mm from the pin site in Fig. 6-8(c). Secondly, the orthotropic elastic constants were reduced to reflect the increased porosity of older bone. This resulted in higher strains at equivalent stresses. The strain raising effect of both of these age-related changes increased the likelihood of exceeding the yield strain and thereby predicting half-pin loosening. It was also observed that ageing resulted in 21–25 % greater displacement of the bone fragment. Since the stiffness of the half-pins did not vary with ageing this implied that the increased displacements resulted from the reduced mechanical properties of the bone fragments. Furthermore, as noted in Fig. 6-9, a couple formed between the far and near pins such that they transferred transverse tensile and compressive forces to the bone fragment respectively. Hence, the bone fragment was subjected to shear loading between the far and near half-pin locations. It is therefore proposed that the increased fragment displacements observed with ageing resulted from the coinciding reduction of cortical area and orthotropic elastic constants. It should also be noted that axial forces in the half-pins necessarily induced radial loading at the pin-bone interface. In Chapter 3, the Young's modulus in this direction was found to reduce more rapidly with ageing than in the other directions. Half-pin fixation therefore applies loading in the direction least adapted to loading (Currey, 2003), and most likely to lead to failure in patients with bone loss.

At all pin locations bone yielding initiated between the periosteal thread and the periosteum, before progressing towards the endosteum. This behaviour can be explained by the greater proximity of the periosteum to the half-pin support. The half-pins followed a cantilever-like bending deformation. In these conditions the resistance of a cross-section to vertical displacement increases as the third power of the proximity to the support point. Half-pins therefore provided greater resistance to vertical displacement at the entrant periosteum than at the corresponding endosteum. This concentrated the transfer of load at the periosteal portion of the pin-bone interface, which therefore induced higher stresses and strains, leading to an earlier onset of yielding. Increased loading beyond the periosteum yield point caused stresses to be transferred to other locations which retained further load bearing capacity; i.e. more endosteal locations, or the opposite cortex.

Current practice prescribes several methods to stabilise cases where pin instability is expected or experienced; increase pin diameters (Chao et al., 1982), compress the fracture site (Weaver and Chalmers, 1966), use more pins (Wu et al., 1984), increase the fixator stiffness (Chao et al., 1982), and use two-plane fixation (Williams et al., 1987). These methods are all intended to increase fixation rigidity (Pettine et al., 1993). The efficacy of using more half-pins was confirmed by the present results; the use of an extra half-pin reduced the yielded bone volume by approximately 66–75 %. While this implied a reduced risk of loosening, it should be noted that yielding continued to occur through the full cortical thickness.

Half-pin location was found to affect the risk of loosening. It was observed that the volume of yielded bone increased with proximity to the fracture gap. Approximately 2 times more peri-implant yielded bone was associated with half-pins immediately neighbouring the fracture gap compared to those most distant from it. Targeting these locations with extra pins could provide an effective method for reducing the risk of loosening. It has been observed that pins nearest to the fracture gap are critical to providing overall stability (Oni et al., 1993). Preventing loosening of these pins is therefore critical to the maintenance of fixator stability.

It has been observed that the superior stiffness of stainless steel orthopaedic implants to bone tissue can lead to stress shielding where load transfer can become concentrated at only a few screw threads (Gefen, 2002). After an extended period of implantation the natural bone remodelling process can diminish the bone density in stress-shielded sites (Frost, 1987; Ang et al., 1997; Soininvaara et al., 2004), leading to increased risk of pin loosening in the long-term. Titanium screws have a lower Young's modulus than stainless steel, resulting in a more even distribution of loading to the bone. They therefore offer improved biomechanical compatibility with bone and lower rates of long-term loosening (Gefen, 2002; Zanetti et al., 2009). The improved biomechanical compatibility of titanium implants may support their use in unilateral fixation of fractures (Ganser et al., 2007). However, the present results demonstrated that this can induce 60–65 % more peri-implant bone yielding. Furthermore, a previous study (Huiskes et al., 1985) predicted 25 % higher contact stresses with titanium rather than stainless steel half-pins. The use of titanium implants would therefore be expected to increase the risk of half-pin loosening. It should be noted that other changes that reduce half-pin bending stiffness would similarly be expected to increase the risk of loosening. The behaviour of the half-pins can be considered similar to that of a cantilever; the bending stiffness can therefore be approximated by $3EI/L_p^3$, where E, I and L_p are the material Young's modulus, the cross-sectional second moment of area, and the pin length from the fixator respectively. It can be inferred that the volume of peri-implant yielded bone would be particularly sensitive to both increased half-pin length and reduced diameter since the bending stiffness is dependent on the third and fourth powers of these parameters respectively (note I is a function of the fourth power of the cross-sectional dimensions). Indeed, these determinants of pin bending stiffness have been demonstrated to be critical to global fixator stiffness (Huiskes and Chao, 1986).

Investigations of the biomechanical behaviour of orthopaedic screws generally use pull-out tests as representative of in-vivo loading (Gefen, 2002; Zanetti et al., 2009; Chatzistergos et al., 2010). In the present case however, bending stiffness influenced the volume of peri-implant yielded bone substantially. The associated conclusions would not have been reached by modelling pull-out tests. The results of this study indicate that when analysing situations where pin bending occurs,

a complete understanding of screw design implications can only be achieved if such deformations are directly modelled in the analyses.

The type of boundary conditions applied to the bone fragments may be a possible limitation of the present methodology. The bone was not modelled superior to the midshaft region studied. This excluded the rotational restraint which could have been provided by the continuity of the bone. Such restraint may have reduced the observed deformations and therefore the volume of bone undergoing plastic strain. However, modelling of the entire tibia superior to the fracture gap would require the application of transverse, bending and torsional loads at the knee which would have the opposite effect to the increased restraint (i.e. increasing the deflection and resulting yielded bone volume). Indeed, considerable variation of loading has been recorded in the leg during different activities and throughout gait cycles; substantial transverse loading and moments have been recorded during the gait cycle (Heinlein et al., 2009). It has been observed that torsional and bending loading have only minor influence on the strain at the fracture gap (Lauer et al., 2000). It can therefore be inferred that these additional loads would be transferred via the bone-implant interface, thus inducing additional bone yielding. The present boundary conditions were selected to simplify the FE modelling process. Through consideration of the preceding arguments it is expected that they represent a reasonable approximation of the reality.

The selection of load magnitude may introduce some uncertainty into the present results. For healthy adults, peak longitudinal loadings of approximately 2.5 and 3.5 times body weight have been recorded during steady walking and on stairs respectively (Taylor et al., 1998; Heinlein et al., 2009). For patients following tibial-fixation surgery less data is available. Kershaw et al. (1993) measured the load-bearing and gap displacement of tibial fractures fixed with half-pins during walking, throughout the post-fracture healing process. It was demonstrated that load bearing returned linearly from zero immediately post-fracture to nearly 80 % of body weight at a mean of 13 weeks later. Similar results were observed in the study by Cunningham et al. (1989). Vijayakumar et al. (2006) employed FE analyses to assess load sharing between the bone callus and fixator during unilateral fixation of the tibial midshaft. It was observed that the peak load in a gait cycle increased during healing; approximately 120 %, 225 % and 275 % of body

weight at 7, 10 and 16 weeks post-fracture. It was further noted that the proportion of the tibial load carried by the fixator dropped steadily from 20 %, to 4 % and 2 % over the same period. Following fracture, the load carried through the leg is considerably reduced as patients use the leg less to aid healing and avoid pain. The loading experienced during healing has been shown to be variable, making the selection of a representative load difficult. This would be further complicated by the possible addition of large (300–1000 N) soft tissue forces resulting from limb lengthening (Simpson et al., 1996; Gardener et al., 1997; Kenwright and Simpson, 2000). In the current study it was assumed that all loading was carried through the fixator. This implied a state in which the callus was not load-bearing, i.e. immediately post-op. The previous studies (Cunningham et al., 1989; Kershaw et al., 1993) indicated that little or no loading of the fracture site occurs at this time. Indeed it is only during the period of 1–7 weeks post-op that loading is increasingly applied. The case studied here was therefore necessarily representative of the patient bearing load on an immature, or absent, callus. In light of the cited data, loading was specified in the present study to represent 100 % of body weight. The selected loading was greater than that observed by Cunningham et al. (1989) and Kershaw et al. (1993) but less than reported by Vijayakumar et al. (2006) at 7 weeks post-op. More generally, it is expected that any fixation implant loosening results from fatigue damage accumulated over repeated cycles of loading. Indeed, it has been observed that dynamic loading leads to substantially higher rates of pin loosening (Pettine et al., 1993). Fatigue loading would be expected to increase the volume of yielded bone over time. It was assumed that the yielded bone observed in the present study corresponded to either a single extreme event or the accumulation of multiple events of lower magnitude.

The use of elastic constants measured at the femoral midshaft to represent those at the tibia was a potential limitation of this study. At the microlevel the longitudinal nano-indentation moduli of osteons and interstitial lamellae in the tibial and femoral midshaft have been shown to be approximately equal (Rho et al., 1997; 2002). Furthermore, since the tibial and femoral midshaft perform similar mechanical functions it seems reasonable to assume that their microstructural adaptation with ageing are also similar. Hence, the elastic properties evaluated in Chapter 3 were expected to be a good approximation for the tibial midshaft location of the present study.

The pin-bone interface was modelled without friction in the present study. In reality, a non-zero friction coefficient would exist between half-pins and bone. However, it was considered reasonable to assume that surface frictional shear stresses are relatively small during fixation, compared to the shear stresses transferred via normal stresses on the screw threads. The interface as modelled can therefore be expected to incorporate the majority of the shear loading that would be transferred by frictional effects. Furthermore, the absence of friction would not be expected to induce slippage since the presence of the screw threads would resist such movement.

The fixator to which half-pins were attached was not modelled in the present study. This represented a possible limitation since displacements resulting from strains within these components were not present in the analyses. The shape and configuration of these components can vary considerably; specific placements are determined by anatomy, surgeon preference, fracture type and location. It was therefore difficult to identify a single configuration that could be considered general. Furthermore, all external fixator components have considerably larger cross-sections than half-pins. Hence, as found in a reference case (Huiskes and Chao, 1986) the bending stiffness of longitudinal elements in unilateral fixation is more than 16 times greater than that of the half-pins; fixator compliance has been found to have negligible effect of upon the overall construct properties (Juan et al., 1992; Karunratanakul et al., 2010). Half-pins can therefore be expected to represent the dominant contribution to fixator construct flexibility, which the present results indicate was a key determinant of the volume of yielded bone at pin-bone interfaces.

Half-pins were restricted to the elastic regime in all analyses. The validity of this assumption was evaluated by considering the maximum von Mises stress which occurred within the half-pins. In the stainless steel half-pins the peak value was 978 MPa, whereas in titanium half-pins it was 464 MPa. The yield strength of such materials as used in surgical applications are 1000 MPa (stainless steel) and 950 MPa (titanium) (Gibbons, 1982; Lewis, 1990; Callister, 2003). The present results therefore do not predict yielding of the half pins. The restriction of the half-pins to elastic behaviour therefore did not influence the results of the present study.

The noted limitations of this study may have introduced some error in the evaluation of the various variables of interest. However, while the absolute values of these variables may be adjusted by further improvements in the modelling process it would be expected that the trends observed in the present study would remain valid. As discussed, it can therefore be concluded that the use of more pins acts to reduce half-pin loosening, stainless steel rather than titanium pins induce lower volumes of peri-implant yielded bone in the tibial midshaft, and age-related bone loss considerably promotes half-pin loosening.

Chapter 7

Ilizarov fixation of tibial midshaft fractures

7.1 Introduction

The Ilizarov fixator was developed in the 1950s by a Russian surgeon named Gavriil Ilizarov (Ilizarov, 1954). Its use in the West was delayed because of the language barrier and travel barrier (Iron Curtain). The Ilizarov method of fracture fixation makes use of pre-tensioned, thin wires (1.5–1.8 mm in diameter) which transfix the bone, supported by circular rings and stiff longitudinal bars. These elements are constructed into frames which provide a stable mechanical environment for the healing of fractures. Unlike other methods of fixation, Ilizarov fixators are characterised by non-linear stiffness in the axial direction (Podolsky and Chao, 1993; Watson et al., 2000; Zamani and Oyadiji, 2008). They also retain comparable stiffness to other fixation methods under lateral, torsional and bending loads (Fleming et al., 1989; Khalily et al., 1998). Their non-linear axial stiffness produces interfragmentary displacements which stimulate osteogenesis by indirect healing (Wu et al., 1984; Goodship and Kenwright, 1985; Claes et al., 1998; Goodship et al., 1998), while their increasing stiffness prevents excessive strains which are deleterious to bone formation. The rapid fracture healing times that have been reported with the Ilizarov technique have been attributed to these mechanical qualities (Fleming et al., 1989; Ilizarov, 1990; Yang et al., 2003).

Fractures which are comminuted or near articular surfaces have been treated using Ilizarov fixators (Calhoun et al., 1992). They are also widely used in the corrective treatment of nonunions, post-trauma residual misalignment and limb

deformities (by distraction osteogenesis) (De Bastiani et al., 1987; Simpson et al., 1996; 1999; Pavolini et al., 2000).

The average age of the global population, and western citizens in particular, is known to be rising (Weinstein, 2000). The density of both cortical (Russo et al., 2006; Cooper et al., 2007) and cancellous (Ding et al., 1997; Stauber and Müller, 2006a) bone reduces with ageing, particularly in post-menopausal women. The stiffness (see Chapter 3) and strength (McCalden et al., 1993) of ageing bone reduce with its density, leading to an exponential increase in the risk of fractures (Weinstein, 2000). A considerably larger number of fractures will therefore be expected in the elderly in the coming decades. Some of these may be best treated with Ilizarov fixation in clinical cases such as those outlined above. However, Ilizarov wires are thin compared to other fixation implants so high stresses may arise at wire-bone interfaces. Coupled with the age-related loss of bone mass, these high stresses could exceed the strength of weaker, lower-density bone and increase the risk of wire loosening.

Despite the relatively thin diameter of Ilizarov wires, they are associated with low rates of loosening at epiphyseal and metaphyseal locations (Ali et al., 2003; Board et al., 2007). However, it has been noted that the mean age of patients receiving fracture fixation is relatively low (< 50) (Ali et al., 2003). It is therefore possible that loosening rates could be higher if treatment with fine wire fixation was extended to older groups. Furthermore, at epiphyseal and metaphyseal locations cancellous bone is present in the medullary canal and bone dimensions are at their largest. At diaphyseal locations bones are at their thinnest and lack cancellous bone. Age-related bone loss results in considerable thinning of diaphyseal cortices (Russo et al., 2006; Cooper et al., 2007) and reduction of their mechanical properties (see Chapter 3). Such locations may therefore be associated with a higher risk of wire loosening. Thus further research is required to improve our understanding of the effect of age-related bone loss on the risk of loosening at wire-bone interfaces.

Previous investigators of the mechanics of Ilizarov fixation have focused on the wire components or the fixator construct. Analytical methods have been used to derive expressions for the load-deflection behaviour of the wires (Nikono-

vas and Harrison, 2005; Zamani and Oyadiji, 2008). Ilizarov wires are non-linear such that as deflections increase they become more stiff. Analytical results indicate that wire stiffness increases approximately linearly with the number of Ilizarov wires if four or more are used. Increased wire pre-tension is associated with reduced wire stiffness non-linearity. However, considerable non-linearity is predicted when fewer wires are used. Zamani and Oyadiji noted that wire non-linearity arises from the fact that the applied loading is not in the direction in which the wire behaves linearly (along its axis). Wire pre-tension and the wire-bone intersection angles were found to be independent of the total wire length (Zamani and Oyadiji, 2008). Surgeons can therefore select ring diameters without fear of inducing wire yielding or failure. It was also reported that small amounts of wire slippage ($\sim 0.5\,\mathrm{mm}$) could result in complete loss of pre-tension (Zamani and Oyadiji, 2008). Wire components (not the frame) were found to be the critical determinant of fixator stiffness (Nikonovas and Harrison, 2005). It was finally concluded that wires could be accurately modelled without material non-linearity (yielding), but that geometrical non-linearity was required to achieve accuracy (Zamani and Oyadiji, 2008).

FE studies of Ilizarov wires (Hillard et al., 1998; Watson et al., 2003; Zhang, 2004) reached similar conclusions to those discussed for analytical studies. It was observed that wire yielding occurred under walking loads at the clamps and periosteum. Considerable work-hardening occurred at these locations until plastic strains sufficient to reduce the wire pre-tension by 20 % had developed (Hillard et al., 1998). Wire yielding and slippage were observed at axial loading greater than 50 N (Watson et al., 2003). It was noted (Zhang, 2004) that Ilizarov fixator stiffness could not be quantified by a single value, but required a full specification of the (geometrically) non-linear response.

The stiffness of Ilizarov fixator frames has been investigated using parametric FE analyses (Juan et al., 1992; Nielsen et al., 2005; Watson et al., 2007). Results indicated that increased fixator stiffness can be achieved by using wires with a higher Young's modulus, increasing wire diameter, using more wires on each fragment and reducing the wire length. Using a hybrid (Ilizarov wires and half-pins) fixator, one study (Nielsen et al., 2005) noted that fixator stiffness could be increased by placing the bone nearer to one end of the wires. Fixator stiffness was

found to increase almost linearly with the number of wires used (Watson et al., 2007). It should be noted however, that the analyses of the latter were restricted to the linear regime of fixator responses. Indeed, the critical role of geometric non-linearity (Zhang, 2004; Zamani and Oyadiji, 2008) appears to have been neglected in previous FE studies of Ilizarov fixators (Juan et al., 1992; Nielsen et al., 2005; Watson et al., 2007). This would be expected to limit their ability to quantify fixator stiffness. Several additional features of previous FE studies also limit their appropriateness for investigating the mechanical environment at the wire-bone interface. Tied contact has been assumed at the wire-bone interface in all studies. This assumption unrealistically enables tensile wire-bone stresses where separation and higher compressive stresses would (in reality) be expected. Additionally, since Ilizarov wires are smooth they would not be expected to resist sliding displacement along the wire-bone tract. The geometry of bone fragments has previously been simplified to either beam or cylindrical profiles which can differ substantially from anatomical profiles; e.g. at the tibial midshaft. The mechanical properties of bone fragments have also been simplified in previous FE analyses; bone has been modelled as isotropic and homogeneous, but is known to be orthotropic (Cowin and Mehrabadi, 1989) and to exhibit considerable stiffness variation with position (see Chapter 3). The ability of previous studies to investigate the risk of bone failure under wire-loading has been further limited by the restriction of bone to its elastic properties. Since considerable stress concentrations would be expected under loading with thin wires it is likely that bone would exceed its yield point at least locally, resulting in a redistribution of stress which would not be captured under elastic conditions. No previous FE studies of Ilizarov fixation have included the substantial reduction of bone stiffness and strength associated with bone loss (Burstein et al., 1976; Zioupos and Currey, 1998). The extent to which ageing and osteoporosis could reduce the stability of Ilizarov wires therefore remains unclear. The aim of the present study was to improve understanding of the interaction between wires and the tibial midshaft and to evaluate any increased risk of wire loosening resulting from age-related osteoporosis.

7.2 Methods

The methods described in the following were implemented using programs written by the author in Matlab (The MathWorks, Inc., Natick, MA, U.S.A.) and Fortran.

In the present study Ilizarov fixation of tibial midshaft fractures was investigated using FE analyses. The general methodology was to apply a vertical load to a tibial bone fragment, supported by Ilizarov wires. Ilizarov devices are installed in a variety of configurations, dependant upon the proximity of the fracture site to articular surfaces, the location of 'safe corridors' for wire insertion and the required rigidity of fixation. Fractures of the mid-diaphysis were selected for study because the geometry and loading is less complex than near articular surfaces. Additionally, there is minimal cancellous bone at this site which simplified the modelling process. The geometry and material properties of the bone fragments were modelled as described in Chapter 6 (Section 6.2.1).

7.2.1 Ilizarov wire definition

Wires of 1.8 mm diameter were used in all analyses. The Young's modulus and Poisson's ratio were 151 GPa and 0.3 respectively, equivalent to experimentally measured values of commercially available stainless steel wires (Hillard et al., 1998). Ilizarov wires are typically installed such that two-wires cross on each ring. Configurations of two-wires (one ring) and four-wires (two rings) were modelled in the present study. The arrangement of wires in the transverse plane matched typical installations at the tibial midshaft location using an external ring of 155 mm diameter; as noted previously, wires at this site are restricted to the safe corridors to minimise interference with the surrounding soft tissues and neurovascular systems (Behrens and Searls, 1986). Additionally, the subcutaneous location of the transverse medial face of the tibia results in tibial placement eccentric to the ring centroid. The resulting placement of the wires is illustrated in Fig. 7-1. Wires were modelled with a crossing angle of 30°. A spacing of at least 30 mm (approximately two finger breadths are left between the skin and the ring in clinical practice) was left between the ring and the bone fragment for access. Wires in each pair were separated by 10 mm (5 mm above and below the ring).

In the case of the four-wire models, each pair was separated by 40 mm. The rings were not modelled in the present study.

A comparison of the load-displacement behaviour of the Ilizarov wires as modelled in the present study and predicted by theory (Zamani and Oyadiji, 2008) is shown in Fig. 7-2. The modelled wire behaviour was similar to the analytical prediction, indicating that Ilizarov wire mechanical behaviour was well represented in the present FE models. Slightly higher reaction forces were observed in the FE results than predicted by Zamani and Oyadiji. However, as illustrated in Fig. 7-1 the bone fragments were not located at the wire midpoints as assumed by Zamani and Oyadiji (2008), who also did not include wire bending stiffness, both of which would be expected to increase the predicted stiffness slightly.

7.2.2 FE specifications

All analyses were solved using explicit numerical integration since it provided more stable interactions at the contact interfaces than implicit integration (see Section 6.2.3). The general contact algorithm was used, which prevented all model surfaces from penetrating each other by transferring normal compressive stresses over all contact interfaces. Unrealistic transfer of tensile stresses between wires and bone was therefore prevented in all analyses.

Vertical loading of 700 N was applied as a pressure load to the superior face of the tibial bone fragment. This represented 100 % of body weight. The bone fragments were restrained by the Ilizarov wires only; no further restraint was applied. A wire pre-tension of 1000 N was applied. Additional analyses were used to investigate the effect of wire pre-tension on peri-implant bone yielding. The wire pre-tension for these analyses varied from 0 N to 2000 N in increments of 500 N. Wire pre-tension was applied as a preliminary analysis step; both ends of the wires were displaced along the wire axis to induce the required tensile force. In the wire configuration used (Fig. 7-1), displacement magnitudes of 0.364 mm and 0.340 mm between sites A–C and B–D respectively were applied to induce 1000 N of pre-tension. Following the application of wire pre-tension, wire ends were fully restrained.

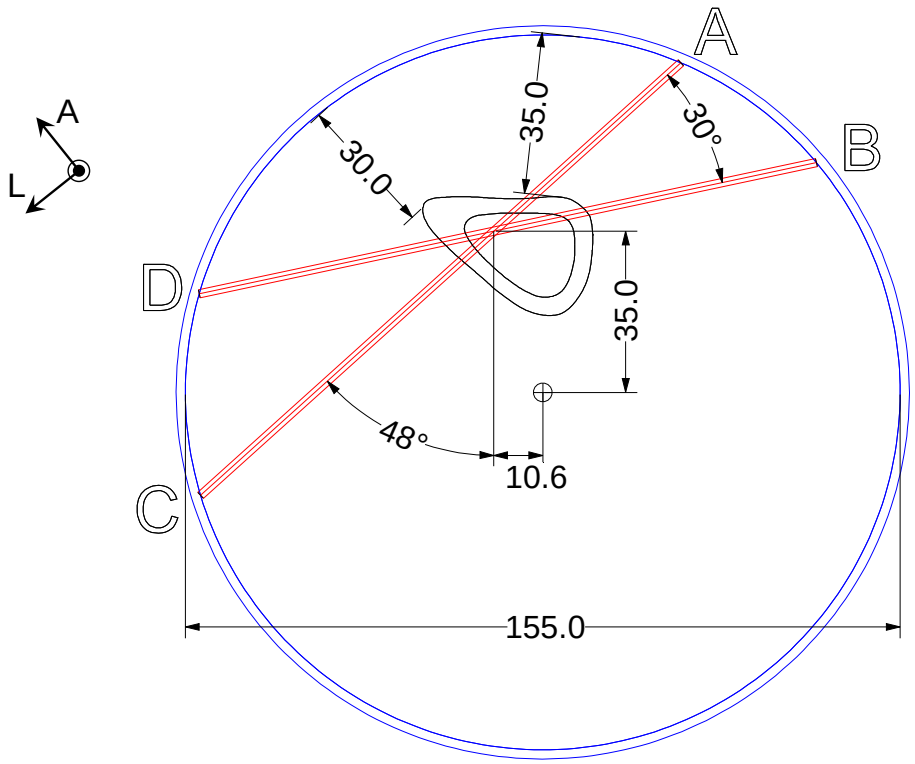

Figure 7-1: Transverse arrangement of Ilizarov wires (red) at the tibial midshaft. The ring (blue) is illustrated here for visualisation but was not included in the analyses. A–D indicate the transverse face medial, medial face medial, transverse face lateral and medial face lateral wire entrance sites respectively. Note all dimensions are in mm. The axes indicate the anterior (A) and left-lateral (L) anatomical directions.

The volume of peri-implant yielded bone was used as an indicator of wire loosening. This was calculated using the same methodology as described previously in Section 6.2.3. Large deformation theory (NLG) was used in all analyses; this was essential to capture the substantial component of fixator stiffness which was induced by the deflection of Ilizarov wires. Ten-noded, second order tetrahedral elements were used to mesh all models. These were used for their superior integration accuracy and mesh convergence properties compared to linear tetrahedra. Approximately 100,000 elements were present in all meshes, with 1,200,000 degrees of freedom. The geometry of the models necessitated the use of a fine mesh resolution in order to achieve solution. The final mesh was designed using a trial-and-error approach. The average element edge length was 0.4 mm at the

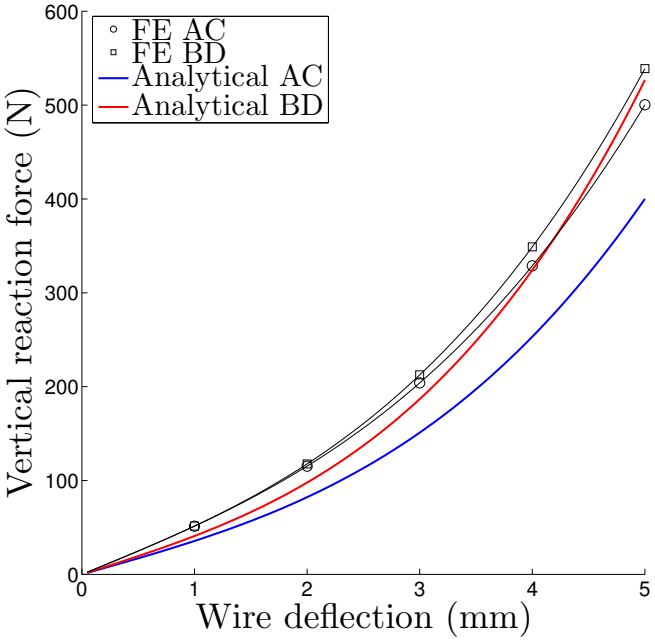

Figure 7-2: Ilizarov wire load-displacement curves for the current models and analytical result of Zamani and Oyadiji (2008) using equivalent settings. The stiffness of Ilizarov wires increases as deflection increases. Note, AC and BD refer to the wires as illustrated in Fig. 7-1

wire-bone interface. Analysis of a model meshed with elements of half the size was made to check for mesh dependency in the results. The yielded bone volume and bone fragment displacement changed by 3.3 % and 0.3 % respectively. This confirmed that the results of the present study were not mesh dependent.

7.3 Results

Cut-through renderings of the tibial bone fragments are presented in Fig. 7-3. Regions of bone which have exceeded the elastic regime are highlighted in red. Bone yielding was observed at all wire entrance sites A–D. Periosteal yielding occurred on the superior (loaded) side of the wires, whereas endosteal yielding occurred on the inferior side. The bone fragments displaced primarily in the axial direction; minimal displacement occurred in the lateral directions. The wire deformation was characterised by bending concentrated at approximately periosteal locations, wires remained relatively horizontal within the medullary canal. Considerable variation in the angle of wire deflection was observed; for example, the

wire segments on the right of Fig. 7-3(b,d) deflected at greater angles than those on the left. Entrance sites of those wires at a greater angle of deflection appeared to be associated with more extensive regions of yielded bone.

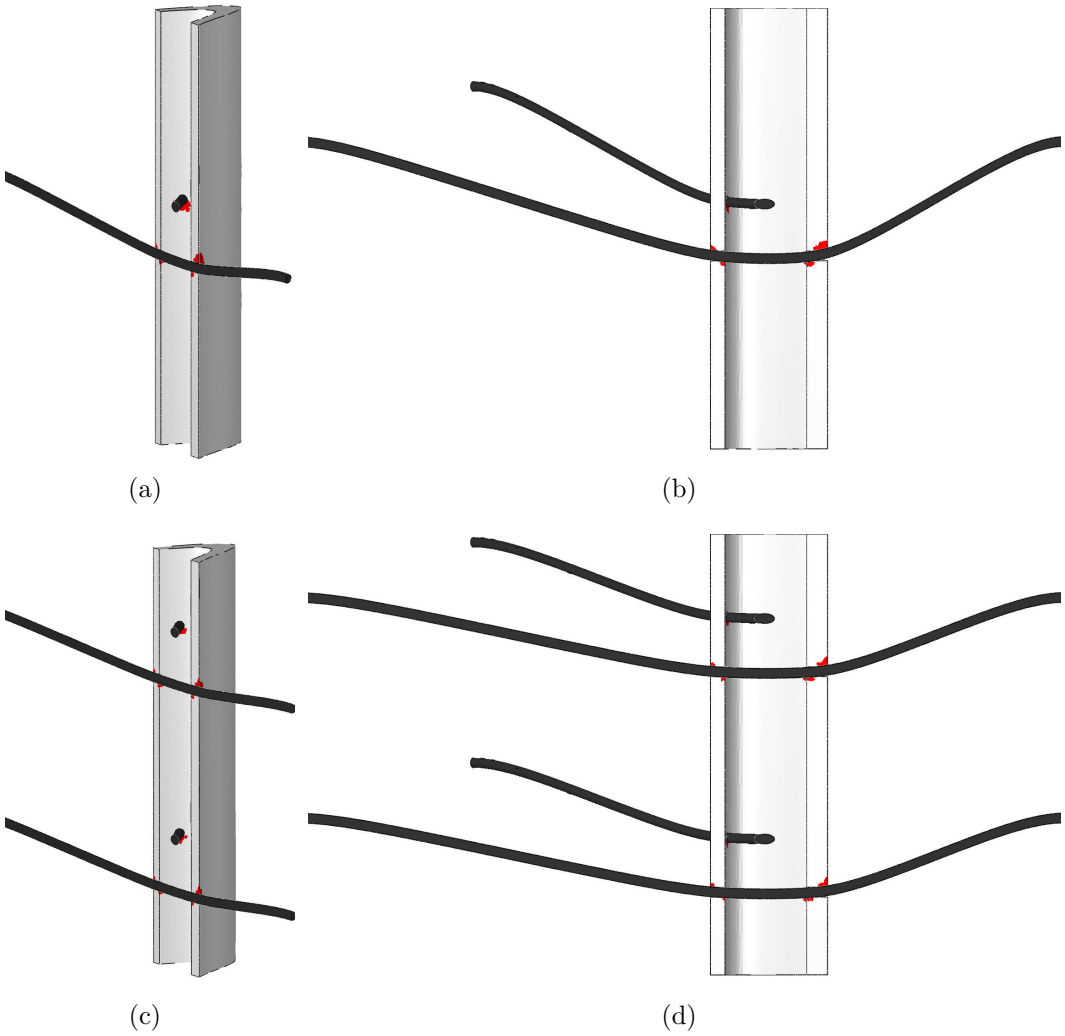

Figure 7-3: Renderings of the old group in two- and four-wire Ilizarov fixation, under the applied vertical loading. Unscaled perspective view (a and c), 5 times deformation, elevation view (b and d). Note: images are cut-through at the midpoint of wires A–C (defined in Fig. 7-1), with A to the left and C to the right of all images. Regions of yielded bone are highlighted in red.

The distribution of yielded bone around sites A and C can be compared in Fig. 7-4. Yielding was concentrated at two distinct locations; superior to the wires at the periosteum and inferior to the wires at the endosteum. Periosteal and endosteal yielded regions did not connect in any analyses. The periosteal

yielded region appeared to be larger than the endosteal, particularly at site A and in the longitudinal direction. More extensive yielding was observed at site A (right) than site C (left) in all analyses. The former corresponded to the shortest exposed wire length, and the latter with the longest. Two-wire fixation (a-c) resulted in more extensive yielding than four-wire fixation (d-f); yielded bone extended further radially and longitudinally. The size of yielded regions appeared to increase slightly with ageing in both fixator configurations.

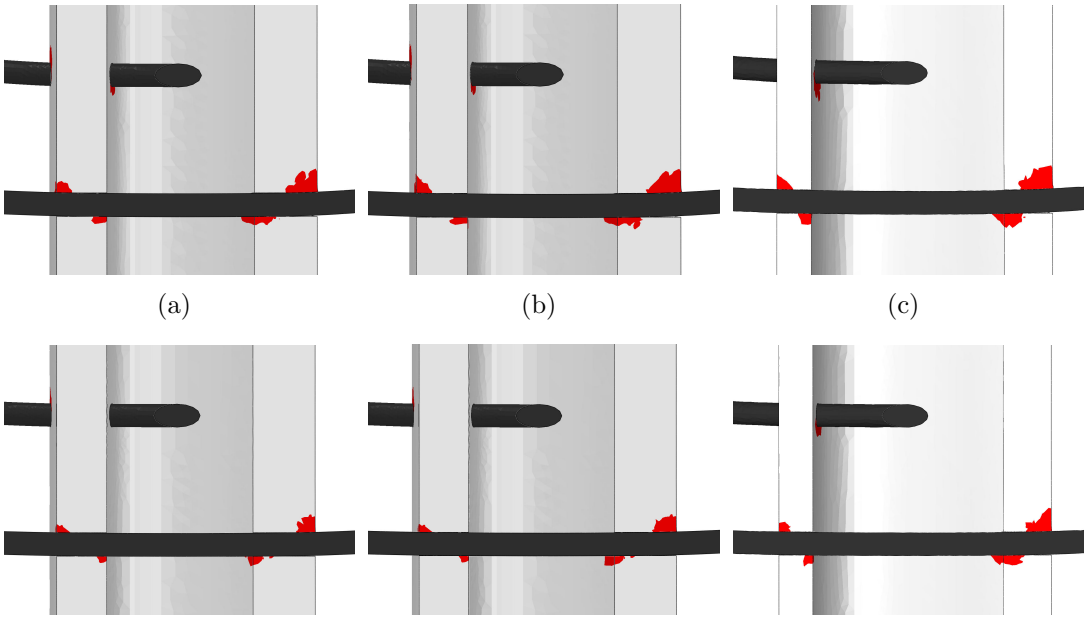

Figure 7-4: Peri-implant yielded bone in two- and four-wire Ilizarov fixation of young (a and d), middle-aged (b and e) and old (c and f) bone fragments. The upper and lower rows contain images from two- and four-wire fixation respectively. In the case of four-wire fixation the two wires furthest from the fracture gap are imaged. Note, yielded bone is shaded red and all images are cut along the midline of wire A–C (defined in Fig. 7-1), such that site A is on the right.

The distribution of minimum principal stress and total strain around site A are presented in Fig. 7-5. Large compressive stresses (approximately 175 MPa) were observed at the periosteum and smaller compressive stresses (approximately 75 MPa) were observed at the endosteum. Large compressive total strains (considerably greater than the yield strain) were observed at the same locations, corresponding to sites of bone yield. A similar distribution of stress and strain was observed in all age-groups. Compressive bone stresses near the wire were

greatest in the young group and reduced with increased ageing. The minimum principal total strains were similar between age groups and increased sharply near to the wires (within 0.5 mm). At distances greater than 1.5 mm from the wire stresses were slightly larger in the old group than the two younger groups.

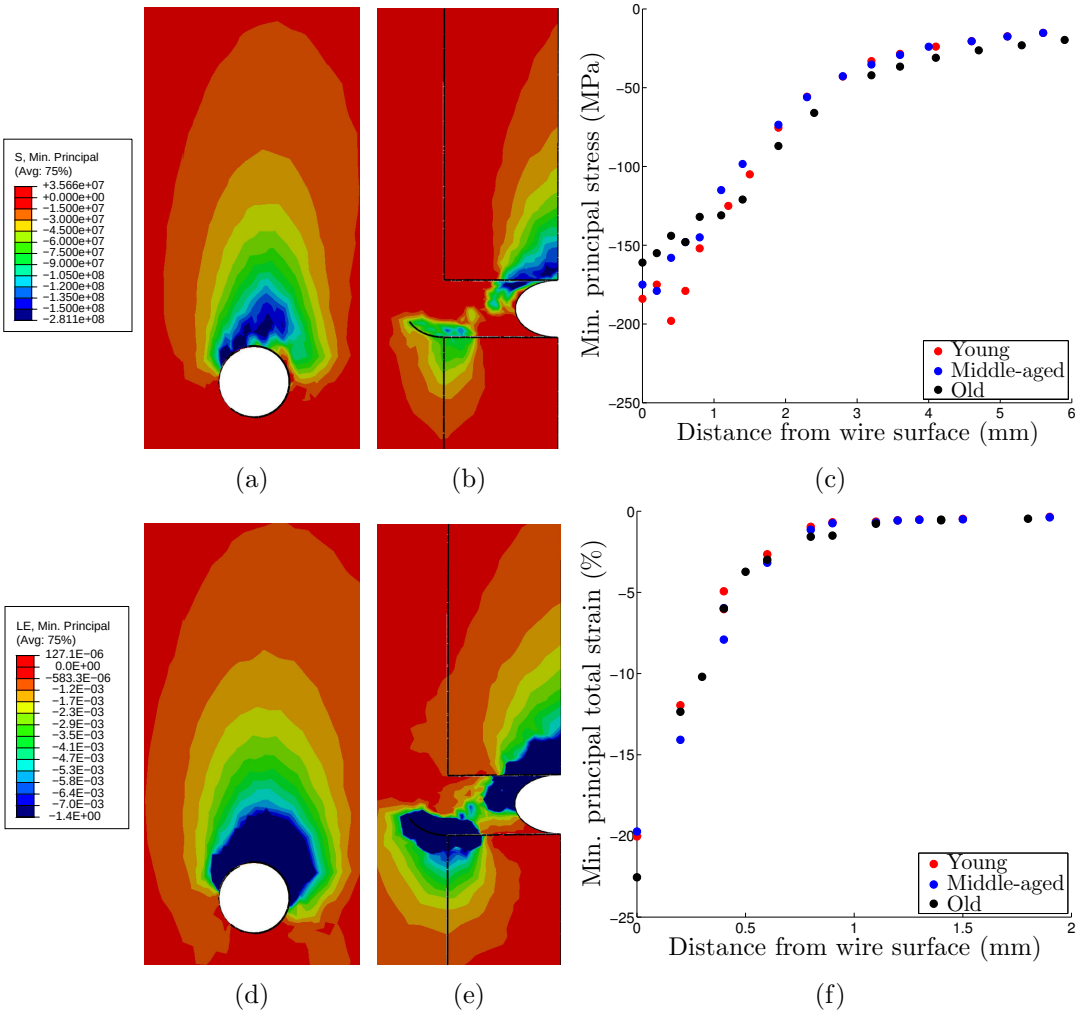

Figure 7-5: Minimum principal stress (a-c) and total strain (d-f) at the wire-bone interface of site A in the old group with two-wire fixation. Contours on elevation views (a,d) and cut-through views (b,e). Variation of parameters with distance from the wire surface (along the periosteum) for all age groups (c,f). Note the stress contours of (a) and (b) are in Pa.

The volume of peri-implant yielded bone at locations A–D is plotted in Fig. 7-6 for two- and four-wire fixation. Considerable variation of the volume of yielded bone was observed between different entrance sites. A similar hierarchy was observed in all analyses; the largest yielded volume occurred at A, the smallest at

C, and sites B and D were intermediate. The exposed length of the wires at each site followed the opposite hierarchy; $l_A < l_D < l_B < l_C$, where l_i is the exposed wire length at site i. Hence, the largest volume of peri-implant yielded bone occurred at the site with the shortest exposed wire length. Yielded bone volume increased substantially with ageing; yielded volumes in the old group were approximately 1.7 times and 2.2 times greater than the young group with two- and four-wire fixation respectively. Two-wire fixation produced larger volumes of yielded bone at all sites than four-wire fixation. At the critical wire entrance site (A), approximately 2.5–2.8 times more peri-implant yielded bone was observed in two-wire fixation than four-wire fixation of equivalent age groups.

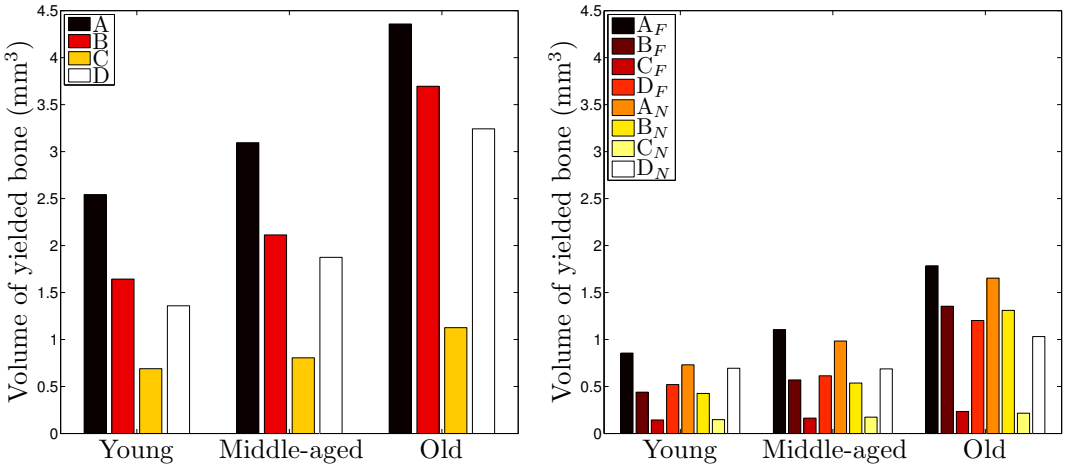

Figure 7-6: Peri-implant yielded bone volume in two- (a) and four-wire (b) Ilizarov fixation of young, middle-aged and old bone fragments. The volume of yielded bone increased with ageing. The volume of yielded bone decreased slightly with greater proximity to the fracture gap. Note, wire entrance sites A–D correspond to Fig. 7-1, and subscripts F and N refer to the pair of wires furthest from and nearest to the fracture respectively.

Propagation of peri-implant bone yielding through the full cortex would be indicative of a particularly high risk of wire loosening. The normalised thickness of yielded bone (ratio of the radial length of yielded bone to the cortical thickness) was evaluated to quantify the risk of stability loss; results are plotted in Fig. 7-7(a) for yielded bone at the periosteum, since yielding was more extensive here than at the endosteum. It was observed that bone yielding did not propagate through the full cortex in any analysis; the maximum extent was approximately

70 % of the cortical thickness. Ageing was associated with higher proportions of yielded cortical thickness; approximately 20 % more of the cortex yielded in the old group than in the young group with both two- and four-wire fixation. Two-wire fixation yielded approximately 15 % more of the cortical thickness than four-wire fixation. Figure 7-7(b) illustrates the displacement of bone fragments in all analyses. It can be seen that bone fragment displacements were independent of age. Two-wire fixation produced displacements approximately 53 % greater than four-wire fixation.

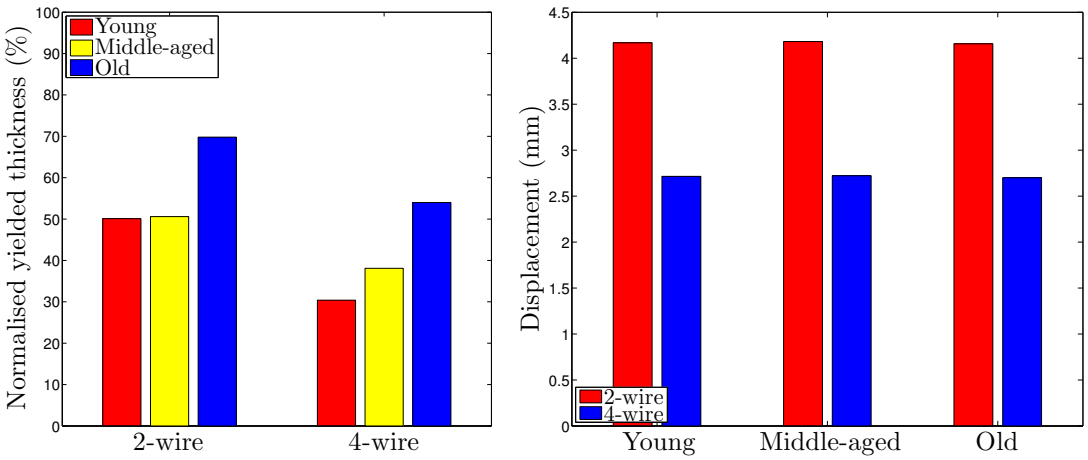

(a) (b)

Figure 7-7: Normalised thickness of yielded bone (a), and bone fragment displacements (b) in Ilizarov wire fixation. A greater proportion of the cortical thickness yielded with increased age. The full cortical thickness was not yielded in any group. Bone fragment displacement variations with age were small relative to the total displacement.

The effect of wire pre-tension on peri-implant yielded bone volume and displacement is illustrated in Fig. 7-8. An approximately linear variation was observed between wire pre-tension and the volume of yielded bone; increased pre-tension corresponded to reduced yielded bone volume and bone fragment displacement at all sites. An increase in wire pre-tension of 500 N produced an approximate reduction of peri-implant yielded bone of 0.6 mm^3, equivalent to 14 % of the critical (site A) yielded volume with typical wire pre-tension (1000 N). Peak wire stresses in all analyses were found to exceed the reported failure stress of Ilizarov wires (Hillard et al., 1998). Peak stresses were located adjacent to wire ends, and at the periosteum. Increased wire pre-tension produced slightly larger regions of stresses greater than the failure stress.

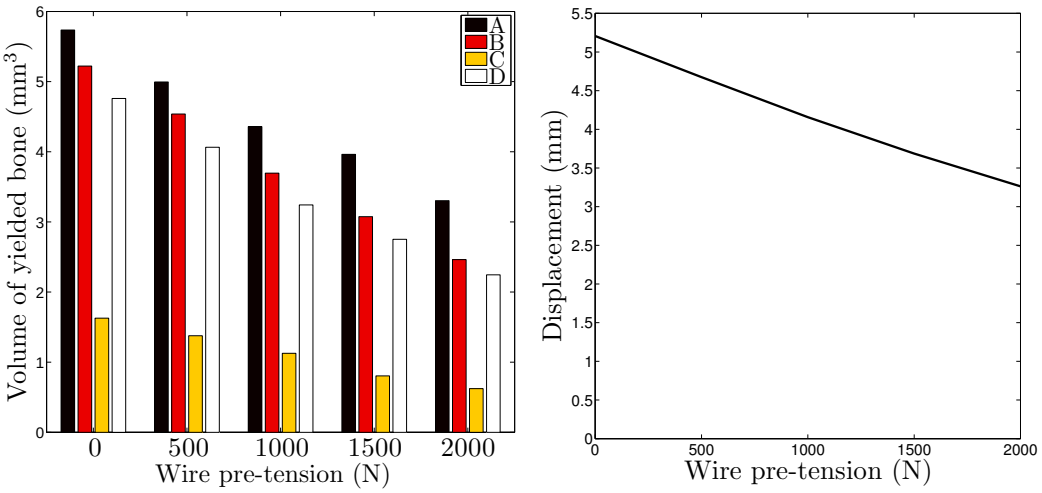

(a) (b)

Figure 7-8: Effect of wire pre-tension on yielded bone volume (a) and displacement (b) in two-wire Ilizarov fixation of the old group. The volume of yielded bone decreased with increased wire pre-tension, which also permitted smaller displacements. Note, in (a) the x-axis indicates wire pre-tension in N and sites A–D correspond to Fig. 7-1.

7.4 Discussion

The aim of the present study was to evaluate the effect of age-related bone loss on the loosening of Ilizarov wires during external fixation. Several conclusions of clinical relevance can be inferred from the present results. The volume of peri-implant yielded bone was used as an indicator of wire loosening; a greater volume of yielded bone was considered representative of a higher risk of loosening. As discussed in Chapter 6 (Section 6.4), yielding observed at the apparent scale can be seen as a homogenised representation of discrete failure processes (such as microcracking) at smaller scales. These processes reduce the resistance of bone tissue to movement, and therefore loosening of the wires. The greater the proportion of peri-implant tissue which is yielded, the less resistance it would be expected to provide to wire movement. Greater wire movement may also increase the ability of infection to enter the insertion site. It therefore seemed reasonable to consider the volume of yielded bone as proportional to the risk of wire loosening. As noted previously in Chapter 6 (Section 6.4), the ability of bone to absorb energy through post-elastic deformation before ultimate failure, and its ultimate strain are both known to reduce substantially with ageing (Currey, 1979; McCalden et al., 1993). The plasticity model used here did not limit the magnitude of post-elastic strain to an ultimate value. It would therefore be expected that

an equivalent volume of yielded bone in an older model would represent a higher risk of loosening than in a younger model.

Peri-implant bone yielding was observed at both the periosteum and the endosteum in all analyses. The minimum principal stresses and total strains were also concentrated at these locations (see Fig. 7-5). It can be inferred from the deformed shapes in Fig. 7-3(b,d) that the concentration of yielding at these locations resulted from the change of angle of the wires relative to the wire-track. The periosteal intersection angles between the wires and the wire-tracks in two-wire fixation of the old model were approximately 3.7°, 2.8°, 1.7°, 2.0° at sites A, B, C and D respectively. Combined with Fig. 7-6(a) this data indicates that greater volumes of yielded bone occurred at sites with larger wire-track intersection angles. Since the wires were not aligned with the wire-track once deformed, contact with the bone occurred at the corner of the periosteum superior to the wire, and at the corner of the endosteum inferior to the wire. Contact at corners, rather than along the length of the wire-track effectively concentrated the stress at these locations, leading to amplified strains and earlier onset of bone yielding. Furthermore, considerable strain was required at the identified corners to enable wire-bone contact, and thus transfer of stress, to occur along the length of the wire-track.

In addition to the concentration of loading at corners, the inclination of wires within their wire-tracks was found to increase the wire-bone stresses required to resist the applied loading. The applied loading acted vertically downwards and was therefore resisted by the compressive contact stresses on the superior side of the wires. However, since the wires were inclined, additional downward loading was applied to the endosteum of the bone fragments from the inferior side of the wires. To satisfy static equilibrium this additional load was resisted by increased compressive stresses acting upwards on the periosteum from the superior side of the wires. Indeed, in the old-aged, two-wire fixation model, downwards contact forces at the endosteum were found to account for approximately 20 % of the upwards contact forces at the periosteum.

Differences in the exposed length of wires can account for the noted variation of wire angles. It was found that the exposed wire length at each site was inversely proportional to the associated volume of yielded bone. Other factors,

such as the cross-sectional geometry of the tibia would be expected to influence the load distribution between wires.

An initial interpretation of these results would suggest that bone yielding could be reduced by increasing the total wire length (increasing exposed wire length). However, increased total wire length would reduce the fixator stiffness and produce greater deflections. This would increase the strain at the callus which could be undesirable for stimulation of bone growth (Wu et al., 1984; Goodship and Kenwright, 1985; Claes et al., 1998; Goodship et al., 1998). Furthermore, it has been shown that the intersection angle is independent of the total wire length for constant load and pre-tension (Zamani and Oyadiji, 2008). The correct interpretation of the present results would be to minimise the difference in exposed lengths of the same wire on opposite sides of the limb, i.e. to locate the bone fragment near the mid-point of the wire. This strategy would maximise the critical exposed wire length, without adversely affecting fixator stiffness or the mechanical environment at the callus site (Podolsky and Chao, 1993). However, in the clinical application it is unlikely that bone fragments could be located at the wire mid-point. The tibia is generally located eccentrically to the ring to accommodate the surrounding soft tissues. Also, the placement of wires is restricted by the need to avoid neurovascular tissues, minimise muscle damage (Behrens and Searls, 1986) and to ease limb movement.

Considerable reduction of bone stiffness and strength was applied between the young and old models in the present study. However, while ageing induced greater localised tissue strains, their contribution to the total bone fragment displacement was relatively small (see Fig. 7-7(b)). It can be inferred that with Ilizarov fixation bone mechanical properties do not substantially influence callus strain, and the consequent mechanical stimulation of bone growth (Wu et al., 1984; Goodship and Kenwright, 1985; Claes et al., 1998; Goodship et al., 1998). Furthermore, the relatively small age-related variation of bone fragment displacement can be attributed to the observed pure axial displacement, characteristic of Ilizarov fixation (Fleming et al., 1989; Calhoun et al., 1992; Podolsky and Chao, 1993; Khalily et al., 1998; Yang et al., 2003).

Age related bone loss increased the volume of yielded bone in both two- and

four-wire Ilizarov fixation by a factor of 1.7 to 2.2 respectively. Since the applied loading was identical between age groups and relatively small change in displacement was observed between age-groups, it can be inferred that the increase in yielded bone volume resulted from the reduced stiffness, yield stress and cross-sectional area in the old models. In addition, the discussed corner loading resulted in considerable radial stresses within the bone fragment (see Fig. 7-9). The Young's modulus (and hence strength) in this direction was found to reduce most rapidly with ageing in Chapter 3. The relative preservation of axial over transverse bone stiffness with ageing would therefore appear to amplify the identified corner loading effect in elderly/osteoporotic patients. The risk of wire loosening would therefore be expected to be greater for older patients or those with osteoporosis. Indeed, in the old models, the normalised yielded thickness of the cortex was greatest at 70 % and 55 % in two- and four-wire configurations respectively. However, while the volume of yielded bone increased with ageing it remained concentrated at the periosteum and endosteum separately (superior and inferior to the wire respectively) and did not progress through the entire cortex. A substantial proportion of the cortical thickness therefore remained in the elastic regime and would continue to provide stable support to the wires. The risk of wire loosening may therefore be lower than is implied by the relatively large volumes of peri-implant yielded bone.

The axial stiffness of Ilizarov fixators is non-linear (Podolsky and Chao, 1993; Watson et al., 2000); wire stiffness increases with axial displacement. This non-linearity derives from the off-axis loading of the wires (Zamani and Oyadiji, 2008). Greater fixator displacement induces greater wire inclination which directs a greater proportion of the wire tension in the vertical direction. While the relationship between wire tension and extension remains linear, the varied vertical proportion of the wire tension produces a non-linear load-displacement response in the axial direction of the fixator. This non-linearity therefore derives from the geometry; hence large deformation theory was used in all analyses of the present study. Due to this non-linearity the use of two times the number of wires did not produce half of the displacement. Indeed, the axial displacements in four-wire fixation were 64 % of those observed with two-wire fixation (see Fig. 7-7(b)). However, the use of two times the number of wires did result in a reduction of yielded bone volume by 2.5–2.8 times; the use of more wires distributes

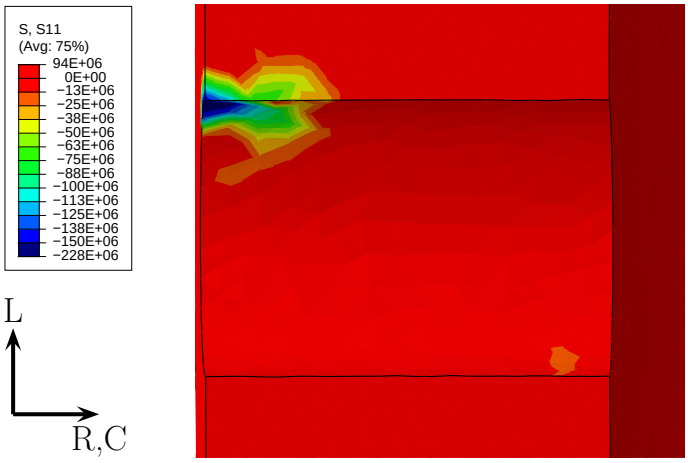

Figure 7-9: Radial stress at the wire-bone interface was concentrated at the periosteum (left side of image), superior to the wire. At this location the radial stresses were similar to the minimum principal stresses (see Fig. 7-5(a-c)) but represented great potential for yielding due to the lower stiffness in the radial direction. The contour plot shows results from site D of the old group, other sites and samples exhibited similar behaviour.

the applied load over greater area, thus inducing lower stresses and strains, leading to lower volumes of bone undergoing plastic straining. The fact that yielded bone volume reduced by a greater proportion than the increase in wire numbers implied that the use of more wires is particularly effective to reduce the risk of loosening.

Increased wire pre-tension was found to reduce the volume of peri-implant yielded bone (Fig. 7-8(b)); an increase of 500 N in pre-tension resulted in reduced yielded bone volume of 14 %. Increased pre-tension effectively increases the constant term of the wire stiffness, and reduces the non-linearity of the axial fixator stiffness (Zamani and Oyadiji, 2008). The stiffness is therefore enhanced, resulting in lower deflections and hence smaller wire-track intersection angles. Since the total axial loading was equal for all wire pre-tensions considered, the total vertical reaction in the direction of loading at the wire-bone interfaces has to be equal. Therefore, since it is the only independent variable, this result confirms the previously discussed role of wire-track intersection angle in determining the volume of yielded bone. The clinical implication of the present result is that increased wire pre-tension would reduce the risk of loosening. However, wire plasticity and slippage have been found to occur at pre-tensions of 1287 N (Hillard et al., 1998)

and 1250 N (Aronson and Harp, 1992) respectively. Improved material properties and wire end fixing techniques would therefore be required to realise substantial reductions of yielded bone volume by increasing wire pre-tension. While higher pre-tension is advantageous from the point of view of bone yielding, it can result in wire yielding as found by Hillard et al. (1998). Wire yielding would have reduced wire tension and hence increased the observed volumes of yielded bone; the trends of the present study would therefore be amplified.

Axial loading was applied to represent 100 % of body weight in the present study. As discussed in Chapter 6 (Section 6.4) the specified loading may be a limitation since it is unclear whether patients would apply such large loads with an absent or immature callus. However, the loading applied here was intermediate to previously reported values; both higher (Vijayakumar et al., 2006) and lower (Cunningham et al., 1989; Kershaw et al., 1993) loading have been measured under tibial fixation at seven weeks post-op. Furthermore, the Ilizarov technique is commonly used in limb-lengthening during which considerable (300–1000 N) soft-tissue forces develop (Simpson et al., 1996; Gardener et al., 1997; Kenwright and Simpson, 2000) which would increase the loading across the fracture gap. The loading applied was also intended to represent the accumulated effect of fatigue, resulting from a few extreme events, or many cycles of lower loading. Moreover, the trends observed in this study would be valid for smaller loadings as well.

A previous FE study (Juan et al., 1992) reported that immature (2–3 weeks post-op) callus can sustain the majority of axial loading under Ilizarov fixation. However, wire pre-tension and large deformation theory were not present in the models of Juan et al. their fixator stiffness would therefore be considerably lower than in reality. This would explain the observed premature transfer of load through the callus under Ilizarov fixation. In reality it would be expected that load transfer would move from the fixator to the callus as the fracture healed. This would be expected to reduce the stresses at wire-bone interfaces and the associated risk of loosening. The transfer of load by direct contact between the bone fragments would be expected to have a similar effect. The inferior bone fragment was not included in the present study. Indeed, it was assumed that the axial displacements of the bone fragments would be smaller than the fracture gap such that that direct load transfer would not occur. However, considerable

axial displacement was observed in the present results, particularly with two-wire fixation which contained displacements in excess of typical fracture gaps of 1–3 mm. It was therefore likely that direct load transfer would have occurred between bone fragments in these cases. This would be expected to reduce the peri-implant yielded bone volumes, particularly under two-wire fixation. Since Ilizarov fixation provides non-linear axial stiffness, the mechanical environment at the wire-bone interface is sensitive to changes of axial displacement. However, inclusion of callus and direct bone fragment contact in the models would cause the results to become specific to the assumed callus properties and fracture gap length.

Elastic constants derived at the femoral midshaft were used to model those at the tibial midshaft in the present study. If the properties varied considerably between these sites this may be a limitation of the present study. However, as discussed previously (see Section 6.4) the properties of femoral and tibial cortical bone do not differ substantially. Furthermore, one of the strengths of the present study was the use of orthotropic elastic bone properties which enabled the anisotropic variation of mechanical properties with ageing to be accurately included.

Wire-bone friction was not included in the analyses. In reality some friction would exist at these interfaces. However, Ilizarov wires can often be pulled out easily through the leg by hand and therefore appear to offer little frictional resistance. Furthermore, lateral stability in Ilizarov fixation is provided by the placement of wires in crossed pairs. The absence of friction was therefore not expected to limit the present analyses.

The external rings and vertical fixator components were not modelled in the present analyses. The compliance of these components would be expected to introduce some additional axial displacement under weight bearing. However, the cross-sectional area of Ilizarov rings and bars are substantially greater than the wires. Also, these components are typically arranged in rigid frames. It would therefore not be expected that the inclusion of the external Ilizarov frame would substantially affect the present results.

7.4.1 Comparison of half-pin and Ilizarov fixation

Ilizarov wires are associated with a lower rate of loosening than half-pins during external fixation (Ali et al., 2003; Board et al., 2007). The location of peri-implant yielded bone observed in the present results differed from those observed under half-pin fixation (Chapter 6). Half-pin fixation was observed to induce cantilever-like bone fragment displacement and thus relied on screw pull-out resistance for lateral stability. Ilizarov wire fixation contrastingly produced axial displacements and retained lateral stability from the fact that wires are installed in crossed pairs. This may account for the greater stability of Ilizarov wires. Specifically, it was observed that bone yielding penetrated the full cortical thickness in half-pin fixation of old models. This would be expected to result in the loss of screw thread purchase and half-pin loosening. However, under Ilizarov fixation the yielded bone remained concentrated separately at the periosteum and endosteum, superior and inferior to the wire respectively. Since a substantial proportion of the cortical thickness did not yield around Ilizarov wires, it would be expected that this remaining bone would continue to provide wire stability. In addition, old models were associated with approximately 3 times the volume of yielded bone around half-pins than young models. However, under Ilizarov fixation age-related bone loss was associated with an increase of approximately 1.7–2.2 times. The proportionally greater increase of peri-implant yielded bone volume with half-pin fixation indicated that implant stability under this method of fixation was particularly sensitive to bone loss.

It should also be noted that the absolute volume of peri-implant yielded bone was generally greater with Ilizarov wires than half-pins. This can be explained by the fact that Ilizarov wires are considerably thinner than half-pins, hence they will induce greater implant-bone stresses and a higher likelihood of exceeding the bone strength. Additionally, Ilizarov wires were observed to induce implant-bone stresses in both the superior and inferior directions. Since the applied loading was resisted by stresses on the superior face, those on the inferior face effectively increased the weight-bearing contact stresses and therefore the yielded bone volume. The presence of bone yielding at both superior and inferior locations under Ilizarov fixation also increased the recorded yielded bone volume relative to half-pin fixation which only showed yielding at the superior implant

face. The discussed differences in the distribution of yielded bone between fixation techniques would be expected to promote half-pin loosening even with lower total volumes of yielded bone. Furthermore, the displacement of bone fragments under Ilizarov fixation was previously noted to be greater than typical fracture gaps. If the inferior bone fragment was included in the models, contact between bone fragments would permit lower displacements and therefore lower volumes of yielded bone would be expected in the Ilizarov models.

Chapter 8

Conclusions

This study considered the effect of microstructural morphology on the macrolevel mechanical properties of bone. The elastic and post-elastic properties of trabecular and cortical bone were represented using virtual modelling, μFE analysis and strain-based plasticity. Some of the developed techniques and data were applied to non-linear FE analyses of implant-bone interactions for external fixators used to fix fractures of the tibial mid-shaft.

The following Section details the key conclusions of this work:

8.1 Conclusions

8.1.1 Virtual modelling of trabecular bone

A virtual modelling technique was developed to generate 3D trabecular bone samples computationally, which were tested for their microarchitectural and mechanical properties. The developed algorithm was able to create features of the rod-like microarchitecture of trabecular bone; sample morphology was found to correspond well to certain key indices of trabecular bone microarchitecture. The algorithm inputs could be calibrated to produce samples with a wide range of mechanical anisotropy, representative of trabecular bone at different anatomical sites. The elastic moduli of virtual models showed a similar variation with apparent density and sample size to real trabecular bone. This study provided a proof of concept that algorithmic methods could be used to generate samples of trabecular bone.

Non-linear analyses of the generated samples were also conducted to investigate the post-elastic properties of these samples as a surrogate for real trabecular bone. Tissue-level non-linearity was represented by a Drucker-Prager plasticity model and instability was included using geometric non-linearity. Similar to real trabecular bone, material rather than geometrical sources of non-linearity were found to dominate the post-elastic response of the virtual samples.

8.1.2 μFE modelling of cortical bone

The μFE technique was employed for the first time to investigate the elastic properties of cortical bone. Samples of female human bone from the anterior femoral midshaft were subjected to FE tests to calculate their orthotropic elastic constants. Morphological analyses of the samples were conducted to evaluate the power of selected microarchitectural indices in predicting the elastic constants of cortical bone. It was found that only a single microarchitectural index, namely Ca.V/TV, was required to strongly predict all orthotropic elastic constants. The predictive power of age was considerably lower than Ca.V/TV. The observed variation of elastic constants with morphology and age compared well with published studies indicating that μFE can be used to study cortical bone elasticity accurately.

Previous studies have reported disproportionately greater age-related bone loss at the endosteum than at the periosteum. The small sample size possible in the present study enabled the first direct quantification of the variation of apparent-level orthotropic elastic constants between these sites. It was found that the elastic constants at the endosteum were considerably lower than at the periosteum and that this trend increased with age-related bone loss. This indicated that macro-FE models should account for the heterogeneous properties of cortical bone in the radial direction, particularly when considering patients with mild or severe bone loss. It was also found that elastic anisotropy increased as bone loss was accumulated. This further indicated that the inclusion of bone anisotropy in FE studies becomes increasingly important as the density of the bone modelled reduces.

8.1.3 Modelling of cortical bone microcracking

FE analyses of microcracking in murine cortical bone were conducted. The results were compared with those obtained through dynamic image-guided failure assessment (DIGFA) experiments on notched samples of murine cortical bone. Macrolevel FE analyses revealed the crack-driving mechanism induced by the DIGFA experiments; the applied axial compressive loading produced tensile stresses and strains in the transverse directions through bending and the Poisson effect. The tensile stresses and strains drove the formation of cracks in the transverse-longitudinal plane. It was also found that tensile stresses and strains were maximal at cortical surfaces which explained the experimentally observed crack initiation at these sites.

Several algorithms were developed to investigate the role of cortical bone microstructure in the initiation and propagation of microcracks. An algorithm which determined the direction of crack propagation as a function of the maximum principal stress gradient around crack tips was most able to reproduce the cracking behaviour observed experimentally. The algorithm predicted crack initiation at canal surfaces and the ability of osteocyte lacuna to direct crack propagation. This compared well with experimental observations. It was also observed that microcracks inhibited the propagation of neighbouring cracks by partially shielding them from the applied stress. Similar behaviour has been reported in the literature as a key toughening mechanism in bone. The applied strain required to induce cracking was compared with canal morphological indices of the samples. It was found that increased canal diameter was associated with lower applied strain required to initiate cracks. This implied that outer cortical geometry plays a more important role in the determination of fracture resistance than canal microstructure in cortical bone.

8.1.4 Strain-based yield criterion for bone

A plasticity algorithm for modelling the post-elastic behaviour of cortical and trabecular bone was developed. The algorithm achieved computational efficiency by employing a piecewise-linear yield surface to which only a single plastic return vector was required from any predictor state. It has been noted in the literature that bone strength is anisotropic but that it exhibits isotropic yield strains. The

developed algorithm represents these features of bone behaviour by employing a yield surface which was isotropic in elastic strain-space; the yield surface was defined by limiting the values of both maximum and minimum principal elastic strains. Benchmark tests were conducted to test the algorithm in typical and singular states of strain; it was found to be robust in all cases. Use of the presented algorithm would enable FE studies to incorporate the realistic strain-based yielding behaviour of anisotropic bone tissues in a computationally efficient and effective way.

8.1.5 External fixation of tibial midshaft fractures

FE analyses of external fixation of the tibial midshaft were conducted. Fixation using typical configurations of unilateral half-pin fixators and Ilizarov fixators were modelled. The models were used to investigate the effect of age-related bone loss on the stability of implants used in external fixation. The present models represented a considerable advance over previous FE studies of external fixation through the inclusion of several key features: a representative macrolevel bone geometry, the orthotropic elastic properties of cortical bone, the heterogeneous variation of elastic properties between the periosteum and endosteum, the inclusion of post-elastic tissue properties, contact mechanics at bone implant interfaces and geometric non-linearity.

A considerable increase in the volume of peri-implant yielded bone and implied risk of loosening was observed with age-related bone loss with both types of fixation. In unilateral fixation, bone yielding was concentrated at the periosteum, superior to the half-pins in younger models. In older models bone yielded through the full cortex which indicated a substantial risk of pin loosening. In Ilizarov fixation bone yielding was noted superior and inferior to the wires at the periosteum and endosteum respectively. However, yielded bone was restricted to these locations in all age groups which implied that sufficient tissue remained unyielded which could preserve wire stability. Results confirmed that the use of more half-pins or wires substantially reduced their risk of loosening. The use of lower-stiffness half-pins was found to increase the volume of peri-implant yielded bone substantially. The present results therefore do not support the use of biomechanically compatible materials with low elastic modulus for half-pins

in fractures of the legs of patients with substantial bone-loss. Increased Ilizarov wire pre-tension was found to reduce the volume of yielded bone. In low-density cortical bone the risk of bone failure may therefore be minimised by improved maintenance of wire tension.

The different patterns of yielded bone observed in half-pin and Ilizarov fixation may explain the higher rate of implant loosening in the former. Since yielding occurred through the full cortex in old-aged half-pin models it would be expected that screw threads would not retain secure purchase on the bone. Contrastingly, since substantial proportions of the cortex remained unyielded in Ilizarov fixation, wire stability would not be lost in all age groups. Furthermore, age-related bone loss was associated with a proportionally greater increase of peri-implant yielded bone in half-pin than in Ilizarov fixation. It can be concluded that reduced bone density poses a greater risk to implant stability in half-pin fixation than Ilizarov fixation.

8.2 Recommendations

The virtual modelling technique can be used to incorporate bone microstructure in macrolevel FE models. Similar algorithms could be developed to represent cortical bone. Future researchers may wish to improve the generated trabecular morphology by directly including plate trabeculae in the algorithm. These would also benefit from the use of meshes which conform to the trabeculae rather than restricting models to a global hexahedral grid.

The μFE approach can be used to investigate the orthotropic elastic constants of cortical bone from additional anatomical sites. It would be particularly effective in identifying local heterogeneous and anisotropic variations. The predictive power of Ca.V/TV indicates the potential for assessment of the elastic constants of bone in patients using CT and DEXA. Further development of the technique would benefit from the identification of osteonal and interstitial bone within sample images and specification of the associated tissue-level properties. Tissue-level material orientations could potentially be improved through skeletonisation of canals to identify their local trajectories.

The FE analyses of microcracking indicated that current notched compression experiments could be improved by the application of different load cases such as three-point bending. This would enable more direct control over the site of crack initiation and produce cracks in the physiologically relevant, transverse plane. The developed microcracking algorithms can be used to investigate the role of bone microstructure in crack propagation. The technique would benefit from the inclusion of cortical surfaces, laminar tissue properties and tissue-level heterogeneity. Future researchers may wish to employ traction-separation laws to include the effect of unmodelled bone toughening mechanisms.

The strain-based yield criterion can be used to include the key macrolevel features of bone failure in FE studies. Further applications may exist in other materials which exhibit yield behaviour similarly dependent upon principal elastic strains. Future research could enhance the present algorithm to include hardening or softening behaviour as appropriate.

The developed models of external fixation can be used to examine the effect of numerous fixator configurations on implant stability. The present models could be used to investigate the effect of half-pin and wire dimensions on their loosening risk and on the mechanical environment at the fracture gap which is key to stimulating bone growth. Future researchers could use similar models to study fixator implant stability at other anatomical sites, such as the metaphysis which contains cancellous bone. Fixator selection could be improved by better understanding of the risk of loosening at different sites and bone densities using models similar to those developed here. Future research could incorporate the callus or fracture gap directly in such models to capture the associated load transfer.

References

Abendschein, W., Hyatt, G. W., 1970. Ultrasonics and selected physical properties of bone. Clinical Orthopaedics and Related Research 69 (1), 294–301.

Addessi, D., Marfia, S., Sacco, E., 2002. A plastic nonlocal damage model. Computer Methods in Applied Mechanics and Engineering 191, 1291–1310.

Akhter, M. P., Cullen, D. M., Pedersen, E. A., Kimmel, D. B., Recker, R. R., 1998. Bone response to *in vivo* mechanical loading in two breeds of mice. Calcified Tissue International 63, 442–449.

Ali, A. M., Burton, M., Hashmi, M., Saleh, M., 2003. Treatment of displaced bicondylar tibial plateau fractures (OTA-41C2&3) in patients older than 60 years of age. Journal of Orthopaedic Trauma 17, 346–352.

Ang, K. C., Das De, S., Goh, J. C. H., Low, S. L., Bose, K., 1997. Periprosthetic bone remodelling after cementless total hip replacement. The Journal of Bone and Joint Surgery (British) 79-B, 675–679.

Apostolopoulos, C. A., Deligianni, D. D., 2009. Prediction of local cellular deformation in bone – Influence of microstructure dimensions. Journal of Musculoskeletal and Neuronal Interactions 9, 99–108.

Arciola, C. R., Montanaro, L., Moroni, A., Giordano, M., Pizzoferrato, A., Donatti, M. E., 1999. Hydroxyapatite-coated orthopaedic screws as infection resistant materials: in vitro study. Biomaterials 20, 323–327.

Aro, H. T., Markel, M. D., Chao, E. Y. S., 1993. Cortical bone reactions at the interface of external fixation half-pins under different loading conditions. The Journal of Trauma 35, 776–785.

Aronson, J., Harp, J. H., 1992. Mechanical considerations in using tensioned wires in a transosseous external fixation system. Clinical Orthopaedics and Related Research 280, 23–29.

Arramon, Y. P., Mehrabadi, M. M., Martin, D. W., Cowin, S. C., 2000. A multidimensional anisotropic strength criterion based on kelvin modes. International Journal of Solids and Structures 37, 2915–2935.

Ascenzi, A., Bonuuci, E., 1967. The tensile properties of single osteons. The Anatomical Record 158, 375–386.

Au, A., Liggins, A. B., Raso, V. J., Amirfazli, A., 2005. A parametric analysis of fixation post shape in tibial knee prostheses. Medical Engineering & Physics 27 (2), 123–134.

Babuška, I., Melenk, J. M., 1997. The partition of unity method. International Journal for Numerical Methods in Engineering 40, 727–758.

Bayraktar, H. H., Morgan, E. F., Niebur, G. L., Morris, G. E., Wong, E. K., Keaveny, T. M., 2004. Comparison of the elastic and yield properties of human femoral trabecular and cortical bone tissue. Journal of Biomechanics 37 (1), 27–35.

Beamer, W. G., Donahue, L. R., Rosen, C. J., Baylink, D. J., 1996. Genetic variability in adult bone density among inbred strains of mice. Bone 18, 397–403.

Behrens, F., 1989. General theory and principles of external fixation. Clinical Orthopaedics and Related Research 241, 15–23.

Behrens, F., Searls, K., 1986. External fixation of the tibia. Journal of Bone and Joint Surgery 68-B, 246–254.

Bentolila, V., Boyce, T. M., Fyhrie, D. P., Drumb, R., Skerry, T. M., Schaffler, M. B., 1998. Intracortical remodelling in adult rat long bones after fatigue loading. Bone 23, 275–281.

Bevill, G., Eswaran, S. K., Gupta, A., Papadopoulos, P., Keaveney, T. M., 2006. Influence of bone volume fraction and architecture on computed large-deformation failure mechanisms in human trabecular bone. Bone 39, 1218–1225.

Bhandari, M., Guyatt, G. H., Swiontkowski, M. F., Tornetta III, P., Hanson, B., Weaver, B., Sprague, S., Schemitsch, E. H., 2001. Surgeons' preferences for the operative treatment of fractures of the tibial shaft : an international survey. The Journal of Bone and Joint Surgery (American) 83, 1746–1752.

Board, T. N., Yang, L., Saleh, M., 2007. Why fine-wire fixators work: An analysis of pressure distribution at the wire–bone interface. Journal of Biomechanics 40, 20–25.

Bousson, V., Bergot, C., Meunier, A., Barbot, F., Parlier-Cuau, C., Lval-Jeantet, A., Laredo, J., 2000. CT of the middiaphyseal femur: cortical bone mineral density and relation to porosity. Radiology 217 (1), 179–187.

Brown, C. U., Yeni, Y. N., Norman, T. L., 2000. Fracture toughness is dependent on bone location–a study of the femoral neck, femoral shaft, and the tibial shaft. Journal of Biomedical Materials Research 49, 380–389.

Brown, T. D., Pedersen, D. R., Radin, E. L., Rose, R. M., 1988. Global mechanical consequences of reduced cement/bone coupling rigidity in proximal femoral arthroplasty: a three-dimensional finite element analysis. Journal of Biomechanics 21, 115–129.

Burstein, A. H., Reilly, D. T., Martens, M., 1976. Aging of bone tissue: mechanical properties. The Journal of Bone and Joint Surgery (American) 58 (1), 82–86.

Calhoun, J. H., Li, F., Ledbetter, R., Gill, C. A., 1992. Biomechanics of the Ilizarov fixator for fracture fixation. Clinical Orthopaedics and Related Research 280, 15–22.

Callister, W. D., 2003. Materials Science and Engineering an Introduction, 6^{th} Edition. John Wiley & Sons, New York.

Campbell, A. A., Song, L., Li, S., Nelson, B. J., Bottoni, C., Brooks, D. E., De Jong, E. S., 2000. Development, characterization, and ani-microbial efficacy of hydroxyapatite-chlorhexidine coatings produced by surface-indeuced mineralization. Journal of Biomedical Materials Research 53, 400–407.

Carter, D. R., 1984. Mechanical loading histories and cortical bone remodeling. Calcified Tissue International 36, S19–S24.

Carter, D. R., Hayes, W. C., 1977. The compressive behaviour of bone as a two-phase porous structure. The Journal of Bone and Joint Surgery (American) 59, 954–962.

Carter, D. R., Schwab, G. H., Spengler, D. M., 1980. Tensile fracture of cancellous bone. Acta Orthopaedica Scandinavica 51, 733–741.

Casey, J., Naghdi, P. M., 1983. On the nonequivalence of the stress space and strain space formulations of plasticity theory. ASME Journal of Applied Mechanics 50, 350–354.

Casey, J., Naghdi, P. M. a., 1982. Discussion: On the formulation of strain-space plasticity with multiple loading surfaces. ASME Journal of Applied Mechanics 49, 460–462.

Chao, E. Y. S., Hein, T. J., 1988. Mechanical performance of standard Orthofix external fixator. Orthopedics 11, 1057–1069.

Chao, E. Y. S., Kasman, R. A., An, K. N., 1982. Rigidity and stress analyses of external fracture fixation devices–a theoretical approach. Journal of Biomechanics 15, 971–983.

Chatzistergos, P. E., Magnissalis, E. A., Kourkoulis, S. K., 2010. A parametric study of cylindrical pedicle screw design implications on the pullout performance using an experimentally validated finite-element model. Medical Engineering & Physics 32, 145–154.

Chen, S. I., Lin, R. M., Chang, C. H., 2003. Biomechanical investigation of pedicle screw-vertebrae complex: a finite element approach using bonded and contact interface conditions. Medical Engineering & Physics 25 (4), 275–282.

Choi, K., Kuhn, J. L., Ciarelli, M. J., Goldstein, S. A., 1990. The elastic moduli of human subchondral, trabecular, and cortical bone tissue and the size-dependency of cortical bone modulus. Journal of Biomechanics 23 (11), 1103–1113.

Ciarelli, M. J., Goldstein, S. A., Kuhn, J. L., Cody, D. D., Brown, M. B., 1991. Evaluation of orthogonal mechanical properties and density of human trabecular bone from the major metaphyseal regions with materials testing and computed tomography. Journal of Orthopaedic Research 9 (5), 674–682.

Claes, L. E., Heigele, C. A., Neidlinger-Wilke, C., Kaspar, D., Seidl, W., Margevicius, K. J., Augat, P., 1998. Effects of mechanical factors on the fracture healing process. Clincal Orthopaedics and Related Research 355S, S132–S147.

Clausen, J., Damkilde, L., Andersen, L., 2006. Efficient return algorithms for associated plasticity with multiple yield planes. International Journal for Numerical Methods in Engineering 66, 1036–1059.

Collinge, C. A., Goll, G., Seligson, D., 1994. Pin tract infections - silver vs uncoated pins. Orthopedics 17, 445–448.

Cooper, D., Turinsky, A. L., Sensen, C., Hallgrímsson, B., 2003. Quantitative 3D analysis of the canal network in cortical bone by micro-computed tomography. The Anatomical Record (Part B: New Anatomist) 274B (1), 169–179.

Cooper, D. M. L., Thomas, C. D. L., Clement, J. G., Turinsky, A. L., Sensen, C. W., Hallgrímsson, B., 2007. Age-dependent change in the 3D structure of cortical porosity at the human femoral midshaft. Bone 40 (4), 957–965.

Cordey, J., Florin, P., Klaue, K., Perren, S. M., 1980. Current Concepts of Internal Fixation of Fractures. Springer-Verlag, Berlin, pp. 192–200.

Courtney, A. C., Hayes, W. C., Gibson, L. J., 1996. Age-related differences in post-yield damage in human cortical bone. Experiment and model. Journal of Biomechanics 29, 1463–1471.

Cowin, S. C., 1986. Wolff's law of trabecular architecture at remodelling equilibrium. Journal of Biomechanical Engineering 108, 83–88.

Cowin, S. C., Laborde, A. J., 1985. The relationship between the elasticity tensor and the fabric tensor. Mechanics of Materials 4 (2), 137–147.

Cowin, S. C., Mehrabadi, M. M., 1989. Identification of the elastic symmetry of bone and other materials. Journal of Biomechanics 22 (6/7), 503–515.

Cowin, S. C., Yang, G., 1997. Averaging anisotropic elastic constant data. Journal of Elasticity 46, 151–180.

Crisfield, M. A., 1997. Nonlinear Finite Element Analysis of Solids and Structures: Advanced topics. Vol. 2. Wiley, New York.

Cunningham, J. L., Evans, M., Kenwright, J., 1989. Measurement of fracture movement in patients treated with unilateral external skeletal fixation. Journal of Biomedical Engineering 11, 118–122.

Cuppone, M., Seedhorn, B. B., Berry, E., Ostell, A. E., 2004. The longitudinal Young's modulus of cortical bone in the midshaft of human femur and its correlation with CT scanning data. Calcified Tissue International 74 (3), 302–309.

Currey, J. D., 1979. Changes in the impact energy absorption of bone with age. Journal of Biomechanics 12, 459–469.

Currey, J. D., 1988. The effect of porosity and mineral content on the Young's modulus of elasticity of compact bone. Journal of Biomechanics 21, 131–139.

Currey, J. D., 2003. The many adaptations of bone. Journal of Biomechanics 36, 1487–1495.

Currey, J. D., 2004. Tensile yield in compact bone is determined by strain, post-yield behaviour by mineral content. Journal of Biomechanics 37, 549–556.

Currey, J. D., Brear, K., Zioupos, P., 1996. The effects of ageing and changes in mineral content in degrading the toughness of human femora. Journal of Biomechanics 29, 257–260.

De Bastiani, G., Aldegheri, R., Renzi-Brivio, L., Trivella, G., 1987. Limb lengthening by callus distraction (callotasis). Journal of Pediatric Orthopedics 7, 129–134.

de Borst, Remmers, J. J. C., Needleman, A., Abellan, M., 2004. Discrete vs smeared crack models for concrete fracture: bridging the gap. International Journal for Numerical and Analytical Methods in Geomechanics 28, 583–607.

de Borst, R., 1987. Integration of plasticity equations for singular yield functions. Computers and Structures 26, 823–829.

de Borst, R., Pankaj, P., Bicanic, N., 1991. A note on singularity indicators for Mohr-Coulomb type yield criteria. Computers and Structures 39, 219–220.

Ding, M., Dalstra, M., Danielsen, C. C., Kabel, J., Hvid, I., Linde, F., 1997. Age variations in the properties of human tibial trabecular bone. The Journal of Bone and Joint Surgery (British) 79-B, 995–1002.

Doblare, M., Garcia, J. M., Gomez, M. J., 2004. Modelling bone tissue fracture and healing: a review. Engineering Fracture Mechanics 71, 1809–1840.

Donahue, T. L. H., Hull, M. L., Rashid, M. M., Jacobs, C. R., 2002. A finite element model of the human knee joint for the study of tibio-femoral contact. Journal of Biomechanical Engineering 124, 273–280.

Donaldson, F., Pankaj, P., Cooper, D. M. L., Thomas, C. D. L., Clement, J. G., Simpson, A. H. R. W., 2009a. Orthotropic elastic constants of cortical bone can be estimated from canal volume ratio. In: Proceedings of the Annual meeting of the British Orthopaedic Research Society, Newcastle, UK.

Donaldson, F., Pankaj, P., Cooper, D. M. L., Thomas, C. D. L., Clement, J. G., Simpson, A. H. R. W., 2010a. Relating age and micro-architecture with apparent-level elastic constants: A μFE study of female cortical bone from the anterior femoral midshaft. IMechE: Journal of Engineering in Medicine, to appear, accepted 15/11/2010.

Donaldson, F., Pankaj, P., Law, A. H., Simpson, A. H., 2008. Virtual trabecular bone models and their mechanical response. IMechE: Journal of Engineering in Medicine 222, 1185–1195.

Donaldson, F. E., Pankaj, P., Cooper, D. M. L., Thomas, C. D. L., Clement, J. G., Simpson, A. H. R. W., 2009b. The variation of orthotropic elastic constants in the female anterior femoral midshaft: a micro-finite-element study. In: Proceedings of the 12th Congress of the International Society of Biomechanics, Cape Town, South Africa.

Donaldson, F. E., Pankaj, P., Cooper, D. M. L., Thomas, C. D. L., Clement, J. G., Simpson, A. H. R. W., 2010b. Orthotropic elastic constants of cortical bone can be estimated from canal volume ratio. In: Proceedings of the 9th International Symposium on Computer Methods in Biomechanics and Biomedical Engineering, Valencia, Spain.

Dong, X. N., Guo, X. E., 2004. The dependence of transversely isotropic elasticity of human femoral cortical bone on porosity. Journal of Biomechanics 37, 1281–1287.

Dong, X. N., Guo, X. E., 2006. Prediction of cortical bone elastic constants by a two-level micromechanical model using a generalized self-consistent method. Journal of Biomechanical Engineering 128, 309–316.

Ebacher, V., Tang, C., McKay, H., Oxland, T. R., Guy, P., Wang, R., 2007. Strain redistribution and cracking behaviour of human bone during bending. Bone 40, 1265–1275.

Evans, G. F., Lebow, M., 1951. Regional differences in some of the physical properties of the human femur. Journal of Applied Physiology 3, 563–572.

Fagan, M. J., Dobson, C. A., Ong, E. K., Jones, B., Langton, C. M., 2004. BMU-Sim3D, a bone modelling environment. In: 6^{th} International Symposium on Computer Methods in Biomechanics and Biomedical Engineering, Madrid, Spain. Vol. 19, Suppl. 1. First Numerics, Cardiff, pp. S365–S365.

Fan, Z., Swadener, J. G., Rho, J. Y., Roy, M. E., Pharr, G. M., 2002. Anisotropic properties of human tibial cortical bone as measured by nanoindentation. Journal of Orthopaedic Research 20 (4), 806–810.

Fantner, G. E., Hassenkam, T., Kindt, J. H., Weaver, J. C., Birkedal, H., Pechenik, L., Cutroni, J. A., Cidada, G. A. G., Stucky, G. D., Morse, D. E., Hansma, P. K., 2005. Sacrificial bonds and hidden length dissipate energy as mineralized fibrils separate during bone fracture. Nature Materials 4, 612–616.

Farahat, A. M., Kawakami, M., Ohtsu, M., 1995. Strain-space plasticity model for the compressive hardening-softening behaviour of concrete. Construction and Building Materials 9, 45–59.

Fenech, C. M., Keaveny, T. M., 1999. A cellular solid criterion for predicting the axial-shear failure properties of bovine trabecular bone. Journal of Biomechanical Engineering 121, 414–422.

Fleming, B., Paley, D., Kristiansen, T., Pope, M., 1989. A biomechanical analysis of the Ilizarov external fixator. Clinical Orthopaedics and Related Research 241, 95–105.

Ford, C. M., Keaveny, T. M., Hayes, W. C., 1996. The effect of impact direction on the structural capacity of the proximal femur during falls. Journal of Bone and Mineral Research 11, 377–383.

Franzoso, G., Zysset, P. K., 2010. Elastic anisotropy of human cortical bone secondary osteons measured by nanoindentation. Journal of Biomechanical Engineering 131, 1–11.

Fratzl, P., Gupta, H. S., Fisher, F. D., Kolednik, O., 2007. Hindered crack propagation in materials with periodically varying Young's modulus - lessons from biological materials. Advanced Materials 19, 2657–2661.

Frost, H. M., 1987. Bone "mass" and the "mechanostat": a proposal. The Anatomical Record 219, 1–9.

Ganser, A., Thompson, R. E., Tami, I., Neuhoff, D., Steiner, A., Ito, K., 2007. An in vivo experimental comparison of stainless steel and titanium schanz screws for external fixation. European Journal of Trauma and Emergency Surgery 33, 59–68.

Gardener, T. N., Evans, M., Simpson, A. H. R. W., Kyberd, P. J., Kenwright, J., 1997. A method of examining the magnitude and origin of "soft" and "hard" tissue forces resisting limb lengthening. Medical Engineering & Physics 19, 405–411.

Gefen, A., 2002. Optimizing the biomechanical compatibility of orthopedic screws for bone fracture fixation. Medical Engineering & Physics 24, 337–347.

Geng, J.-P., Ten, K. B. C., Liu, G.-R., 2001. Application of finite element analysis in implant dentistry: A review of the literature. The Journal of Prosthetic Dentistry 85, 585–598.

George, W. T., Vashishth, D., 2005. Damage mechanisms and failure modes of cortical bone under components of physiological loading. Journal of Orthopaedic Research 23, 1047–1053.

Gibbons, 1982. Biocompatibility of Orthopedic Implants. CRC Press, Boca Raton, USA, Ch. 4, p. 116.

Gibson, L. J., 1985. The mechanical behaviour of cancellous bone. Journal of Biomechanics 18 (5), 317–328.

Goldstein, S. A., 1987. The mechanical properties of trabecular bone: dependence on anatomic location and function. Journal of Biomechanics 20 (11-12), 1055–1061.

Goodship, A. E., Cunningham, J. L., Kenwright, J., 1998. Strain rate and timing of stimulation in mechanical modulation of fracture healing. Clinical Orthopaedics and Related Research 355S, S105–S115.

Goodship, A. E., Kenwright, J., 1985. The influence of induced micromovement upon the healing of experimental tibial fractures. Journal of Bone and Joint Surgery (British) 67-B, 650–655.

Goslings, J., 2002. Internal Fixation in Osteoporotic Bone. Thieme, New York, USA, Ch. 14, pp. 186–193.

Gravouil, A., Moës, N., Belytschko, T., 2002. Non-planar 3D crack growth by the extended finite element and level sets–Part II: Level set update. International Journal for Numerical Methods in Engineering 53, 2569–2586.

Guichet, J.-M., Deromedis, B., Donnan, L. T., Perettie, G., Lascombes, P., Bado, F., 2003. Gradual femoral lengthening with the Albizzia intramedullary nail. The Journal of Bone and Joint Surgery (American) 85, 838–848.

Guo, X., 2001. Bone Mechanics Handbook, 2^{nd} Edition. CRC Press, London, UK, Ch. Mechanical properties of cortical bone and cancellous bone tissue, pp. 10.1 – 10.23.

Guo, X. E., Kim, C. H., 2002. Mechanical consequence of trabecular bone loss and its treatment: a three-dimensional model simulation. Bone 30 (2), 404–411.

Guo, X. E., Zysset, P. K., Goldstein, S. A., 1995. Study of post-yield behaviour of trabecular bone using a 3-D microstructural model. ASME, Advances in Bioengineering, BED-Vol. 31, 165–166.

Gupta, A., Bayraktar, H. H., Fox, J. C., Keaveny, T. M., Papadopoulos, P., 2007. Constitutive modeling and algorithmic implementation of a plasticity-like model for trabecular bone structures. Computational Mechanics 40, 61–72.

Gupta, H. S., Wagermaier, W., Zickler, G. A., Aroush, D. R., Funari, S. S., Roschger, P., Wagner, H. D., Fratzl, P., 2005. Nanoscale deformation mechanisms in bone. Nano Letters 5, 2108–2111.

Hahn, M., Vogel, M., Pompesius-Kempa, M., Delling, G., 1992. Trabecular bone pattern factor – a new parameter for simple quantification of bone microarchitecture. Bone 13, 327–330.

Harrigan, T. P., Jasty, M., Mann, R. W., Harris, W. H., 1988. Limitations of the continuum assumption in cancellous bone. Journal of Biomechanics 21 (4), 269–275.

Hart, R. T., Davy, D. T., Heiple, K. G., 1984. Mathematical-modeling and numerical-solutions for functionally dependent bone remodeling. Calcified Tissue International 36, S104–S109.

Hart, R. T., Hennebel, V. V., Thongpreda, N., Van Buskirk, W. C., Anderson, R. C., 1992. Modelling the biomechanics of the mandible: A three-diomensional finite element study. Journal of Biomechanics 25, 261–286.

Heinlein, B., Kutzner, I., Graichen, F., Bender, A., Rohlmann, A., Halder, A. M., Beier, A., Bergmann, G., 2009. ESB clinical biomechanics award 2008: Complete data of total knee replacement loading for level walking and stair climbing measured in vivo with a follow-up of 610 months. Clinical Biomechanics 24, 315–326.

HES, 2010. Total procedures and interventions, 2008-2009. Tech. rep., NHS: The Health and Social Care Information Centre.
URL `http://www.hesonline.nhs.uk,accessed15/10/2010`

Hildebrand, T., Laib, A., Müller, R., Dequeker, J., Rüegsegger, P., 1999. Direct three-dimensional morphometric analysis of human cancellous bone: microstructural data from spine, femur, iliac crest, and calcaneus. Journal of Bone and Mineral Research 14 (7), 1167–1174.

Hildebrand, T., Rüegsegger, P., 1997a. A new method for the model-independent assessment of thickness in three-dimensional images. Journal of microscopy 185, 67–75.

Hildebrand, T., Rüegsegger, P., 1997b. Quantification of bone microarchitecture with the structure model index. Computer Methods in Biomechanics and Biomedical Engineering 1, 15–23.

Hillard, P. J., Harrison, A. J., Atkins, R. M., 1998. The yielding of tensioned fine wires in the Ilizarov frame. IMechE: Journal of Engineering in Medicine 212, 37–47.

Hiriart-Urruty, J. B., Lemarechal, C., 1993. Convex Analysis and Minimization Algorithms. Vol. 1. Springer-Verlag, Berlin.

Hoffman, O., 1967. The brittle strength of orthotropic materials. Journal of Composite Materials 1, 200–206.

Hollister, S. J., Kikuchi, N., 1992. A comparison of homogenization and standard mechanics analyses for periodic porous composites. Computational Mechanics 10 (2), 73–95.

Homminga, J., Van-Rietbergen, B., Lochmüller, E. M., Weinans, H., Eckstein, F., Huiskes, R., 2004. The osteoporotic vertebral structure is well adapted to the loads of daily life, but not to infrequent "error" loads. Bone 34, 510–516.

Hu, Q., Qian, G., Nowinski, W. L., 2005. Fast connected-component labelling in three-dimensional binary images based on iterative recursion. Computer Vision and Image Understanding 99, 414–434.

Huang, J., Griffiths, D. V., 2008. Observations on return mapping algorithms for piecewise linear yield criteria. International Journal of Geomechanics, ASCE 8, 253–265.

Huiskes, R., Chao, E. Y. S., 1986. Guidelines for external fixation frame rigidity and stresses. Journal of Orthopaedic Research 4, 68–75.

Huiskes, R., Chao, E. Y. S., Crippen, T. E., 1985. Parametric analysis of pin-bone stresses in external fracture fixation devices. Journal of Orthopaedic Research 3 (3), 341–349.

Huiskes, R., Ruimerman, R., van Lenthe, G. H., Janssen, J. D., 2000. Effects of mechanical forces on maintenance and adaptation of form in trabecular bone. Nature 405, 704–706.

Il'iushin, A. A., 1961. On the postulate of plasticity. Journal of Applied Mathematics and Mechanics 25, 746–752.

Ilizarov, G. A., 1954. A new principle of osteosynthesis with the use of crossing pins and rings. In: Collection of Scientific Works of the Kurgan Regional Sceintific Medical Society. Kurgan, USSR.

Ilizarov, G. A., 1989a. The tension-stress effect on the genesis and growth of tissues. Part I. The influence of stability of fixation and soft-tissue preservation. Clinical Orthopaedics and Related Research 238, 249–281.

Ilizarov, G. A., 1989b. The tension-stress effect on the genesis and growth of tissues. Part II. The influence of the rate and frequency of distraction. Clinical Orthopaedics and Related Research 239, 263–285.

Ilizarov, G. A., 1990. Clinical application of the tension–stress effect for limb lengthening. Clinical Orthopaedics and Related Research 250, 8–26.

Inoue, N., Chao, E. Y. S., 2002. Internal Fixation in Osteoporotic Bone. Thieme, New York, USA, Ch. 2, pp. 9–21.

Jepsen, K. J., Davy, D. T., Akkus, O., 2001. Bone Mechanics Handbook, 2^{nd} Edition. CRC Press, London, UK, Ch. Observations of damage in bone, pp. 17.1 – 17.18.

Juan, J. A., Prat, J., Vera, P., Hoyos, J. V., Sanchez-Lacuesta, J., Peris, J. L., Dejoz, R., Alepuz, R., 1992. Biomechanical consequences of callus development in Hoffmann, Wagner, orthofix and Ilizarov external fixators. Journal of Biomechanics 25, 995–1006.

Kabel, J., van Rietbergen, B., Dalstra, M., Odgaard, A., Huiskes, R., 1999a. The role of an effective isotropic tissue modulus in the elastic properties of cancellous bone. The Journal of Biomechanics 32, 673–680.

Kabel, J., van Rietbergen, B., Odgaard, A., Huiskes, R., 1999b. Constitutive relationships of fabric, density, and elastic properties in cancellous bone architecture. Bone 25 (4), 481–486.

Kanit, T., Forest, S., Galliet, I., Mounoury, V., Jeulin, D., 2003. Determination of the size of the representative volume element for random composites: statistical and numerical approach. International Journal of Solids and Structures 40 (13-14), 3647–3679.

Karunratanakul, K., Schrooten, J., Van Oosterwyck, H., 2010. Finite element modelling of a unilateral fixator for bone reconstruction: Importance of contact settings. Medical Engineering & Physics 32, 461–467.

Keaveny, T. M., Wachtel, E. F., Ford, C. M., Hayes, W. C., 1994. Differences between the tensile and compressive strengths of bovine tibial trabecular bone depends on modulus. Journal of Biomechanics 27 (9), 1137–1146.

Keller, T. S., 1994. Predicting the compressive mechanical behaviour of bone. Journal of Biomechanics 27, 1159–1168.

Kenwright, J., Simpson, A. H. R. W., 2000. Orthofix External Fixation in Trauma and Orthopaedics. Springer-Verlag, London, UK, Ch. 4, The biology of soft tissue distraction, pp. 18–24.

Kershaw, C., Cunningham, J. L., Kenwright, J., 1993. Tibial external fixation, weight bearing and fracture movement. Clinical Orthopaedics and Related Research 293, 28–36.

Keyak, J. H., 2001. Improved prediction of proximal femoral fracture load using nonlinear finite element models. Medical Engineering & Physics 23, 165–173.

Keyak, J. H., Rossi, S. A., 2000. Prediction of femoral fracture load using finite element models: an examination of stress- and strain-based failure theories. Journal of Biomechanics 33 (2), 209–214.

Keyak, J. H., Rossi, S. A., Jones, K. A., Les, C. M., Skinner, H. B., 2001. Prediction of fracture location in the proximal femur using finite element models. Medical Engineering & Physics 23, 657–664.

Keyak, J. H., Rossi, S. A., Jones, K. A., Skinner, H. B., 1998. Prediction of femoral fracture load using automated finite element modeling. Journal of Biomechanics 31, 125–133.

Khalily, C., Voor, M. J., Seligson, D., 1998. Fracture site motion with Ilizarov and "hybrid" external fixation. Journal of Orthopaedic Trauma 12, 21–26.

Knauβ, P., 1981. Material properties and strength behaviour of spongy bone tissue at the coxal human femur. Biomedical Technology 26, 200–210.

Knets, I. V., 1978. Mechanics of biological tissues. a review. Polymer Mechanics 13 (2), 434–440.

Kodama, Y., Dimai, H. P., Wergedal, J., Sheng, M., Malpe, R., Kutilek, S., Beamer, W., Donahue, L. R., Rosen, C., Baylink, D. J., Farley, J., 1999. Cortical tibial bone volume in two strains of mice: effects of sciatic neurectomy and genetic regulation of bone response to mechanical loading. Bone 25, 183–190.

Koester, K. J., Ager III, J. W., Ritchie, R. O., 2008. The true toughness of human cortical bone measured with realistically short cracks. Nature Materials 7, 672–677.

Kopperdahl, D. L., Keaveny, T. M., 1998. Yield strain behaviour of trabecular bone. Journal of Biomechanics 31, 601–608.

Kowalczyk, P., 2006. Orthotropic properties of cancellous bone modelled as parameterised cellular material. Computer Methods in Biomechanics and Biomedical Engineering 9 (3), 135–147.

Kowalski, M. J., Schemitsch, E. H., Harrington, R. M., Chapman, J. R., Swiontkowski, M. F., 1996. A comparative biomechanical evaluation of a noncontacting plate and currently used devices for tibial fixation. The Journal of Trauma 40, 5–9.

Lacroix, D., Prendergast, P. J., 2002. A mechano-regulation model for tissue differentiation during fracture healing: analysis of gap size and loading. Journal of Biomechanics 35, 1163–1171.

Laib, A., Newitt, D. C., Lu, Y., Majumdar, S., 2002. New model-independent measures of trabecular bone strength applied to in vivo high-resolution MR images. Osteoporosis International 13, 130–136.

Lan, Y. M., Sotelino, E. D., Chen, W. F., 2003. The strain-space consistent tangent operator and return mapping algorithm for constitutive modelling of confined concrete. International Journal of Applied Science and Engineering 1, 17–29.

Lauer, S. K., Aron, D. N., Evans, M. D., 2000. Finite element method evaluation: articulations and diagonals in an 8-pin type 1B external skeletal fixator. Veterinary Surgery 29, 28–37.

Lennon, A. B., Britton, J. R., MacNiocaill, R. F., Byrne, D. P., Kenny, P. J., Prendergast, P. J., 2007. Predicting revision risk for aseptic loosening of femoral components in total hip arthroplasty in individual patients - a finite element study. Journal of Orthopaedic Research 25 (6), 779–788.

Lettry, S., Seedhom, B. B., Berry, E., Cuppone, M., 2003. Quality assessment of the cortical bone of the human mandible. Bone 32 (1), 35–44.

Levchuk, A., Schneider, P., Meier, M., Vogel, P., Müller, R., 2010. Dynamic 3D investigation of microdamage behavior in murine cortical bone. In: Proceedings of the 17th Congress of the European Society of Biomechanics, Edinburgh, UK.

Lewallen, D. G., Edwards, C. C., 1994. Complications of Orthopaedic Surgery, 3^{rd} Edition. J. B. Lippincott, Philadelphia, Pennsylvania, USA, Ch. Complications of external fixation.

Lewis, G., 1990. Selection of Engineering Materials. Prentice Hall, Englewood Cliffs, New Jersey, USA.

Lim, T.-H., Eck, J. C., An, H., Hong, J. H., Ahn, J.-Y., You, J. W., 1996. Biomechanics of transfixation in pedicle screw instrumentation. Spine 21, 2224–2229.

Liu, D., Weiner, S., Wagner, H. D., 1999. Anisotropic mechanical properties of lamellar bone using miniature cantilever bending specimens. Journal of Biomechanics 32, 647–654.

Lotz, J. C., Cheal, E. J., Hayes, W. C., 1991a. Fracture prediction for the proximal femur using finite element models: Part 1 – linear analysis. Journal of Biomechanical Engineering 113, 353–360.

Lotz, J. C., Cheal, E. J., Hayes, W. C., 1991b. Fracture prediction for the proximal femur using finite element models: Part 2 – nonlinear analysis. Journal of Biomechanical Engineering 113, 361–365.

Lotz, J. C., Gerhart, T. N., Hayes, W. C., 1990. Mechanical properties of trabecular bone from the proximal femur: a quantitative CT study. Journal of Computer Assisted Tomography 14, 107–114.

Lotz, J. C., Gerhart, T. N., Hayes, W. C., 1991c. Mechanical properties of metaphyseal bone in the proximal femur. Journal of Biomechanics 24, 317–329.

McCalden, R. W., McGeough, J. A., Barker, M. B., Court-Brown, C. M., 1993. Age-related changes in the tensile properties of cortical bone. Journal of Bone and Joint Surgery (American) 75 (8), 1193–1205.

McNamara, L. M., Van der Linden, J. C., Weinans, H., Predergast, P. J., 2006. Stress-concentrating effect of resorption lacunae in trabecular bone. Journal of Biomechanics 39, 734–741.

Mercer, C., He, M. Y., Wang, R., Evans, A. G., 2006. Mechanisms governing the inelastic deformation of cortical bone and application to trabecular bone. Acta Biomaterialia 2, 59–68.

Mizuno, E., Hatanaka, S., 1992. Compressive softening model for concrete. Journal of Engineering Mechanics 118, 1546–1563.

Moës, N., Gravouil, A., Belytschko, T., 2002. Non-planar 3D crack growth by the extended finite element and level sets–Part I: Mechanical model. International Journal for Numerical Methods in Engineering 53, 2549–2568.

Moroni, A., Vannini, F., Mosca, M., Giannini, S., 2002. Techniques to avoid pin loosening and infection in external fixation. Journal of Orthopaedic Trauma 16, 189–195.

Naghdi, P. M., Trapp, J. A., 1975. The significance of formulating plasticity theory with reference to loading surfaces in strain-space. International Journal of Engineering Science 13, 785–797.

Nagtegaal, J. C., 1982. On the implementation of inelastic constitutive equations with special reference to large deformation problems. Computer Methods in Applied Mechanics and Engineering 33, 469–484.

Nalla, R. K., Kinney, J. H., Ritchie, R. O., 2003. Mechanistic fracture criteria for the failure of human cortical bone. Nature Materials 2, 164–168.

Nalla, R. K., Kruzic, J. J., Kinney, J. H., Ritchie, R. O., 2004a. Effect of aging on the toughness of human cortical bone: evaluation by R-curves. Bone 35, 1240–1246.

Nalla, R. K., Kruzic, J. J., Kinney, J. H., Ritchie, R. O., 2005. Mechanistic aspects of fracture and R-curve behavior in human cortical bone. Biomaterials 26, 217–231.

Nalla, R. K., Kruzic, J. J., Ritchie, R. O., 2004b. On the origin of the toughness of mineralized tissue: microcracking or crack bridging? Bone 34, 790–798.

Needleman, A., 1987. A continuum model for void nucleation by inclusion debonding. Journal of Applied Mechanics 54, 525531.

Newitt, D. C., van Rietbergen, B., Majumdar, S., 2002. Processing and analysis of in vivo high-resolution MR images of trabecular bone for longitudinal studies: reproducibility of structural measures and micro-finite element analysis derived mechanical properties. Osteoporosis International 13, 278–287.

Nicolella, D. P., Moravits, D. E., Gale, A. M., Bonewald, L. F., Lankford, J., 2006. Osteocyte lacunae tissue strain in cortical bone. Journal of Biomechanics 39, 1735–1743.

Niebur, G. L., 2000. A computational investigation of multiaxial failure in trabecular bone. Ph.D. thesis, Mechanical Engineering, Graduate Division, The University of California, Berkley, USA.

Niebur, G. L., Feldstein, M. J., Yuen, J. C., Chen, T. J., Keaveny, T. M., 2000. High-resolution finite element models with tissue strength asymmetry accurately predict failure of trabecular bone. Journal of Biomechanics 33 (12), 1575–1583.

Niebur, G. L., Keaveny, T. M., 2001. Biaxial yield strains in bovine tibial trabecular bone do not depend of volume fraction. In: ASME Bioengineering Conference. Vol. BED-Vol 50. pp. 23–24.

Nielsen, J. K., Saltzman, C. L., Brown, T. D., 2005. Determination of ankle external fixation stiffness by expedited interactive finite element analysis. Journal of Orthopaedic Research 23, 1321–1328.

Nikonovas, A., Harrison, A. J. L., 2005. A simple way to model wires used in ring fixators: analysis of the wires stiffness effect on overall fixator stiffness. IMechE: Journal of Engineering in Medicine 219, 31–42.

O'Brien, F., Taylor, D., Lee, T. C., 2005. The effect of bone microstructure on the initiation and growth of microcracks. Journal of Orthopaedic Research 23, 475–480.

Oden, Z. M., Selvitelli, D. M., Bouxsein, M. L., 1999. Effect of local density changes on the failure load of the proximal femur. Journal of Orthopaedic Research 17, 661–667.

Odgaard, A., Gunderson, H. J. G., 1993. Quantification of connectivity in cancellous bone, with special emphasis on 3-D reconstructions. Bone 14, 173–182.

Odgaard, A., Hvid, I., Linde, F., 1989. Compressive axial strain distributions in cancellous bone specimens. Journal of Biomechanics 22, 829–835.

Oni, O. O. A., Capper, M., Soutis, C., 1993. A finite element analysis of the effect of pin distribution on the rigidity of a unilateral external fixation system. Injury 24, 525–527.

Pankaj, Moin, K., 1996. On the use of strain softening for prediction of post-peak seismic response of structures. In: 11th World Conference on Earthquake Engineering, Acapulco, Mexico. Elsevier Science Limited.

Pankaj, P., 1990. Finite element analysis in strain softening and localisation problems. Ph.D. thesis, University College of Swansea.

Pankaj, P., Bicanic, N., 1997. Detection of multiple active yield conditions for mohr coulomb elasto-plasticity. Computers and Structures 62, 51–61.

Pankaj, P., Lin, E., 2005. Material modelling in the seismic response analysis for the design of RC framed structures. Engineering Structures 27 (7), 1014–1023.

Pankaj, P., Perrone, C., Beeson, F. A., Phillips, A. T. M., Simpson, A. H. R. W., 2006. Virtual modelling of normal and osteoporotic bone. In: 7th International Symposium on Computer Methods in Biomechanics and Biomedical Engineering. First Numerics, Cardiff, pp. 717–721.

Parameswaran, A. D., Roberts, C. S., Seligson, D., Voor, M., 2003. Pin tract infection with contemporary external fixation: how much of a problem? Journal of Orthopaedic Trauma 17, 503–507.

Parfitt, A. M., 1984. Age-related structural changes in trabecular and cortical bone: cellular mechanisms and biomechanical consequences. Calcified Tissue International 36, 123–128.

Parfitt, A. M., Drezner, M. K., Glorieux, F. H., Kanis, J. A., Malluche, H., Meunier, P. J., Ott, S. M., Recker, R., 1987. Bone histomerphometry: standardization of nomenclature, symbols, and units. Journal of Bone and Mineral Research 2, 595–610.

Pavolini, B., Maritato, M., Turelli, L., D'Arienzo, M., 2000. The Ilizarov fixator in trauma: a 10-year experience. Journal of Orthopaedic Science 5, 108–113.

Peerlings, R. H. J., de Borst, R., Brekelmans, W. A. M., Geers, M. G. D., 2002. Localisation issues in local and nonlocal continuum approaches to fracture. European Journal of Mechanics A/Solids 21, 175–189.

Perilli, E., Baleani, M., Öhman, C., Fognani, R., Baruffaldi, F., Viceconti, M., 2008. Dependence of mechanical compressive strength on local variations in microarchitecture in cancellous bone of proximal human femur. Journal of Biomechanics 41, 438–446.

Peterlik, H., Roschger, P., Klaushofer, K., Fratzl, P., 2006. From brittle to ductile fracture of bone. Nature Materials 5, 52–55.

Petersen, K. B., Pedersen, M. S., oct 2008. The matrix cookbook. Version 20081110.
URL `http://www2.imm.dtu.dk/pubdb/p.php?3274,accessed15/11/2010`

Pettine, K. A., Chao, E. Y. S., Kelly, P. J., 1993. Analysis of the external fixator pin-bone interface. Clinical Orthopaedics and Related Research 293, 18–27.

Phani, K. K., Sanyal, D., 2007. A new approach for estimation of Poisson's ratio of porous powder compacts. Journal of Materials Science 42 (19), 8120–8125.

Phillips, A. T. M., Pankaj, P., Howie, C. R., Usmani, A. S., Simpson, A. H. R. W., 2006. 3D non-linear analysis of the acetabular construct following impaction grafting. Computer Methods in Biomechanics and Biomedical Engineering 9 (3), 125–133.

Phillips, A. T. M., Pankaj, P., Usmani, A. S., Howie, C. R., 2004. The effect of acetabular cup size on the short-term stability of revision hip arthroplasty: a finite element investigation. IMechE: Journal of Engineering in Medicine 218 (4), 239–249.

Pietruszczak, S., Inglis, D., Pande, G. N., 1999. A fabric-dependent fracture criterion for bone. Journal of Biomechanics 32, 1071–1079.

Pistoia, W., van Rietbergen, B., Lochmüller, E.-M., Lill, C. A., Eckstein, F., Rüegsegger, P., 2002. Estimation of distal radius failure load with micro-finite element analysis models based on three dimensional peripheral quantitative computed tomography images. Bone 30 (6), 842–848.

Podolsky, A., Chao, E. Y. S., 1993. Mechanical performance of Ilizarov circular external fixators in comparison with other external fixators. Clinical Orthopaedics and Related Research 293, 61–70.

Pothuaud, L., van Rietbergen, B., Charlot, C., Ozhinsky, E., Majumdar, S., 2004. A new computational efficient approach for trabecular bone analysis using beam models generated with skeletonized graph technique. Computer Methods in Biomechanics and Biomedical Engineering 7, 205–213.

Praemer, A., Furner, S., Rice, D. P., 1992. Musculoskeletal Conditions in the United States. American Academy of Orthopaedic Surgeons, Park Ridge, Illinois, USA.

Prat, J., Juan, J. A., Vera, P., Hoyos, J. V., Dejoz, R., Peris, J. L., Sánchez-Lacuesta, J., Comín, M., 1994. Load transmission through the callus site with external fixation systems: theoretical and experimental analysis. Journal of Biomechanics 27, 469–478.

Prendergast, P. J., Huiskes, R., 1996. Microdamage and osteocyte lacuna strain in bone: a microstructural finite element analysis. Journal of Biomechanical Engineering 118, 240–246.

Qiu, S., Rao, D. S., Fyhrie, D. P., Palnitkar, S., Parfitt, A. M., 2005. The morphological association between microcracks and osteocyte lacunae in human cortical bone. Bone 37, 10–15.

Ramotowski, W., Granowski, R., 1991. Zespol, an original method of stable osteosynthesis. Clinical Orthopaedics and Related Research 272, 67–75.

Rapoff, A. J., Haftka, R. T., 2005. Image-based interpolation of anisotropic elastic constants. In: ASME Summer Bioengineering Conference, Vail, Colorado, USA, June.

Reilly, D. T., Burstein, A. H., 1975. The elastic and ultimate properties of compact bone tissue. Journal of Biomechanics 8 (6), 393–405.

Reilly, G. C., 2000. Observations of microdamage around osteocyte lacunae in bone. Journal of Biomechanics 33, 1131–1134.

Remmers, J. J. C., de Borst, R., Needleman, A., 2003. A cohesive segments method for the simulation of crack growth. Computational Mechanics 31, 69–77.

Ren, F., Case, E. D., Morrison, A., Tafesse, M., Baumann, M. J., 2009. Resonant ultrasound spectroscopy measurement of Young's modulus, shear modulus and Poisson's ratio as a function of porosity for alumina and hydroxyapatite. Philosophical Magazine 89 (14), 1163–1182.

Rho, J. Y., 1996. An ultrasonic method for measuring the elastic properties of human tibial cortical and cancellous bone. Ultrasonics 34 (8), 777–783.

Rho, J. Y., Hobatho, M. C., Ashman, R. B., 1995. Relations of mechanical properties to density and CT numbers in human bone. Medical Engineering & Physics 17 (5), 347–355.

Rho, J. Y., Tsui, T. Y., Pharr, G. M., 1997. Elastic properties of human cortical and trabecular lamellar bone measured by nanoindentation. Biomaterials 18 (20), 1325–1330.

Rho, J. Y., Zioupos, P., Currey, J. D., Pharr, G. M., 2002. Microstructural elasticity and regional heterogeneity in human femoral bone of various ages examined by nano-indentation. Journal of Biomechanics 35 (2), 189–198.

Rice, J. C., Cowin, S. C., Bowman, J. A., 1988. On the dependence of the elasticity and strength of cancellous bone on apparent density. Journal of Biomechanics 21 (2), 155–168.

Rüedi, T. P., Murphy, W. M., 2000. AO Principles of Fracture Management, Volume 1. Thieme, New York.

Russo, C. R., Lauretani, F., Seeman, E., Bartali, B., Bandinelli, S., Di Iorio, A., Guralnik, J., Ferrucci, L., 2006. Structural adaptations to bone loss in aging men and women. Bone 38 (1), 112–118.

Saha, P. K., Chaudhuri, B. B., 1994. Detection of 3-D simple points for topology preserving transformations with application to thinning. IEEE Transactions on Pattern Analysis and Machine Intelligence 16, 1028–1032.

Sakai, M., Bradt, R. C., 1993. Fracture toughness testing of brittle materials. International Materials 38, 53–78.

Schaffler, M. B., Burr, D. B., 1988. Stiffness of compact bone: effects of porosity and density. Journal of Biomechanics 21, 13–16.

Schaffler, M. B., Choi, K., Milgrom, C., 1995. Aging and matrix microdamage accumulation in human compact bone. Bone 17, 521–525.

Schileo, E., Taddei, F., Cristofolini, L., Viceconti, M., 2008. Subject-specific finite element models implementing a maximum principal strain criterion are able to estimate failure risk and fracture location on human femurs tested in vitro. Journal of Biomechanics 41, 356–367.

Schneider, P., Levchuk, A., Vogel, P., Müller, R., 2010. The importance of bone ultrastructure for microdamage accumulation. In: Proceedings of the 17th Congress of the European Society of Biomechanics, Edinburgh, UK.

Schneider, P., Stauber, M., Voide, R., Stampanoni, M., Donahue, L. R., Müller, R., 2007. Ultrastructural properties in cortical bone vary greatly in two inbred strains of mice as assessed by synchrotron light based micro- and nano-CT. Journal of Bone and Mineral Research 22, 1557–1570.

Selby, S., 1974. Standard Mathematical Tables. CRC Press.

Sevostianov, I., Kachanov, M., 2000. Impact of the porous microstructure on the overall elastic properties of the osteonal cortical bone. Journal of Biomechanics 33 (7), 881–888.

Shahar, R., Shani, Y., 2004. Fracture stabilization with type II external fixator vs. type I external fixator with IM pin. Veterinary and Comparative Orthopaedics and Traumatology 17 (2), 91–96.

Silva, M. J. Gibson, L. J., 1997. Modelling the mechanical behaviour of vertebral trabecular bone: effects of age-related changes in microstructure. Bone 21 (2), 191–199.

Simo, J. C., Taylor, R. L., 1985. Consistent tangent operators for rate-independent elastoplasticity. Computer Methods in Applied Mechanics and Engineering 48, 101–118.

Simon, U., Abel, J., Claes, L., March 2006. Minimal size of cubic μFE-models of trabecular bone to predict the apparent stiffness. In: 7^{th} International Symposium on Computer Methods in Biomechanics and Biomedical Engineering, Antibes, France. First Numerics, Cardiff, pp. 661–665.

Simpson, A. H. R. W., Cole, A. S., Kenwright, J., 1999. Leg lengthening over an intramedullary nail. The Journal of Bone and Joint Surgery (British) 81-B, 1041–1045.

Simpson, A. H. R. W., Cunningham, J. L., Kenwright, J., 1996. The forces which develop in the tissues during leg lengthening. Journal of Bone and Joint Surgery (British) 78-B (6), 979–983.

Snyder, S. M., Schneider, E., 1991. Estimation of mechanical properties of cortical bone by computed tomography. Journal of Orthopaedic Research 9, 422–431.

Soininvaara, T. A., Miettinen, H. J. A., Jurvelin, J. S., Suomalainen, O. T., Alhava, E. M. A., Kröger, 2004. Periprosthetic tibial bone mineral density changes after total knee arthroplasty. Acta Orthopaedica 75, 600–605.

Solomon, L., Warwick, D. J., Nayagam, S., 2005. Apley's Concise System of Orthopaedics and Fractures, 3^{rd} Edition. Hooder Arnold, London, UK.

Stauber, M., Müller, R., 2006a. Age-related changes in trabecular bone microstructures: global and local morphometry. Osteoporosis International 17, 616–626.

Stauber, M., Müller, R., 2006b. Volumetric spatial decomposition of trabecular bone into rods and plates - a new method for local bone morphometry. Bone 38, 475–484.

Stauber, M., Rapillard, L., van Lenthe, G. H., Zysset, P., Müller, R., 2006. Importance of individual rods and plates in the assessment of bone quality and their contribution to bone stiffness. Journal of Bone and Mineral Research 21, 586–595.

Stoffel, K., Dieter, U., Stachowiak, G., Gächter, A., Kuster, M. S., 2003. Biomechanical testing of the LCP how can stability in locked internal fixators be controlled? Injury 34, SB11–SB19.

Stolk, J., Verdonschot, N., Mann, K. A., Huiskes, R., 2003. Prevention of mesh-dependent damage growth in finite element simulations of crack formation in acrylic bone cement. Journal of Biomechanics 36, 861–871.

Stölken, J. S., Kinney, J. H., 2003. On the importance of geometric nonlinearity in finite-element simulations of trabecular bone failure. Bone 33, 494–504.

Suquet, P. M., 1985. Elements of homogenization theory for inelastic solid mechanics. In: Sanchez-Palencia, E., Zauoi, A. (Eds.), Homogenization Techniques for Composite Media. Springer, Berlin.

Suwito, W., Keller, T. S., Basu, P. K., Weisberger, A. M., Strauss, A. M., Spengler, D. M., 1992. Geometric and material property study of the human lumbar spine using the finite element method. Journal of Spinal Disorders 5, 50–59.

Swadener, J. G., Pharr, G. M., 2001. Indentation of elastically anisotropic half-spaces by cones and parabolae of revolution. Philosophical Magazine A 81, 447–466.

Tai, K., Ulm, F. J., Ortiz, C., 2006. Nanogranular origins of the strength of bone. Nano Letters 6 (11), 2520–2525.

Taylor, S. J. G., Walker, P. S., Perry, J. S., Cannon, S. R., Woledge, R., 1998. The forces in the distal femur and the knee during walking and other activities measured by telemetry. The Journal of Arthroplasty 13, 428–437.

Tencer, A. F., 2002. Internal Fixation in Osteoporotic Bone. Thieme, New York, New York, USA, Ch. 4, pp. 40–50.

Tencer, A. F., Hampton, D., Eddy, S., 1995. Biomechanical properties of threaded inserts for lumbar interbody spinal fusion. Spine 20, 2408–2414.

Thompson, J. B., Kindt, J. H., Drake, B., Hansma, H. G., Morse, D. E., Hansma, P. K., 2001. Bone indentation recovery time correlates with bond reforming time. Nature 414, 773–776.

Thomson, W. K., 1856. Elements of a mathematical theory of elasticity. Philosophical Transactions of the Royal Society 166, 481–498.

Thurner, P. J., Wyss, P., Voide, R., Stauber, M., Stamponi, M., Sennhauser, U., Müller, R., 2006. Time-lapsed investigation of three-dimensional failure and damage accumulation in trabecular bone using synchrotron light. Bone 39, 289–299.

Tomar, V., 2008. Modeling of dynamic fracture and damage in two-dimensional trabecular bone microstructures using the cohesive finite element method. Journal of Biomechanical Engineering 130, 021021.

Tsai, S. W., Wu, E. M., 1971. A general theory of strength for anisotropic materials. Journal of Composite Materials 5, 58–80.

Turner, C. H., Burr, D. B., 1993. Basic biomechanical measurements of bone: a tutorial. Bone 14 (4), 595–608.

Turner, C. H., Hsieh, Y-F, M. R., Bouxsein, M. L., Baylink, D. J., Rosen, C. J., Grynpas, M. D., Donahue, L. R., Beamer, W. G., 2000. Genetic regulation of cortical and trabecular bone strength and microstructure in inbred strains of mice. Journal of Bone and Mineral Research 15, 1126–1131.

Turner, C. H., Rho, J., Takano, Y., Tsui, T. Y., Pharr, G. M., 1999. The elastic properties of trabecular and cortical bone tissues are similar: results from two microscopic measurement techniques. Journal of Biomechanics 32, 437–441.

Ulrich, D., van Rietbergen, B., Laib, A., Rüegsegger, P., 1999. The ability of three-dimensional structural indices to reflect mechanical aspects of trabecular bone. Bone 25 (1), 55–60.

Ulrich, D., van Rietbergen, B., Weinans, H., Rüegsegger, P., 1998. Finite element analysis of trabecular bone structure: a comparison of image-based meshing techniques. Journal of Biomechanics 31 (12), 1187–1192.

Ural, A., 2009. Prediction of colles' fracture load in human radius using cohesive finite element modeling. Journal of Biomechanics 42, 22–28.

Ural, A., Vashishth, D., 2007. Effects of intracortical porosity on fracture toughness in aging human bone: a μCT-based cohesive finite element study. Journal of Biomechanical Engineering 129, 625–631.

Vahey, J. W., Lewis, J. L., Vanderby, R., 1987. Elastic moduli, yield stress, and ultimate stress of cancellous bone in the canine proximal femur. Journal of Biomechanics 20, 29–33.

Van Buskirk, W. C., Cowin, S. C., Ward, R. N., 1981. Ultrasonic measurement of orthotropic elastic constants of bovine femoral bone. Journal of Biomechanical Engineering 103 (2), 67–72.

van Lenthe, G. H., Stauber, M., Müller, R., 2006. Specimen-specific beam models for fast and accurate prediction of human trabecular bone mechanical properties. Bone 39, 1182–1189.

van Rietbergen, B., 2001. Micro-FE analysis of bone, state of the art. In: ASME Bioengineering Conference. Vol. BED-Vol 50. pp. 107–108.

van Rietbergen, B., Majumdar, S., Pistoia, W., Newitt, D. C., Kothari, M., Laib, A., Ruegsegger, P., 1998a. Assessment of cancellous bone mechanical properties from micro-FE models based on micro-CT, pQCT and MT images. Technology and Health Care 6 (5-6), 413–420.

van Rietbergen, B., Odgaard, A., Kabel, J., Huiskes, R., 1996. Direct mechanics assessment of elastic symmetries and properties of trabecular bone architecture. The Journal of Biomechanics 29 (12), 1653–1657.

van Rietbergen, B., Odgaard, A., Kabel, J., Huiskes, R., 1998b. Relationships between bone morphology and bone elastic properties can be accurately quantified using high resolution computer reconstructions. The Journal of Orthopaedic Research 16, 23–28.

van Rietbergen, B., Pistoia, W., Ulrich, D., Huiskes, R., Rüegsegger, P., 2000. Prediction of trabecular bone failure parameters using a tissue failure and μFE analysis. Journal of Computer Modelling and Simulation in Medicine 1 (2), 98–101.

Vanderoost, J., Jaecques, S., Van der Perre, Boonen, S., D'hooge, J., Lauriks, W., van Lenthe, G. H., 2008. A novel skeleton-based finite element mesh for fast assessment of trabecular bone competence. In: Proceedings of the 8^{th} International Symposium on Computer Methods in Biomechanics and Biomedical Engineering, Porto, Portugal.

Vashishth, D., 2004. Rising crack-growth-resistance behavior in cortical bone: implications for toughness measurements. Journal of Biomechanics 37, 943–946.

Vashishth, D., Behiri, J. C., Bonfield, W., 1997. Crack growth resistance in cortical bone: concept of microcrack toughening. Journal of Biomechanics 30, 763–769.

Vashishth, D., Tanner, K. E., Bonfield, W., 2003. Experimental validation of a microcracking-based toughening mechanism for cortical bone. Journal of Biomechanics 36, 121–124.

Vijayakumar, V., Marks, L., Bremmer-Smith, A., Hardy, J., Gardener, T., 2006. Load transmission through a healing tibial fracture. Clinical Biomechanics 21, 49–53.

Vogel, P., 2008. Investigation of microdamage in murine bone under dynamic load. Master's thesis, Institute for Biomechanics, ETH Zurich, Switzerland.

Voide, R., Schneider, P., Stauber, M., Wyss, P., Stampanoni, M., Sennhauser, U., 2009. Time-lapsed assessment of microcrack initiation and propagation in murine cortical bone at submicrometer resolution. Bone 45, 164–173.

Voor, M. J., Anderson, R. C., Hart, R. T., 1997. Stress analysis of halo pin insertion by non-linear finite element modeling. Journal of Biomechanics 30, 903–909.

Wachter, N. J., Augat, P., Krischak, G. D., Mentzel, M., Kinzl, L., Claes, L., 2001. Prediction of cortical bone porosity in vitro by microcomputed tomography. Calcified Tissue International 68, 38–42.

Watson, M. A., Mathias, K. J., Maffulli, N., 2000. External ring fixators: an overview. IMechE: Journal of Engineering in Medicine 214, 459–470.

Watson, M. A., Matthias, K. J., Maffulli, N., Hukins, D. W. L., 2003. Yielding of the clamped-wire system in the Ilizarov external fixator. IMechE: Journal of Engineering in Medicine 217, 367–374.

Watson, W., Mathias, K. J., Maffulli, N., Hukins, D. W. L., Shepherd, D. E. T., 2007. Finite element modelling of the Ilizarov external fixation system. IMechE: Journal of Engineering in Medicine 221 (8), 863–871.

Weaver, J. K., Chalmers, J., 1966. Cancellous bone: its strength and changes with aging and an evaluation of some methods for measuring its mineral content. The Journal of Bone and Joint Surgery (American) 48-A, 289–298.

Weinans, H., Huiskes, R., Grootenboer, H. J., 1992. The behaviour of adaptive bone-remodeling simulation-models. Journal of Biomechanics 25, 1425–1441.

Weinstein, S. L., 2000. 2000-2010: The bone and joint decade. The Journal of Bone and Joint Surgery (American) 82, 1–3.

Wells, G. N., Sluys, L. J., 2001. A new method for modelling cohesive cracks using finite elements. International Journal for Numerical Methods in Engineering 50, 2667–2682.

Whitehouse, W. J., 1974. The quantitative morphology of anisotropic trabecular bone. Journal of Microscopy 101, 153–168.

Wikenheiser, M. A., Markel, M. D., Lewallen, D. G., Chao, E. Y. S., 1995. Thermal response and torque resistance of five cortical half-pins under simulated insertion technique. Journal of Orthopaedic Research 13, 615–619.

Williams, E. A., Rand, J. A., An, K. N., Chao, E. Y., Kelly, P. J., 1987. The early healing of tibial osteotomies stabilized by one-plane or two-plane external fixation. The Journal of Bone and Joint Surgery (American) 69, 355–365.

Williams, J. L., Lewis, J. L., 1982. Properties and an anisotropic model of cancellous bone from the proximal tibial epiphysis. Journal of Biomedical Engineering 104, 50–56.

Wirtz, D. C., Schiffers, N., Pandorf, T., Radermacher, K., Weichert, D., Forst, R., 2000. Critical evaluation of known bone material properties to realize anisotropic FE-simulation of the proximal femur. Journal of Biomechanics 33, 1325–1330.

Wolff, J., 1892. Das gesetz der transformation der knochen. Tech. rep., Hirschwald, Berlin.

Wu, J. J., Shyr, H. S., Chao, E. Y., Kelly, P. J., 1984. Comparison of osteotomy healing under external fixation devices with different stiffness characteristics. Journal of Bone and Joint Surgery (American) 66, 1258–1264.

Xu, X. P., Needleman, A., 1995. Numerical simulations of dynamic interfacial crack growth allowing for crack growth away from the bond line. International Journal of Fracture 74, 253–275.

Yang, G., Kabel, J., van Rietbergen, B., Odgaard, A., Huiskes, R., Cowin, S. C., 1999. The anisotropic hookes law for cancellous bone and wood. Journal of Elasticity 53 (1), 125–146.

Yang, L., Nayagam, S., Saleh, M., 2003. Stiffness characteristics and interfragmentary displacments with different hybrid external fixators. Clinical Biomechanics 18, 166–172.

Yeni, Y. N., Fyhrie, D. P., 2003. A rate-dependent microcrack-bridging model that can explain the strain rate dependency of cortical bone apparent yield strength. Journal of Biomechanics 36, 1343–1353.

Yoder, P. J., Iwan, W. D., 1981. On the formulation of strain-space plasticity with multiple loading surfaces. Journal of Applied Mechanics 48, 773–778.

Yoon, H. S., Katz, J. L., 1976. Ultrasonic wave propagation in human cortical bone - I theoretical considerations for hexagonal symmetry. Journal of Biomechanics 9 (6), 407–412.

Yoon, Y. J., Cowin, S. C., 2008. The estimated elastic constants for a single bone osteonal lamella. Biomechanics and Modeling in Mechanobiology 7 (1), 1–11.

Youquan, Y., 1986. Stress space and strain space formulation of the elasto-plastic constitutive relations for singular yield surface. Acta Mechanica Sinica 2, 169–177.

Zamani, A. R., Oyadiji, S. O., 2008. Analytical modelling of Kirschner wires in Ilizarov circular external fixators using a tensile model. IMechE: Journal of Engineering in Medicine 222, 967–976.

Zanetti, E. M., Salaorno, M., Grasso, G., Audenino, A. L., 2009. Parametric analysis of orthopedic screws in relation to bone density. The Open Medical Informatics Journal 3, 19–26.

Zhang, G., 2004. Geometric and material nonlinearity in tensioned wires of an external fixator. Clinical Biomechanics 19, 513–518.

Zhang, Q. H., Tan, S. H., Chou, S. M., 2004. Investigation of fixation screw pull-out strength on human spine. Journal of Biomechanics 37, 479–485.

Zioupos, P., Currey, J. D., 1994. The extent of microcracking and the morphology of microcracks in damaged bone. Journal of Materials Science 29, 978–986.

Zioupos, P., Currey, J. D., 1998. Changes in the stiffness, strength, and toughness of human cortical bone with age. Bone 22 (1), 57–66.

Zioupos, P., Wang, X. T., Currey, J. D., 1996. The accumulation of fatigue microdamage in human cortical bone of two different ages *in vitro*. Clinical Biomechanics 11, 365–375.

Zysset, P. K., Curnier, A., 1996. A 3D damage model for trabecular bone based on fabric tensors. Journal of Biomechanics 29, 1549–1558.

Appendices

Appendix A

Local strain over notched regions

As discussed in Chapter 4, experimental compressive testing was applied to notched samples of murine bone to induce cracking. It was necessary to evaluate the applied strain over the notch region to relate it to the observed cracking behaviour. However, the strain was applied over the full notched samples and it was unclear what strain was applied locally at the notched region. In the following, equations were derived to enable calculation of the strain over the notch.

Under the applied axial compressive strains, the geometry of the notched models can be simplified to that of a column with varied cross-sectional area as illustrated in Fig. A-1. The two different cross-sectional areas are labelled A_n and A_u representing the notched and unnotched regions of the exposed bone. The total (applied) strain over this region is denoted ϵ^{app}. It was required to find the axial strains in the notched and unnotched sections (ϵ_n and ϵ_u).

The total strain can be expressed as the following function of the applied displacement (D) and the lengths (L_n and L_u) of the two sections

$$\epsilon^{\text{app}} = \frac{D}{L_n + L_u} \tag{A.1}$$

Since D is itself the sum of the change in length of each section ($\Delta L_n = \epsilon_n L_n$ and $\Delta L_u = \epsilon_u L_u$), Eq. A.1 becomes

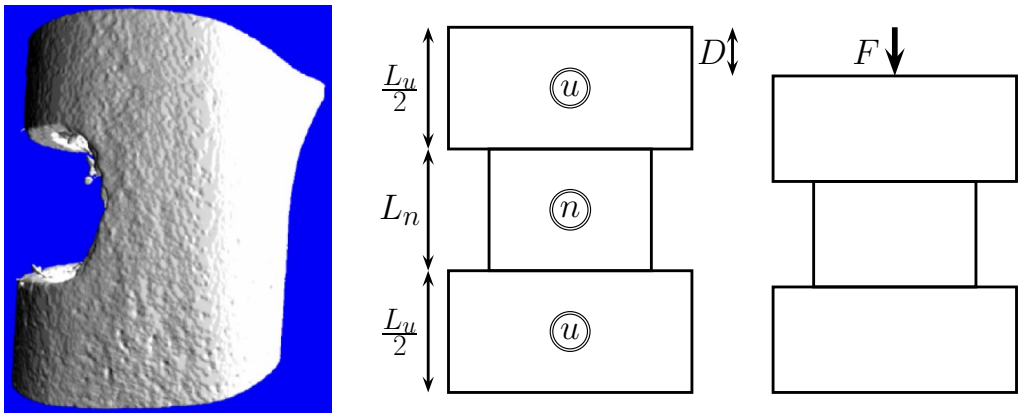

(a) (b)

Figure A-1: Assumed notched model geometry for calculation of the compressive strain over the notch. A typical notched sample and the idealised geometry with applied compressive strain are shown in (a) and (b) respectively. Note the sections labelled 1 and 2 correspond to the unnotched and notched regions respectively.

$$\epsilon^{\text{app}} = \frac{\epsilon_n L_n + \epsilon_u L_u}{L_n + L_u} \tag{A.2}$$

It is required to solve for ϵ_n and ϵ_u using Eq. A.2. Force equilibrium necessitates that the force carried by both sections must be equal (i.e. $F_n = F_u = F$)

$$\begin{aligned} F_n &= F_u \\ \epsilon_n A_n E &= \epsilon_u A_u E \\ \epsilon_n \frac{A_n}{A_u} &= \epsilon_u \end{aligned} \tag{A.3}$$

Substitution of Eq. A.3 into Eq. A.2 produces the following expression for the total strain

$$\begin{aligned} \epsilon^{\text{app}} &= \frac{\epsilon_n L_n + \epsilon_n L_u \frac{A_n}{A_u}}{L_n + L_u} \\ &= \epsilon_n \left[\frac{L_n + L_u \frac{A_n}{A_u}}{L_n + L_u} \right] \end{aligned} \tag{A.4}$$

Which can be rearranged to give the strain in the notched and unnotched sections

$$\epsilon_n = \epsilon^{\text{app}} \left[\frac{L_n + L_u}{L_n + L_u \frac{A_n}{A_u}} \right] \tag{A.5}$$

$$\epsilon_u = \epsilon^{\text{app}} \left[\frac{L_n + L_u}{L_n \frac{A_u}{A_n} + L_u} \right] \tag{A.6}$$

These are a function of both the area and the length of each section. If we set $L_n = L_u$ we get a simpler result

$$\epsilon_n = \frac{2\epsilon^{\text{app}}}{1 + \frac{A_n}{A_u}}$$

In the present study the notch length was approximately 0.89 mm and the total length 4 mm, meaning $L_n = 0.89$ mm and $L_u = 3.11$ mm. This gives the following relation

$$\epsilon_n = \epsilon^{\text{app}} \left[\frac{4}{0.89 + 3.11 \frac{A_n}{A_u}} \right]$$

$$\epsilon_u = \epsilon^{\text{app}} \left[\frac{4}{0.89 \frac{A_u}{A_n} + 3.11} \right]$$

The ratio $\frac{A_n}{A_u}$ was approximately 0.48 in B6 samples and 0.55 in C3H samples. The following expressions can therefore be used to calculate the strains in the notched samples

$$\epsilon_n^{B6} = 1.679\epsilon^{\text{app}} \quad \text{and} \quad \epsilon_n^{C3H} = 1.538\epsilon^{\text{app}}$$
$$\epsilon_u^{B6} = 0.806\epsilon^{\text{app}} \quad \text{and} \quad \epsilon_u^{C3H} = 0.846\epsilon^{\text{app}}$$

Appendix B

Coordinate transformation

The transformation of tensor quantities between general xyz and principal $\hat{x}\hat{y}\hat{z}$ coordinate systems is required in Chapter 5. This can be achieved following the derivation of Clausen et al. (2006). A coordinate transform matrix $\underset{\sim}{\Omega}$ can be formed from the direction cosines of between the two sets of axes such that $\psi^i_{\hat{j}} = \cos(\psi^i_{\hat{j}})$

$$\underset{\sim}{\Omega} = \begin{bmatrix} \psi^x_{\hat{x}} & \psi^x_{\hat{y}} & \psi^x_{\hat{z}} \\ \psi^y_{\hat{x}} & \psi^y_{\hat{y}} & \psi^y_{\hat{z}} \\ \psi^z_{\hat{x}} & \psi^z_{\hat{y}} & \psi^z_{\hat{z}} \end{bmatrix} \tag{B1}$$

$\underset{\sim}{\Omega}$ which relates the general and principal stress or strain coordinate systems can be formed from the eigenvectors of the stress or strain state expressed as a second order tensor. The corresponding coordinate transformation matrix $\underset{\sim}{A}$ which operates on tensor quantities expressed in Voigt form, can be defined as

$$\underset{\sim}{A} = \begin{bmatrix} \psi^x_{\hat{x}}\psi^x_{\hat{x}} & \psi^y_{\hat{x}}\psi^y_{\hat{x}} & \psi^z_{\hat{x}}\psi^z_{\hat{x}} & \psi^x_{\hat{x}}\psi^y_{\hat{x}} & \psi^z_{\hat{x}}\psi^x_{\hat{x}} & \psi^y_{\hat{x}}\psi^z_{\hat{x}} \\ \psi^x_{\hat{y}}\psi^x_{\hat{y}} & \psi^y_{\hat{y}}\psi^y_{\hat{y}} & \psi^z_{\hat{y}}\psi^z_{\hat{y}} & \psi^x_{\hat{y}}\psi^y_{\hat{y}} & \psi^z_{\hat{y}}\psi^x_{\hat{y}} & \psi^y_{\hat{y}}\psi^z_{\hat{y}} \\ \psi^x_{\hat{z}}\psi^x_{\hat{z}} & \psi^y_{\hat{z}}\psi^y_{\hat{z}} & \psi^z_{\hat{z}}\psi^z_{\hat{z}} & \psi^x_{\hat{z}}\psi^y_{\hat{z}} & \psi^z_{\hat{z}}\psi^x_{\hat{z}} & \psi^y_{\hat{z}}\psi^z_{\hat{z}} \\ 2\psi^x_{\hat{x}}\psi^x_{\hat{y}} & 2\psi^y_{\hat{x}}\psi^y_{\hat{y}} & 2\psi^z_{\hat{x}}\psi^z_{\hat{y}} & \psi^x_{\hat{x}}\psi^y_{\hat{y}} + \psi^x_{\hat{y}}\psi^y_{\hat{x}} & \psi^z_{\hat{x}}\psi^x_{\hat{y}} + \psi^z_{\hat{y}}\psi^x_{\hat{x}} & \psi^y_{\hat{x}}\psi^z_{\hat{y}} + \psi^y_{\hat{y}}\psi^z_{\hat{x}} \\ 2\psi^x_{\hat{z}}\psi^x_{\hat{x}} & 2\psi^y_{\hat{z}}\psi^y_{\hat{x}} & 2\psi^z_{\hat{z}}\psi^z_{\hat{x}} & \psi^x_{\hat{z}}\psi^y_{\hat{x}} + \psi^x_{\hat{x}}\psi^y_{\hat{z}} & \psi^z_{\hat{z}}\psi^x_{\hat{x}} + \psi^z_{\hat{x}}\psi^x_{\hat{z}} & \psi^y_{\hat{z}}\psi^z_{\hat{x}} + \psi^y_{\hat{x}}\psi^z_{\hat{z}} \\ 2\psi^x_{\hat{y}}\psi^x_{\hat{z}} & 2\psi^y_{\hat{y}}\psi^y_{\hat{z}} & 2\psi^z_{\hat{y}}\psi^z_{\hat{z}} & \psi^x_{\hat{y}}\psi^y_{\hat{z}} + \psi^x_{\hat{z}}\psi^y_{\hat{y}} & \psi^z_{\hat{y}}\psi^x_{\hat{z}} + \psi^z_{\hat{z}}\psi^x_{\hat{y}} & \psi^y_{\hat{y}}\psi^z_{\hat{z}} + \psi^y_{\hat{z}}\psi^z_{\hat{y}} \end{bmatrix} \tag{B2}$$

Appendix C

Singularity indicators

Singular in tension-tension region

Here it is assumed that yield surface g_{1t} has been violated and that a single return to this surface will result in a state such that $\epsilon_2^e > \epsilon_1^e$. We can derive an indicator μ_{tt} such that $\mu_{tt} > 0$ for a strain state which is singular in this way. After the return to g_{1t} the two relevant principal strains can be found as ϵ_1^e and ϵ_2^e in Eq. 5.30

$$\begin{aligned} \epsilon_1^e &= \epsilon_{T1}^e - g_{1t} \\ \epsilon_2^e &= \epsilon_{T2}^e - g_{1t}\frac{\hat{C}_{21}^e}{\hat{C}_{11}^e} \end{aligned}$$

We can then define the singularity indicator such that

$$\begin{aligned} \mu_{tt} &= \epsilon_2^e - \epsilon_1^e > 0 \\ \mu_{tt} &= \left\{\epsilon_{T2}^e - g_{1t}\frac{\hat{C}_{21}^e}{\hat{C}_{11}^e}\right\} - \{\epsilon_{T1}^e - g_{1t}\} \end{aligned} \tag{C1}$$

Singular in tension-compression region

Here it is assumed that yield surface g_{1t} has been violated and that a single return to this surface will result in a state such that $\epsilon_3^e < Y_c$. We can derive an indicator μ_{tc} such that $\mu_{tc} > 0$ for a strain state which is singular in this way. After the

return to g_{1t} the two relevant principal strains can be found as ϵ_1^e and ϵ_3^e in Eq. 5.30

$$\begin{aligned} \epsilon_1^e &= \epsilon_{T1}^e - g_{1t} \\ \epsilon_3^e &= \epsilon_{T3}^e - g_{1t}\frac{\hat{C}_{31}^e}{\hat{C}_{11}^e} \end{aligned}$$

We then define the singularity indicator such that

$$\begin{aligned} \mu_{tc} &= -\epsilon_3^e + Y_c > 0 \\ \mu_{tc} &= \left\{ -\epsilon_{T3}^e + g_{1t}\frac{\hat{C}_{31}^e}{\hat{C}_{11}^e} \right\} + Y_c \end{aligned} \tag{C2}$$

Singular in compression-tension region

Here it is assumed that yield surface g_{3c} has been violated and that a single return to this surface will result in a state such that $\epsilon_1^e > Y_t$. We can derive an indicator μ_{ct} such that $\mu_{ct} > 0$ for a strain state which is singular in this way. After the return to g_{3c} the two relevant principal strains can be found as ϵ_1^e and ϵ_3^e in Eq. 5.31

$$\begin{aligned} \epsilon_1^e &= \epsilon_{T1}^e + g_{3c}\frac{\hat{C}_{13}^e}{\hat{C}_{33}^e} \\ \epsilon_3^e &= \epsilon_{T3}^e + g_{3c} \end{aligned}$$

We can then define the singularity indicator such that

$$\begin{aligned} \mu_{ct} &= \epsilon_1^e - Y_t > 0 \\ \mu_{ct} &= \left\{ \epsilon_{T1}^e + g_{3c}\frac{\hat{C}_{13}^e}{\hat{C}_{33}^e} \right\} - Y_t \end{aligned} \tag{C3}$$

Singular in compression-compression region

Here it is assumed that yield surface g_{3c} has been violated and that a single return to this surface will result in a state such that $\epsilon_2^e < \epsilon_3^e$. We can derive an indicator μ_{cc} such that $\mu_{cc} > 0$ for a strain state which is singular in this way. After the return to g_{3c} the two relevant principal strains can be found as ϵ_3^e and ϵ_2^e in Eq. 5.31

$$\begin{aligned} \epsilon_3^e &= \epsilon_{T3}^e + g_{3c} \\ \epsilon_2^e &= \epsilon_{T2}^e + g_{3c}\frac{\hat{C}_{23}^e}{\hat{C}_{33}^e} \end{aligned}$$

We then define the singularity indicator such that

$$\begin{aligned} \mu_{cc} &= \epsilon_3^e - \epsilon_2^e > 0 \\ \mu_{cc} &= \{\epsilon_{T3}^e + g_{3c}\} - \left\{\epsilon_{T2}^e + g_{3c}\frac{\hat{C}_{23}^e}{\hat{C}_{33}^e}\right\} \end{aligned} \tag{C4}$$

Singular in tension-tension-tension region

In the present yield criterion a singularity could also occur during a return to a line. This would indicate the need to return to a point at the intersection of three yield surfaces. Consider violation of g_{1t} and g_{2t}. A return to the line marking their intersection leads to

$$\begin{aligned} \underset{\sim}{\hat{\epsilon}}^e &= t\underset{\sim}{\hat{r}}^l + \underset{\sim}{\hat{\epsilon}}^l \\ \begin{Bmatrix} \epsilon_1^e \\ \epsilon_2^e \\ \epsilon_3^e \end{Bmatrix} &= t\begin{Bmatrix} 0 \\ 0 \\ 1 \end{Bmatrix} + \begin{Bmatrix} Y_t \\ Y_t \\ 0 \end{Bmatrix} \end{aligned}$$

from Eq. 5.20 (note only terms relating to the principal directions are shown - all others are 0). The parameter t is defined as in Eq. 5.25, such that in the present example

$$t = \frac{\hat{D}^e_{31}\left(\epsilon_{T1} - Y_t\right) + \hat{D}^e_{32}\left(\epsilon_{T2} - Y_t\right) + \hat{D}^e_{33}\epsilon_{T3}}{\hat{D}^e_{33}}$$

If this return results in $\epsilon^e_3 > \epsilon^e_1$ then the predictor state is in a singular region which requires a return to a point. We can then define a singularity indicator as

$$\begin{aligned} \mu_{ttt} &= \epsilon^e_3 - \epsilon^e_1 > 0 \\ \text{or } \mu_{ttt} &= t - Y_t \\ &= \left\{ \frac{\hat{D}^e_{31}\left(\epsilon_{T1} - Y_t\right) + \hat{D}^e_{32}\left(\epsilon_{T2} - Y_t\right) + \hat{D}^e_{33}\epsilon_{T3}}{\hat{D}^e_{33}} \right\} - Y_t \end{aligned} \tag{C5}$$

Singular in tension-tension-compression region

Following a return to the same line it is possible that the state of strain lies in violation of the remaining compressive yield surface. If this return results in $\epsilon^e_3 < Y_c$ then the predictor state is in a singular region which requires a return to a point. From Eq. C5 we can then define a singularity indicator as

$$\begin{aligned} \mu_{ttc} &= Y_c - \epsilon^e_3 > 0 \\ \text{or } \mu_{ttc} &= Y_c - t \\ &= Y_c - \left\{ \frac{\hat{D}^e_{31}\left(\epsilon_{T1} - Y_t\right) + \hat{D}^e_{32}\left(\epsilon_{T2} - Y_t\right) + \hat{D}^e_{33}\epsilon_{T3}}{\hat{D}^e_{33}} \right\} \end{aligned} \tag{C6}$$

Singular in tension-compression-tension region

Consider violation of g_{1t} and g_{3c}. A return to the line marking their intersection leads to

$$\begin{aligned} \underset{\sim}{\hat{\epsilon}}^e &= t\underset{\sim}{\hat{r}}^l + \underset{\sim}{\hat{\epsilon}}^l \\ \begin{Bmatrix} \epsilon^e_1 \\ \epsilon^e_2 \\ \epsilon^e_3 \end{Bmatrix} &= t \begin{Bmatrix} 0 \\ 1 \\ 0 \end{Bmatrix} + \begin{Bmatrix} Y_t \\ 0 \\ Y_c \end{Bmatrix} \end{aligned}$$

from Eq. 5.20. The parameter t is defined as in Eq. 5.25, such that in the present example

$$t = \frac{\hat{D}^e_{21}\left(\epsilon_{T1} - Y_t\right) + \hat{D}^e_{22}\epsilon_{T2} + \hat{D}^e_{23}\left(\epsilon_{T3} - Y_c\right)}{\hat{D}^e_{22}}$$

If this return results in $\epsilon^e_2 > \epsilon^e_1$ then the predictor state is in a singular region which requires a return to a point. We can then define a singularity indicator as

$$\begin{aligned} \mu_{tct} &= \epsilon^e_2 - \epsilon^e_1 > 0 \\ \text{or } \mu_{tct} &= t - Y_t \\ &= \left\{ \frac{\hat{D}^e_{21}\left(\epsilon_{T1} - Y_t\right) + \hat{D}^e_{22}\epsilon_{T2} + \hat{D}^e_{23}\left(\epsilon_{T3} - Y_c\right)}{\hat{D}^e_{22}} \right\} - Y_t \end{aligned} \tag{C7}$$

Singular in tension-compression-compression region

Following a return to the same line it is possible that the state of strain lies in violation of the remaining compressive yield surface. If this return results in $\epsilon^e_2 < \epsilon^e_3$ then the predictor state is in a singular region which requires a return to a point. From Eq. C7 we can then define a singularity indicator as

$$\begin{aligned} \mu_{tcc} &= \epsilon^e_3 - \epsilon^e_2 > 0 \\ \text{or } \mu_{ttc} &= Y_c - t \\ &= Y_c - \left\{ \frac{\hat{D}^e_{21}\left(\epsilon_{T1} - Y_t\right) + \hat{D}^e_{22}\epsilon_{T2} + \hat{D}^e_{23}\left(\epsilon_{T3} - Y_c\right)}{\hat{D}^e_{22}} \right\} \end{aligned} \tag{C8}$$

Singular in compression-compression-compression region

Consider violation of g_{3c} and g_{2c}. A return to the line marking their intersection leads to

$$\begin{aligned} \underset{\sim}{\hat{\epsilon}}^e &= t\underset{\sim}{\hat{r}}^l + \underset{\sim}{\hat{\epsilon}}^l \\ \begin{Bmatrix} \epsilon_1^e \\ \epsilon_2^e \\ \epsilon_3^e \end{Bmatrix} &= t \begin{Bmatrix} 1 \\ 0 \\ 0 \end{Bmatrix} + \begin{Bmatrix} 0 \\ Y_c \\ Y_c \end{Bmatrix} \end{aligned}$$

from Eq. 5.20. The parameter t is defined as in Eq. 5.25, such that in the present example

$$t = \frac{\hat{D}_{11}^e \epsilon_{T1} + \hat{D}_{12}^e (\epsilon_{T2} - Y_c) + \hat{D}_{13}^e (\epsilon_{T3} - Y_c)}{\hat{D}_{11}^e}$$

If this return results in $\epsilon_1^e < \epsilon_3^e$ then the predictor state is in a singular region which requires a return to a point. We can then define a singularity indicator as

$$\begin{aligned} \mu_{ccc} &= \epsilon_3^e - \epsilon_1^e > 0 \\ \text{or } \mu_{ccc} &= Y_c - t \\ &= Y_c - \left\{ \frac{\hat{D}_{11}^e \epsilon_{T1} + \hat{D}_{12}^e (\epsilon_{T2} - Y_c) + \hat{D}_{13}^e (\epsilon_{T3} - Y_c)}{\hat{D}_{11}^e} \right\} \end{aligned} \tag{C9}$$

Singular in compression-compression-tension region

Following a return to the same line it is possible that the state of strain lies in violation of the remaining tensile yield surface. If this return results in $\epsilon_1^e > Y_t$ then the predictor state is in a singular region which requires a return to a point. From Eq. C9 we can then define a singularity indicator as

$$\begin{aligned} \mu_{cct} &= \epsilon_1^e - Y_t > 0 \\ \text{or } \mu_{cct} &= t - Y_t \\ &= \left\{ \frac{\hat{D}_{11}^e \epsilon_{T1} + \hat{D}_{12}^e (\epsilon_{T2} - Y_c) + \hat{D}_{13}^e (\epsilon_{T3} - Y_c)}{\hat{D}_{11}^e} \right\} - Y_t \end{aligned} \tag{C10}$$

Publications

This research has resulted in the publications listed below.

Journal papers

Donaldson, F., Pankaj, P., Law, A. H., Simpson, A. H., 2008a. Virtual trabecular bone models and their mechanical response. IMechE: Journal of Engineering in Medicine 222, 1185–1195.

Donaldson, F., Pankaj, P., Cooper, D. M. L., Thomas, C. D. L., Clement, J. G., Simpson, A. H. R. W., Relating age and micro-architecture with apparent-level elastic constants: A μFE study of female cortical bone from the anterior femoral midshaft. IMechE: Journal of Engineering in Medicine. To appear, accepted 15/11/2010.

Conference oral presentations

Pankaj, P., Donaldson, F. E., Law, A. H., Simpson, A. H. R. W., 2008. Pseudo-randomised virtual modelling of trabecular bone. In: Proceedings of the 8th International Symposium on Computer Methods in Biomechanics and Biomedical Engineering, Porto, Portugal.

Donaldson, F. E., Law, A. H., Pankaj, P., Simpson, A. H. R. W., 2008b. The modelling of trabecular bone using idealised structures. In: Proceedings of the 8th International Symposium on Computer Methods in Biomechanics and Biomedical Engineering, Porto, Portugal.

Donaldson, F. E., Pankaj, P., Cooper, D. M. L., Thomas, C. D. L., Clement, J. G., Simpson, A. H. R. W., 2009c. The variation of orthotropic elastic con-

stants in the female anterior femoral midshaft: a micro-finite-element study. In: Proceedings of the 12th Congress of the International Society of Biomechanics, Cape Town, South Africa.

Donaldson, F. E., Pankaj, P., Cooper, D. M. L., Thomas, C. D. L., Clement, J. G., Simpson, A. H. R. W., 2010b. Orthotropic elastic constants of cortical bone can be estimated from canal volume ratio. In: Proceedings of the 9th International Symposium on Computer Methods in Biomechanics and Biomedical Engineering, Valencia, Spain.

Pankaj, P., Donaldson, F. E., Simpson, A. H. R. W., 2010. Micro-finite-element analysis of the interactions of cortical bone with fixator wires and half-pins. In: Proceedings of the 9th International Symposium on Computer Methods in Biomechanics and Biomedical Engineering, Valencia, Spain.

Conference poster presentations

Donaldson, F., Pankaj, P., Cooper, D. M. L., Thomas, C. D. L., Clement, J. G., Simpson, A. H. R. W., 2009a. Orthotropic elastic constants of cortical bone can be estimated from canal volume ratio. In: Proceedings of the Annual meeting of the British Orthopaedic Research Society, Newcastle, UK.

Donaldson, F., Pankaj, P., Simpson, A. H. R. W., 2009b. Micro-finite-element analysis of the interactions of cortical bone with fixator wires and half-pins. In: Proceedings of the Annual meeting of the British Orthopaedic Research Society, Newcastle, UK.

Donaldson, F. E., Pankaj, P., Simpson, A. H. R. W., 2010c. External fixation; should fixator configuration be adapted for loss of bone competence. In: Proceedings of the Annual meeting of the British Orthopaedic Research Society, Cardiff, UK.

Donaldson, F., Pankaj, P., Simpson, A. H. R. W., 2010a. The effect of age-related osteoporosis on fixator performance and cortical bone failure at fixator-bone interfaces. In: Proceedings of the 17th Congress of the European Society of Biomechanics, Edinburgh, UK.